Mesoscopic transport through graphene and molybdenum disulfide constrictions

Von der Fakultät für Mathematik, Informatik und Naturwissenschaften der RWTH Aachen University zur Erlangung des akademischen Grades eines Doktors der Naturwissenschaften genehmigte Dissertation

vorgelegt von

Master of Science
Alexander Epping
aus Bocholt

Berichter:
Universitätsprofessor Dr. Christoph Stampfer
Universitätsprofessor Dr. Joachim Knoch

Tag der mündlichen Prüfung: 18.10.2019

Diese Dissertation ist auf den Internetseiten der Universitätsbibliothek online verfügbar.

Abstract

This thesis reports on the investigation of graphene and molybdenum disulfide (MoS_2) nanostructures in low-temperature transport experiments. Two different techniques are employed to study mesoscopic transport and quantum confinement of charge carriers in these two different two-dimensional materials. All devices are fabricated from two-dimensional heterostructures by a state-of-the transfer process.

In a first transport experiment, etched graphene nanoribbons with a width around 40 nm and length of 100 nm fully encapsulated in hexagonal boron nitride (hBN) are investigated. At zero magnetic field the devices show a qualitatively comparable behavior to graphene nanoribbons on SiO_2 or hBN. The magnetotransport reveals a crossover from the Coulomb blockade regime to a regime of completely suppressed transport which is dominated by a much larger energy gap of up to 30 meV induced by electronic correlation effects completely.

In a following set of experiments a novel device scheme to investigate mesoscopic transport through molybdenum disulfide (MoS_2) constrictions using long-lasting photo-induced doping is explored. The doping process is homogeneous and efficient throughout the entire device and yields metallic behavior of the devices at cryogenic temperatures, while preserving the charge carrier mobility of up to $\mu = 600\ \mathrm{cm}^2/(\mathrm{Vs})$ at low temperatures (2 K). Subsequently, the photodoping technique is used to define MoS_2 constrictions by using metal shadow masks. This demonstrates a way to produce complex doping profiles on a scale close to the diffraction limit and allows to observe quantum transport and reproducible signatures of quantum confinement effects in MoS_2 constrictions.

Finally, the photodoping technique is used to fabricate nanoconstrictions by reducing the constriction size. Here, we observe a gate and bias voltage tunable multilevel negative differential conductance (NDC). The NDC shows a maximum peak-to-valley ratio of 1.2. Comparing our results to simulations of the ballistic current through a nanoconstriction based on the non-equilibrium Green's function formalism already published by another group shows a qualitative agreement which indicates that our constrictions might only have a length on order of a few tens of nanometer.

Zusammenfassung

Diese Arbeit berichtet über die Untersuchung von Graphen- und Molybdändisulfid- (MoS_2) Nanostrukturen durch Tieftemperaturtransportexperimenten. Zwei verschiedene Techniken werden verwendet, um den mesoskopischen Transport und die Quanteneinschließung von Ladungsträgern in diesen zwei unterschiedlichen zweidimensionalen Materialien zu untersuchen. Alle Bauteile werden aus zweidimensionalen Heterostrukturen durch einen modernen trockenen Transferprozess hergestellt.

In einem ersten Transportversuch werden geätzte einschichtige Graphen-Nanobänder mit einer Breite von etwa 40 nm und einer Länge von 100 nm, die vollständig in hexagonalem Bornitrid (hBN) eingeschlossen sind, untersucht. Ohne Magnetfeld zeigen die Bauelemente ein qualitativ vergleichbares Verhalten mit Graphen basierten Nanobändern auf SiO_2 oder hBN. Der Magnetotransport zeigt einen Übergang vom Coulomb-Blockade-Regime zu einem Regime komplett unterdrückter Leitfähigkeit, welche von einer sehr größeren Energielücke von bis zu 30 meV dominiert werden, welche durch elektronische Korrelationseffekte induziert wird.

In anschließenden Experimenten wird ein neuartiges Bauteilschema zur Untersuchung des mesoskopischen Transports durch Molybdändisulfid- (MoS_2) Einschnürungen unter Verwendung von photoinduzierter Dotierung untersucht. Der Dotierungsprozeß ist über das gesamte Bauteil homogen, effizient und ergibt ein metallisches Verhalten bei kryogenen Temperaturen (2 K) mit einer Ladungsträgerbeweglichkeit von bis zu $\mu = 600\ \mathrm{cm}^2/(\mathrm{Vs})$. Anschließend wird die Technik angewendet, um mit Hilfe vom Metall-Schattenmasken MoS_2-Einschnürungen zu definieren. Damit erzeugen wir komplexer Dotierungsprofile auf einer Skala nahe dem Beugungslimit, wodurch der Quantentransport und reproduzierbare Signaturen von Quantenein- schluss-Effekten in MoS_2 -Einschnürungen beobachtet werden kann.

Schließlich wird ein Ansatz vorgestellt um die Photodoping-Technik durch Verringerung der Einschnürungsgröße zur Herstellung von MoS_2-Nanobänder zu nutzen. Diese zeigen einen negativer differentieller Leitwert (NDL), welcher durch die Gatter- und Biasspannung abstimmbar ist. Der NDL zeigt ein maximales Spitze-zu-Tal-Verhältnis von 1,2. Der Vergleich zu bereits durch eine andere Gruppe publizierten Simulationen des ballistischen Stroms durch eine Nanoeinschnürung basierend auf dem Nicht-Gleichgewichts-Green'schen Funktionsformalismus zeigen eine qualitative Übereinstimmung und deuten auf auf eine Größe unserer Nano-bänder im Bereich von wenigen Nanometern.

Contents

1 Introduction **1**

2 Graphene and molybdenum disulfide **7**

2.1 Introduction 7

2.2 Band structure of graphene 7

2.3 Band structure of molybdenum disulfide 10

2.4 Hexagonal boron nitride 16

3 Quantum transport in two-dimensional nanostructures **19**

3.1 Transport through a one-dimensional channel 19

3.2 Coulomb blockade effect 20

4 Device fabrication **25**

4.1 Introduction 26

4.2 Mechanical exfoliation 26

4.3 Raman spectroscopy 28

4.4 Assembly of fully encapsulated graphene quantum dots 30

4.5 Assembly of encapsulated molybdenum disulfide contacted with few-layer graphene 32

5 Insulating state in low-disorder graphene nanoribbons **37**

5.1 Introduction 37

5.2 Device characterization 39

5.3 Magnetotransport 41

5.4 Insulating state as a tunnel barrier for a graphene single electron transistor 46

5.5 Conclusion 48

6 Photo-induced remote doping of hBN/MoS_2/hBN heterostructures **51**

6.1 Introduction . . . 51
6.2 Photodoping of layered van-der-Waals materials on hexagonal boron nitride . . . 52
6.3 Photodoping of layered van-der-Waals materials on SiO_2 . . . 55
6.4 Transport characterization before the photodoping . . . 56
6.5 Transport characterization after the photodoping . . . 57
6.6 "Photodoping" effect in MoS_2 on SiO_2 . . . 60
6.7 Conclusion . . . 61

7 Quantum transport through MoS_2 constrictions defined by photodoping 63
7.1 Introduction . . . 64
7.2 Defining constrictions in MoS_2 by photodoping . . . 64
7.3 Transport characterization in two- and four-terminal configuration . . . 66
7.4 Magnetotransport . . . 69
7.5 Conclusion . . . 71

8 Negative differential conductance in molybdenum disulfide nanoconstriction 73
8.1 Introduction . . . 73
8.2 Characterization of charge transport in MoS_2 nanoconstriction . . . 74
8.3 Discussion . . . 80
8.4 Conclusion . . . 82

9 Summary and outlook 85
9.1 Main results . . . 85
9.2 Outlook . . . 87

Appendices 91
A Weak localization in MoS_2 contacted by few-layer graphene . . . 91
A.1 Introduction . . . 91
A.2 Transport characterization . . . 91
A.3 Weak localization measurements at 2 K . . . 92
A.4 Weak localization measurements between 30 mK and 40 K . . . 96
A.5 Conclusion . . . 98
B Fabrication of nanostructures with integrated membrane based on hBN/graphene heterostructures on local gate structures . . . 99

C Probing the nonlinear elasticity of 2d materials via nanoindentation experiments . . . 105
C.1 Introduction . . . 105
C.2 Fabrication . . . 105
C.3 Force indentation measurements . . . 107
C.4 Conclusion . . . 113
D Process parameters . . . 115
E List of samples . . . 122

Publications **125**

Bibliography **127**

List of abbreviations

Abbreviation	Explanation
2DEG	two dimensional electron gas
AFM	atomic force microscopy
CG	central gate
DFT	density functional theory
DI	deionized
DOS	density of states
EBL	electron beam lithography
FLG	few-layer graphene
FWHM	full width at half maximum
GAA	generalized-gradient approximation
hBN	hexagonal boron nitride
LDA	local-density approximation
LED	light emitting diode
LG	left gate
MoS_2	molybdenum disulfide
NDC	negative differential conductance
NEGF	non-equilibrium Green's function formalism
NN	nearest neighbor
PD	photodoping
PMMA	polymethylmethacrylate
PVA	polyvinylalcohol
PVR	peak-to-valley ratio
QD	quantum dot
QHE	quantum Hall effect
QPC	quantum point contact

Abbreviation	Explanation
RG	right gate
RIE	reactive ion etching
SET	single electron transistor
SEM	scanning electron microscopy
SLG	single layer graphene
TMD	transition-metal dichalcogenide
WL	weak localization

Chapter 1

Introduction

Looking at the past one hundred years, the everlasting progress in micro electronics has not only enabled some of the greatest achievements in the younger history such as space exploration, but, maybe much more subtle, changed our everyday life. Twenty years ago a personal computer was rarely seen in the common household and most people had not even heard of the Internet. Today, basically everyone is using information technology at any time and any location without even think about it. This development has been fueled by the enormous increase in processing power, the progress in miniaturization and the reduction of the fabrication costs making electronic devices much more available for everyone. The first transistor developed in the Bell labs in 1947 by John Bardeen, Walter Brattain, and William Shockley had roughly the size of an adult's hand while modern transistors approach dimensions which are not any longer fathomable by most non-scientists. For example, modern smart phones have million times the processing power of NASA computers in the 60's, which guided the lunar missions. This rapid technological advancement has been mostly governed by the great improvement in silicon technology, i. e. material quality, availability and processing tools. Already in 1965, this development has been well predicted by Gordon Moore with his famous Moore's Law stating that the number of transistors in integrated circuits will approximately be doubled every two years [1]. This rapidly increasing processing power enabled through the miniaturization leads to the development of potent supercomputers which are capable of solving computationally highly intensive problems. For example, these supercomputers are vital for our understanding of the weather and climate or of highly complex chemical, biological or physical problems like the structure and properties of chemical compounds, the still limited understanding of the human brain or exploring the early moments of our universe. At some point they might even lead to the development of a real artificial intelligence.

However, in the last couple of years it becomes apparent, that this everlasting progress is indeed not everlasting and that other computational concepts might be much more efficient in solving certain problems. Modern electronics, reaching into the nanometer scale, have to face the challenge of overcoming the physical limits of

downscaling due to quantum effects. Currently, there are many attempts to either push these limits to the extreme by further improving the processing technology, e.g. by implementing new materials into the standard silicon technology or by extending the device geometry into the third dimension [2], or to actually use these quantum effects for entirely new concepts like spintronics [3] or quantum information [4]. A promising way to actually do quantum computation is to use the electron spin of coupled single-electron quantum dots, which has first been proposed by David DiVincenzo and Daniel Loss [5] in 1998. Here, the electrons are confined on nanometer scaled isolated islands, which are called quantum dots (QDs) and can be coupled at will. The computation is done by manipulating and detecting the state of the electron spin. These quantum dots resemble classical transistors which are a key building block of todays central processing units [6, 7] and hence a quantum dot is often refereed to as a quantum bit (qbit). These ideas have been first implemented in gallium-arsenide (GaAs) heterostructures as they offer a well-known material system with already extremely high quality [8] but which suffers from hyperfine interaction [6, 9] leading to decoherence of the spin system. Although there has been recently made a lot of progress to diminish this effect or even to use it in order to recover the spin coherence [6, 10–13], other materials and material systems, which promise intrinsically weak hyperfine interaction and very long spin coherence times, have come into the focus of current research. One of these materials systems is silicon (Si) and its related silicon-germanium (SiGe) heterostructure as the natural composition of Si is already 95% of non-magnetic isotopes and recent efforts optimized a purifying process, which yields nearly 100% zero-nuclearspin ^{28}Si [7]. Since then, the field is picking up a lot of momentum. Fully controllable two-qbit devices have recently been achieved [14, 15] and industrial partners like Intel are heavily supporting academia with money and their highly advanced silicon foundries [16].

As another route, a completely new class of materials, the two-dimensional (2d) van-der-Waals crystals, have sparked the interest of many scientists across the world. Since the discovery of a very simple fabrication method of single layers of graphite by Konstantin Novosolev and Andre Geim in 2004 [17], this research field is developing with an enormous speed. Remarkably, a single layer of graphite called graphene can be extracted from the graphitic source material by just using an adhesive tape. Hence, even a single atomic layer is relatively cheap and easy to fabricate. The huge interest has been sparked due to graphene's extraordinary mechanical, optical and electrical properties. Graphene, arranged in a honeycomb-like crystal structure, has a linear band structure around zero energy without a bandgap where the charge carriers resemble massless Dirac fermions [18]. Additionally, the chiral character of the charge carriers in graphene prevents direct backscattering from long range scattering centers. Recently, an extraordinary charge carrier mobility of 350,000 $cm^2\ V^{-1}\ s^{-1}$ at room temperature has been shown [19]. Despite the absence of a band gap, this extremely high room temperature mobility makes graphene a very exciting material for gigahertz electronics [20] or even for terahertz applications

[21]. In combination with the extraordinary strength, graphene exhibits a Young's modulus of 1 TPa [22], and its light weight graphene is also a very promising material for flexible electronics and devices based on nanomechanics [23]. In the framework of new concepts for data processing, scientists envision graphene since the beginning as a potential host for QDs [24, 25]. Graphene is of particular interest as long spin relaxation times due to its weak spin-orbit interaction [26, 27] and a weak hyperfine coupling [28] are expected. However, the linear non-gaped bandstructure responsible for the extraordinary electrical properties also presents a great challenge for the implementation of quantum dots in single layer graphene. In order to confine electrons we need to induce an energy gap and circumvent the Klein tunneling present in graphene [29]. The most common strategy of opening up a gap is by etching graphene into nanostructures and using a disorder-induced energy gap [30–33], which results in limited control over the introduced tunnel barriers.

Still, a lot of fundamental phenomena like the electron-hole crossover [34], the observation of spin states [35], the measurement of charge relaxation times [36] or the back-action of two stacked graphene QDs [37] have been investigated using nanostructured single-layer graphene QDs. All these experiments have in common that they rely on disorder induced energy gaps in narrow graphene constrictions, which is to a large degree uncontrollable. It has been shown in a wide variety of studies that the use of hexagonal boron nitride (hBN) as a substrate for graphene has the potential to significantly reduce the disorder yielding devices with very high electronic quality [38–42] and thus give hope for more reproducibility also for tuning nanostructures. Unfortunately, recent studies have shown that a significant part of the overall disorder results from the rough edges for devices with dimensions around 100 nm [43] or less. Additionally, the extrinsic disorder induced e.g by the fabrication process still can limit the device performance [44]. The next level of device quality is reached by fully encapsulating graphene in hBN [40] and consequently reducing the extrinsic disorder by preventing contaminations on the graphene flake. It has to be taken into account that, for structured graphene, the edges are still subject to the environment. An alternative to single-layer graphene is to electrostatically confine electrons in bilayer graphene by opening up a band gap with a perpendicular electric field [45–48] in similarity to more classical two-dimensional electron gases (2DEGs). This technique suffered until recently [49–52] from relatively limited maximum resistances. By increasing the homogeneity of the perpendicular electric field especially at the edges of the bilayer graphene flake the maximum resistance can be significantly increased but which comes along with additional technological challenges.

Other alternatives to bilayer graphene have emerged over the last years as the class of 2d crystals has expanded into a whole group of different materials with very different properties ranging from two-dimensional superconductors to semiconductors or insulators making it possible to tailor heterostructures to specific needs. Among these materials are the transition-metal dichalcogenides (TMDs) represented by the chemical formula MX_2 with M a transition metal element and X a chalcogen

element. In contrast to graphene, TMDs offer a band gap in the range of visible light while still promising a high charge carrier mobility compared to silicon. Remarkably, the band gap shows a transition from indirect (bulk to bilayer) to direkt (singe-layer) [53] while being additionally tunable by strain [54]. For classical transistor devices TMDs are of great interest as e.g. monolayer molybdenum disulfide (MoS_2) field-effect transistors show no short-channel effects [55], a high maximal current density of up to 300 μA/μm [56] and large current on/off ratio around 10^8 [57]. Especially for optoelectronic devices, combining these electrical and optical properties give rise for many potential applications including LEDs, lasers or photodetectors. E.g. hybrid phototransistors based on few-layer MoS_2 and lead sulfide quantum dots show a very high photoresponsivity of 6×10^5 A/W in phototransistors [58]. Recently, MoS_2 phototransistors achieved very high specific detectivities around 3.5×10^{14} [59]. Additionally, first LEDs have been realized in ultrathin WSe_2 and MoS_2 gated by liquid electrolytes [60]. Besides the great potential for classical electronics and optoelectronics, the semiconducting nature of MX_2 allows to electrostatically confine charge carriers in well defined nanostructures and hence these materials are considered as a suitable platform to host qubits. The conduction band offers the possibility of implementing spin-valley (Kramers) qubits in single-layer MX_2 as it exhibits a strong spin-orbit splitting [61]. Especially with optical access these QDs could prove as an ideal system to study spatial confined electrons. Recently, scientists start to experimentally investigate quantum transport in MoS_2 and WSe_2 which has become possible by the improvements in the fabrication technology of 2d heterostructures. By encapsulating MoS_2 in hexagonal boron nitride (hBN) using an entirely dry transfer technique and implementing graphitic contacts the charge carrier mobility reaches values of around 30,000 $cm^2\ V^{-1}\ s^{-1}$ in few-layer devices with low contact resistances of around 2 k$\Omega\,\mu$m at large gate voltages [62]. Still, the field of quantum transport in MoS_2 and other TMDs is scarcely explored so far. Very recently first experiments on broken symmetry states [63, 64] and quantum confinement in one- and zero-dimensional structures [65, 66] have been demonstrated.

The following work focuses on mesoscopic transport and quantum confinement of charge carriers in graphene and MoS_2 heterostructures in order to find alternative approaches to order dominated nanostructures of etched single-layer graphene. The first approach is to further reduce the disorder in nanostructured single-layer graphene by fully encapsulating the graphene between hBN and thus to study the first fully encapsulated singe-layer graphene nanostructures. A second approach focuses around a new method of obtaining confinement in MoS_2 heterostructures. Here, a remote photodoping effect, which has already been observed in hBN-graphene heterostructures [67, 68], will be exploited and the effect of the photodoping on the charge carrier mobility will be discussed. In combination wit metallic shadow masks, this technique is used to define stable and smooth sub-wavelength lateral doping profiles in MoS_2. Further, we use this technique to create lateral tunnel junctions purely from MoS_2 which enable us to study the influence of potential defects intrinsically present in natural MoS_2 on the tunneling characteristic of such

devices revealing negative differential conductance.

This thesis is organized on the following way: In chapter 2 the crystal structure and electronic bandstructure of single-layer graphene and MoS_2 will be briefly discussed. Additionally, the crystal structure of hBN will be introduced. Chapter 3 will introduce the main transport phenomena encountered in the thesis. Chapter 4 will cover the key elements of the fabrication methods used. The following chapter 5 reports on the electrical characterisation of etched single-layer graphene nanoconstrictions with a width around 40 nm and length around 100 nm fully encapsulated in hexagonal boron nitride. Chapter 6 report on the photodoping effect of MoS_2 resting hBN and its effect on the contact resistance and charge carrier mobility. In chapter 7 the quantum transport through constrictions in MoS_2 defined by the photodoping is discussed. Chapter 8 discusses MoS_2 tunnel junctions resulting from the photodoping if the shadow masks are separated by less than the diffraction limit of the light used to photodope. The thesis is concluded in chapter 9 by summarizing the results and giving an outlook for future experiments and tasks to improve the quality of MoS_2 quantum transport devices for further studies on confined charge carriers in MoS_2 and related TMD materials.

Chapter 2

Graphene and molybdenum disulfide

2.1 Introduction

Van-der-Waals heterostructures based on graphene and transition metal dichalcogenides (TMDs) have attracted a lot of attention in solid-state research in the last years. This interest is related to the remarkable electronic and optical properties which are a direct consequence of their two-dimensional nature and the resulting unique electronic band structures. In the following chapter a short summary of the derivation of the electronic band structure of single-layer graphene (SLG) and molybdenum disulfide (MoS_2) in the frame of tight-binding is presented. As for the tight-binding calculations the crystal structure is very important each material will be shortly introduced. For a more detailed review please see references [18, 69, 70] for graphene and references [71–73] for MoS_2.

2.2 Band structure of graphene

Graphene is a monolayer of carbon atoms arranged in a hexagonal crystal structure as depicted in Figure 2.1 (a) with six electrons per atom. Key for the electronic, mechanical and optical properties are the the $2s^2$ and $2p^2$ electrons whereas the $1s^2$ electrons are tightly bound to the atomic core and can be neglected. The $2s^2$ and the $2p^2$ orbitals hybridize and form three covalently bonded sp^2-orbitals with an angle of 120° which results in the hexagonal x-y-plane crystal structure. Due to their high overlap, the sp^2-orbitals are strongly bound. Consequently, the formed bonding and antibonding σ-bands have a large energy separation. The remaining p_z-orbital is orientated perpendicular to the sp^2-orbitals with a relatively small overlap to the neighboring p_z-orbital. Focusing on the low-energy transport properties which is useful for low-temperature transport measurements in pristine graphene we can concentrate on the p_z-orbital.

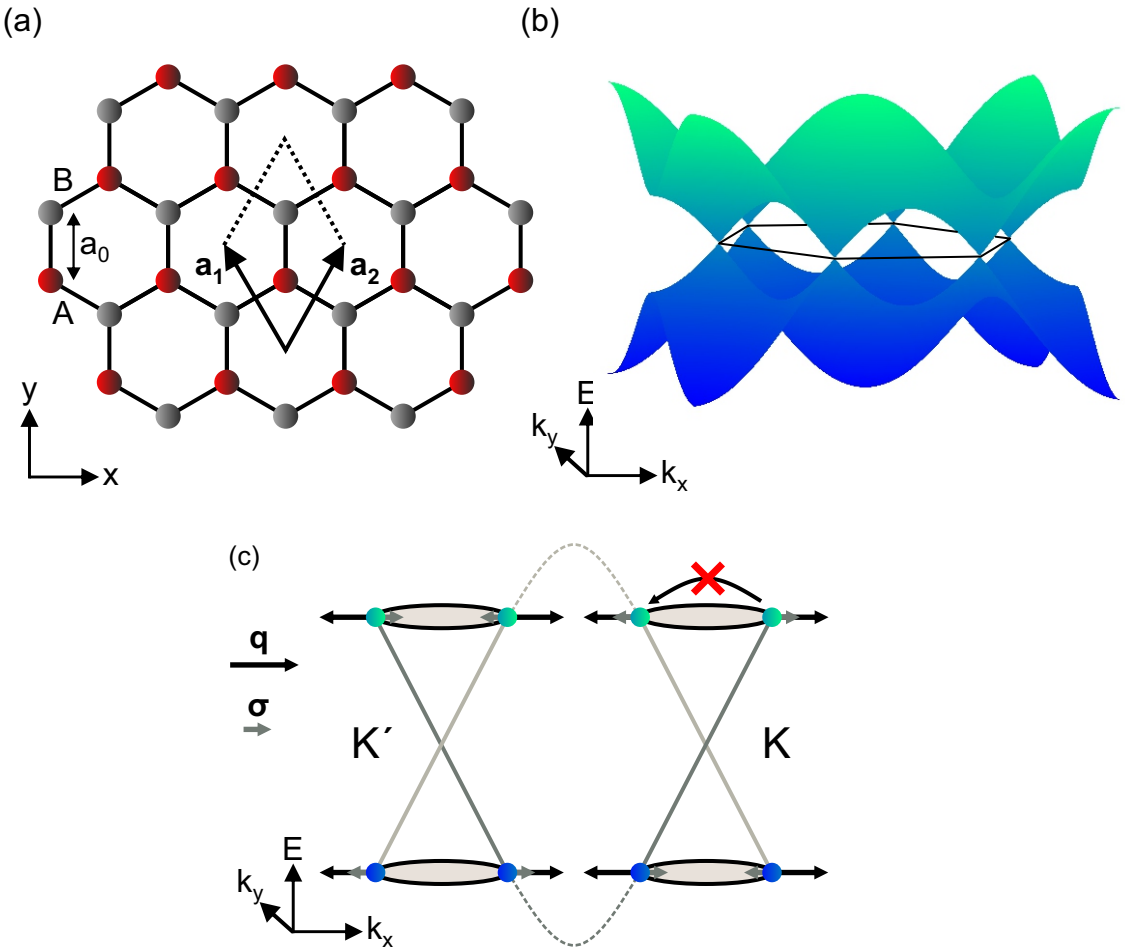

Figure 2.1: (a) Schematic illustration of the graphene lattice. Two different atoms A (red) and B (gray), with a distance of $a_0 = 1.42$ Å between each other, denote the two sublattices. $\boldsymbol{a}_1$ and $\boldsymbol{a}_1$ represent the two basis vectors forming the unit cell. (b) Band structure of graphene with the valence (π) band in blue and conduction (π^*) band in green. (c) Schematic of the linear low energy dispersion of graphene at K and K' with the direction of the momentum $\boldsymbol{q}$ (black arrows) and pseudo-spin $\boldsymbol{\sigma}$ (gray arrows). Direct intra-valley scattering of electrons is suppressed as it would require a change of the symmetry of the wave function (pseudo-spin flip).

Thus, a reasonable approach to approximate the electronic properties of graphene is the tight-binding method using a superposition of the atomic p_z-orbitals at each lattice site and a triangular Bravais lattice with a two atomic basis with the atoms A and B and a bond length of $a_0 = 1.42$ Å. The two basis vectors are given by $\mathbf{a_1} = (a/2)(-1, \sqrt{3})$ and $\mathbf{a_2} = (a_0/2)(1, \sqrt{3})$ with the lattice constant $a = \sqrt{3}\, a_0$. This simple approach has already been considered as early as 1947 by R. P. Wallace [74] long before the experimental discovery of the material. The Schrödinger equation is solved considering only the nearest neighbor atoms which yields the following energy

dispersion [18, 69, 70, 74]

$$E(k_x, k_y) \;=\; \pm t\sqrt{1 + 4\cos\left(\frac{\sqrt{3}ak_y}{2}\right)\cos\left(\frac{ak_x}{2}\right) + 4\,\cos^2\left(\frac{ak_x}{2}\right)}, \tag{2.1}$$

where t denotes the nearest neighbor hopping integral and can be approximated to $t \approx 3$ eV and $a = \sqrt{3}\,a_0 \approx 2.46$ Å is the in-plane lattice constant [18]. The resulting band structure with the valence (π) and conduction (π^*) band in the first Brillouin zone is shown in Figure 2.1 (b). In the center of the Brillouin zone, which is named Γ-point, the energy difference between the conduction and valence band is around $6t \approx 18$ eV. Only at the edges of the Brillouin zone the two bands touch at six points providing graphene its famous semi-metal band structure. These six points correspond to two non-equivalent groups of three equivalent points each, conventionally denoted by K and K', and are known as the Dirac points. As we consider the band structure in the limit of small energies the dispersion relation can be further approximated by a linear expansion around K and K'. This is justified as in undoped graphene the Fermi energy E_F is exactly at the touching points. This leads to the following energy dispersion of massless Dirac fermions [18, 69, 70, 74]

$$E(\boldsymbol{\kappa}) \;=\; \pm\hbar v_F \mid \boldsymbol{\kappa} \mid, \tag{2.2}$$

where $\boldsymbol{\kappa} \;=\; \boldsymbol{k} - \boldsymbol{K}$ is a small vector relative to K respectively K' and $v_F \;=\; 3a_0t/2\hbar \;\approx\; 10^6\,\mathrm{m/s}$ is the Fermi velocity. The linear dispersion relation resembles the dispersion relation of massless Dirac fermions but with the velocity v_F in place of the speed of light. Accordingly, in the low energy regime the related Hamiltonian H_K can be expressed in terms of the Pauli matrices $\boldsymbol{\sigma} = (\sigma_x, \sigma_y)$ at the K-point (at K', $\boldsymbol{\sigma}^\star = (\sigma_x, -\sigma_y)$) and the Bloch wave vector $\boldsymbol{\kappa}$ relative to the K/K'-point and has the form of the two-dimensional Dirac-Weyl Hamiltonian [18, 75]

$$\mathbf{H}_K = v_F\hbar\,\boldsymbol{\sigma}\cdot\boldsymbol{\kappa}. \tag{2.3}$$

The eigenvalue problem can be solved at K and K' each by a two-component vector ("(pseudo-)spinor"), whose components are the $\boldsymbol{\kappa}$-dependent expansion coefficients of the Bloch wave function when expanded in a basis of Wannier functions localized on the two sublattices. The corrsponding eigenfunctions at the K- and K′-point are given by

$$\psi_{\pm,\boldsymbol{K}}(\boldsymbol{\kappa}) \;=\; \frac{1}{\sqrt{2}}\begin{pmatrix} e^{-i\theta_{\boldsymbol{\kappa}}/2} \\ \pm e^{i\theta_{\kappa}/2} \end{pmatrix} \text{ and } \psi_{\pm,\boldsymbol{K'}}(\boldsymbol{\kappa}) \;=\; \frac{1}{\sqrt{2}}\begin{pmatrix} e^{i\theta_{\boldsymbol{\kappa}}/2} \\ \pm e^{-i\theta_{\boldsymbol{\kappa}}/2} \end{pmatrix}. \tag{2.4}$$

The sign ± refers to the bonding π and the antibonding $\pi^\star$ band and $\theta_{\boldsymbol{\kappa}}$ is the angle $\theta(\boldsymbol{\kappa}) = \arg(\kappa_x + i\kappa_y)$ in the momentum plane. Formally very similar to a spin state, $\boldsymbol{\sigma}$ is referred as the pseudo-spin but linked to the symmetry of the

wave function. Importantly, the projection of the pseudo-spin onto the direction of momentum adds a helicity $\hat{h} = \boldsymbol{\sigma} \cdot \boldsymbol{\kappa} / (2 |\boldsymbol{\kappa}|)$ to the system, which can be regarded as a good quantum number. The helical character of charge carriers in graphene has an important consequence for the electronic transport considering the different scattering processes. Intra-valley scattering of electrons is suppressed as the wave function would need to change its symmetry and "flip" the pseudo-spin. Inter-valley backscattering on the other hand can only take place by a large momentum transfer which is generally only provided by sharp scattering potentials in real space like defect states [18, 76, 77]. Consequently, a remarkably large electron mobility even at room temperature in pristine graphene can be found [40, 78]. Figure 2.1 (c) illustrates the linear dispersion relation at K and K' with $\boldsymbol{\kappa}$ and $\boldsymbol{\sigma}$ projected onto the $k_x - k_y$ plane.

2.3 Band structure of molybdenum disulfide

Graphene's linear, non-gapped band structure leads to unqiue electronic properties. However, at the same time, it makes it very difficult to electrostatically confine charge carriers in well-defined device geometries due to the effect of Klein tunneling [29]. By contrast, molybdenum disulfide (MoS_2) is a two-dimensional semiconductor and allows soft electrostatic confinement similar to two-dimensional electron gases (2DEGs) in conventional semiconductor heterostructures such as e.g. AlGaAs/GaAs [9, 79, 80].

The basic building block of a MoS_2 crystal consists of three atomic planes with an inner plane of molybdenum (Mo) atoms between two planes of sulfur (S) atoms [81]. Each of the three atomic planes has a triangular lattice structure. The molybdenum atom is covalently bound to six sulfur atoms and each sulfur atom to three molybdenum atoms. When projecting the three atomic planes onto one single plane, they form a two-dimensional triangular lattice with a triatomic base, where one sublattice (A) is given by one molybdenum atom per site and a second sublattice (B) by two sulfur atoms per site, as depicted in Figure 2.2 (a)). Bulk MoS_2 is formed by an infinitely extended stack of these monolayers, with each single-layer being rotated by 180° with respect to the vertical neighbors. The A-sublattice of one layer is directly on top of the B-sublattice of the neighboring one (see Figure 2.2 (b)). The individual layers are bound by van-der-Waals forces to each other. The distance between a pair of in-plane nearest-neighbor molybdenum atoms or sulfur atoms is the in-plane lattice constant $a = 3.16$ Å. The nearest-neighbor molybdenum-sulfur distance is $b = \sqrt{7/12}\, a = 2.41$ Å and the molybdenum and sulfur planes are separated by $u = 1.59$ Å [81, 82]. The distance between two molybdenum planes is $c' = 6.14$ Å, resulting in an out-of-plane lattice constant of $c = 2c'$ (see Figure 2.2 (c)). MoS_2 features a perfect trigonal prism structure. The two in-plane lattice vectors for the single-layer are $\mathbf{a}_1 = (a/2)(-1, \sqrt{3})$ and $\mathbf{a}_2 = (a/2)(1, \sqrt{3})$ [81, 83]. Symmetry-wise, it is important to note that the structure of bulk MoS_2 is inversion-

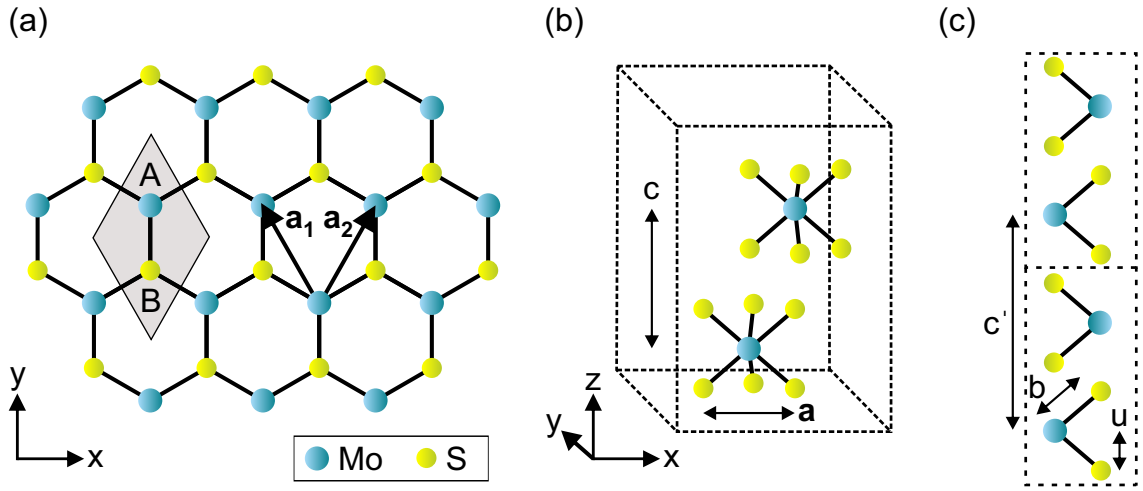

Figure 2.2: (a) Schematic illustration of a single layer molybdenum disulfide crystal (MoS_2) lattice projected in-plane. The different atoms, one molybdenum atom (blue) and two sulfur (yellow) per site (see also (c)), denote the two sublattices A and B. The corresponding unit cell is donated by the gray area. $\boldsymbol{a}_1$ and $\boldsymbol{a}_1$ represent the two basis vectors. (b) Two single-layers form the bulk unit cell with the distance $c = 6.14$ Å between two molybdenum planes. (c) The single-layers are alternatingly rotated by 180°, with the A-sublattice of one layer on top of the B-sublattice of the other. The out-of-plane lattice constant is $c' = 12.28$ Å. The distance between nearest neighbor molybdenum-sulfur atoms is $b = \sqrt{7/12}\ a_0$ and the molybdenum and sulfur planes are separated by $u = 1.59$ Å.

symmetric, while single-layer MoS_2 (or more generally multilayer MoS_2 with an odd number of layers) is not. In the following, we will outline how to approximate the band structure of MoS_2 at the high-symmetry points of the Brillouin zone in the frame of tight-binding. As in graphene, we write the electronic wave function as a superposition of atomic wave functions at each lattice site. In particular, we will focus on the band structure of single-layer MoS_2 near the K-point. Several theoretical studies have been performed with varying degrees of complexity by limiting the amount of orbitals used in the calculation [82–88]. The simplest models, which only consider the d-orbitals of the molybdenum, can approximate the low-energy dispersion of single-layer MoS_2 at the K-point but break down for the rest of the Brillouin zone or multilayer MoS_2. In order to obtain a suitable tight-binding model for a single-layer, which is valid in the entire Brillouin zone and which can easily be generalized to multilayer MoS_2 by including the interlayer hopping, we also have to consider the p-orbitals of the sulfur. For single-layer MoS_2 in particular, we have to include the five $4d$-orbitals of the molybdenum and six $3p$-orbitals of the two sulfur atoms, which together cover 93% of the total orbital weight [82]. This results in a total of eleven orbitals and consequently can describe the first four conduction and seven valence bands between -7 and 5 eV around the Fermi level [82, 83]. Density

functional theory (DFT) is commonly used as a reference [82, 83]. Following reference [82] and [83], using these eleven orbitals we can now construct the following orbital wave function for single-layer (SL) MoS_2:

$$\phi_{pd} = \phi_{p^t}, \phi_d, \phi_{p^b} = (p_x^t, p_y^t, p_z^t, d_{3z^2}, d_{x^2-y^2}, d_{xy}, d_{xz}, d_{yz}, p_x^b, p_y^b, p_z^b). \tag{2.5}$$

The contribution of the top (t) and bottom (b) plane of sulfur atoms is donated by p_α^t and p_α^b, respectively. Fourier-transforming ϕ_{pd} into momentum space, the tight-binding Hamiltonian in the orbital basis of Eq. 2.5 is found to be

$$\boldsymbol{H}^{SL} = \sum_{i,j,\boldsymbol{k}} \phi_i^\dagger(\boldsymbol{k}) \hat{H}_{ij}(\boldsymbol{k}) \phi_j(\boldsymbol{k}). \tag{2.6}$$

The Hamiltonian is composed of the intra-plane hopping of the top and bottom sulfur plane ($\boldsymbol{H}_{p^t,p^t}, \boldsymbol{H}_{p^b,p^b}$) and of the molybdenum plane ($\boldsymbol{H}_{d,d}$) on the diagonal and the inter-plane hopping between the top and bottom sulfur plane ($\boldsymbol{H}_{p^t,p^b}$) and between the molybdenum and sulfur atoms ($\boldsymbol{H}_{d,p^t}, \boldsymbol{H}_{d,p^b}$). This results in the following Hamiltonian

$$\boldsymbol{H} = \begin{pmatrix} \boldsymbol{H}_{p^t,p^t} & \boldsymbol{H}_{d,p^t}^\dagger & \boldsymbol{H}_{p^t,p^b} \\ \boldsymbol{H}_{d,p^t} & \boldsymbol{H}_{d,d} & \boldsymbol{H}_{d,p^b} \\ \boldsymbol{H}_{p^b,p^b}^* & \boldsymbol{H}_{d,p^b}^\dagger & \boldsymbol{H}_{p^b,p^b} \end{pmatrix}. \tag{2.7}$$

Eq. 2.6 can explicitly be solved to obtain the energy dispersion for the first four conduction and seven valence bands in the whole Brillouin zone. In the frame of a nearest-neighbor (NN) approximation, this involves a total of 36 free parameters, which describe the hopping integrals and the on-site energy [83]. The resulting band structure of single-layer MoS_2 is shown in Figure 2.3. The electronic dispersion obtained from these tight-binding calculations corresponds well to the results obtained from density functional theory (DFT).

Following reference [87], if we focus on the conduction band minimum and valence band maximum at the K and K'-valley, the complexity can be significantly reduced by only considering the $|\phi_1^1\rangle = d_{z^2}$, $|\phi_1^2\rangle = d_{xy}$ and $|\phi_2^2\rangle = d_{x^2-y^2}$ orbitals of the molybdenum and the hopping between these orbitals of nearest-neighbor atoms [87]. The NN-Hamiltonian in this three-band approximation is then given by

$$\boldsymbol{H}_K^{NN} = \begin{pmatrix} H_0 & H_1 & H_2 \\ H_1^* & H_{11} & H_{12} \\ H_2^* & H_{12}^* & H_{22} \end{pmatrix}, \tag{2.8}$$

with

$$H_0 = 2E_{11}^{11}(\cos 2\alpha + 2\cos\alpha\cos\beta) + \epsilon_1, \tag{2.9}$$

$$H_1 = -2\sqrt{3}E_{12}^{12}\sin\alpha\sin\beta + 2iE_{12}^{11}(\sin 2\alpha + 2\sin\alpha\sin\beta), \tag{2.10}$$

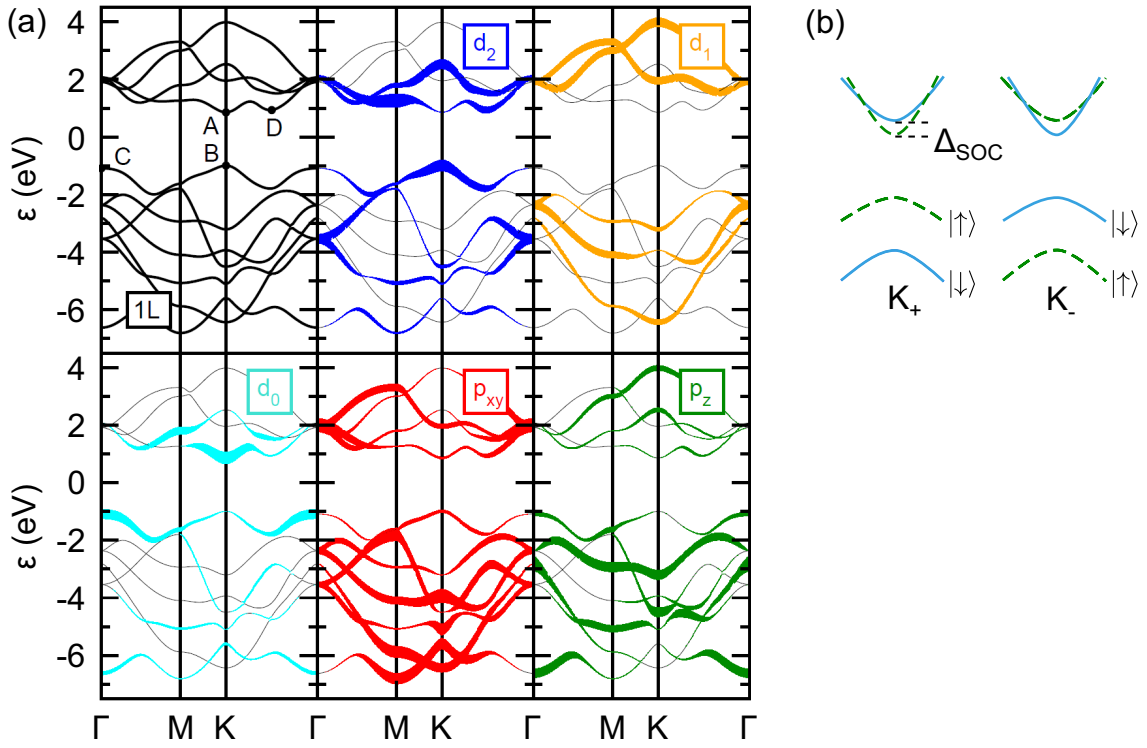

Figure 2.3: (a) Band structure of single-layer MoS_2 showing the weight of the different orbitals ($4d$ Mo-orbitals: $d_2 = d_{x^2-y^2}, d_{xy}, d_1 = d_{xz}, d_{yz}; d_0 = d_{3z^2}$, 3p S-orbitals: $p_{xy} = p_x, p_y; p_z$) where the line width represents the orbital weight in a particular band. The conduction and valance band minimum/maximum is labeled A and B, a secondary maximum is located at the Γ-point (C), a secondary minimum is located at the Q-point (D). Reprinted with permission from [82]. Copyright (2013) by the American Physical Society. (b) Schematic of the conduction band (CB) minimum and the valance band (VB) maximum at $K\pm$ illustrating the spin-orbit interaction-induced splitting of the bands. The green dashed lines and the blue solid lines represent the splitting into a spin-up and spin-down state, respectively. The CBs are separated by $\Delta_{SOC,CB} = 1.5$ meV [61] and the VBs by $\Delta_{SOC,VB} = 150$ meV [89].

$$H_2 = 2E_{12}^{12}(\cos 2\alpha - \cos\alpha\cos\beta) + 2\sqrt{3}E_{12}^{11}\cos\alpha\sin\beta, \tag{2.11}$$

$$H_{11} = 2E_{22}^{11}\cos 2\alpha + (E_{22}^{11} + 3E_{22}^{22})\cos\alpha\cos\beta + \epsilon_2, \tag{2.12}$$

$$H_{22} = 2E_{22}^{22}\cos 2\alpha + (3E_{22}^{11} + E_{22}^{22})\cos\alpha\cos\beta + \epsilon_2, \tag{2.13}$$

$$H_{12} = \sqrt{3}(E_{22}^{22}(\mathbf{R}) - E_{22}^{11}(\mathbf{R}))\sin\alpha\sin\beta + 4iE_{22}^{12}(\mathbf{R})\sin\alpha(\cos\alpha - \cos\beta). \tag{2.14}$$

Here, $E_{ii'}^{jj'}$ corresponds to the hopping integral between the different orbitals, ϵ_i is given by the on-site energy of $\left|\phi_i^j\right\rangle$ and $(\alpha, \beta) = \left(a/2 \cdot k_x, \sqrt{3}a/2 \cdot k_y\right)$. This reduces the number of free tight-binding parameters from the previous 36 down to eight (E_{11}^{11}, E_{12}^{12}, E_{12}^{11}, E_{22}^{11}, E_{22}^{22}, E_{22}^{12}, ϵ_1, and ϵ_2). To determine these parameters, the NN-tight-binding model is fitted to a band structure obtained from first-principle calculations on a path along the high-symmetry points Γ, K, and M [87]. The parameters obtained from a fit to the band structure computed with density functional theory on the level of the local-density approximation (LDA) and generalized-gradient approximation (GGA) are given in reference [87].

Single-layer MoS_2 is a direct semiconductor with an absolute valance band maximum and conduction band minimum at the K-point, around which the bands are mostly composed of the d-orbitals of the molybdenum with minor contributions from the p_x and p_y sulfur orbitals. To approximate the quasi-particle energy gap and the effective electron mass at the K-point, DFT calculations on the level of the LDA and GGA are used, which yield a direct quasi-particle band gap of 1.6 to 1.9 eV [90–93] and effective electron masses of $0.45\,m_e$ to $0.6\,m_e$ [61, 94], while correcting the DFT results on the level of the GW approximation leads to a gap around 2.8 eV [95–97] and an effective mass around $0.35\,m_e$ [95, 97]. The p_z-orbitals of the sulfur atoms give rise to an additional local valance band maximum at the Γ-point and an additional local minimum of the conduction band at the Q-point [82].

For multilayer MoS_2 we have to extend the orbital wave function ϕ by introducing one additional basis as given in Eq. 2.5 for each layer and further include parameters describing the interlayer hopping between the p-orbitals of the sulfur atoms of each single-layer block of MoS_2 by introducing two additional Slater-Koster parameters [82]. The resulting band structure of bulk MoS_2 is shown in Figure 2.4. Analyzing the electronic dispersion for an increasing number of layers, we see that the band structure undergoes a striking change from a direct semiconductor to an indirect semiconductor. This is already the case for bilayer MoS_2, where the highest valence band state at the Γ-point increases in energy resulting in a new valence band maximum while the energy of the conduction band state at the Q-point decreases which results in a new conduction band minimum. The band gap gradually decreases to the bulk value of 0.7 to 1.15 eV, depending on the exact theoretical approach [90–92, 98] calculated on the level of the LDA and GGA. Experimental results, e.g. scanning tunneling microscopy studies, show quasi-particle energy gaps between the results from LDA/GGA and the GW approximations. For MoS_2 directly grown by chemical vapor deposition on graphite the energy gap is shown to decrease from 2.4 eV for a single layer over 2.10 eV for bilayer and 1.75 eV for trilayer towards 1.5 eV for the bulk material [99]. A second study also for single-layer MoS_2 grown on graphite shows a quasi-particle energy gap of around 2.15 eV [100], which is in good agreement with a study on single-layer MoS_2 exfoliated on fused quartz, which features an energy gap of around 2.17 eV [101]. For transport experiments the transition from a direct to an indirect semiconductor is of particular importance as the K-point is two-fold degenerate whereas the Q-point has a six-fold degeneracy. For a

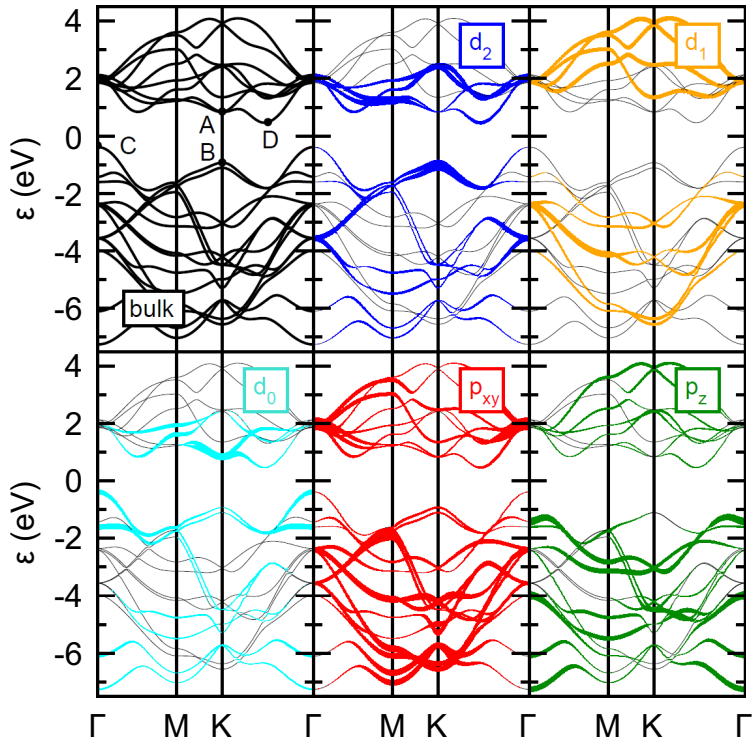

Figure 2.4: Band structure of bulk MoS_2 showing the weight of the different orbitals (4*d* Mo-orbitals: $d_2 = d_{x^2-y^2}, d_{xy}, d_1 = d_{xz}, d_{yz}; d_0 = d_{3z^2}$, 3p S-orbitals: $p_{xy} = p_x, p_y; p_z$) where the line width represents the orbital weight in a particular band. The conduction and valance band minimum/maximum is labeled D and B. Compared to single-layer MoS_2, the former conduction band minimum (A) becomes a secondary minimum. Reprinted with permission from [82]. Copyright (2013) by the American Physical Society.

more detailed derivation of the band structure at all high-symmetry points and an in-detail description of all tight-binding parameters see references [82, 83, 87, 88].

In single-layer MoS_2, the broken inversion symmetry in combination with the high atomic mass of molybdenum results in a spin-orbit splitting in the whole Brillouin Zone save at the Γ- and *M*-points, where the bands retain the degeneracy [61, 89]. Theoretical calculations predict a band splitting due to the spin-orbit coupling (SOC) at the conduction band (CB) minimum of around $\Delta_{SOC,CB} = 1.5$ meV [61] and a much larger splitting of around $\Delta_{SOC,VB} = 150$ meV [89] at the valance band maximum. As the inversion symmetry is only broken for an odd numbers of layers the spin splitting of the bands in multilayer MoS_2 is much more complicated. In addition to the spin-orbit coupling also the interlayer coupling has to be considered, which further contributes to the splitting of bands. For a detailed analysis please see references [102–104].

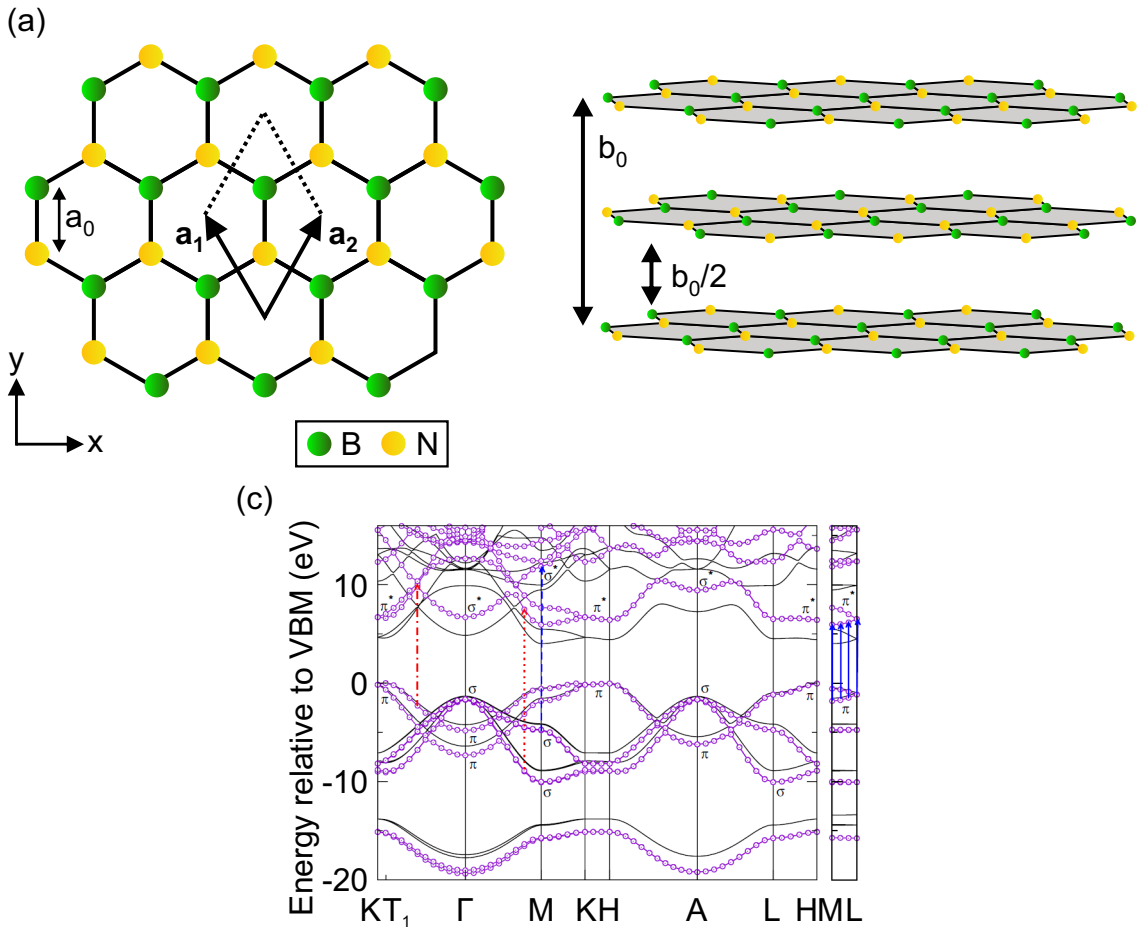

Figure 2.5: (a) Schematic illustration of the hexagonal born nitride (hBN) lattice. Two different atoms, boron (green) and nitrogen (yellow), with a distance of $a_0 = 1.45$ Å between each other, denote the two sublattices. (b) Stacking order of the two-dimensional hBN layers bonded by van-der-Waals interaction. $b_0 = 6.66$ Å denotes the out-of-plane lattice constant. (c) Electronic band structure obtained from LDA (solid line) GW (circles) calculations. Figure (c) is reprinted with permission from [105]. Copyright (2006) by the American Physical Society.

2.4 Hexagonal boron nitride

Due to their two-dimensional nature, graphene and MoS_2 are intrinsically very sensitive to the environment. For example, process induced contaminations and corrugation can heavily limit the electronic quality of a device [106–108]. Therefore, state-of-the-art high quality samples are usually shielded from the environment by encapsulation. For this purpose, hexagonal boron nitride (hBN) proved to be the ideal material [38–42]. It has a similar hexagonal lattice structure as graphite or graphene, with boron and nitrogen atoms donating the two sublattices. The distance between a neighboring boron and nitrogen atom $a_0 = 1.45$ Å is two percent larger

than the distance of adjacent graphene atoms. The out-of-plane lattice constant is given by $b_0 = 6.66$ Å. As illustrated in Figure 2.5 (a) and (b), the two-dimensional layers are stacked with alternating boron and nitrogen atoms on sublattice A and B and bonded by van-der-Waals interaction. As a consequence of the different on-site potential at each sublattice, hBN is an insulator with a band gap of 6.4 eV [105, 109], which has a thickness depended dielectric constant of $\epsilon \approx 3 \sim 4$ [110–112] comparable to the one of SiO_2 [110]. The electronic band structure obtained from GW calculation [105, 113, 114] is shown in Figure 2.5 (c). In-plane the atoms show strong ionic bonding. This results in hBN exhibiting mostly no dangling bond and consequently only a small amount of charge trap at the interface. In addition, hBN is atomically flat, which reduces the corrugation of other two-dimensional materials transfered onto hBN or stacked in between hBN and hence provides an ideal substrate material for electronic devices [38–40, 115].

Chapter 3

Quantum transport in two-dimensional nanostructures

In course of this work we investigate mesoscopic transport and quantum confinement of charge carriers in graphene and MoS_2. Here, the Fermi wavelength $\lambda_F = 2\pi/k_F$ of the carriers is an important quantity to classifiy the transport. In order to observe size-quantization effects λ_F has to be on the order of the device size which, for commonly achieved carrier densities, requires feature sizes on the order of 100 nm (or below). In the following chapter the most important transport phenomena for these nanostructures will be introduced. In particular, we focus on small energies around the Fermi level at low temperatures where transport, depending on the device geometry and electronic quality, can be governed by mode transport or tunneling processes. For a more comprehensive review of the transport properties of two-dimensional nanostructures see references [70, 116–118].

3.1 Transport through a one-dimensional channel

When discussing the electron transport properties of two-dimensional micro and nanostructures, where electrons are confined in one direction and propagate along the other (see Figure 3.1), we have to consider two different transport regimes. When the elastic mean free path l_m is larger than the sample dimensions we can consider the transport to be ballistic where, without magnetic field, electrons travel on straight trajectories and only scatter elastically when they hit the boundaries of the sample (see Figure 3.1 (a)). In this case, the system can be described by an electron wave moving in an effective potential $V(x)$ related to the shape of the confinement with an eigenenergy $E_n(x)$, where n denotes the mode [118]. In terms of an adiabatic approximation with a slowly varying confinement potential and thus a smoothly changing wave function the current through such a one-dimensional channel then corresponds to the sum of the microscopic currents of all modes n. Additionally, we have to consider the spin degeneracy g_s and valley degeneracy g_v of each mode, the Fermi-Dirac distribution function $f_i(E)$ in the right and left

contact lead and an energy dependent transmission $T_n(E_F)$ through the channel as $V(x)$ depends on the mode of the electron wave function. Approximating the current by linear response theory for sufficiently low temperatures and small source-drain voltages yields the well-known quantized conductance where each mode n contributes a quantized conductance value of $g_s g_v e^2/h$, if the transmission for this particular mode is one [116, 118]. This will be the case as long the Fermi energy is well above $V(x)$, while the transmission will rapidly decrease when the Fermi energy is lowered below the maximum of $V(x)$ reducing the contribution of this mode to the overall conductance. Quantized conductance has been first seen experimentally in a AlGaAs/GaAs heterostructure by B. van Wees et. al. [79] in 1988 and by now in many other material systems, especially also in graphene [119, 120], while being described theoretically in a variety of papers. A theoretical review can be found in reference [116].

In contrast, for disordered systems with considerable edge roughness, substrate corrugation, defects or (charged) impurities, l_m is significantly smaller than the sample dimensions and the electrons are frequently scattered when they are accelerated by an electric field E_{el} which leads to a constant drift velocity $v_D = \mu E_{el}$ (see Figure 3.1 (b)). In this frame, the transport is called diffusive and can be described by the well-known Drude formula $\sigma = en\mu$. The random and non-uniform disorder leads to the formation of electron-hole puddles. If the Fermi energy is below the maximum of the disorder potential fluctuations the charge puddles in combination with the energy gap ΔE_{con} induced by the quantum confinement lead to the formation of isolated islands resulting in transport being governed by tunneling through a series of these islands characterized by Coulomb blockade physics [33, 121]. Crucial for the effective energy gap ΔE_g, which governs the energy dependence of the transport properties of such a nanoconstriction, is the potential profile. Here, the characteristic energy scale is the Coulomb energy E_c of the charge puddles which is related to the size of the charge puddles. The amplitude of the disorder potential defines the range of Fermi energy ΔE_F where Coulomb blockade governs the transport properties [33, 122]. For single-layer graphene, this can be an effective tool to create tunnel barriers in order to confine charge carriers on a graphene island connected via two of these nanoconstrictions [31, 33, 121] or even to couple two individual islands [123–126]

3.2 Coulomb blockade effect

After introducing the transport through one-dimensional channels we next turn to quasi zero-dimensional systems, where an isolated island is capacitively coupled to two charge carrier reservoirs (e.g. source and drain contacts) (see Figure 3.2 (a)) and the states in this potential well can be described similar to atomic orbitals. In these so-called single-electron transistors (SETs) the Coulomb energy E_C required to add an additional electron to the system becomes the important energy scale. In

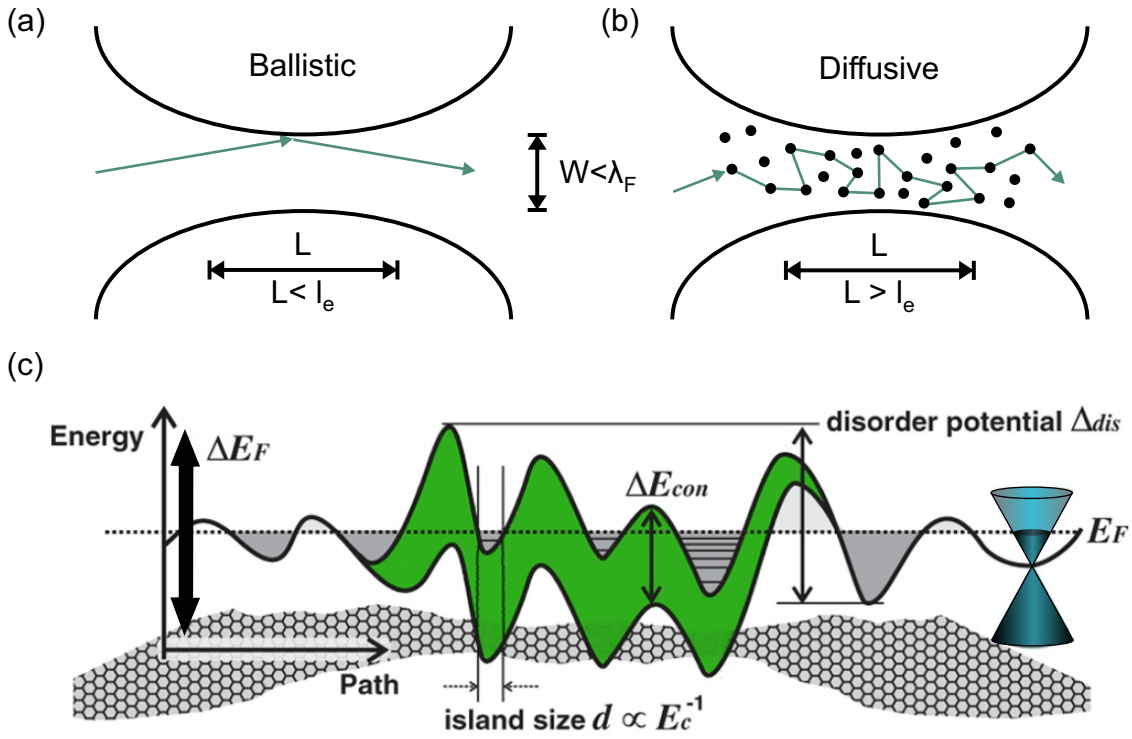

Figure 3.1: (a) If the elastic mean free path l_m is larger than the sample dimensions we can consider the transport to be ballistic where, without magnetic field, electrons travel on straight trajectories. In a one-dimensional channel this leads to a quantization of the conductance with integer values of $g_s g_v\, e^2/h$. (b) For disordered systems with considerable edge roughness, substrate corrugation, defects or impurities, l_m is significantly smaller than the sample dimensions and the electrons frequently scatter inelastically. (c) Schematic illustration of the potential landscape in nanostructured graphene ribbons. Large disorder forms islands of isolated charge puddles. The characteristic energy scales in the system are the charging energy E_c, which is related to the size of the charge puddles, the quantum confinement gap ΔE_{con}, which prevents Klein tunneling, and ΔE_F, which represents the range of Fermi energy, where the transport properties are governed by Coulomb blockade. Figure (c) is reprinted with permission from [121]. Copyright (2009) by the American Physical Society.

particular, we now focus on the Coulomb blockade effect as a result of the Coulomb interaction of the electrons on the island from a phenomenological point of view. To estimate the Coulomb energy E_C of N electrons on the island, we assume as a most basic model a metallic disk with the capacitance C [117, 118, 127, 128]. The energy to add one electron $(N+1)$ to the island ($N_{total} \gg 1$) is then approximated by

$$E_C(N+1) \approx \frac{e^2}{C} N. \tag{3.1}$$

However, because of the often unknown number of electrons it is usually refereed to the difference between the N- and the (N+1)-state, which is then called charging energy ΔE_C [118]:

$$\Delta E_C \approx E_C(N+1) - E_C(N) = \frac{e^2}{C}. \tag{3.2}$$

When the dimension of the island is on the order of the Fermi wave length λ_F of the electrons the confinement energy of a quantum well-like structure (so-called quantum dots) with single particle energy levels ϵ has to be considered. Consequently, in this case the addition of one electron requires also the energy $\epsilon(N+1)$. The difference between these two levels is refereed to as the single particle level spacing

$$\Delta = \epsilon(N+1) - \epsilon(N). \tag{3.3}$$

In case of a quantum dot, the total energy difference between to adjacent levels is called addition energy E_{add} and is equal to the chemical potentials difference between the N- and the (N+1)-state:

$$E_{add} = \Delta E_C + \Delta = \mu(N+1) - \mu(N). \tag{3.4}$$

For a SET we can omit Δ. This equation now has an important consequence for the transport in a system consisting of an island which is capacitively coupled to a reservoir via tunnel barriers and where the Fermi energy can electronically be tuned (see Figure 3.2 (a)). In order to drive a current, we apply a bias voltage $V_{bias} = (\mu_S - \mu_D) / \mid e \mid$ which defines the so called transport window. The bias voltage is simply related to the chemical potential at the source and at the drain contact. Whether transport occurs or is blocked now depends on the relative position of the chemical potential of the island with respect to the chemical potentials in the reservoir. No transport occurs (see Figure 3.2 (b)) when no state is inside the transport window. Adding an additional electron would require more energy than provided by the applied bias ($\mid e \mid \cdot V_{bias} < E_{add}$) and no current can be measured. In order to establish transport we have to either adjust the bias voltage and consequently change the transport window or change the chemical potential of the island by changing the Fermi energy with the electrostatic gate applying a gate voltage $V_{(g)}$. This can place a state inside the transport window enabling electrons (or holes) to tunnel onto and out of the island (see Figure 3.2 (c)). Here, the tunnel current can be approximated by a sequential tunneling model considering the tunnel rates Γ_S and Γ_D through the two tunnel barriers and the occupation of the states in the contact areas described by the Fermi distribution $f_{S,D}$ to [117, 118, 127, 128]:

$$I_S = -\frac{\mid e \mid}{\hbar} \frac{\Gamma_S \Gamma_D}{\Gamma_S + \Gamma_D} \frac{\mid e \mid V_{bias}}{4 k_B T \cosh^2 \left[(\mu_N - \mu_D) / 2 k_B T \right]}. \tag{3.5}$$

When the resonance condition $\mu_N = \mu_D$ is met, a peak in the current can be found. Usually in our experiments the resonance condition is controlled through

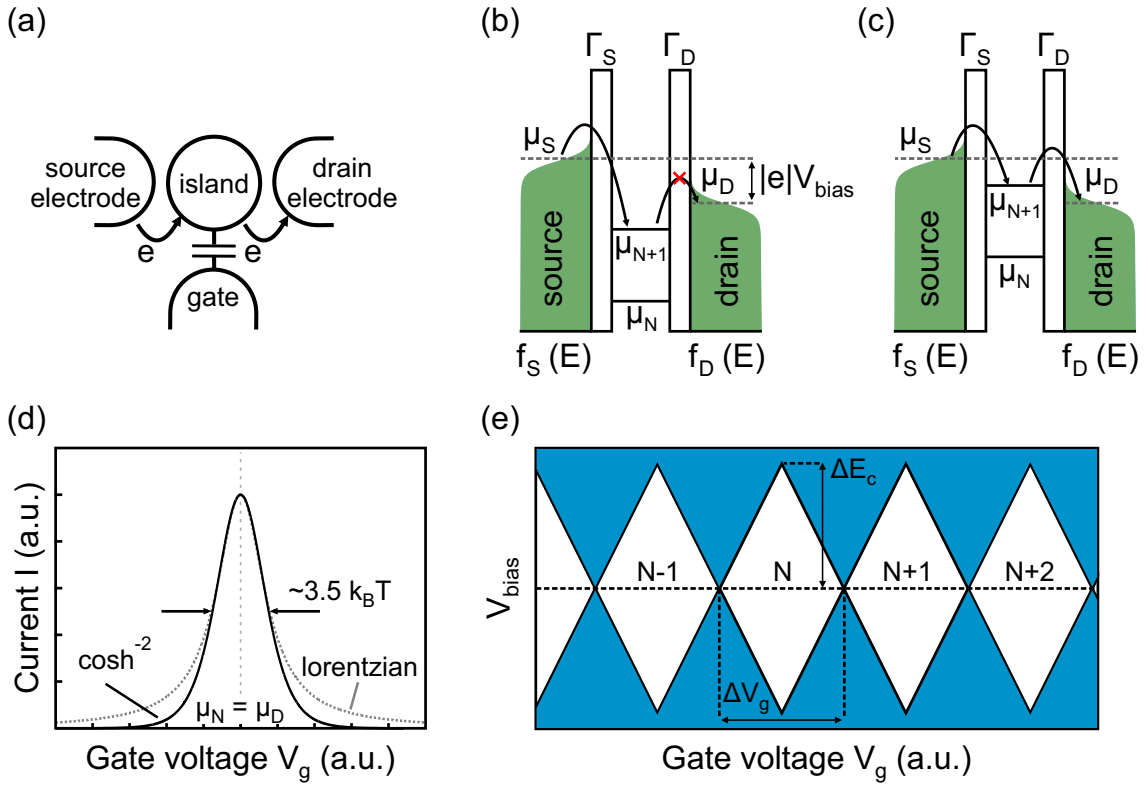

Figure 3.2: (a) Schematic illustration of a single electron transistor (SET), where an isolated island is connected through tunneling barriers to a source and a drain contact. The chemical potential on the island μ_N can be tuned by a capacitive coupled gate. (b) and (c) Schematic representation of the Coulomb blockade effect at finite temperature in a SET. $\mu_{S,D}$ denotes the chemical potential in the source and drain reservoir, V_{bias} the applied bias voltage, $\Gamma_{S,D}$ the tunnel coupling between the leads and the island and the Fermi distribution in the leads $f_{S,D}$. Transport only occurs if a state is inside the transport window. (d) Shape of a Coulomb resonance due to temperature broadening ($\cosh^{-2}$) and large tunnel coupling (Lorentzian). (e) Illustration of finite bias spectroscopy measurements in a SET as a function of V_{bias} and gate voltage V_G. Inside the diamond-shaped regions the device is in Coulomb blockade and no current is flowing with a set number of electrons on the island. Outside the diamond transport is allowed. The charging energy ΔE_c or a change of μ_N by changing the gate voltage ΔV_g is necessary to add the next electron N+1 onto the island. Adapted from [118] and [129]

the gate voltage. By varying both the bias voltage and the gate voltage the typical diamond-shaped bias spectroscopy measurements can be obtained. Importantly, these equations can only be used for small bias voltages and hence for a single level inside the transport window. This also satisfies the requirement of $\mid e \mid \cdot V_{bias} < k_b T$ to prevent extensive thermal broadening. Additionally, in case of a high coupling

between the contact areas and the discrete energy levels a super-imposed Lorentzian-shaped broadening of the peaks has to be taken into account (see 3.2 (d)). In order to relate the charging energy in the transport measurements with the gate voltage we have to consider the so-called gate lever arm

$$\alpha_{gate} = \frac{\Delta E_c}{\Delta V_{gate}}. \tag{3.6}$$

As ΔE_c provides the relevant energy scale we can compare this value to the corresponding change of gate voltage ΔV_{gate} which directly presents the conversion factor between the energy and gate axis. Figure 3.2 (e) shows a schematic illustration of a finite bias spectroscopy measurements. The diamond-shaped regions indicate the regime of V_{bias} and V_G where the transport is blocked by Coulomb interaction and no current is flowing (see 3.2 (b)) with a fixed number of electrons on the island. In the regime outside the diamond, V_{bias} and V_G are adjusted so that a state is within the transport window and a finite current is measured. The charging energy ΔE_c as the extend of the diamond in bias direction can be extracted from these types of measurements.

Chapter 4

Device fabrication

This chapter has been published in parts in

Quantum transport through MoS_2 constrictions defined by photodoping
A. Epping, L. Banszerus, J. Güttinger, L. Krückeberg, K. Watanabe, T. Taniguchi, F. Hassler, B. Beschoten, and C. Stampfer
J. Phys.: Condens. Matter, **30**, 205001 (2018)
©2018 IOP Publishing Ltd
https://doi.org/10.1088/1361-648X/aabbb8

and

Insulating state in low-disorder graphene nanoribbons
A. Epping, C. Volk, F. Buckstegge K. Watanabe, T. Taniguchi, and C. Stampfer
Phys. Status Solidi B, **256**, 1900269 (2019)
©2019 WILEY-VCH Verlag GmbH & Co. KGaA
https://doi.org/10.1002/pssb.201900269

Contributions

In case of the **Quantum transport through MoS_2 constrictions defined by photodoping**: A.E. contributed to planning of the experiment, designed and fabricated the devices and performed measurements. Additionally, he performed data analysis and wrote the manuscript. L.B. contributed to planning of the experiment, designed and fabricated the devices and performed measurements. Additionally, he wrote the manuscript. J.G. performed the simulation of the light intensity distribution. K.W. and T.T. provided the hexagonal boron nitride. F.H. provided the theoretical support. B.B. and C.S. supervised the study and wrote the manuscript. All authors provided input to data analysis, discussed the results and assisted in manuscript preparation.

In case of the **Insulating state in low-disorder graphene nanoribbons**: A.E. planned the experiment and supervised as well as performed the measurements. Additionally, he performed data analysis and wrote the manuscript. F.B. contributed to the fabrication of the devices and performed measurements. C.V. contributed to the fabrication of the devices. K.W. and T.T. provided the hexagonal boron nitride. C.S. supervised the study and wrote the manuscript. All authors provided input to data analysis, discussed the results and assisted in manuscript preparation.

4.1 Introduction

As described in chapter 1, two-dimensional materials promise remarkable mechanical, optical and, most importantly for the work presented in this thesis, unique electronic properties. In various studies it has been shown, that these two-dimensional (2d) crystals are due to their 2d nature highly influenced by their environment making the fabrication process crucial. To obtain high quality devices, the material has to be shielded from there surrounding and protected from fabrication related degradation due to resists, organic solvents, etchants or simply degradation due to the exposure to air. A perfect protection for graphene and MoS_2 is to encapsulate them in hexagonal boron nitride (hBN). Hexagonal boron nitride serves as a widely used substrate as it has the same lattice structure as graphene and MoS_2, is atomically flat with no dangling bonds and exhibits only a few charge traps at the surface. Although there has been a lot of progress regarding the synthesis of 2d crystals like e.g. chemical vapor deposition (CVD) of graphene on cooper and MoS_2 on various substrates [130–137], epitaxial growth on different substrates [138–140] or the bottom-up fabrication of graphene devices by chemical synthesis using molecular precursor [141, 142], exfoliated flakes still provide more flexibility in how to fabricate heterostructures consisting of more than two different materials combined with a high structural and electronic quality. Hence, all flakes are prepared by exfoliation. To fabricate the heterostructures we use a state-of-the-art dry transfer process which enables us to stack different layered van-der-Waals materials with micrometer precision which does not contaminate our conducting 2d-material. The two sections describing the assembly of the different heterostructures also contain a brief overview of the contacting and patterning of the devices. A detailed list of all process parameters can be found in the appendix.

4.2 Mechanical exfoliation

A central aspect of the device fabrication is the preparation of thin flakes by mechanical exfoliation established first for graphene by Novoselov et al. [17], but which can be applied to many two-dimensional crystals including hBN and MoS_2. This technique exploits the weak interlayer van-der-Waals interactions and the strong

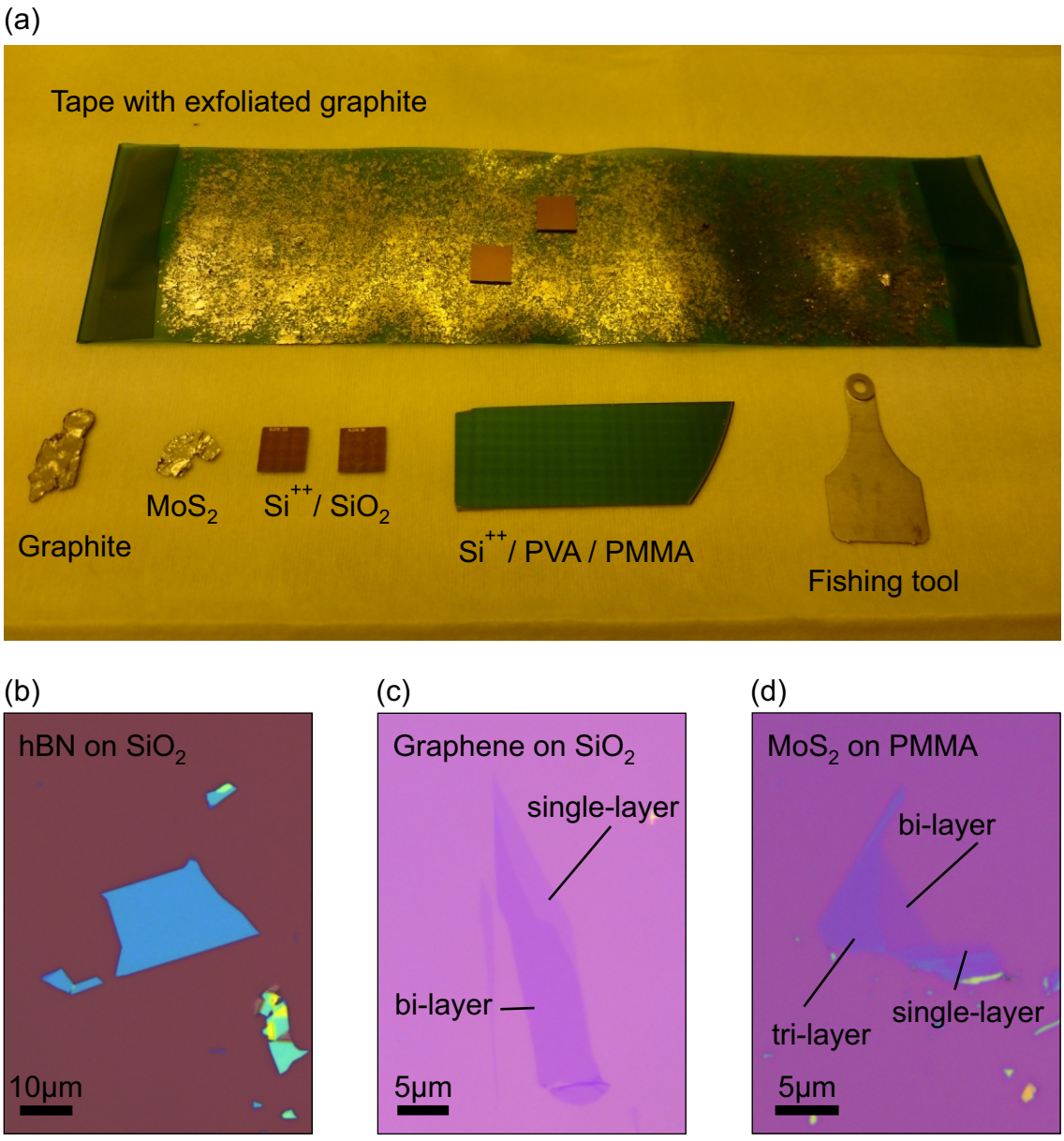

Figure 4.1: (a) Photograph of the different tools and materials necessary for the fabrication of the heterostructures. (b) Optical micrograph of a 20 nm thin exfoliated hBN flake on a Si^{++}/SiO_2 substrate. (c) Optical micrograph of an exfoliated graphene flake on a Si^{++}/SiO_2 substrate. (d) Optical micrograph of an exfoliated MoS_2 flake on a sacrificial PVA/PMMA layer spincoated onto a Si^{++} wafer.

in-plane bonds of these materials. The two-dimensional crystals used are natural graphite purchased from NGS Naturgraphit GmbH, natural MoS_2 purchased from HQ Graphene and hBN provided by K. Watanabe and T. Taniguchi from the National Institute for Material Science in Japan. The exfoliation is done with two different wafer tapes (Nitto Denko model no. BT-150E-CM or Minitron Ultron 1008R and 1009R) which yield similar results. The crystals are simply placed onto the tape and removed again followed by folding the tape several times. It is crucial, especially for the MoS_2, to start the exfoliation with a rather large but already thin and smooth flake freshly separated from the main crystal to maximize the size of the exfoliated flakes. For the fabrication of our heterosturctures we need to prepare the flakes on two different substrates by pressing these substrates onto the corresponding prepared tapes and removing them again after a couple of seconds. On a highly p-doped 7×7 mm^2 silicon chip covered by 285 nm thick thermal oxide (Si^{++}/SiO_2, Nova Electronic Materials) we exfoliate hBN, which is the basis of all our devices. For a precise alignment of all fabrication steps metallic alignment marks (chromium/gold) have been fabricated on these chips by standard electron beam lithography and a metal evaporation step before to the exfoliation. To transfer the additional flakes onto the initial hBN flake we use a sacrificial polymer stack of roughly 100 nm water-soluble polyvinyl alcohol (PVA) followed by 270 nm polymethyl methacrylate 950k (PMMA-950k), which is transparent and can be removed after the successful transfer, as a second substrate. This sacrificial polymer stack is prepared by coating a four inch silicon wafer in order to ensure mechanical stability during the exfoliation. The thickness of the polymers is optimized for an high optical contrast of the 2d-materials. Afterwards, the wafer is divided into 16 roughly similar sized pieces using a diamond scriber. and the pieces can be pressed onto the prepared tape. The different tools and materials are depicted in Figure 4.1 (a). Additional information regarding the exfoliation can be found in reference [143]. An optical micrograph of a typical hBN flake with a thickness of around 20 nm on a Si^{++}/SiO_2 chip, a graphene flake on a Si^{++}/SiO_2 chip and a MoS_2 flake on PVA/PMMA is shown in Figure 4.1 (b)-(d).

4.3 Raman spectroscopy

In the following we will use scanning confocal Raman spectroscopy as a powerful tool to investigate the structural quality of the fabricated heterostructures. Raman spectroscopy uses coherent laser light (in our case $\lambda = 532$ nm) to probe the sample within the laser spot by creating electron-hole pairs. These electron-hole pairs can relax back into their ground state emitting photons. The energy of the emitted photons can be shifted with respect to the incoming photons corresponding to the phonons created (Stokes process) or annihilated (anti-Stokes process) in this process. Each material shows a different set of characteristic resonances. The three most prominent features in the graphene Raman spectrum are the G-, 2D- and D-peak

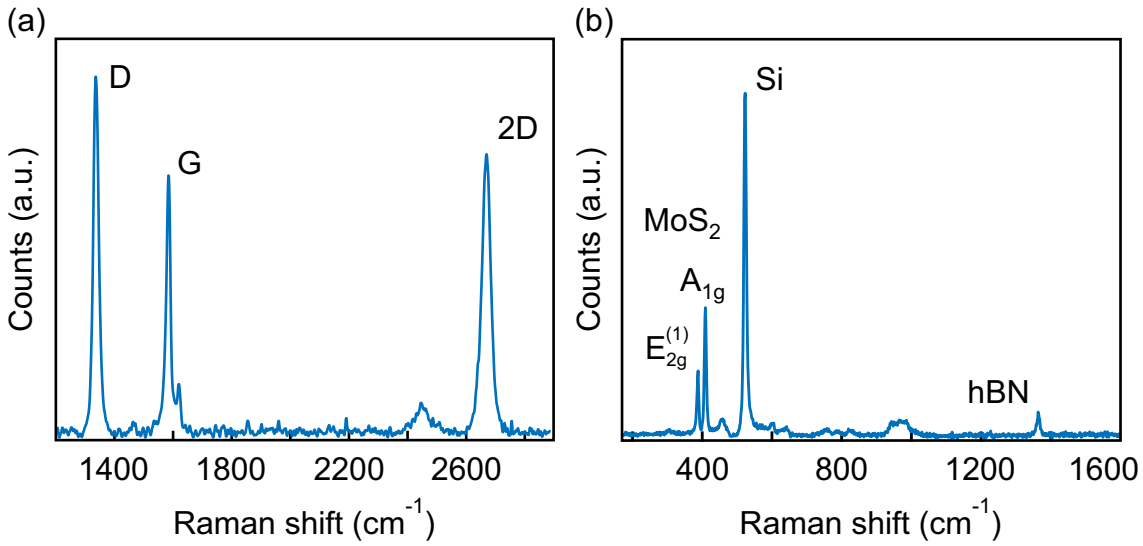

Figure 4.2: (a) Raman spectrum of a highly defective graphene flake. (b) Raman spectrum of MoS_2 transfered onto hBN. The heterostructure was fabricated on a Si^{++}/SiO_2 substrate.

with the first two involving only the pristine graphene lattice. The latter requires a defect and hence is usually not seen in high quality graphene heterostructures. The typical positions for single layer graphene of these peaks are $\omega_G \approx 1585$ cm^{-1}, $\omega_{2D} \approx 2680$ cm^{-1} and $\omega_D \approx 1350$ cm^{-1}. A Raman spectrum with all three peaks is shown in Figure 4.2 (a). Theoretical details about Raman spectroscopy of graphene can be found in reference [144]. The second important component of the heterostructure, the hBN, can also be identified easily with the characteristic peak being located at $\omega_{hBN} \approx 1365$ cm^{-1}. For MoS_2 we use the in-plane E_1^{2g} mode and the out-of-plane A_{1g} mode to identify the material and to distinguish between the different number of layers as the separation between the two modes decreases with decreasing thickness. In bulk MoS_2 these peaks are positioned at $\omega_{E_1^{2g}} \approx 383.5$ cm^{-1} and $\omega_{A_{1g}} \approx 408.6$ cm^{-1} [145, 146]. For decreasing thickness the E_1^{2g} mode shift upwards while the A_{1g} mode shifts downward. To determine the thickness of the MoS_2 we can use the following formula: $\Delta\omega = \omega_{A_{1g}} - \omega_{E_1^{2g}} = 25.8 - 8.4/N$ with N being the number of layers [146]. Theory for the phonon spectrum of MoS_2 can be found in reference [147]. A typical spectrum of few-layer MoS_2 on hBN is shown in Figure 4.2 (a). Compared to other analysis techniques, scanning Raman spectroscopy is fast, non-invasive and allows to probe a number of material properties. For graphene this includes the number of layers [148, 149], strain parameters [150–153], doping to some extent [154–156], point defect density [157, 158] and nanometer-scale strain variations [159] by analyzing the position and the width of the characteristic peaks. Of particular interest for graphene heterostructures is the averaged width of the 2D-peak $\overline{\Gamma}_{2D}$ across a whole device as a connection between $\overline{\Gamma}_{2D}$ and the electron

mobility μ of a sample can be made. It has been observed that the electron mobility μ is maximal for devices where the average width of the 2D-peak $\overline{\Gamma}_{2D}$ is smallest corresponding to a devices with overall a small amount of random strain fluctuations [108]. For our MoS_2 devices the number of layers and the alignment of the different materials is of great interest. As has been discussed in chapter 2.3 the number of layers determines if the inversion symmetry is inherently broken and hence the valley degeneracy lifted. Additionally, as we fabricate graphene contacts it is highly important to monitor the alignment of each flake with respect to each other after the transfer for the further processing steps.

4.4 Assembly of fully encapsulated graphene quantum dots

As previously mentioned, the key to preserving a high structural and electronic quality of the two-dimensional crystal during the fabrication is to prevent the crystal from getting into contact with any fabrication related contaminations like resist or organic solvents. This can be achieved by completely encapsulating the crystal between two exfoliated hBN flakes via a well-established dry transfer method [40]. For the fabrication of the hBN/graphene/hBN heterostructures we use a hBN flake and a single-layer graphene flake prepared on two different Si^{++}/SiO_2 chips and a second hBN flake prepared on the sacrificial polymer stack.

In a first step of the transfer process, the PMMA layer is separated from the Si wafer by dissolving the PVA with deionized water (DI) creating a thin membrane floating on the DI water. Afterwards the membrane is captured by a specially design metal plate exhibiting a hole in its middle. In a second step the hBN flake on the membrane is aligned to and brought into contact with a single layer graphene flake on the Si^{++}/SiO_2 chip using micro manipulators and an optical microscope. Due to their strong van-der-Waals interaction, the graphene sticks to the hBN and detaches from the substrate when the membrane is retracted again. The second step is repeated with the hBN/graphene stack now on the membrane and the hBN flake on the Si^{++}/SiO_2 chip but without retracting the membrane. Instead the PMMA is heated above its glass transition temperature to around 120° C. In a last step the assembled hBN/SLG/hBN heterostructure on the Si^{++}/SiO_2 chip is released by removing the PMMA with organic solvents.

Each transferred heterostructure is investigated by Raman spectroscopy prior to the structuring as areas with a low amount of strain fluctuations are preferred for the device to ensure a high electronic quality [108, 159]. For the later study of fully encapsulated SLG quantum dots areas with a small (< 20 cm^{-1}) FWHM of the 2D line and low variance are chosen to fabricate the device in. In comparison, the FWHM of the 2D line on SiO_2 is typically around 25 cm^{-1}. An example of such a Raman spectrum can be seen in Figure 4.4 (b). The peak of the LO phonon of the hBN is at 1367 cm^{-1}, the graphene G-peak is at 1585 cm^{-1} and the 2D-

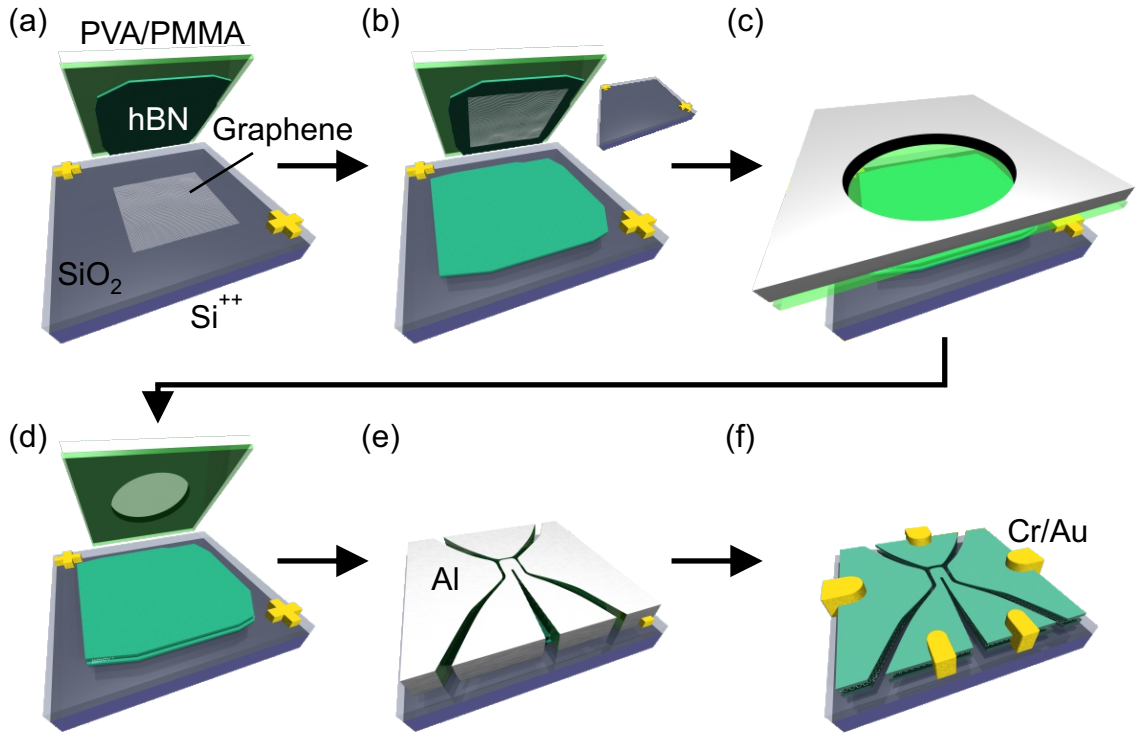

Figure 4.3: Schematical illustration of the fabrication process. (a)-(d) A graphene flake and a hBN flake are prepared on a Si^{++}/SiO_2 substrate and the sacrificial polyvinyl alcohol (PVA) / polymethyl methacrylate (PMMA) membrane, respectively. The membrane is aligned to and brought into contact with the graphene flake. After the graphene is picked up by the hBN, the hBN/graphene stack on the membrane is aligned with a second hBN flake on a second Si^{++}/SiO_2 substrate. The membrane is again brought into contact with the substrate. Now, the hBN/graphene can be transfered either by dry delamination or by melting the polymer membrane. (e) Subsequently the desired device geometry is patterned into the heterostructure by using electron beam lithography (EBL), deposition of an aluminum hardmask and reactive ion etching. (f) The resulting device is contacted in a second EBL step and a subsequent metal evaporation of Cr/Au.

peak is centered around 2687 cm^{-1} with a FWHM of 17 cm^{-1}. Subsequently the desired device geometry is patterned into the heterostructure by using EBL (resist stack: 50k/950k PMMA), deposition of an Al hardmask (20 nm) and reactive ion etching with a SF_6/O_2 plasma. After the etching, the Al hardmask is removed by a solution of 2% tetramethylammonium hydroxide/98% DI water. The resulting graphene quantum dots are then contacted in a second EBL step and a subsequent metal evaporation of Cr/Au (5 nm/75 nm). The fabrication process is illustrated in Figure 4.3. An optical micrograph and a scanning force micrograph of a finished device can be seen in Figure 4.4 (a) and in Figures 4.4 (c) and (d), respectively.

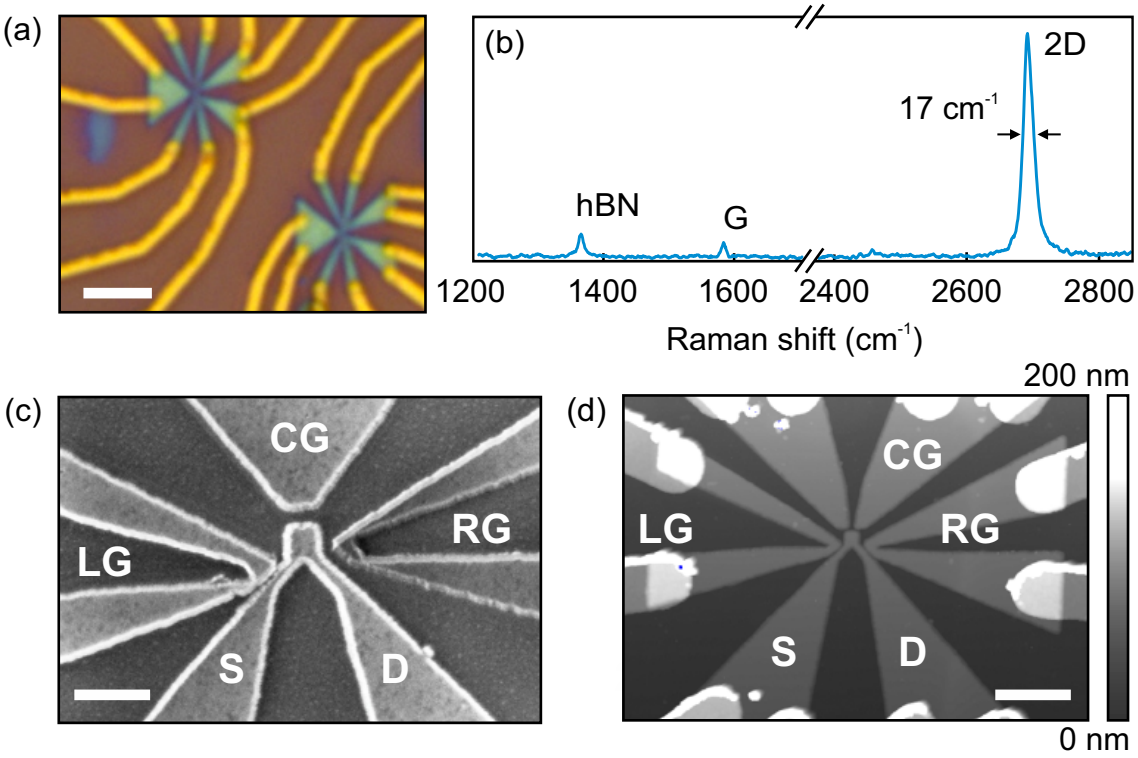

Figure 4.4: (a) Optical image of contacted single layer graphene quantum dots fully encapsulated in hexagonal boron nitride (hBN). The scale bar corresponds to 5 μm. Adapted from [160]. (b) Raman spectrum of a hBN/graphene/hBN heterostructure with a FWHM of the 2D-peak of 17 cm^{-1}. (c) Scanning electron micrograph (scale bar corresponds to 200 nm, adapted from [160]) and (d) atomic force micrograph (scale bar corresponds to 400 nm) of two etched graphene quantum dots with a diameter of 100 nm.

The quantum dots have a island size of 100 $\times$ 100 nm^2 and they are connected via two nanoconstriction with a width of 35 nm (left constriction) and 50 nm (right constriction) and a length of 100 nm to the source (S) and drain (D). The connection to the measurement setup is made by wire-bonding the sample with a semi-automatic wedge bonder (TPT HB06) into a Kyocera chip carrier (8C-QFN PB-C88084) which can be mounted to the corresponding chip socket of the setup.

4.5 Assembly of encapsulated molybdenum disulfide contacted with few-layer graphene

Similar to the description in the previous section we again use the dry van-der-Waals stacking technique to fabricate molybdenum disulfide (MoS_2) heterostructures. As contacting the MoS_2 with standard metals yields contacts with substantial Schottky

barriers [161, 162], the transfer process has to be slightly altered in order to employ few-layer graphene (FLG) contacts, which have been shown to exhibiting a low Schottky barriers to the MoS_2, especially at high charge carrier densities of the FLG [62, 163, 164]. Instead of picking up the 2d crystals from Si^{++}/SiO_2 chips with the hBN on the transfer membrane, all 2d materials except of the bottom hBN flake are exfoliated on the sacrificial PVA/PMMA layer as described above. First, a few-layer MoS_2 crystal is transfered onto the bottom hBN flake without melting the polymer membrane by bringing the two materials into contact and slowly peeling of the membrane again. As long as the MoS_2 flake is smaller than the hBN, the MoS_2 will detach from the PMMA and is contamination-free transfered to the hBN. This process is repeated for the top hBN. In order to electrically contact MoS_2 from the top surface, the left and the right parts of the MoS_2 flake remain uncovered by the upper hBN crystal. At the same time, the inner fully encapsulated area of MoS_2 is well protected against transfer related degradation and contamination ensuring a high electronic quality of the device. Afterwards, one large flake of FLG is placed on top of the entire structure which is in direct contact with MoS_2 in all parts that are not protected by the upper hBN flake. Only then the membrane is melted. Figure 4.5 (a) shows an optical micrograph of such a complete van-der-Waals stack. In contrast to previous reports [62, 163, 164], where multiple flakes of FLG have been transferred to fabricate electrical contacts, we only transfer a single large FLG flake that is subsequently patterned (see Figure 4.5 (a) and (b)). Using a single flake to contact multi-terminal MoS_2 devices is convenient, as it saves several transfer steps or crystal phase engineering of the MoS_2 [165]. Furthermore, it prevents any direct contact of solvents or wet chemistry with the MoS_2. When immersed in solvents, even the outer parts of the MoS_2 are fully encapsulated by the FLG. EBL (50k/50k/950k PMMA), deposition of an Al hard mask (20 nm) and reactive ion etching (RIE) with an Ar/O_2 plasma (flow: 32 sccm/8 sccm; power: 60 W) allow to selectively etch the FLG and the MoS_2 while the etching rate is negligible for the top hBN. As we need a considerable time to etch through the FLG, which can damage the SiO_2, we additionally protect the future bond pad areas by predefining their position with EBL and the deposition of protective Al layer in the hard mask step.

The graphene above the top hBN and several trenches through the MoS_2 are etched. The trenches are needed to separate the individual contacts on each side of the multi-terminal devices, which is illustrated in Figure 4.5 (c). In a last step, Ti/Au contacts to the FLG, as well as the shadow mask structure for the constriction on the top hBN are evaporated, followed by lift-off. Figure 4.5 (d) shows a scanning electron microscopy (SEM) image of a finished constriction device where the constriction created by the shadow mask structure has a width of 250 nm and a length of 175 nm. After the structuring, the devices are characterized by scanning confocal Raman microscopy which allows to spatially probe the structural (and partly electronic) quality of all individual layers of the van-der-Waals heterostructure. Figure 4.5 (e) depicts two typical Raman spectra. The upper spectrum in Figure 4.5 (e) is

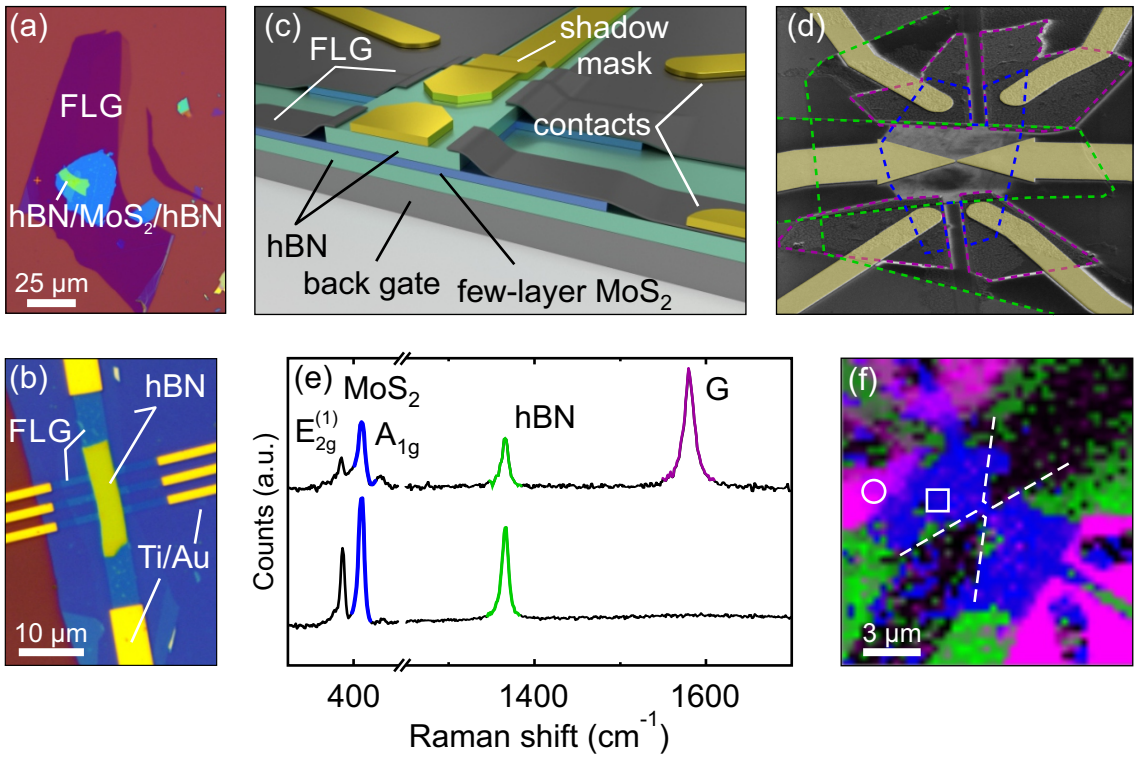

Figure 4.5: (a) Optical micrograph of the complete van-der-Waals heterostructure after transfer. The MoS_2 is partially encapsulated by two hBN flakes. The hole structure is completely covered by a few-layer graphene flake. (b) Optical micrograph of a finished hallbar device. (c) Schematic illustration of a typical multi-terminal constriction device (d) Corresponding scanning electron micrograph of a four-terminal constriction device. The individual flakes are highlighted by dashed lines (hBN in green, graphene in purple and MoS_2 in blue). (e) Raman spectra on a final device recorded in the contact area indicated by the white circle in panel (f) (top) and in the sandwiched part of the device indicated by the white square in panel (f) (bottom) showing the individual Raman peaks highlighted by the same color as in (c). (f) Raman map showing the integrated intensities of the hBN peak, the G-peak of the FLG and the A_{1g} mode of the MoS_2, represented by the colors purple, blue and green, respectively. The black areas are covered by metal whose boundaries are indicated by the white dashed lines.

recorded in the contact area (see open circle in Figure 4.5 (f)), where the MoS_2 is covered with FLG. The Raman G-peak at 1583 cm^{-1} (purple) originates from the FLG [166]. The hBN peak is located at around 1365 cm^{-1} (green) [167] while the A_{1g} and the E^1_{2g} modes of the MoS_2 are located at 409 cm^{-1} (blue) and 386 cm^{-1}, respectively [145, 146]. The lower spectrum in Figure 4.5 (e) is recorded on the hBN/MoS_2/hBN area of the device, close to the shadow masks, where only the two peaks from the hBN and the MoS_2 are visible (see open square in Figure 4.5 (f).

Figure 4.5 (f) shows a Raman map of the intensities of the above characteristic Raman peaks of the different 2D materials in use. Green represents the intensity of the hBN peak, purple depicts the G-peak intensity of the FLG, blue shows the intensity of the A_{1g} mode of the MoS_2. The dark areas are the gold electrodes which define the constriction in the underlying MoS_2 layer. Figure 1h shows a SEM image of a typical device. The boundaries of the individual flakes are indicated by the dashed colored lines where we use the same color code as in Figure 4.5 (e). Similar to the graphene QDs, the samples are glued into a chip carrier and wire-bonded.

Chapter 5

Insulating state in low-disorder graphene nanoribbons

This chapter has been published in parts in

Insulating state in low-disorder graphene nanoribbons
A. Epping, C. Volk, F. Buckstegge K. Watanabe, T. Taniguchi, and C. Stampfer
Phys. Status Solidi B, **256**, 1900269 (2019)
©2019 WILEY-VCH Verlag GmbH & Co. KGaA
https://doi.org/10.1002/pssb.201900269

Contributions

A.E. planned the experiment and supervised as well as performed the measurements. Additionally, he performed data analysis and wrote the manuscript. F.B. contributed to the fabrication of the devices and performed measurements. C.V. contributed to the fabrication of the devices. K.W. and T.T. provided the hexagonal boron nitride. C.S. supervised the study and wrote the manuscript. All authors provided input to data analysis, discussed the results and assisted in manuscript preparation.

5.1 Introduction

Graphene nanoribbons offer an interesting playground to study mesoscopic physics at the nanoscale combining size confinement effects and the Dirac fermion nature of electrons in graphene [168–170]. Especially electron-electron interaction in graphene nanoribbons has been studied theoretically to quite some extend [171–177]. In particular, the presence of a magnetic field should give rise to a number of transport phenomena unique to the Dirac fermions. For example, high quality graphene has already revealed anomalous patterns in the magnetoconductance called Hofstadter's

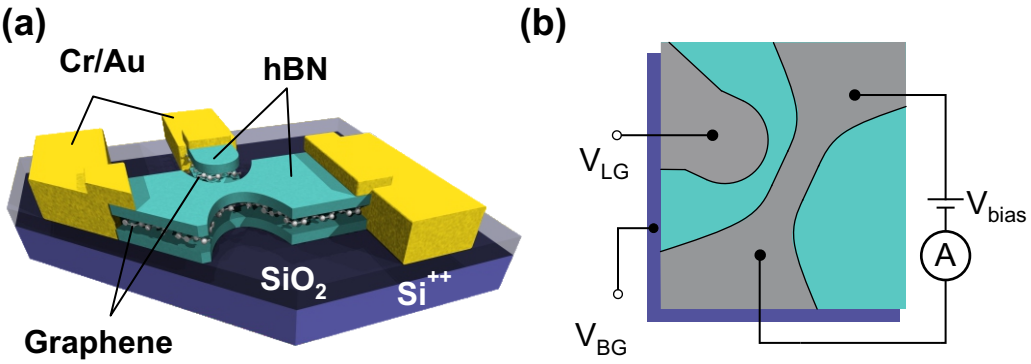

Figure 5.1: (a) Schematic of the heterostructure including one-dimensional contacts, the highly doped silicon BG and the lateral side gate. (b) Illustration of the measurement configuration. The chemical potential is locally adjusted by the lateral gate (LG) while the Fermi level of the whole sample is tuned by the back gate (BG).

butterfly due to the moiré superlattice of graphene/hBN heterostructures [178, 179] or quantum Hall ferromagnetism at the Dirac point [110, 180–182]. The latter has also been realized in high mobility suspended graphene nanoribbons [183] but they suffer from the limited control in the fabrication process [184]. Additionally, these devices exhibit a poor gate tunability. So far, in substrate supported graphene nanostructures the disordered potential landscape dictates the transport properties [32, 33, 121, 122, 185–187]. An alternative way to achieve very high electronic quality is placing graphene on hexagonal boron nitride which can significantly reduce the disorder potential [38–42]. However, in nanostructures the contribution of edge disorder to the overall disorder remains significant [43, 188]. Besides the remaining substrate and edge induced disorder, surface contaminations, e.g lithography residues, have to be taken into account [44]. A step towards further reducing this type of disorder is to encapsulate graphene in hBN [40], which prevents process-induced contaminations on the graphene flake, although the edges are still exposed. This results in substrate-supported devices with reproducibly high electronic quality and enables the observation of quantum phenomena like quantized conductance in sub-micron structured graphene constrictions [120, 189].

In this chapter we study two fully encapsulated nanostructured graphene ribbons with a width of 35 (device D1) and 40 nm (device D2) which have a length of 100 nm and 150 nm and are fabricated from hBN/graphene/hBN heterostructures. Figure 5.1(b) shows an illustration of the measurement geometry. We perform two-terminal conductance measurements where the bias voltage is applied between the source and drain. The chemical potential can locally be tuned by the lateral graphene gate (LG) which has a distance below 10 nm to the nanoribbon. Globally, the Fermi level can be adjusted by the back gate (BG). An optical micrograph and a scanning force and scanning electron micrographs of the devices are shown in

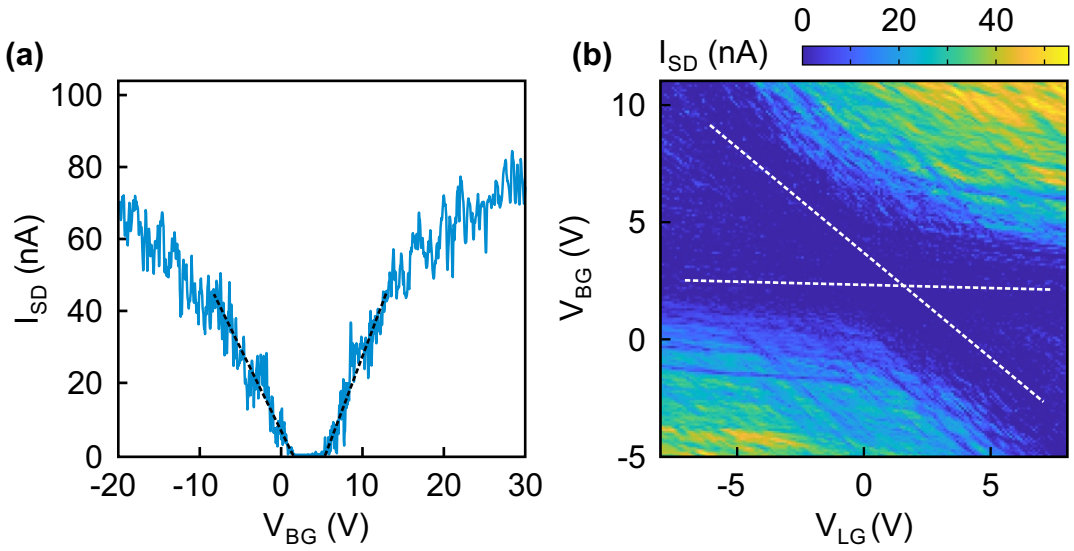

Figure 5.2: (a) Source-drain current I_{SD} as a function of back gate voltage V_{BG} for a fixed bias $V_{bias} = 1$ mV of a nanoribbon with a width of 40 nm and length of 150 nm. (b) I_{SD} as a function of V_{BG} and the lateral side gate voltage V_{LG} of the same device. The transport gap (black region) can be tuned by V_{BG} and V_{LG}. The source/drain regions are only influenced by the back gate while the region of the nanoribbon is tuned nearly identical by both gates (see the white dashed lines). All transport measurements have been performed at $T \approx 30$ mK.

chapter 4.4, Figure 4.4. All measurements are performed in a dilution refrigerator at a base temperature around 30 mK. At first, the devices are characterized at zero magnetic field revealing a comparatively small transport gap due to the reduced disorder. Inside the transport gap, statistical Coulomb blockade can be observed. At moderate magnetic fields (B $\approx$ 1 T) the Coulomb blockade is strongly suppressed due to the increasing density of states around zero energy as the electrons condense into Landau levels. Further increasing the magnetic field leads to the formation of a strongly insulating state around the charge neutrality point, which creates a large energy gap. This insulating $\nu = 0$ state is related to the valley symmetry breaking induced by the perpendicular magnetic field similar to what has been observed in high mobility extended graphene sheets [110, 180–182] but the resulting energy gap is considerably larger potentially due to enhanced electron-electron interaction.

5.2 Device characterization

In Figure 5.2(a) we show the source-drain current I_{SD} as a function of the applied back gate voltage V_{BG} through device D2 for a fixed bias $V_{bias} = 1$ mV with the lateral gate at 0 V. The region of suppressed current, commonly called transport gap ΔV_{BG}, is estimated by the distance between the intersection points of a linear

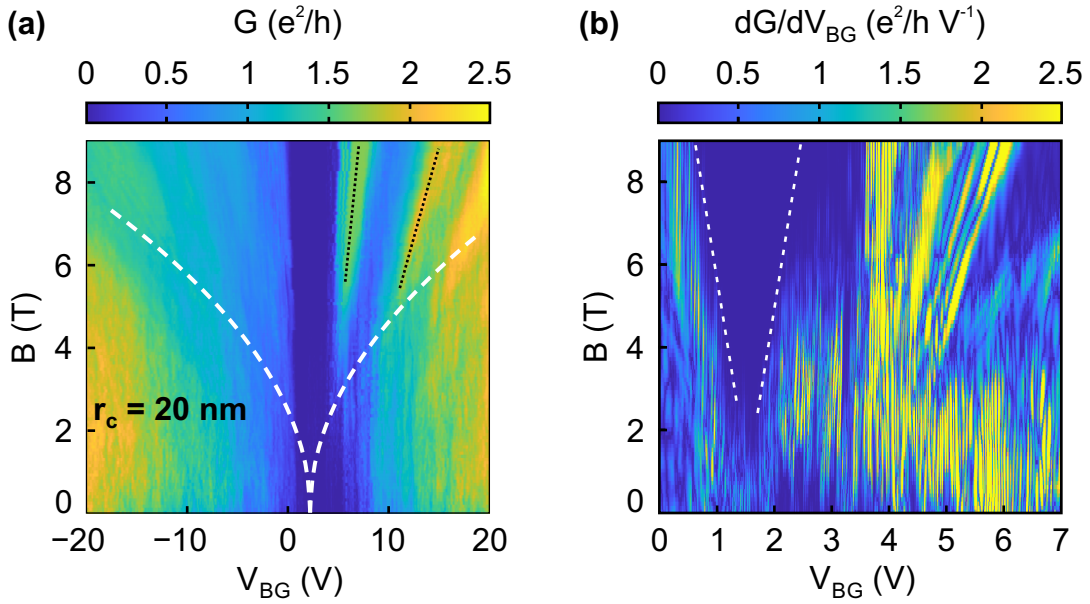

Figure 5.3: (a) Transconductance dG/dV_{BG} of the 40 nm wide ribbon as function of V_{BG} and the magnetic field B with $V_{LG} = 0$ V. The white dashed lines correspond to a cyclotron radius of $r_c = 20$ nm. (b) Transconductance dG/dV_{BG} as a function of V_{BG} and the magnetic field B with $V_{LG} = 0$ V. The white dashed lines mark a region of suppressed conductance that evolves with increasing magnetic field.

approximation of the back gate characteristic outside the gap region with zero I_{SD} as depicted in Figure 5.2(a). The transport gap arises due to statistical Coulomb blockade in the nanoribbon, where the gap is related to the tunneling of electrons through charged islands and localized states in the ribbon, which result from both, bulk and edge disorder [33, 121]. It has been shown that using hBN as a substrate material substantially reduces the bulk disorder [38–42]. However, in nanostructure devices edge disorder is playing an important role [43, 188], giving rise to a significant disorder potential. Nevertheless, this results in an overall slightly reduced disorder potential and thus to a reduced transport gap. With the described method we extract $\Delta V_{BG} = 4.5$ V, which is smaller than what has been reported for graphene nanoribbons with a similar size on SiO_2 [34–36, 190] or on hBN [43]. Additionally, the charge neutrality point is close to $V_{BG} = 0$ V. Both results indicate a low residual doping of the sample and a reduced amount of disorder compared to such small structures fabricated on SiO_2 or without full encapsulation with hBN. Device D1 shows a very similar behavior. Fixing V_{BG} inside the transport gap enables us to observe Coulomb peaks due to resonant tunneling through a network of charge islands [121] (see e.g. the $B = 0$ T trace in Figure 5.5(a)). In order to study the characteristic of the device in more detail we investigate the dependence of I_{SD} on the lateral gate with respect to V_{BG}. In Figure 5.2(b) we show I_{SD} as a function of V_{BG} and V_{LG} at fixed $V_{bias} = 1$ mV. The dark region denotes the transport gap

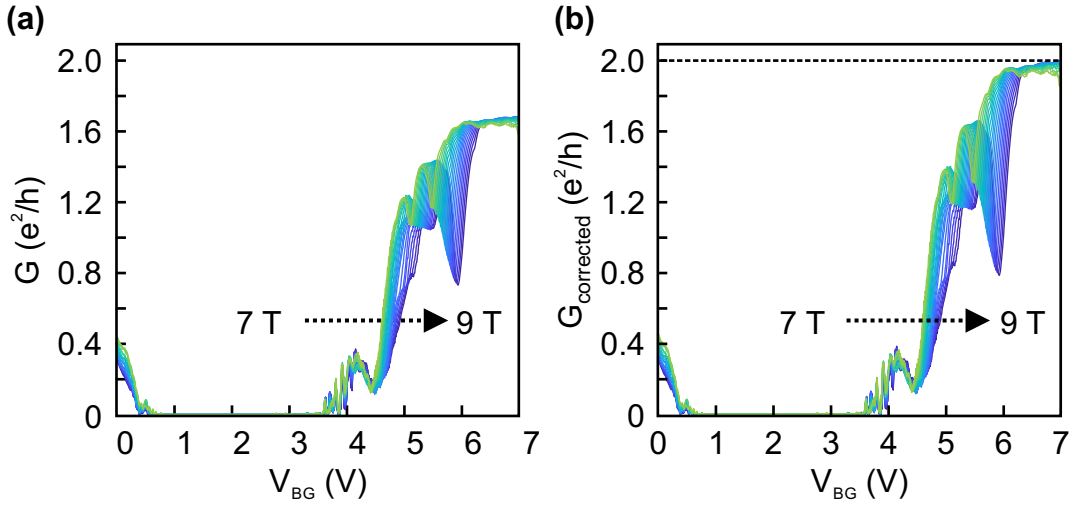

Figure 5.4: (a) Conductance G as a function of V_{BG} between B = 7 and 9 T in steps of 100 mT. (b) Conductance corrected by an estimated constant contact resistance of 2450 Ω as a function of V_{BG} between B = 7 and 9 T in steps of 100 mT. All data from device D2.

which can be tuned by both the back gate and (partly) by the lateral gate. Two different slopes marked by the white dashed lines can be identified originating from tuning different regions of the device. The nanoribbon region is tuned by both gates whereas the leads (source/drain contacts) are mostly independent on the voltage applied to the lateral gate. Similar measurements are performed for both devices and result in a typical relative lever arm of $\alpha_{BG/LG} \approx 0.9$ to tune the transport gap, which is comparable to previous studies [121].

5.3 Magnetotransport

So far we have shown that our devices behave qualitatively very similar to graphene nanoribbons on SiO_2 or hBN, although the transport gap is considerably smaller. We now focus on the magnetotransport properties. In Figure 5.3(a) we show the conductance G of device D2 as function of V_{BG} and the perpendicular magnetic field B with $V_{LG} = 0$ V. Outside the transport gap, we observe features, which move linearly with increasing B-field and which can be related to Landau level quantization, i.e. to quantum Hall edge states (see the black dashed lines in Figure 5.3(a))). Consistently, these features are only visible once the cyclotron radius is below half of the ribbon width ($r_c < w/2$, white dashed lines in Figure 5.3(a)), which corresponds to the requirement for having edge channel transport through the ribbon. The cyclotron radius is given by $r_c = \hbar\sqrt{\pi n}/(eB)$, where $n = \alpha(V_{BG} - V^0_{BG})$ is the charge carrier density, α the lever arm (see below) and V^0_{BG} the charge neutrality point. A quantum Hall plateau can for example be seen on the electron side above 6 T (see

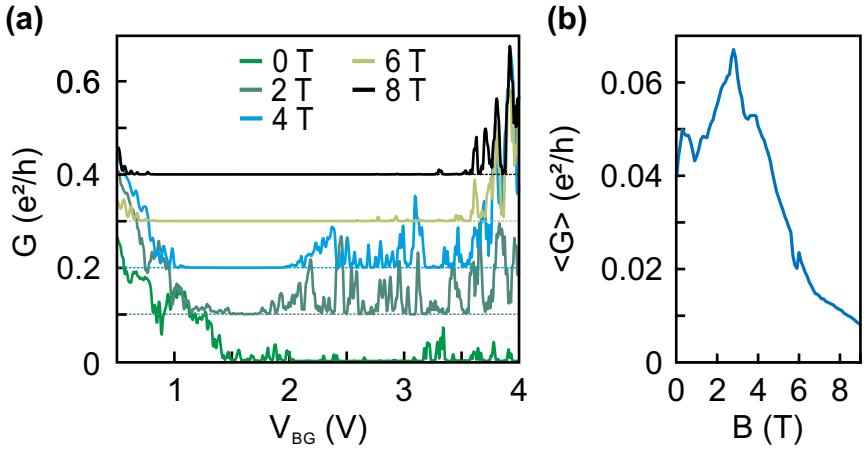

Figure 5.5: (a) Conductance G as a function of V_{BG} for $B = 0, 2, 4, 6$ and 8 T between $V_{BG} = -0.5$ V and $V_{BG} = 4$ V. Each trace is offset by an additional 0.1 e^2/h for clarity. (b) Averaged conductance $\langle G \rangle$ between $V_{BG} = -0.5$ and 3.75 V as a function of magnetic field. All data from device D2.

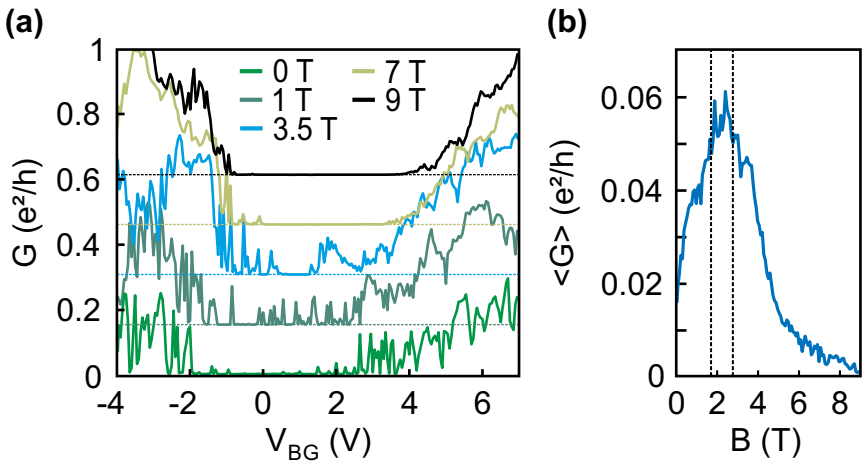

Figure 5.6: (a) Conductance G as a function of V_{BG} for $B = 0, 1, 3.5, 7$ and 9 T between $V_{BG} = -4$ V and $V_{BG} = 6.5$ V. Each trace is offset by an additional 0.15 e^2/h for clarity. (b) Averaged conductance $\langle G \rangle$ between $V_{BG} = -1$ and 4 V as a function of B. All data from device D1.

also Figure 5.3(b) around $V_{BG} \approx 6$ V). The quantum Hall plateau becomes more apparent in Figure 5.4(a) where we show G as function of V_{BG} for magnetic fields between 7 and 9 T in steps of 100 mT. Above $V_{BG} = 6$ V the traces form a nearly perfect plateau. Due to the two-terminal configuration we can only assume a filling factor of $\nu = 2$ which would correspond a lever arm of $\alpha = 1 \times 10^{11}$ cm^{-2} V^{-1}. This is slightly larger than the lever arm estimated for a parallel plate capacitor model of 7.4×10^{10} cm^{-2} V^{-1} but well in agreement with an enhanced lever arm due to electrostatic fringe fields, also seen in a similar study on graphene ribbons [120, 183].

Assuming $\nu = 2$, we approximate a constant contact resistance of 2450 Ω (see Figure 5.4 (b)).

The region of suppressed conductance around $V_{BG} = 2$ V is also heavily influenced by the magnetic field (see Figure 5.3(b)). At $B = 0$ T, the region of suppressed conductance is dominated by statistical Coulomb blockade (see also Figure 5.5(a)). For increasing magnetic field we still observe Coulomb peaks inside the gap region while the average conductance increases with a maximum around 2.5 T (see also Figure 5.8(b)). Above 2 T a new region evolves where the conductance is completely suppressed and no Coulomb peaks can be observed at all. With further increasing the B-field this region rapidly increases suppressing all conductance at 9 T from around $V_{BG} = 1$ V up to nearly $V_{BG} = 2.7$ V. In Figure 5.5(a) we show the conductance as a function V_{BG} between $V_{BG} = 1$ V and $V_{BG} = 3.5$ V for different magnetic field values. Similar measurements are also performed for the smaller nanoribbon D1 (see Figure 5.6(a)). The change in conductance with respect to the magnetic field becomes even more pronounced when averaging G in the regime of the suppressed transport. The range of back gate voltage for the averaging is chosen by a linear approximation at 9 T similar as described in section "device characterization" in order to approximate the maximum extend of the region of suppressed current. Figure 5.6(b) shows $\langle G \rangle$ from $V_{BG} = -1$ V to $V_{BG} = 4$ V as a function of B-field for device D1. From $B = 0$ to slightly below 2 T $\langle G \rangle$ increases by a factor of five due to (i) an increase of density of states around zero energy because of the formation of Landau levels and (ii) due to an increase of the average mode transmission as, from a semi-classical point of view, straight trajectories ($B = 0$ T) are less likely to enter the nanoribbon than curved ones ($B > 0$ T). Between $B = 1.8$ and 2.8 T, $\langle G \rangle$ stays roughly constant, most likely because of smearing out the condition to enter the quantum Hall regime ($r_c(n) < w/2$, see white dashed line in Figure 5.3(a)) due to charge carrier inhomogeneities. This is obviously most pronounced around the charge neutrality point and the shifted transition point to enter the quantum Hall regime for a n^* between 1×10^{11} and 2×10^{11} cm^{-2} is indicated by the black dashed lines in Figure 5.6(b). Above $B = 3.0$ T, $\langle G \rangle$ decreases heavily. This suppression of transport with increasing magnetic field has already been seen in studies with high mobility suspended graphene [110, 180, 181, 183] or dual-gated graphene flakes supported on hBN [182] but, so far, not on substrate supported nanoribbons. Device D2 shows the same behavior (see Figure 5.5(b)).

To investigate the energy dependency of this gap, we perform bias spectroscopy measurements in dependency of the lateral gate voltage V_{LG} for different magnetic fields. In Figure 5.7(a) we show dI/dV_{bias} at $B0$ T as function of V_{bias} and V_{LG} in the center of the transport gap at $V_{BG} = 1.5$ V, which shows the typical behavior of a nanoribbon dominated by statistical Coulomb blockade between $V_{LG} = -5$ V and $V_{LG} = 2.5$ V. We determine an effective energy gap of $E_g \approx 14$ meV (at $B = 0$ T) by estimating the maximum extend of suppressed current in bias voltage direction. The estimated E_g is a factor of two to three smaller than what has been reported for similar sized ribbons on SiO_2 [190, 191]. At 2.25 T (see Figure

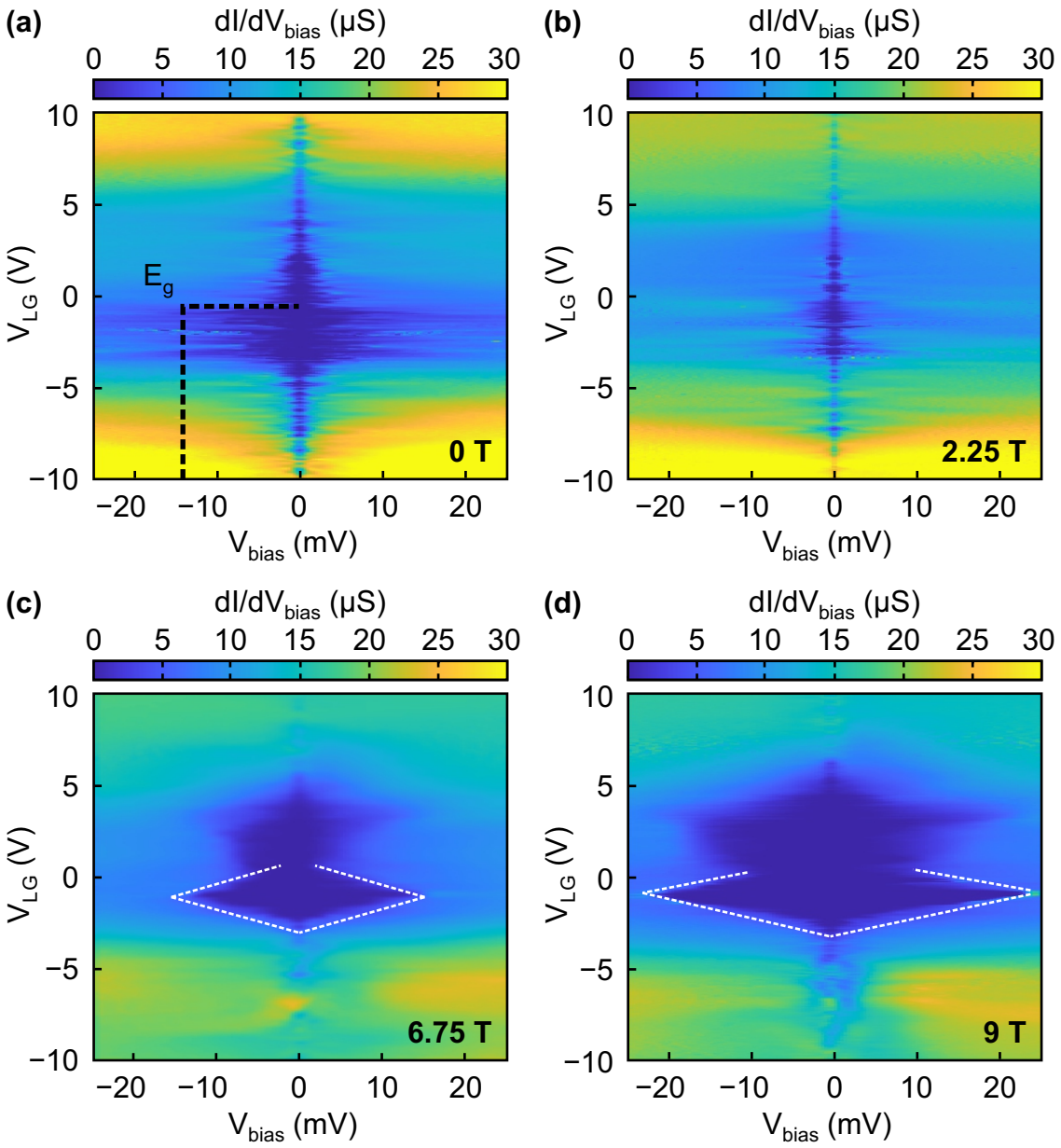

Figure 5.7: (a) Finite bias spectroscopy measurements at $B = 0$ T as function of V_{LG} in the center of the transport gap at $V_{BG} = 1.5$ V exhibiting statistical Coulomb diamonds with a charging energy E_g around 14 meV. (b) Finite bias spectroscopy measurements at $B = 2.25$ T still exhibiting statistical Coulomb diamonds with E_g around 6 meV. (c) Finite bias spectroscopy measurements at $B = 6.75$ T. A extended diamond-like feature indicated by the white dashed lines emerges around $V_{LG} = -1$ V where all transport is suppressed. (d) Finite bias spectroscopy measurements at $B = 9$ T. The diamond-like feature increases in size with the increased magnetic field and exhibits a maximum of 20 meV. All data from device D1.

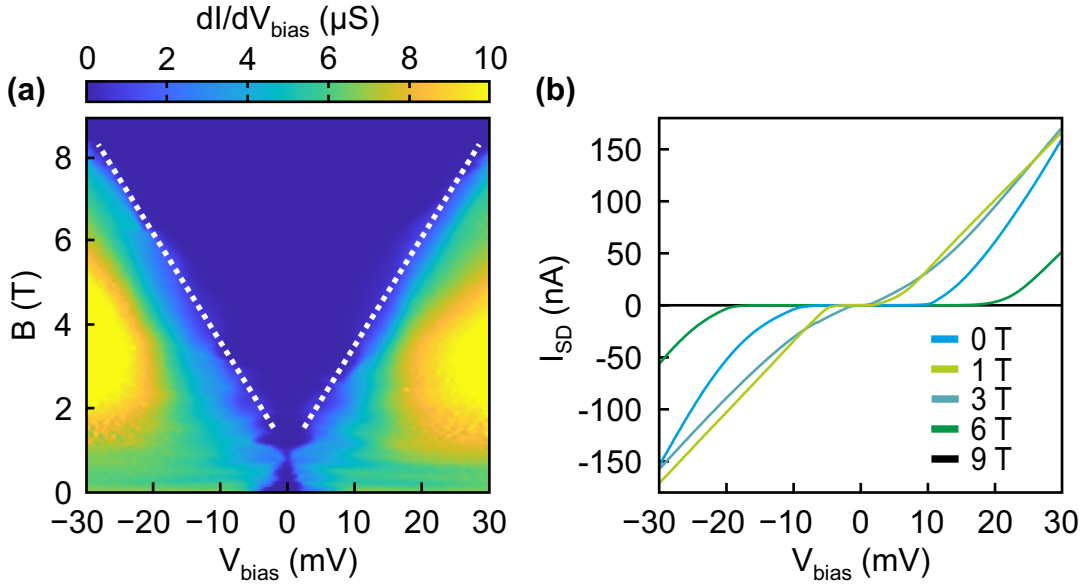

Figure 5.8: (a) Finite bias spectroscopy as function of B-field with $V_{BG} = 1.5$ V and $V_{LG} = 0$ V. Between $B = 2$ and 9 T a V-shaped insulating state with an energy gap increasing with roughly 3.75 meV/T up to 30 meV is visible. (b) I-V characteristic at $B = 0, 1, 3, 6$ and 9 T. All data from device D2.

5.7(b)) the effective energy gap is reduced considerably ($E_g \approx 6$ meV) due to the elevated transmission transparency. At 6 and 9 T (see Figure 5.7(c) and (d)) the statistical Coulomb blockade is strongly suppressed and we observe extended regions of completely blocked transport between $V_{LG} = -3$ V and $V_{LG} = 5$ V. The energy gap increases with magnetic field and exhibits a maximum of 20 meV around $V_{LG} = -1$ V at 9 T around the charge neutrality point of the ribbon (see white dashed line). In order to investigate the B-field dependency in more detail we perform finite bias spectroscopy measurements as function of the magnetic field (see Figure 5.9(a)) at $V_{LG} = -1$ V. Between $B = 0$ and 3.5 T we observe statistical Coulomb blockade of a disordered system which gets suppressed with increasing magnetic field as the density of states increases with magnetic field. Up to $B = 0.5$ T the effective energy gap of the Coulomb blockade varies around 10 meV and a non-linear I-V characteristic can be seen (see the blue trace in Figure 5.9(b)). When further increasing the B-field, E_g nearly shrinks to zero with an almost linear I-V characteristic (see 1T-trace in Figure 5.9(b)) consistent with the large increase in average conductance seen in Figure 5.6(b). In contrast, between $B = 3.5$ T and 9 T we see a second typ of energy gap, which increases with a slope of roughly 3 meV/T up to 20 meV at 9 T (see also high B-field traces in in Figure 5.9(b)). A similar behavior is seen for device D2 where the energy gap evolves roughly with a slightly smaller slope of 3.75 meV/T (see Figure 5.8).

Previous studies have proposed that the increasing magnetic field breaks the valley symmetry and opens up an electron-electron interaction induced $\nu = 0$ energy

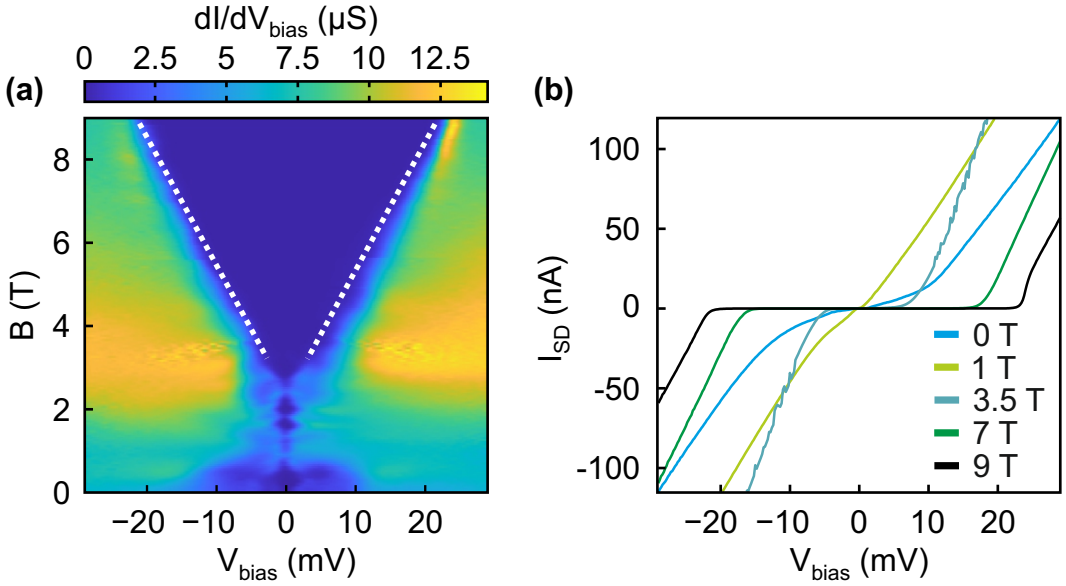

Figure 5.9: (a) Finite bias spectroscopy as function of B-field with $V_{BG} = 1.5$ V, $V_{LG} = -1$ V. Between $B = 3.5$ and 9 T a V-shaped insulating state with an energy gap increasing with roughly 3 meV/T up to 20 meV is visible. (b) I-V characteristic at $B = 0, 1, 3.5, 7$ and 9 T. All data from device D1.

gap [110, 181, 182, 192]. Remarkably, in all studies this $\nu = 0$ state scales linearly with magnetic field. Most simply, we can estimate the electron-electron interaction strength by the Coulomb energy $E_c = e^2/(\epsilon_0 \epsilon_r l_B)$ [110, 182], where l_B is the magnetic length $l_B = \sqrt{(\hbar/eB)}$ and $\epsilon_r = 4$ (due to hBN). Thus, E_c scales with $\sqrt{B}$ and can not explain the observed linear dependence. However, taking into account valley symmetry breaking terms of higher order given by $\delta E_c = (a/l_B)E_c$ [110, 182, 192], where a is the carbon-carbon bond length, the observed linear dependency ($\delta E_c \propto$B) can be explained. Estimating this higher order contribution yields a gap of $\delta E_c \approx 1$ meV/T [182]. For extended graphene this approximation shows good agreement with experimental values [182] but it is roughly three to four times smaller compared to the value we extract for the graphene nanoribbon devices, indicating that size-confinement effects are playing a crucial role. This is indeed likely as δE_c scales directly with the electron-electron interaction strength (E_c), which increases with an increased density of states when turning from a two-dimensional electronic system to an effectively one-dimensional system.

5.4 Insulating state as a tunnel barrier for a graphene single electron transistor

Next, we utilize this magnetic field dependent energy gap in the nanoribbon of device D1 as a reproducible tunnel barrier to form a single electron transistor (SET). The

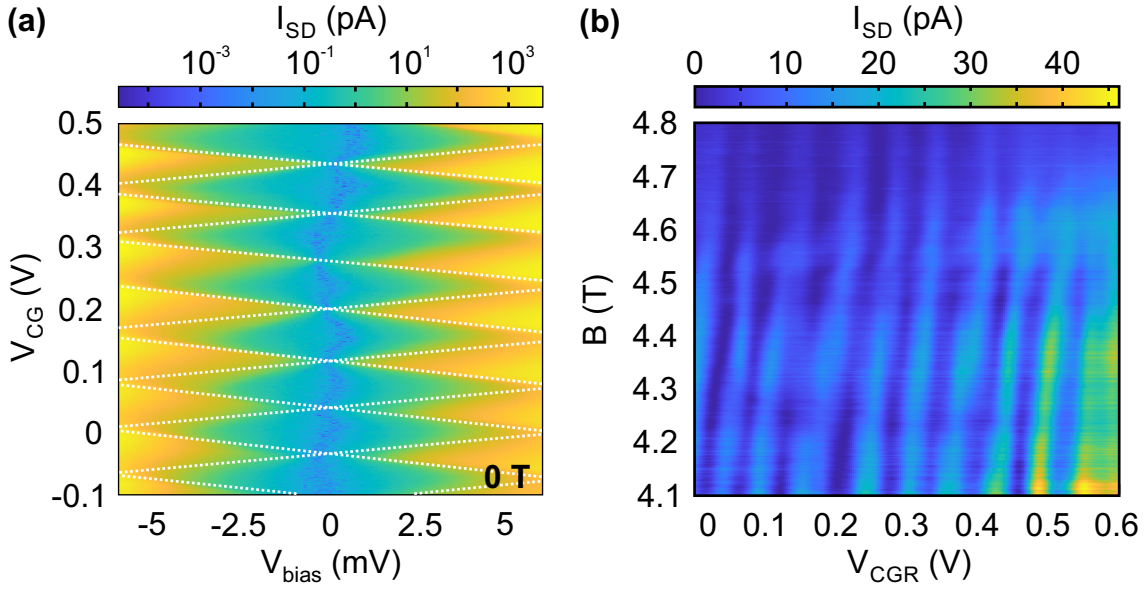

Figure 5.10: (a) Finite bias spectroscopy measurements at $B = 0$ T exhibiting Coulomb diamonds with a charging energy E_c around 6 meV. (b) Source-drain current I_{SD} as function of magnetic field B and V_{CGR} with the back gate and side gate voltages fixed at the edge of the insulating state ($V_{BG} = 1.35$ V and $V_{LG} = 0$ V). The Coulomb resonance shift slightly and decrease in amplitude with increasing B. All data from device D1.

nanoribbon connects a 100×100 nm^2 graphene island via a second nanoribbon with a width w of 50 nm and a length of 100 nm to a source and a drain contact. The chemical potential of the island can be locally tuned by a central gate (CG) (see chapter 4.4, Figure 4.4 (c)). First, we characterize the SET without magnetic field. In Figure 5.10 (a) a finite bias spectroscopy measurement in the Coulomb blockade regime of the ribbon at $B = 0$ T is presented, which shows a series of regular Coulomb diamonds originating from the graphene island with a charging energy E_c around 6 meV, which is in reasonable agreement with values reported for similar sized graphene SETs on SiO_2 [36] and on hBN [43]. Afterwards, we tune the device into the regime of the insulating state and measure the source-drain current in dependence of the central gate, which mainly tunes the graphene island. Figure 5.10 (b) shows I_{SD} as a function of V_{CGR} and B-field for $V_{BG} = 1.35$ V, $V_{LG} = 0$ V and $V_{bias} = 8$ mV. We observe Coulomb oscillations which slightly shift with the applied magnetic field. Additionally, the amplitude of these Coulomb oscillations decrease as we reduce the tunnel rate with increasing B-field, completely suppressing the transport around $B = 4.8$ T. In Figure 5.11 (a) single traces at $B = 4.35, 4.50$ and 4.65 T are shown, where the amplitude decreases from 15 pA at 4.35 T to below 5 pA at 4.65 T within only 30 mT. In Figure 5.11 (b) the integrated amplitude of the Coulomb oscillations between $V_{CGR} = 0$ and 0.6 V, which can be correlated to the tunnel rate into the SET, is shown. Beside the overall nearly linear decrease in

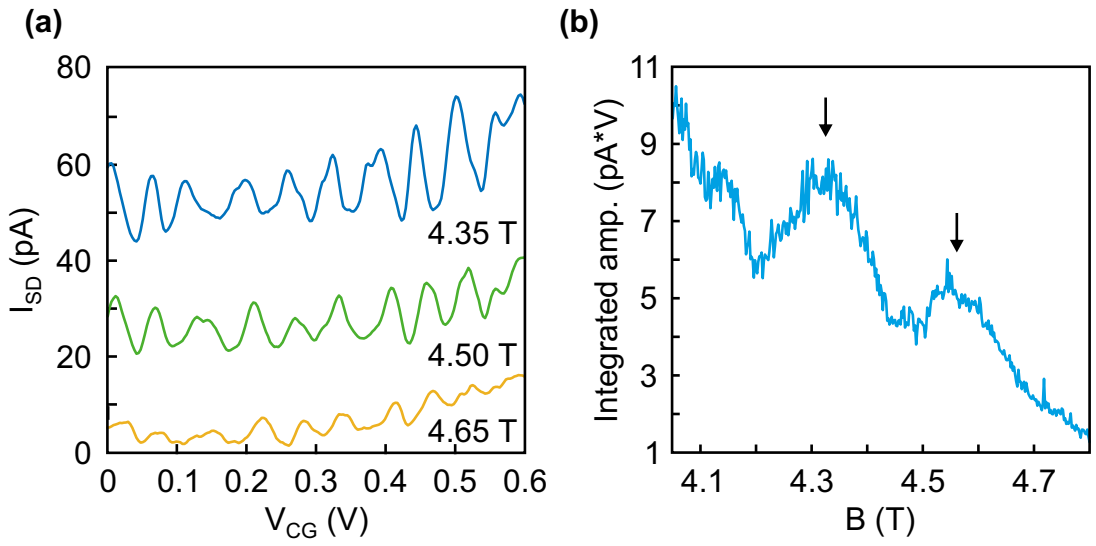

Figure 5.11: (a) I_{SD} as a function of V_{CGR} for $B = 4.35, 4.50$ and 4.65 T. Each trace is offset by 20 pA for clarity. (b) Integrated amplitude of the Coulomb peaks between $V_{CGR} = 0$ and 0.6 V. Beside the overall nearly linear decrease in intensity, a substructure of two peaks slightly above $B = 4.3$ T and $B = 4.55$ T is visible, which coincide with local minima in the energy gap dependency on the magnetic field seen in Fig. 5.9(a). All data from device D1.

amplitude, we see an additional substructure of two peaks slightly above $B = 4.3$ T and at $B = 4.55$ T (see arrows in Figure 5.11 (b)). These two peaks coincide with local minima of the energy gap seen in Figure 5.9 (a) and hence relate the change of tunnel rate to the insulating state.

5.5 Conclusion

In summary, we present an investigation of encapsulated graphene nanoribbons with a width around 35 and 40 nm. The measurements at zero magnetic field show disorder dominated transport similar to what has been observed for nanoribbons on SiO_2 and hBN. However, our fully encapsulated devices exhibit a smaller transport and effective energy gap. Interestingly, the magnetotransport is similar to high mobility suspended extended graphene sheets [110, 180, 181] and nanoribbons [183] or larger dual-gated graphene flakes supported on hBN [182]. At low magnetic fields of $B \approx 1$ T we observe a crossover from the Coulomb blockade regime to a regime of elevated average conductance due an increase of density of states at zero energy as the electrons condense into Landau levels. At a moderate magnetic field of $B \approx 2.5$ to 3.5 T the transport starts to be dominated by a density of states induced energy gap due to electronic correlation, which prevents all transport

and increases considerably with a slope of roughly 3 meV/T up to 20 meV and 3.75 meV/T up to 30 meV at 9 T for devices D1 and D2 accordingly. The linear increase of this $\nu = 0$ energy gap points toward a valley symmetry breaking induced by the magnetic field. Compared to extended graphene sheets on hBN [182] our observed slope is a factor of three larger potentially due to an enhancement of the electron-electron interaction by the spacial confinement. This insulating state inside the nanoribbon can be used as a reproducible and tunable tunnel barrier to the graphene island. Adjusting the gate voltages at the edge of the insulating state enables us to measure Coulomb oscillations, which amplitude can be, overall, linearly decreased by increasing magnetic field. The additional peaks visible can be related to a not completely linear energy dependency of the insulating state with respect to the magnetic field.

Chapter 6

Photo-induced remote doping of hBN/MoS_2/hBN heterostructures

This chapter has been published in parts in:

Quantum transport through MoS_2 constrictions defined by photodoping
A. Epping, L. Banszerus, J. Güttinger, L. Krückeberg, K. Watanabe, T. Taniguchi, F. Hassler, B. Beschoten, and C. Stampfer
J. Phys.: Condens. Matter, **30**, 205001 (2018)
©2018 IOP Publishing Ltd
https://doi.org/10.1088/1361-648X/aabbb8

Contributions

A.E. contributed to planning of the experiment, designed and fabricated the devices and performed measurements. Additionally, he performed data analysis and wrote the manuscript. L.B. contributed to planning of the experiment, designed and fabricated the devices and performed measurements. Additionally, he wrote the manuscript. J.G. performed the simulation of the light intensity distribution. K.W. and T.T. provided the hexagonal boron nitride. F.H. provided the theoretical support. B.B. and C.S. supervised the study and wrote the manuscript. All authors provided input to data analysis, discussed the results and assisted in manuscript preparation.

6.1 Introduction

As we have seen in the previous chapters mesoscopic physics in graphene is, due to the absence of a band gap, mostly studied in devices where the material has been etched into the desired shape [120, 193]. These devices typically suffer from

scattering and trap states on their rough edges [119, 120, 194]. We have seen that an insulating state induced by a perpendicular magnetic field could potentially be used as more controllable tunnel barriers for single layer graphene quantum dots. Another approach is to use bilayer graphene [47–49] and semiconducting TMDCs [65, 66], which allow for soft electrostatic confinement with the help of metallic gates, similarly to what has been pioneered in two-dimensional electron gases (2DEGs) in conventional semiconductor heterostructures for the past decades [9, 79, 80]. Atomically thin TMDCs such as MoS_2 hold great promise for investigating mesoscopic transport as they offer coupled spin-valley physics in combination with the possibility to electrostatic confine charge carriers. The advances in making increasingly complex van-der Waals heterostructures consisting of stacks of different van-der-Waals materials opened the door for investigating these mesoscopic transport properties in MoS_2 and related semiconducting transition metal dichalcogenides like WSe_2. Recently, first experiments on broken symmetry states and quantum confinement in one- and zero-dimensional structures have been demonstrated [63, 64, 66, 195–198]. In the next two chapters we will demonstrate an interesting method of defining arbitrary doping profiles in van-der-Waals heterostructures based on few-layers MoS_2 (two to five) encapsulated in hexagonal boron nitride (hBN). In analogy to remote doping in semiconductor 2DEGs, we make use of the photodoping effect recently observed in hBN/graphene heterostructures [67, 68, 199]. We use this effect to define stable and smooth sub-wavelength lateral doping profiles in MoS_2 employing metal shadow masks that are lithographically defined on top of a hBN/MoS_2/hBN heterostructure. Our photo-induced remote doping approach enables us to reach free charge carrier densities of up to 10^{13} cm^{-2}, when using an additional gate voltage during light illumination. We explore the photodoping (PD) of hBN/MoS_2/hBN heterostructure and the capability of the PD technique to confine charge carriers in well defined device geometries. All samples are fabricated using the well-established dry delamination van-der-Waals stacking technique [40, 115] described in chapter 4.5. A few-layer MoS_2 crystal gets partially encapsulated between two hBN flakes and contacted by a few-layer graphene (FLG) flake, which is patterned into the required contact configuration. The devices are characterized by scanning confocal Raman microscopy [149] which enables us to spatially probe the structural (and partly electronic) quality of all individual layers of the van-der-Waals heterostructure as shown in chapter 4.5. The highly doped Si^{++} substrate is used as a global back gate.

6.2 Photodoping of layered van-der-Waals materials on hexagonal boron nitride

Although perfect hexagonal boron nitride is regarded as one of the best substrates for electronic devices of two-dimensional semiconductors and graphene, it has to be noted that the hBN commonly used exhibits nitrogen vacancies and oxygen and

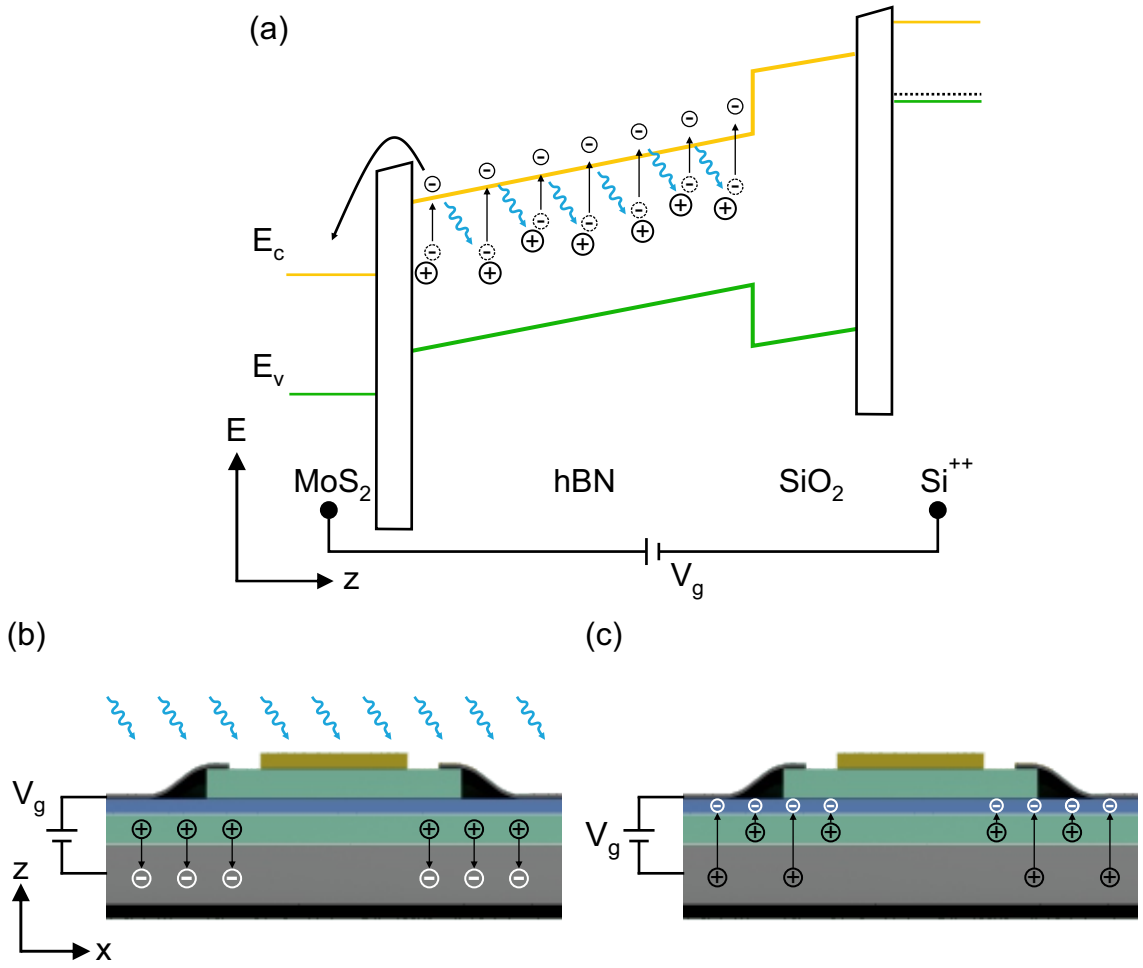

Figure 6.1: (a) Photons excite electrons (-) of donor-like nitrogen vacancies (+) (or holes of acceptor-like carbon impurities) in hBN to the conduction (or valance band). These excited charge carriers are mobile and follow the electrical field applied via the silicon back gate entering the layered van-der-Waals material. Adapted from reference [67]. (b) The ionized defects are positively (+) (or negatively, depending on the sign of the gate voltage) charged up until the electrical field (arrow) originating from the negative (-) charges (or positive, depending on the sign of the gate voltage) in the silicon layer is effectively screened. The area underneath the gate is not effected as the underlying 2d materials are not illuminated. (c) The charged defects (here positive (+)) create an additional electrical field which adds up to any field applied externally (here positive (+))) to the non-illuminated device resulting in an additional doping of the device (here negative (-)).

carbon impurities with a density on the order of 10^{18} atoms/cm^3 [200]. Theoretical studies predict that the nitrogen vacancies have a light absorption resonance around 2.8 eV while carbon impurities give rise to an absorption resonance at 2.6 eV [201]. The ionization of these defects by UV light can be exploited for a so called

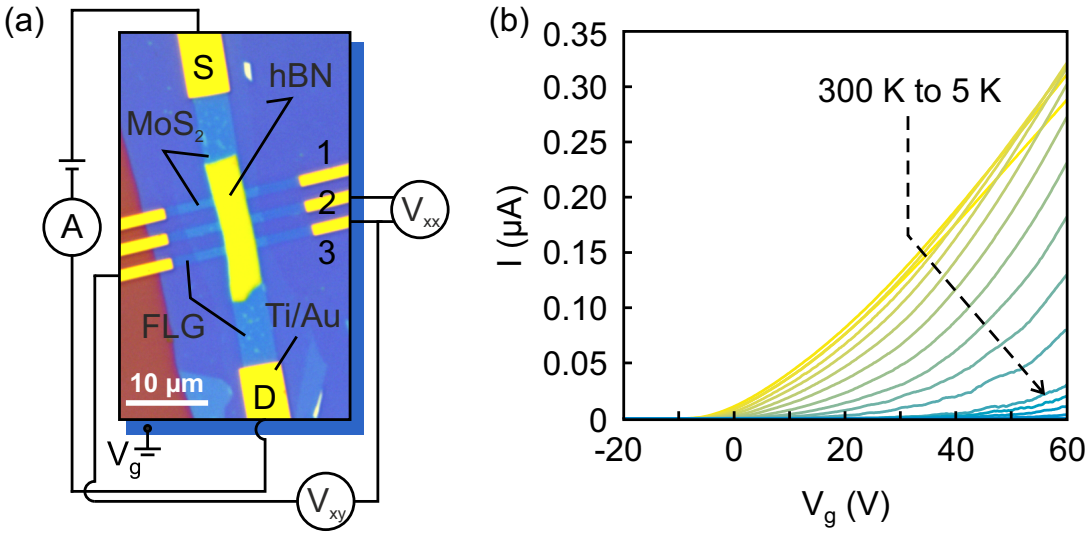

Figure 6.2: (a) Optical micrograph of a Hall bar device fabricated from a hBN/trilayer MoS_2/hBN/FLG heterostructure. (b) Current through the trilayer Hall bar as function of back gate voltage for temperatures ranging from 300 K to 5 K in steps of 25 K between 300 K and 25 K and steps of 5 K between 25 K and 5 K.

photodoping effect. The charged defects, which are spatially separated from the two-dimensional semiconductors or the graphene, act as a remote dopant. From a conceptual point of view this is similar to the remote modulation doping in traditional AlGaAs/GaAs semiconductor heterostructures where an ionized dopant layer located inside the insulator of the heterostructure is introduced during the growth and hence is spatially separated from the interface where the two-dimensional electron gas resides [202]. With the photodoping approach the doping level of the two-dimensional semiconductors or graphene resting on a hBN substrate can be adjusted by illuminating the device with light while applying an electrical field between the two-dimensional van-der-Waals material and, for example, a back gate. The photons excite electrons of donor-like nitrogen vacancies or holes of acceptor-like carbon impurities in hBN to the conduction or valance band, respectively. Due to the applied electrical field these charge carriers can transfer to the MoS_2 (see Figure 6.1 (a)). Consequently, the defects are charged up either positively (+) or negatively (-) depending on the sign of the gate voltage until the electrical field is effectively screened (see Figure 6.1 (b)) [67]. When the device is no longer illuminated the defects remain charged as without photons the electrons or holes are not able to relax back as no free charge carriers inside the hBN are available. The charged defects create a additional electrical field exactly opposite to the field they where charged with and which adds up to any field applied externally to the non-illuminated device (see Figure 6.1 (c)). The positive doping process is considerable slower, probably

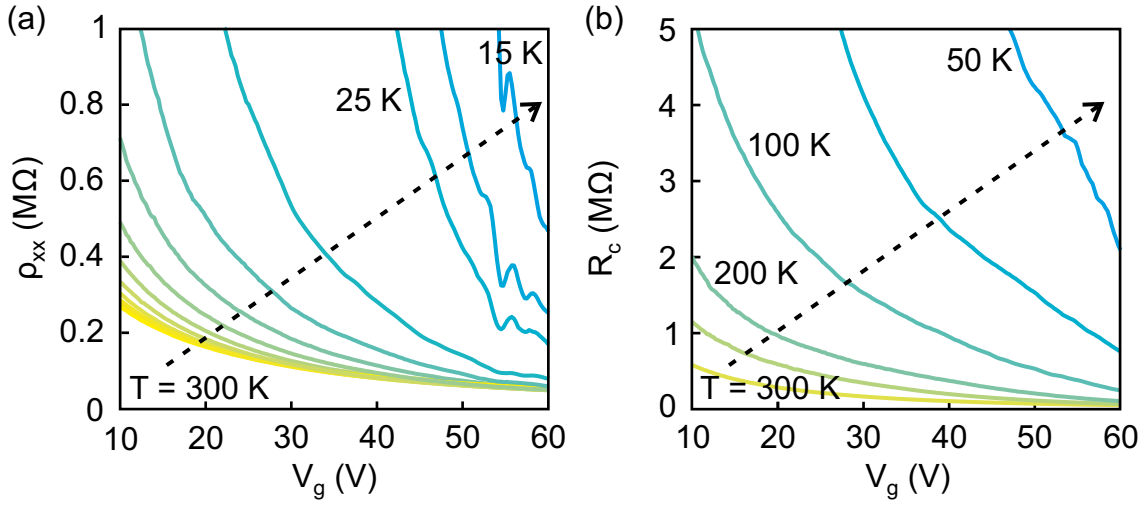

Figure 6.3: Sheet resistance ρ_{xx} (a) and contact resistance R_C (b) of the trilayer Hall bar depicted in Figure 6.2 (a) as function of back gate voltage V_g for different temperatures prior to photodoping. In panel (a) between 300 K and 25 K the temperature was changed in steps of 25 K and in steps of 5 K between 25 K and 15 K. The step size in panel (b) is 50 K.

due to a lower concentration of acceptor-like defects in hBN [67, 199]. Because the ionized defects are localized in the hBN and on average tens of nanometer away from the layered van-der-Waals material they introduce a minimum of extra scattering, similar to the modulation doping in traditional semiconductors, as we will demonstrated in chapter 6.

6.3 Photodoping of layered van-der-Waals materials on SiO_2

Additionally, we have to consider the role of the underlying SiO_2 in the photodoping process. The illumination of a layered van-der-Waals material on top of the SiO_2 layer without the hBN in-between also results in a change of the doping level but, in contrast to the photodoping on hBN, it is not time stable as will be shown in section 6.6. On SiO_2 the doping effect originates from charge traps in the silicon oxide or at the SiO_2/graphene interface [203, 204] induced by impurities or defects or the removal of adsorbates [205]. Here, photons excite electrons from the charge traps, which then transfer to the two-dimensional material, but which is independent of any applied gate voltage. An applied electrical field just increases the efficiency of the doping process while the total doping introduced is only depending on the trapped-charge density. Additionally, the UV light can potentially decompose adsorbed molecules also leading to a change in the surface charge. In both cases, the introduced doping starts to relax after the illumination is stopped on timescales of

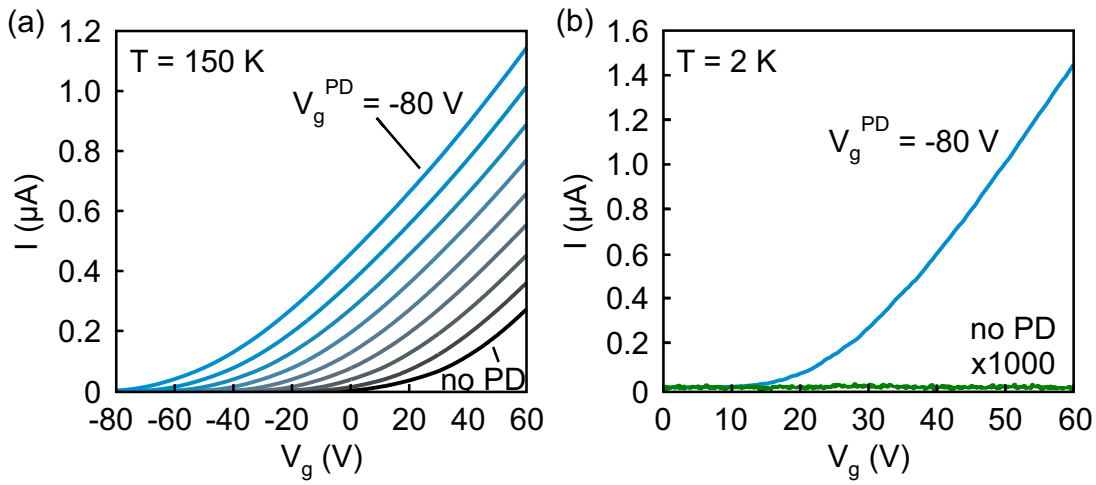

Figure 6.4: (a) Current as function of the gate voltage of the trilayer Hall bar depicted in Figure 6.2 (a) for several consecutive photodoping (PD) steps of $\Delta V_g^{PD} = -10$ V. (b) Current as function of gate voltage at T=2 K before and after the photodoping at $V_g^{PD} = -80$ V.

hours at temperatures around 150 K as trap states neutralize again by electrons tunneling from the layered van-der-Waals material back into the gate oxide. In contrast, the doping introduced by the photodoping on hBN persists at least for days making it much more reproducible and controllable as we will demonstrated in section 6.5.

6.4 Transport characterization before the photodoping

We start by discussing charge transport in a trilayer MoS_2 Hall bar structure and explore the method of photodoping before discussing transport through the MoS_2 constrictions. The Hall bar device (see Figure 6.2 (a)) was fabricated the same way as described above and in chapter 4.5. In Figure 6.2 (b) we show the current I flowing through the Hall bar, which is measured in standard four-terminal geometry in longitudinal configuration as function of the applied gate voltage V_g for temperatures ranging between 300 K to 5 K at a constant bias voltage of $V_b = 100$ mV. Prior to photodoping (PD), the overall current strongly decreases with decreasing temperature and falls below our detection limit for temperatures less than 10 K (see corresponding green curve taken at 2 K in the inset of Figure 6.4 (b)). The strong decrease of current at low temperatures is due to (i) a strong increase of the MoS_2 resistance and partially (ii) to an increase of the contact resistance. Figures 6.3 shows the four-terminal resistivity (a) and the contact resistance (b) as

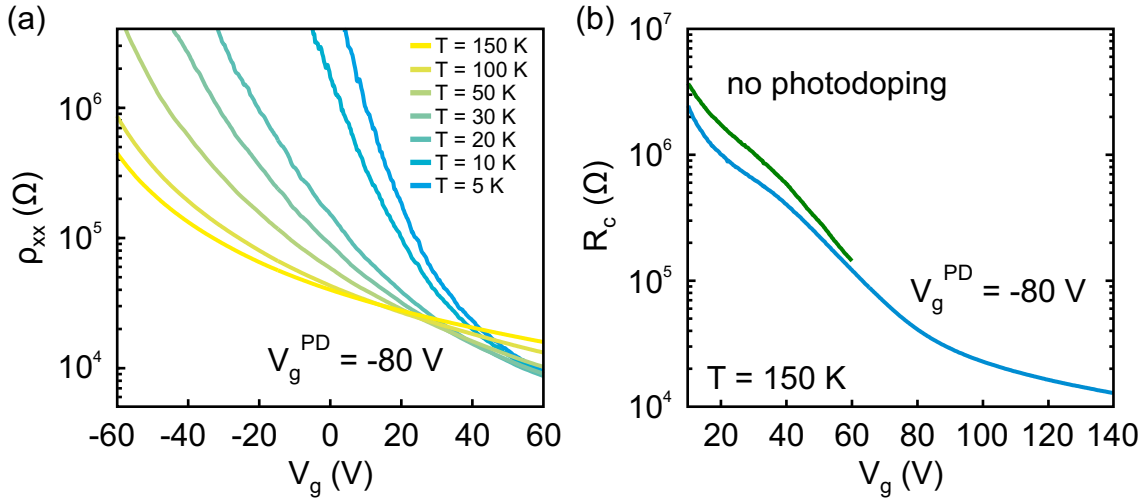

Figure 6.5: (a) Sheet resistance as function of back gate voltage and temperature. The measurements were taken on the trilayer Hall bar device depicted in Figure 6.2 (a) after photodoping at $V_g = -80$ V. (b) Contact resistance as function of back gate voltage before and after photodoping. To account for the photodoping the green trace has been shifted by 80 V. The measurements were performed at 150 K.

function of the applied back gate voltage and temperature prior to photo-induced doping of the Hall bar discussed in Figure 6.2. As a result of the low charge carrier density, the device becomes insulating at low temperatures as previously observed [206], which results in a strong increase of the sheet resistance. In addition, the contact resistance strongly increases, as thermal excitations of charge carriers over the Schottky-barriers at the contacts are suppressed at low temperatures. The increase in resistivity of the MoS_2 is most likely due to localization effects. At higher temperatures, we observe a gate dependent insulator-to-metal transition identified by the onset of the current flow in Figure 6.2 (b), which continuously shifts to smaller gate voltages with increasing temperature. Similar observations of a charge carrier density dependent insulator-to-metal transition in MoS_2 have been recently reported [206–208]. Metallic conductance at low temperatures can be observed for high charge carrier densities around $n \approx 10^{13}$ cm^{-2}.

6.5 Transport characterization after the photodoping

In order to adjust the charge carrier density in our devices we make use of the recently reported photodoping mechanism across a hBN-to-graphene interface (see section 6.1 and references [67, 68, 199]). Nitrogen vacancies and/or carbon impurities in the hBN crystal can be optically activated and act as a charge reservoir. By illuminating our hBN/MoS_2/hBN Hall bar using a high energy light emitting diode (LED) with

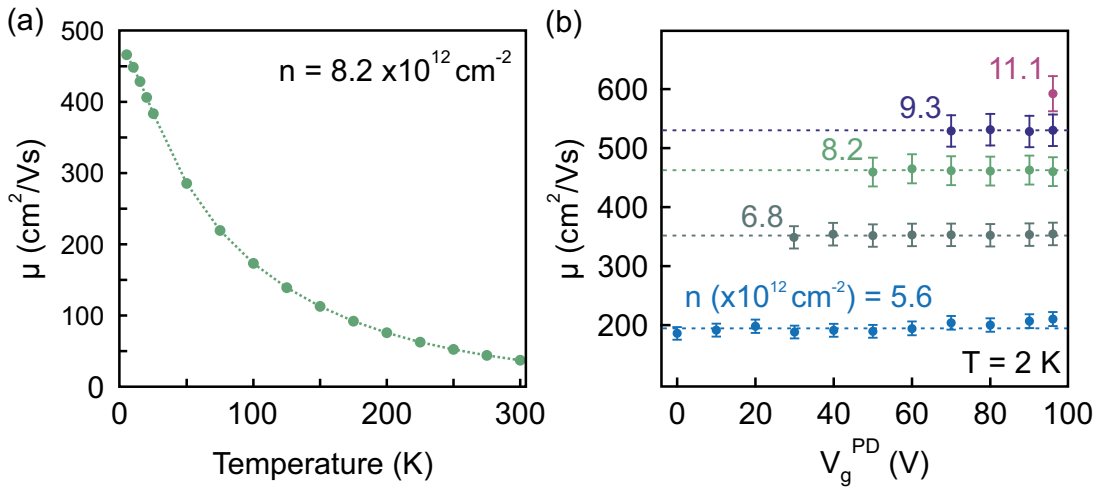

Figure 6.6: (a) Charge carrier mobility of a five-layer Hall bar as function of temperature, showing increased carrier mobility at low temperatures after photodoping at 150 K. (b) Charge carrier mobility as function of the photodoping gate voltage for different charge carrier densities, indicating that photodoping does not influence the charge carrier mobility of the device.

a center wavelength of 470 nm, these hBN defect states get optically excited. By applying a gate voltage, the activated charges are transferred into the MoS_2 layer leaving behind oppositely charged states in the hBN layer. The charge transfer continues until the applied (back gate induced) electric field gets fully screened by the charged hBN layer. When turning off the LED, the charges become trapped in the hBN resulting in a constant carrier doping of the illuminated area of MoS_2. In agreement with earlier work on similar photodoping of graphene [67, 68], we observe that the doping is stable over the entire measurement period (up to several weeks) in the temperature range between 2 K and 250 K. All transport measurements have been performed after the LED has been switched off. As any excitation of charge carriers due to the illumination and their relaxation happens in MoS_2 on the order of ps to ns [209, 210] we consider the effect of the illumination only to be relevant for the photodoping process.

Figure 6.4 (a) shows a series of gate characteristics of the trilayer Hall bar depicted in figure 6.2 (a) at 150 K before and after photodoping. The device was illuminated (photodped) for 10 minutes at constant gate voltages V_g^{PD} varying between $V_g^{PD} = -10$ V and $V_g^{PD} = -80$ V in steps of $\Delta V_g = -10$ V. The illumination time is chosen in such a way that the the photodoping process is saturated. The gate characteristics show a respective overall increase in current, which corresponds well to shifts of $\Delta V_g^{PD} = -10$ V in gate voltage. At the same time the gate characteristics remain identical in slope and shape indicating a constant charge carrier mobility and a homogeneous and efficient doping process throughout the entire device. After

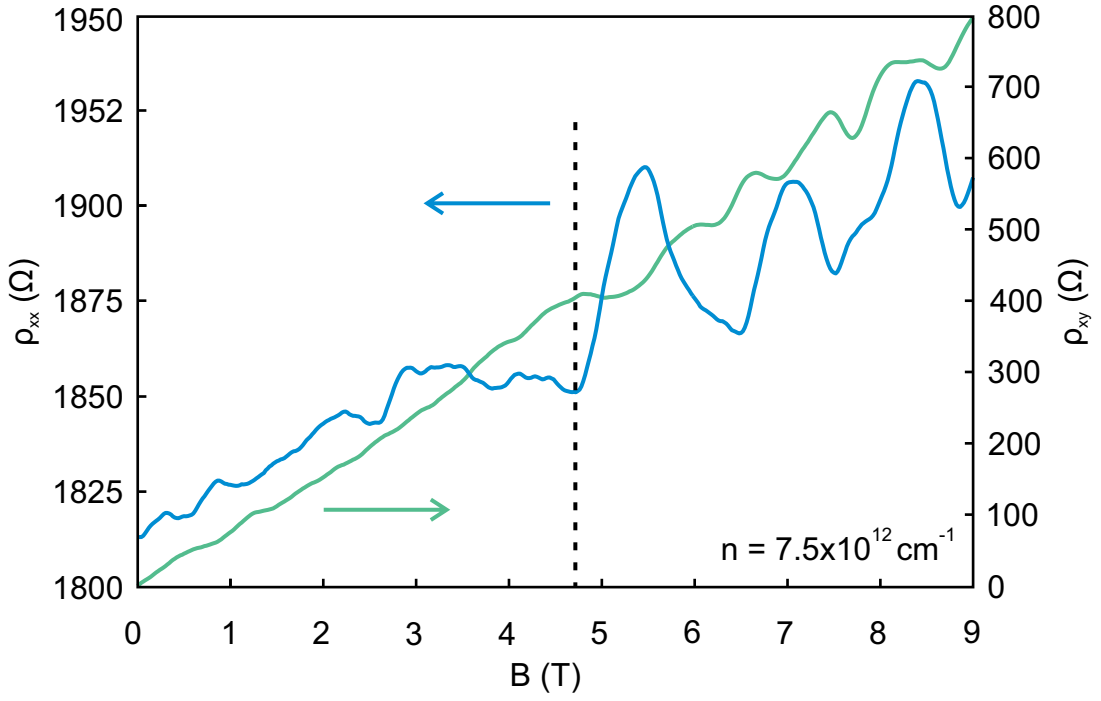

Figure 6.7: Longitudinal resistivity ρ_{xx} (blue) and Hall resistivity ρ_{xy} (red) of the trilayer Hall bar discussed in Figure 6.2 (a) as function of magnetic field at 2 K. Shubnikov-de-Haas oscillations appear at around 5 T.

illuminating the Hall bar at $V_g^{PD} = -80$ V, the device shows metallic behavior, i.e. it remains well conductive at 2 K when applying moderate gate voltages (see Figure 6.4 (b). In more detail, Figure 6.5 (a) shows the sheet resistance of the Hall bar as function of back gate voltage and temperature after photodoping at $V_g^{PD} = -80$ V. For gate voltages lower than 10 V, the device still becomes insulating with decreasing temperature, whereas the sample remains conductive at low temperatures for gate voltages larger than $V_g = 10$ V indicating a metallic behavior. This is supported by an increase of the carrier mobility with decreasing temperature at high charge carrier densities. Figure 6.5 (b) shows the contact resistance as function of the applied back gate voltage at 150 K before and after photodoping at $V_g^{PD} = -80$ V (blue and green trace, respectively). To account for the photodoping the green trace has been shifted by 80 V. Interestingly, the contact resistance is also effected by photodoping, allowing to achieve contact resistances as low as 15 kΩ.

Charge carrier mobilities extracted from Hall measurements on a typical five layer MoS_2 Hall bar device show values on the order of $\mu = 600$ cm^2/(Vs) at low temperatures (2 K), which decreases to a value of around 45 cm^2/(Vs) at room temperature most likely due to electron-phonon scattering [206] (see Figure 6.6 (a)). In the Figure 6.6 (b), the extracted charge carrier mobility at 2 K is plotted erent photodoping steps. For each photodoping step the device is warmed up to 150 K (as the LED is freezing out at low temperatures), the photodoping is performed and the

device is cooled down again to 2 K to extract the low temperature carrier mobility. The different colors represent different charge carrier densities. The photodoping significantly increase the available range of charge carrier density n as in the non-photodoped device n was limited to 5.6×10^{12} cm^{-2} when applying reasonable gate voltages. Similar to remote doping in 2DEGs [211], the mobility of the device is not affected by the process of photodoping, as the charge that is introduced in the hBN flake is spatially separated from the MoS_2 (see colored dashed lines in Figure 6.6 (b)). Additionally, we do not observe any significant change of n at a fixed gate voltage with respect to the temperature after the photodpoing up to T=150 K. In order to underline the high electronic quality of the heterostructures, we also measure the quantum Hall effect in the five-layer MoS_2 Hall bar [62]. The longitudinal resistivity ρ_{xx} (see blue trace in Figure 6.7) shows Shubnikov-de-Haas-oscillations with an onset of the oscillations slightly below B=5 T (black dashed line), which corresponds to a quantum mobility of around 2000 cm^2/(Vs). In red the corresponding transverse Hall resistivity ρ_{xy} is shown. At high B field ρ_{xy} begins to reveal plateau-like structures.

6.6 "Photodoping" effect in MoS_2 on SiO_2

In order to investigate the influence of the hBN for the photodoping effect, we perform a control experiment, where a five-layer MoS_2 flake is resting directly on SiO_2. For this the MoS_2 flake is directly exfoliated on the SiO_2 substrate while we follow the same process steps afterwards as described in the main manuscript. Figure 6.8 (a) shows the gate characteristics at 150 K before and after photodoping for the device shown in the inset. The device was illuminated by a high energy light emitting diode (LED) with a center wavelength of 470 nm for 15 minutes at constant back gate voltages. After the initial illumination with $V_g^{PD} = -10$ V the gate characteristic shows an overall increase in current similar to a doping shift of roughly 7 V. A second photodoping step with $V_g^{PD} = -60$ V leads to an additional shift of around 35 V. Interestingly, illuminating the device again with $V_g^{PD} = -10$ V for 15 minutes shifts the gate characteristics even further, which is in clear contrast to the photodoping on hBN, where the shift saturates at the applied gate voltage regardless of time or power of the illumination making the photodoping on hBN controllable and useful for systematic investigations. In the control experiment the increase of the voltage leads to an increased efficiency of the doping process consistent with previous studies of "photodoping" on graphene on SiO_2 [203, 204]. Kim et al. [203] and Yurgens et al. [204] relate this "photodoping" effect to charge traps in the silicon oxide or at the SiO_2/graphene interface (see section 6.6). Figure 6.8 (b) shows the time evolution of the measured current through the device at fixed $V_g = 40$ V for T= 150 K and T= 5 K after photodoping the device over night at $V_g^{PD} = -60$ V. For comparison, a similar measurement at T= 150 K and T= 25 K for a device supported by hBN is shown. Time equal zero hours marks

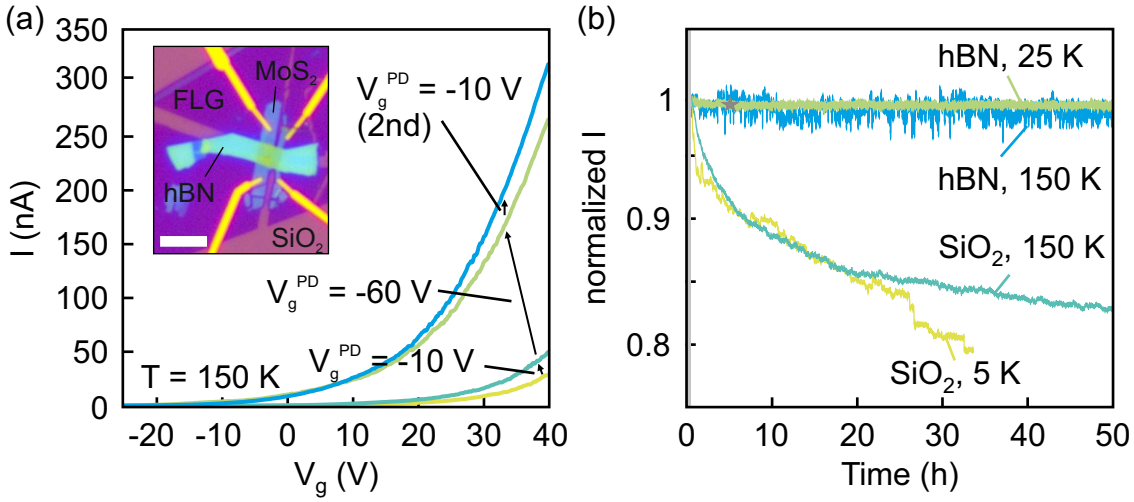

Figure 6.8: (a) Current as function of the gate voltage for a five-layer MoS_2 flake on SiO_2 before and after photodoping for the device shown in the inset. All data were measured at 150 K. (b) Current as function of time with V_g = 40 V after photodoping at $V_g^{PD} = -60$ V of the device shown in panel a and a device supported by hBN for comparison. At time = 0 h the LED was turned off. The current is shown for times ¿30 min. The measurement on hBN at 25 K has been slightly corrected at a single data point for an additional transient event in the contact (see star).

the switching off of the LED. As the time directly after switching off the LED is dominated by transient effects in the contacts and as we are only interested in the long-time stability of the induced doping effect, the current is shown for times ¿30 min. Both measurements on SiO_2 show an initial rapid decrease of the current corresponding to a back shift of the gate characteristic followed by a slow down of the decay after around 24 hours, although it is still significant after 50 hours with no visible saturation. The devices on hBN do not show a decay of the doping.

6.7 Conclusion

In summary, we present a technique to fabricate transport devices based on few-layer MoS_2 partially and fully encapsulated in hBN using an entirely dry transfer process. The MoS_2 is contacted using few-layer graphene and we adjust the charge carrier concentration using photodoping. By transferring only a single FLG flake to fabricate a large number of contacts to the MoS_2, we reduced the complexity of the required van-der-Waals heterostructure significantly. Similar to remote doping in 2DEGs, we are able to adjust the doping level in MoS_2. Our photo-induced remote doping approach enables us to reach free charge carrier densities of up to 10^{13} cm^{-2}, when using an additional gate voltage during light illumination. The

doping process is homogeneous and efficient throughout the entire device and yields metallic behavior, i.e. the Hall bar remains well conductive at 2 K, while preserving the charge carrier mobility of up to $\mu = 600$ cm^2/(Vs) at low temperatures (2 K).

Chapter 7

Quantum transport through MoS_2 constrictions defined by photodoping

This chapter has been published in parts in:

Quantum transport through MoS_2 constrictions defined by photodoping
A. Epping, L. Banszerus, J. Güttinger, L. Krückeberg, K. Watanabe, T. Taniguchi, F. Hassler, B. Beschoten, and C. Stampfer
J. Phys.: Condens. Matter, **30**, 205001 (2018)
©2018 IOP Publishing Ltd
https://doi.org/10.1088/1361-648X/aabbb8

Contributions

A.E. contributed to planning of the experiment, designed and fabricated the devices and performed measurements. Additionally, he performed data analysis and wrote the manuscript. L.B. contributed to planning of the experiment, designed and fabricated the devices and performed measurements. Additionally, he wrote the manuscript. J.G. performed the simulation of the light intensity distribution. K.W. and T.T. provided the hexagonal boron nitride. F.H. provided the theoretical support. B.B. and C.S. supervised the study and wrote the manuscript. All authors provided input to data analysis, discussed the results and assisted in manuscript preparation.

7.1 Introduction

After we have established a reliable method to adjust the charge carrier density using photodoping while preserving the charge carrier mobility, we explore the feasibility of our approach for carrier confinement by defining the shape of a constriction with a metallic structure which acts as a shadow masks during photodoping and study quantum transport through the resulting MoS_2 constrictions. Semiconducting van-der-Waals heterostructures based transition metal dichalcogenides (TMDs) are in particular interesting as one of the main challenges in this field of mesoscopic physics is to find ways of confining charge carriers in well defined device geometries [63, 64, 66]. Achieving a high degree of control over carrier confinement is necessary for manipulating individual charges or spins [212–214], as well as for investigating mesoscopic physics phenomena such as quantized conductance or valley filtering. Moreover, good control over carrier confinement is a necessary requirement for studying fundamental material properties such as the Landé g-factor and the charge carrier's effective mass in mesoscopic devices. For observing size-quantization effects, including quantized conductance, the Fermi wavelength of the carriers has to be on the order of the constriction width. For reasonable carrier densities this requires devices with feature sizes on the order of 100 nm (or below). In order to harness photodoping for such small device feature sizes, we employ a shadow masking technique using non-transparent metal structures.

7.2 Defining constrictions in MoS_2 by photodoping

Notably, this approach is in contrast to previous work, where some of us demonstrated photodoping in graphene/hBN heterostructures with micron-scale spatial resolution using a confocal laser set-up [68]. The metallic shadow masks, predefined by electron beam lithography, allow to define long-lasting doping profiles in arbitrary geometries (see e.g. inset of Figure 7.2). Using this shadow masking technique, we illuminate only the source and drain contact areas (leads) and the constriction, while everything covered by the metal masks is unaffected by the photodoping process. As the MoS_2 is non-conductive at 2 K prior to the photodoping no depletion is necessary to form a constriction between the metallic shadow masks. In contrast to conventional constrictions in 2DEGs, we neither have to etch our sample nor have to use electrostatic gates to define the structure as free carriers are only available in the regions, where the sample has been photodoped. In the following, the metallic shadow mask is only used to define the constriction by the photodoping. The devices are only tuned by applying a gate voltage V_g to the highly doped Si^{++} back gate.

In order to estimate the expected width of the constriction we perform numerical simulations[1] of the (lateral) light intensity profile responsible for forming the con-

[1]The simulation was performed using the COMSOL Multiphysics package and assumes vertical

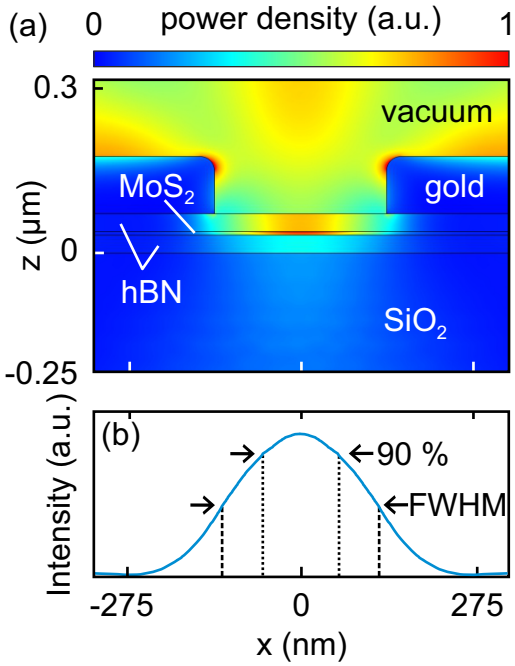

Figure 7.1: (a) Simulation of the intensity distribution in the constriction region defined by a shadow mask assuming vertical illumination of the sample. (b) Intensity profile of a cross-section through the bottom hBN for 275 nm spaced shadow masks. The full-width-at-half-maximum yields a width of 240 nm. If we assume that we need 90% of the light intensity for forming the constriction the width of it would reduce to around 120 nm or below.

striction during photodoping. Figure 7.1 shows the simulated intensity distribution in the constriction region defined by a 275 nm spaced shadow mask. The simulation indicates that the light intensity underneath the shadow mask is strongly suppressed, with a lateral extend of the intensity profile at full-width-at-half-maximum (FWHM) of 240 nm (see arrows in Figure 7.1 (b)). It has to be emphasized that this value can only be regarded as an upper limit as we do not know (i) the intensity at which photodoping becomes efficient, (ii) to which extend electrostatic effects from the metallic shadow mask and (iii) additional plasmonic effects between the shadow masks may affect the potential landscape in the constriction region. When assuming 90% of the light intensity is needed to form the constriction its width would reduce to around 120 nm or below. To further investigate the influence of these effects, additional experiments are necessary which are beyond the scope of this work. Similar simulations have been performed for different constriction width showing similar results.

illumination of the sample.

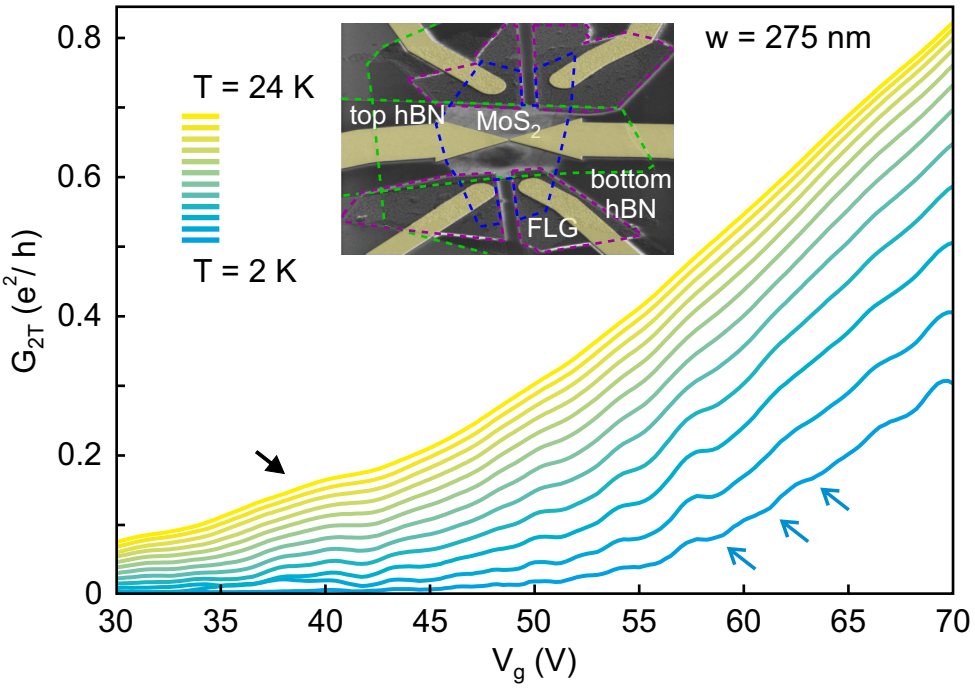

Figure 7.2: Two-terminal conductance G_{2T} through a bilayer MoS_2 constriction as function of gate voltage for different temperatures in steps of 2 K. Step-like features in the conductance are observed at low temperatures. These features vanish at 15 K, as the MoS_2 underneath the metallic shadow mask becomes conductive.

7.3 Transport characterization in two- and four-terminal configuration

Figure 7.2 shows the two-terminal conductance through a 275 nm wide constriction fabricated from a bilayer MoS_2 flake at constant bias of $V_b = 3$ mV for temperatures ranging from 2 K to 24 K (after photodoping the device at 50 K and $V_g^{PD} = -60$ V). The conductance trace at 2 K shows step-like features suggesting confinement effects in the constriction (see Figure 7.3 (c)). A very similar behavior is observed for all four measured constriction devices (see Figure 7.3). The step-like features in the conductance traces remain visible up to 15 K (Figure 7.2) with increasing two-terminal conductance. The increasing conductance with a fixed position of the features with respect to V_g could well be a sign of increasing transmission through the constriction until the confinement gets destroyed when the MoS_2 underneath the metallic shadow masks starts to contribute to the transport. Overall the two-terminal conductance is heavily device dependent most likely due to a large variance of the contact resistances. Especially the sample contacted by just 5 nm Ti / 95 nm Au (see Figure 7.3 (d)) shows an overall low conductance on the order of 0.01 e^2/h

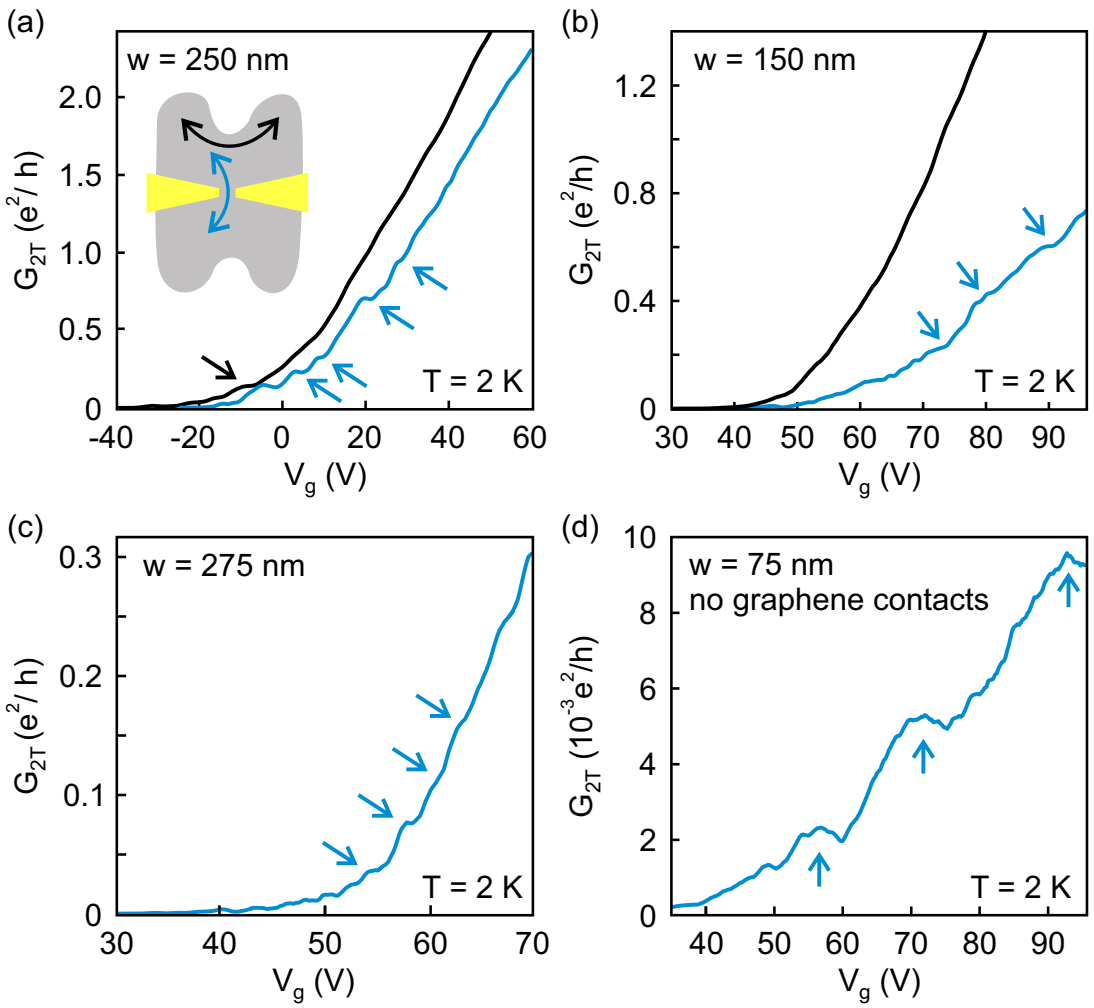

Figure 7.3: (a) Two-terminal conductance G_{2T} alongside (black trace) and through a four-terminal trilayer MoS_2 constriction (blue trace) as function of gate voltage after photodoping. The conductance trace alongside the constriction are smooth, whereas only the trace through the constriction exhibits step-like features in the current. Inset: schematic of the current flow corresponding to the different conductance traces. (b) G_{2T} of a 150 nm seven layer MoS_2 constriction after photodoping at V_g=-96 V alongside (black trace) and through the constriction (blue trace) as function of gate voltage. (c) G_{2T} through the constriction shown in 7.2 at 2 K, showing kinks in the conductance (see blue arrows). (d) G_{2T} of a 75 nm bilayer MoS_2 constriction after photodoping at V_g=-96 V. The device was fabricated without graphene leads using just 5 nm Ti / 95 nm Au contacts, resulting in a strongly reduced conductance.

but still clear plateaus are observed. In order to verify that the conductance steps originate from the constriction, we perform two-terminal measurements in different

contact configurations on two separate multi-terminal devices (see Figure 7.3 (a) and (b)) with a constriction width of 250 nm (trilayer MoS_2) and 150 nm (seven layer MoS_2), respectively. The black traces in Figure 7.3 (a) and (b) show the conductance between two contacts on one lead, i.e. on one side of the constriction of the four-terminal devices (see the black arrows in the inset of Figure 7.3 (a)). The measurements were performed at 2 K after photodoping the devices at $V_g^{PD} = -60$ V and V_g=-96 V, respectively. Both traces show a smooth and monotonic increase of the conductance with the applied gate voltage except for a feature close to the onset of the conductance at around $V_g = -5$ V (see black arrows) and are overall very similar in shape to the traces obtained from several Hall bar devices. The feature close to the transport onset is most likely related to localized states due to the random potential variations from trapped charges [215]. In contrast, the conductance through the constriction (blue trace in Figure 7.3 (a) and (b)) show the similar extended step-like features as they were observed for the two-terminal devices. The total resistance from the two-terminal data shown in Figure 7.3 heavily depends on the particular device. It ranges between 10 and 100 kΩ and is thus significantly larger than the conductance quantum, as the contact resistances heavily contributes to the overall resistance. A subtraction of these parasitic resistances proves difficult as both are strongly gate voltage and bias dependent. In order to reduce the influence of these additional device resistances on the measurement, we performed four-terminal measurements on the multi-terminal trilayer MoS_2 device (see inset of Figure 7.5 (a)). It is important to point out that this four-terminal measurement allows to extract an effective two-terminal conductance as the voltage is probed roughly 4 μm away from the constriction. This length is significantly larger than the elastic mean free path in the MoS_2 2DEG. In Figure 7.5 (a) we show the four-terminal conductance G_{4T} in unit of the conductance quantum e^2/h as a function of the applied gate voltage measured at 2 K. The conductance ranges from 0 to 11 e^2/h and exhibits step-like features which are roughly spaced by 1 to 2 e^2/h (see blue arrows). This observation is in contrast to the expected appearance of steps at multiples of 6 e^2/h for a narrow constriction in trilayer MoS_2 due to the six-fold degeneracy of the three Q and three Q' valleys, which govern the transport [63, 64].

However, it is in reasonable agreement with recent measurements performed on a gate-defined nanoconstriction in a MoS_2-based heterostructure [64]. It might be explained by lifting of the level degeneracies due to the additional confinement of the constriction and/or a reduced transmission through the constriction while we cannot completely exclude that the FLG/MoS_2 interface and the MoS_2 regions leading to the constriction cause an additional series resistance. The reduced transmission would also explain (i) that the observed step sizes do not meet precisely multiples of 1 or 2 e^2/h and (ii) the substructure observed on the gate voltage derivative of G_{4T} (Figure 7.5 (b)) and the bias-dependent measurements (Figure 7.5 (c)). The latter exhibit well developed diamond-like features for high gate voltages (> 30 V) from which we extract an energy scale of around 3 to 4 meV for the involved subband

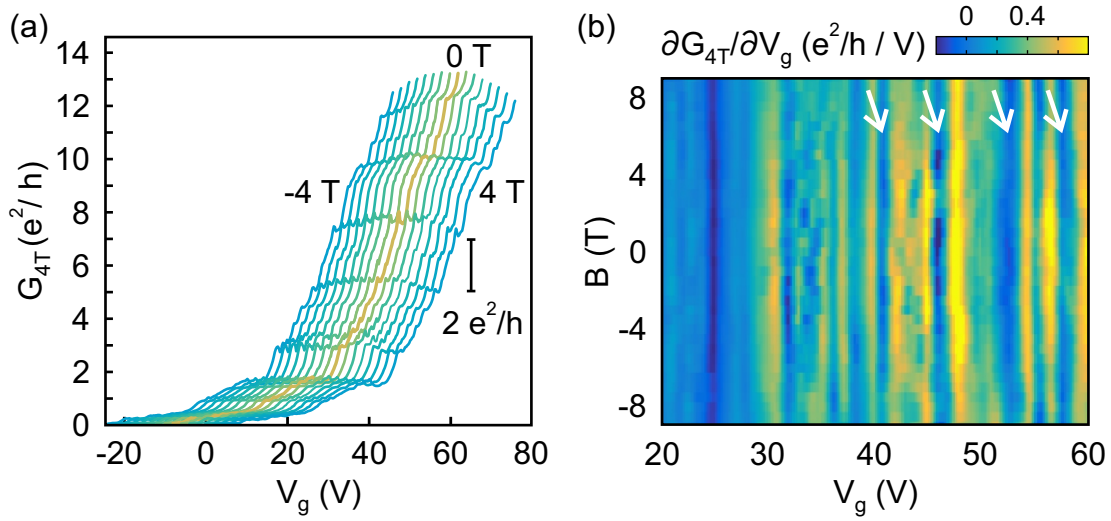

Figure 7.4: (a) Four-terminal conductance as function of the applied gate voltage at 2 K for a constant bias of V_b = -6 mV at fixed perpendicular magnetic fields B ranging from -4 T to 4 T for the same device shown in Figure 7.5 after a second cool-down. Again we observe step-like features which are roughly spaced by one e^2/h. (b) Transconductance dG/dV_g as a function of the applied gate voltage and the magnetic field for V_b = -6 mV. The white arrows highlight the same features marked by the blue arrows in panel a.

spacings, where the degeneracy is potentially lifted. At lower carrier density (smaller gate voltages) the bias spectroscopy measurements show signatures of intersecting diamonds, which we attribute to localized states forming in the narrow constriction.

7.4 Magnetotransport

In Figure 7.4 we show the four-terminal conductance as function of gate voltage for different perpendicular magnetic fields B ranging from $B = -4$ to 4 T. These measurements have been taken on the same device shown in Figure 7.5 but at a different cool-down. The traces are offset by $V_g = \pm 2$ V for clarity. We again observe well-developed step-like features with a step height on the order of 1 or 2 e^2/h (see e.g. the step from $G = 5$ to 7 e^2/h at 4 T). Most importantly, we observe that the step-like features are virtually not tuned by the applied B-field. This, on one hand, rules out universal conductance fluctuations as a possible explanation for the observed step- and kink-like features in our measurements. On the other hand, it provides strong indication that the formed constriction is rather narrow such that orbital effects are not playing an important role. Figure 7.4 (b) shows the transconductance dG_{4T}/dV_g as function of V_g and B-field highlighting that the step-like features are indeed not shifting much with B-field. We do not know why the experimental data show this weak dependence and why the step-like features only

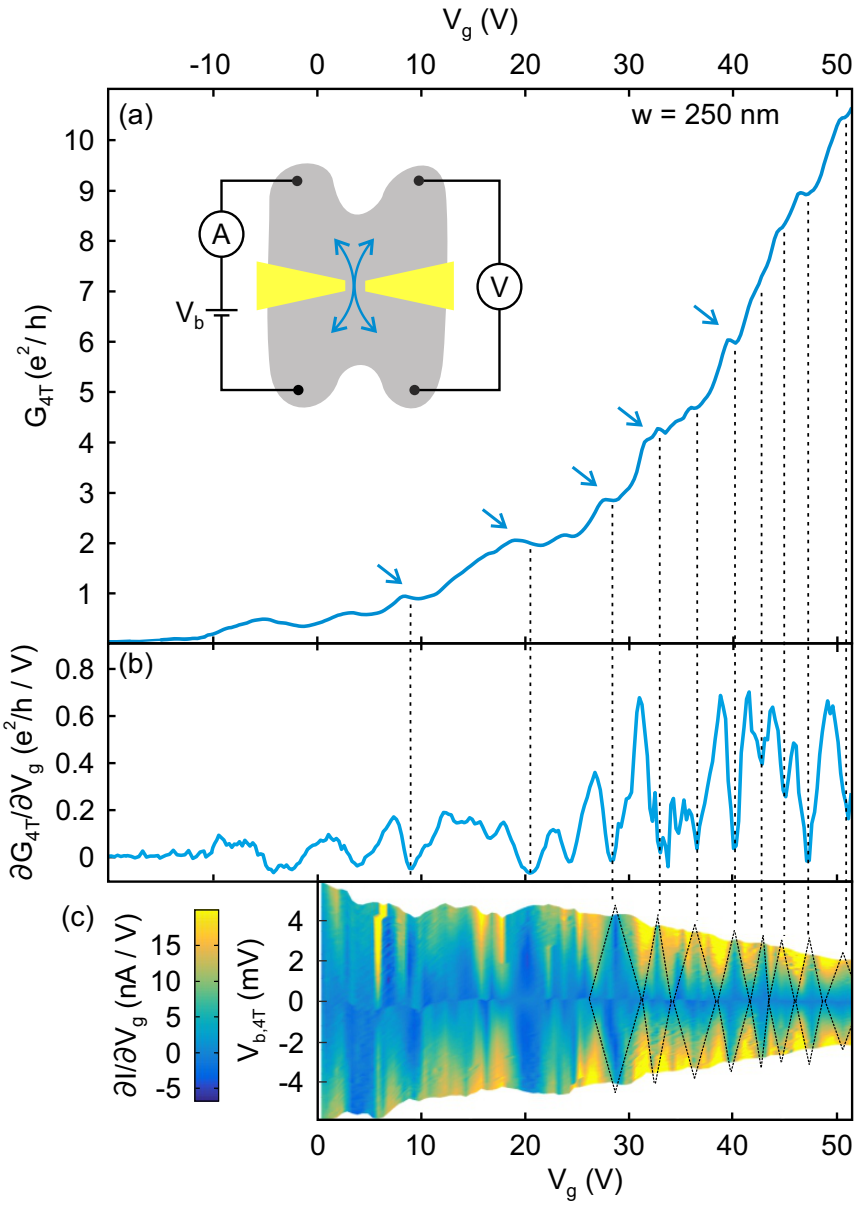

Figure 7.5: (a) Four-terminal conductance as function of the applied gate voltage at 2 K for $V_b = 7$ mV showing step-like features which are roughly spaced by one e^2/h. (b) Derivative with respect to the applied gate voltage of the trace shown in (a), showing dips that correspond to the steps in (a). (c) Bias spectroscopy measurement showing diamonds at the positions of the steps, indicated by the black dashed lines.

qualitatively match quantized conductance. Further improvement of the device, i.e. MoS_2-material quality is needed for more detailed studies on quantized conductance steps in MoS_2 or related TMD materials.

7.5 Conclusion

In summary, we present a technique to fabricate mesoscopic devices based on MoS_2 encapsulated by hBN. By using metal shadow masks combined with photodoping, we demonstrate a way to produce complex doping profiles on a scale close to the diffraction limit of the light used to photodope, allowing to observe quantum transport in MoS_2 constrictions. In low temperature transport measurements, we reproducibly observe signatures of quantum confinement effects in MoS_2 constrictions. Even though gaining precise control over the exact confinement potential proves still to be difficult, our simulations and measurements show that the shadow masking technique can prove useful to generate smooth and long-lasting doping profiles in van-der-Waals heterostructures although most likely the lateral size of structures induced by photodoping is limited by the diffraction limit. This technique could pave the way towards the fabrication of more complex mesoscopic devices in TMDs, such as for example Aharonov-Bohm rings or antidot lattices, which are difficult to realize using electrostatic gating.

Chapter 8

Negative differential conductance in molybdenum disulfide nanoconstriction

8.1 Introduction

As we have seen in the last chapter, we can use the photodpoing technique to define stable and smooth lateral doping profiles in MoS_2 which have an extend of less than the wavelength used to photodope in order to confine charge carriers by using metallic shadow masks in form of a constriction. However, the device quality is still limited due to the relatively large amount of disorder induced by crystallographic defects like missing sulfur atoms or molybdenum replacing sulfur in MoS_2 [216–219]. In order to further investigate the influence of these defect states on the quantum transport we fabricate even smaller constriction with a size likely far below 100 nm by harnessing the band gap of MoS_2, our photodoping technique and further reducing the size of the metallic shadow mask. These nanoconstrictions reveal negative differential conductance (NDC) which is potentially driven by a change of the transmission through the constriction with respect to the applied bias voltage. The defect states heavily influence the number of states near the conduction band edge and thus are responsible for the multi-level nature of the observed NDC. NDC itself has already been seen in a number of experiments using tunneling transistors based on single- and bilayer graphene as the conductive material with either hexagonal born nitride (hBN) [220–223] or transition metal dichalcogenides (TMDs) [224] as a tunnel barrier, in synthetic vertical van der Waals heterostructures [225] or in heterojunctions of different two-dimensional semiconductors [226–228]. All these devices require a vertical heterostructure of different two-dimensional materials with multiple transfer steps or multiple growth processes while still ensuring high quality interfaces to obtain a strong interlayer coupling. In contrast, our approach allows the realization of devices showing NDC which rely on a single MoS_2 flake only. These devices can be of particular interest for novel interband tunneling field-effect transistors (IT-

FETs) as they exhibit a gate-tunable NDC in the current-voltage characteristics [229]. Potently, the multi-level NDC could be used for Boolean and non-Boolean logic [230–232], logic-in-memory [233] or neuromorphic computing [234].

8.2 Characterization of charge transport in MoS_2 nanoconstriction

The samples have been fabricated using the dry van-der-Waals stacking technique described in section 4.5. Figure 8.1 (a) shows an optical micrograph and Figure 8.1 (b) atomic force micrograph of a finished device depicting the contacts used. After the fabrication process, the devices are characterized by scanning confocal Raman microscopy to ensure the correct alignment of all individual layers of the van-der-Waals heterostructure. In Figure 8.1 (b) the first Raman spectrum shows a typical spectrum in the lead area (see open square in Figure 8.1 (b)) of the device. Here, the MoS_2, represented by the A_{1g} and the E^1_{2g} modes at 409 cm^{-1} and 386 cm^{-1} (cyan) [145], is contacted by the FLG with its G-peak at 1583 cm^{-1} (yellow) [166] and resting on hBN with a corresponding Raman peak at around 1365 cm^{-1} (green) [167]. The second spectrum in Figure 8.1 (b) is taken on the hBN/MoS_2/hBN area of the device. Only the two peaks from the hBN and the MoS_2 can be seen (see open circle in Figure 8.1 (c)). The intensity map of the characteristic Raman peaks of the 2D materials is shown in Figure 8.1 (d). The shaded green area marks the intensity of the hBN peak, yellow shows the G-peak intensity of the few-layer graphene (FLG) and cyan shows the intensity of both MoS_2 peaks. The constriction has a size of 100×100 nm. All measurements have been performed using a home-build I-V converter which is used to apply a symmetric bias around a "virtual" ground in the center of the device while simultaneously measuring the current. The four-terminal measurements have been performed by using a home-build differential amplifier to probe the voltage drop across the nanoconstriction.

We start by discussing the charge transport in the lead region of the device. Figure 8.2 (a) shows the current I through the right lead region between contact 3 and 4 (see Figure 8.1 (a)) as function of the applied gate voltage V_g before and after the photodoping at a constant bias of $V_{bias} = 10$ mV. Initially, prior to photodoping (PD) and higher temperatures the device is conductive but the overall current strongly decreases with decreasing temperature resulting in no detectable current at temperatures below 2 K (see inset of Figure 8.2 (a)). As has been pointed out in chapter 6 a explanation for the decreasing current at low temperatures is a strong increase of the MoS_2 resistance and an increasing contact resistance. As has been shown for the Hallbar and QPC devices metallic conductance established with the photodoping technique for sufficiently high charge carrier densities ($n \approx 10^{13}$ cm^{-2}). After illuminating the device at T = 140 K and at $V_g^{PD} = -96$ V, the device remains conductive at 2 K when applying moderate gate voltages. The features close to the onset of the current around $V_g = -30$ V are similar in shape to the features observed

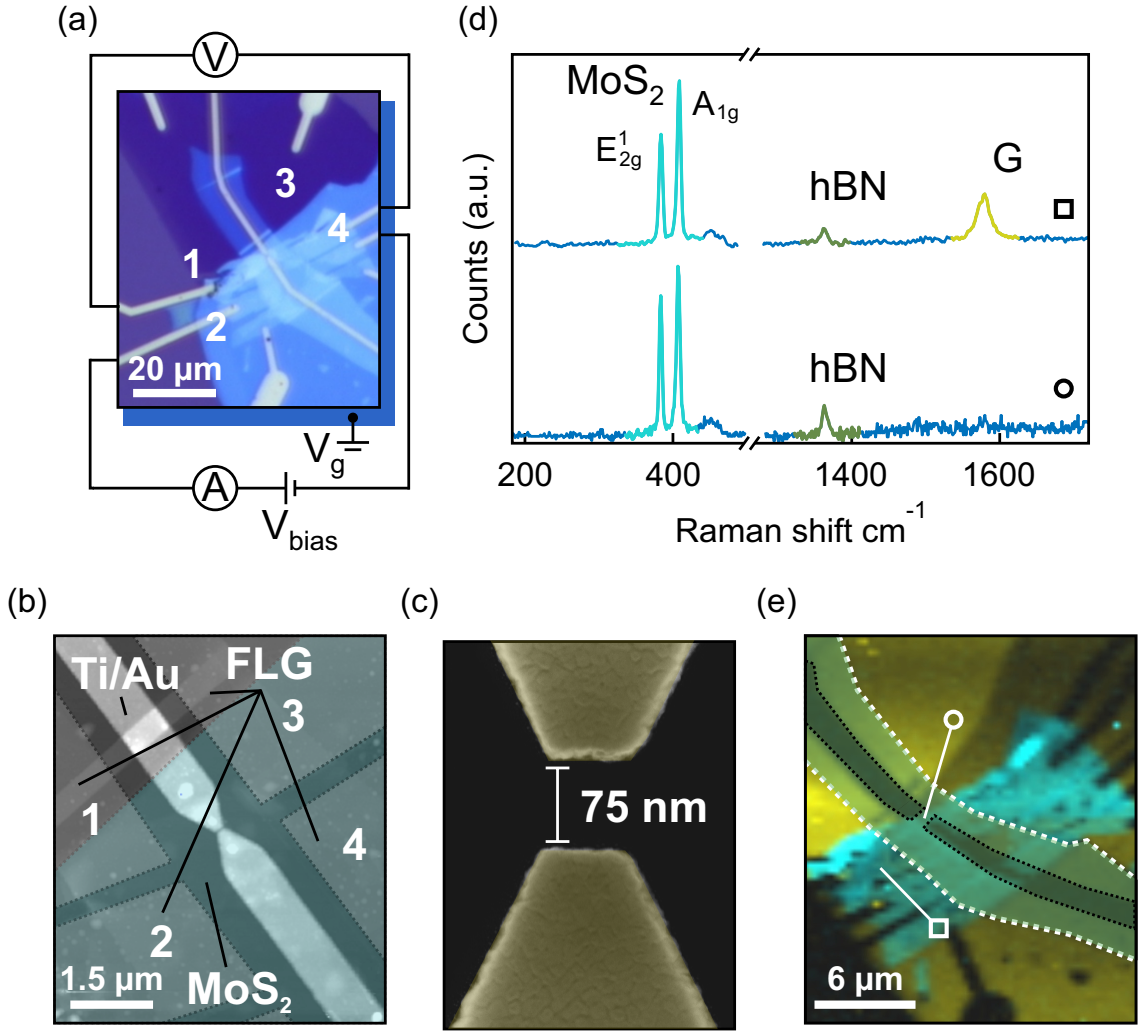

Figure 8.1: (a) Optical microscope image of the complete van-der-Waals heterostructure with an illustration of the four-terminal measurement geometry. (b) Atomic force micrograph of central region of the device shown in (a). The constriction has a width and length of 100 nm x 100 nm which is contacted by four individual few-layer graphene contacts. (c) Scanning electron micrograph of a second device with a constriction width and length of 75 nm x 75 nm and no graphene contacts. (d) Raman spectra on a final device recorded in the lead area (upper spectrum) indicated by the white square in panel (c) and in the sandwiched part (lower spectrum) of the device indicated by the white circle in panel (c) showing the individual Raman peaks of hBN (green), graphene (yellow) and MoS_2 (cyan). (e) Integrated intensities of the G-peak of the FLG and the combined peaks the MoS_2, represented by the colors yellow and cyan, respectively. The white dashed lines outline the top hBN flake.

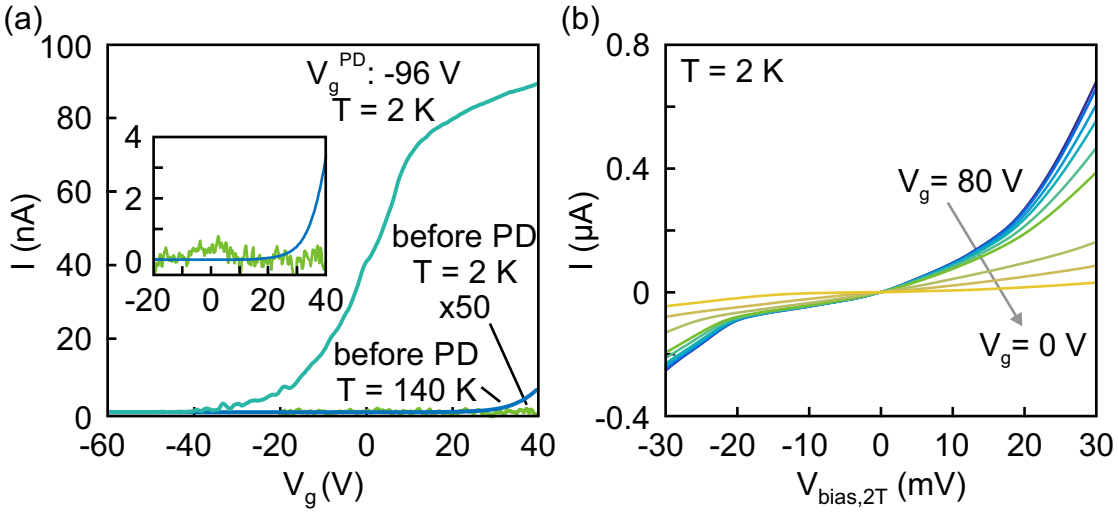

Figure 8.2: (a) Current I as function of the applied gate voltage V_g before and after the photodoping at a constant bias of V_{bias} = 10 mV and a temperature of 2 K between contact 3 and 4 marked in Figure 8.1 (a). The photodoping has been performed at T = 140 K and at $V_g^{PD} = -96$ V. The inset shows a close-up of the current at large gate voltages before the photodoping at T = 140 K (green) and at T = 2 K (green). The current at 2 K is artificially increased by a factor of 50. (b) Current I as function of the applied bias voltage $V_{bias,2T}$ for at constant gate voltages varying between V_g = 0 V and V_g = 80 V in steps of ΔV_g = 10 V. (c) Current I as function of the measured bias voltage $V_{bias,4T}$ at V_g = 80 V. The peak-to-valley ratio (PVR) is extracted by dividing the maximum current value before the minimum by the current value at the minimum (see black dashed lines).

in our Hall bar and the larger constriction devices. This is most likely related to the transport being governed by hopping transport through localized states in this carrier density regime (see chapter 7 or reference [215]). For high gate voltages the two-terminal resistance is on the order of 100 kΩ. Figure 8.2 (b) shows a series of I-V curves at constant gate voltages varying between V_g = 0 V and V_g = 80 V in steps of ΔV_g = 10 V. Over the whole gate voltage regime the curves show a strong non-linearity and asymmetry with respect to the applied bias voltage indicating that the carrier injection is limited by a Schottky barrier [218, 235–239]. Besides the limitation due to the Schottky contact the current is monotonously increasing for increasing bias voltage in the whole gate voltage range.

Next, we turn to discuss the charge transport across the nanoconstriction. In Figure 8.3 (a) we show the current I as function of the applied gate voltage V_g before and after the photodoping at a constant bias voltage of V_b = 40 mV and a temperature of 2 K. Consistent with the measurements in the leads, prior to the PD only single spikes in the current-gate voltage characteristic which likely result from resonant tunneling through localized states can be seen. After the PD the current

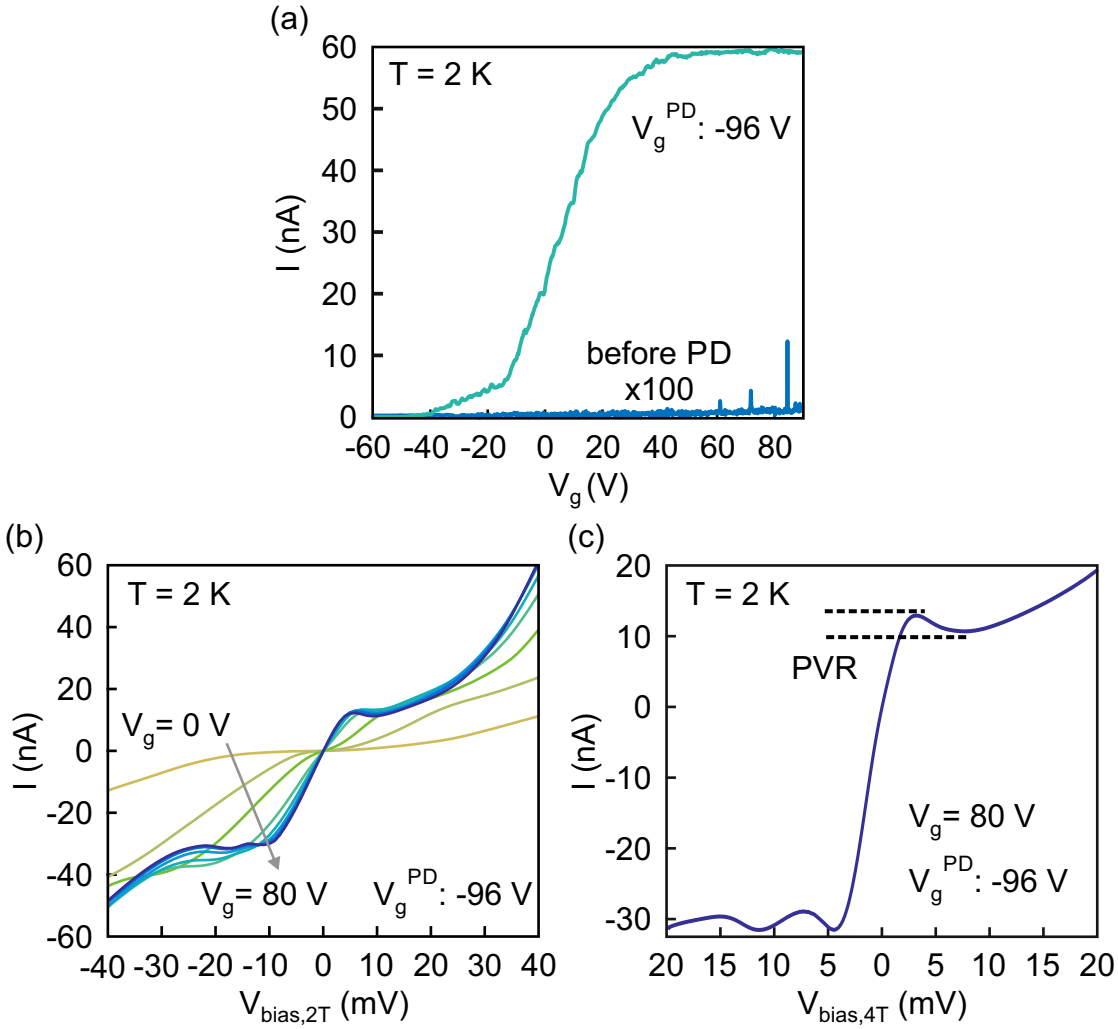

Figure 8.3: (a) Current I as function of the applied gate voltage V_g before and after the photodoping at a constant bias of $V_b = 40$ mV and a temperature of 2 K through the nanoconstriction. (b) Current I as function of the measured bias voltage $V_{bias,4T}$ for at constant gate voltages varying between $V_g = 0$ V and $V_g = 80$ V in steps of $\Delta V_g = 10$ V.

is significantly increased but starts to saturate around $V_g = 40$ V at a current of 80 nA corresponding to a two-terminal resistance of 0.5 MΩ which is at least a factor of five larger then the two-terminal resistance in the two leads indicating that the current is limited for high gate voltages by another mechanism than pure contact resistances. This current saturation might be related to a mobility degradation due to a carrier velocity saturation and increased scattering which is a typical short channel effect in metal-oxide-semiconductor (MOS) devices [240, 241]. In Figure 8.3 (b) the I-V characteristic at constant gate voltages between $V_g = 0$ V and $V_g = 80$ V in steps of $\Delta V_g = 10$ V measured in four-terminal configuration is shown. For low

gate voltages near the conduction onset we observe a non-linearity typical for a transport regime which is governed by localization (see chapter 7 or reference [215]). For increasing gate voltage a shoulder in the I-V characteristic for both negative and positive V_{bias} appears which evolves into one local minimum for positive bias voltages (slightly below $V_b = 5$ mV) and into two local minima for negative bias voltages (around -13 mV and slightly above $V_b = -5$ mV) resulting in three features of negative differential conductance (NDC) which is in stark contrast to the linear I-V characteristic we observe in our larger constriction devices (separation of the shadow masks above 200 nm).

Figure 8.4 (a) and (b) show the corresponding differential conductance as function of bias voltage V_{bias} and gate voltage V_g where the NDC becomes more apparent. Around -13 mV, slightly above $V_b = -5$ mV and slightly below $V_b = 5$ mV a pronounced minimum in the differential conductance can be seen. The amplitude and V_{bias} position of all three minima is very sensitive to V_g while the exact dependency varies. The peak-to-valley ratio (PVR), which is here defined as the maximum current value before the minimum divided by the current value at the minimum (see Figure 8.4 (b)), and the peak position (see Figure 8.4 (c)) of the feature at positive V_{bias} in the I-V characteristic is constant between $V_g = 80$ V and 70 V with a maximum PVR of 1.2 while the PVR decreases rapidly with further decreasing gate voltage with a simultaneous up-shift in V_{bias} position. Around $V_g = 32$ V the NDC vanishes. The NDC features for negative V_{bias} show a very similar dependence on V_{bias} and V_g except of vanishing already around $V_g = 40$ V and 50 V, respectively.

Figure 8.5 (a) shows the temperature dependence of the differential conductance between 3 K and 30 K as a function of applied bias voltage at fixed $V_g = 75$ V with the corresponding PVRs in Figure 8.5 (b). For all three features the PVR decreases with increasing temperature. For positive V_{bias} the NDC vanishes around 13 K. For negative V_{bias} the high bias feature persists up to 18 K while the low bias feature already vanishes around 7 K.

We observe a similar gate tunable bias dependent decrease of the differential conductance in a second sample with a designed constriction dimension of 75×100 nm (see Figure 8.1 (c) and the list of samples in the appendix, sample Alex5 70) which also showed step-like features in the conductance as function of the applied gate voltage (see Figure 7.3 (d)). The sample has been photodoped at T = 50 K and $V_g^{PD} = -96$ V while the transport measurements have been performed at 2 K. In contrast to the first sample only two-terminal measurements have been performed. In Figure 8.6 (a) the corresponding differential conductance as a function of V_{bias} and V_g is shown. Similar to the first sample, positive and negative bias voltage show a different number of features. While we observe three dips in differential conductance for negative V_{bias} only two are visible for positive V_{bias}. The dips show a strong tuning of the V_{bias} position of up to 100 mV within 30 V. Figure 8.5 (b) shows the differential conductance as a function of the magnetic field B and V_{bias} at a fixed $V_g = 85$ V. The dip in the differential conductance due to localization around zero bias voltage is independent on the magnetic field. In contrast, the dips

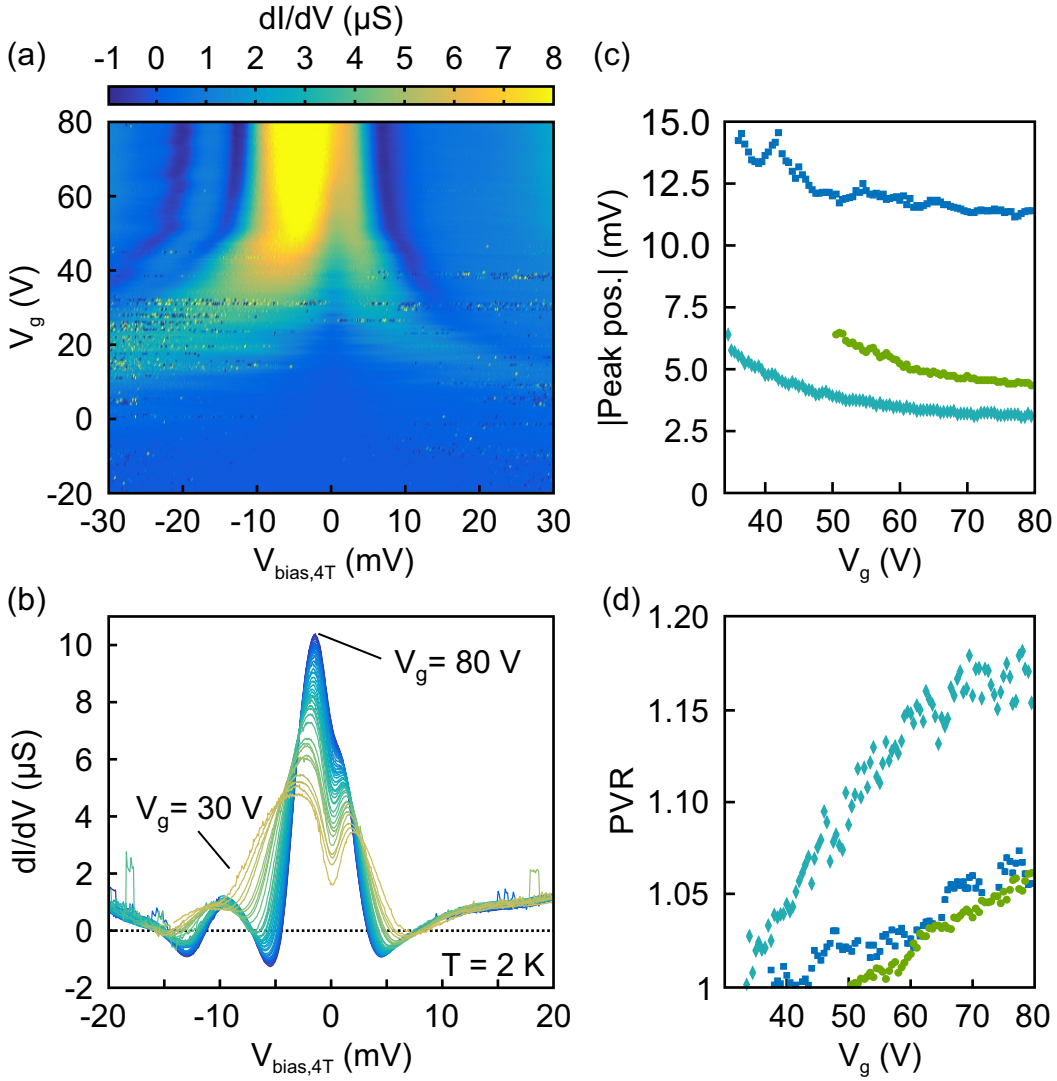

Figure 8.4: (a) Differential conductance dI/dV as function of the measured bias voltage $V_{bias,4T}$ and the and gate voltage V_g. (b) Differential conductance dI/dV as function of the measured bias voltage $V_{bias,4T}$ for constant gate voltages between $V_g = 0$ V and $V_g = 80$ V in steps of $\Delta V_g = 1$ V at T=2 K. (c) Extracted peak-to-valley ratio between $V_g = 30$ V and $V_g = 80$ V for the three different negative differential conductance (NDC) features visible in (a) and (b). (d) Corresponding bias voltage position of the NDC features between $V_g = 35$ V and $V_g = 80$ V.

at higher bias voltages shift to even higher values for both bias voltage polarities, although the up-shift is more pronounced for negative V_{bias}. The shift can be linearly approximated to roughly 1 mV/T indicated by the white dashed lines in Figure 8.6 (b). The extraction of an energy scale is problematic because of the bias and gate voltage dependent contact resistance R_C. As we can only measure in a two-terminal geometry, we have to estimate R_C. Here, we use the results from chapter 7. As-

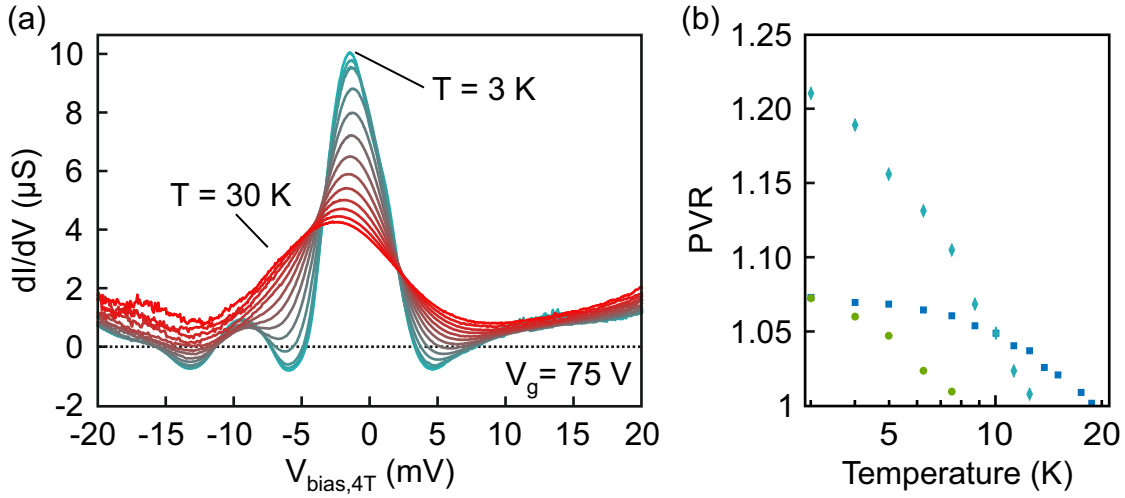

Figure 8.5: (a) Differential conductance dI/dV as a function of the measured bias voltage $V_{\mathrm{bias,4T}}$ at $\mathrm{V_g}$ = 75 V for constant temperatures between T=3 K and 30 K. (b) Corresponding peak-to-valley ratio as a function of the temperature for the three different negative differential conductance features.

suming the kinks in the conductance shown in Figure 7.3 (d) of the two-terminal device have the same origin as the kinks in the conductance of the the four-terminal constriction shown in Figure 7.5 the conductance needs to be on the order of 1 e^2/h. Consequently, we can roughly estimate a contact resistance around 100 kΩ. As the sample is fabricated without graphene contacts we can not compare this value with the results from chapter 6 but the contact resistance is on the order reported by studies on MoS_2 transistors with metallic contacts [218, 238, 239, 242]. As a result we can then extract an energy scale on the order of 10 meV.

8.3 Discussion

Historically, negative differential conductance has first been observed in p-n junctions by Esaki in 1958 [243] where the NDC is governed by a specific energy band alignment and the resulting inter-band tunneling which is also the foundation of the many experiments on NDC in the different two-dimensional semiconductor and semi-metal devices [220–223, 226–228] but usually does not show a multi-level behavior because of the specific band-alignment requirements [227]. An alternative explanation which also covers a multi-level NDC is the ballistic transport through a very narrow short-channel constriction. This has been investigated by A. Sengupta and S. Mahapatra [244] for a MoS_2 armchair nanoconstriction with a length of 10 nm and width of 3.5 nm.

They use the non-equilibrium Green's function formalism (NEGF) [245, 246] to calculate the ballistic current through a MoS_2 nanoconstriction placed between two

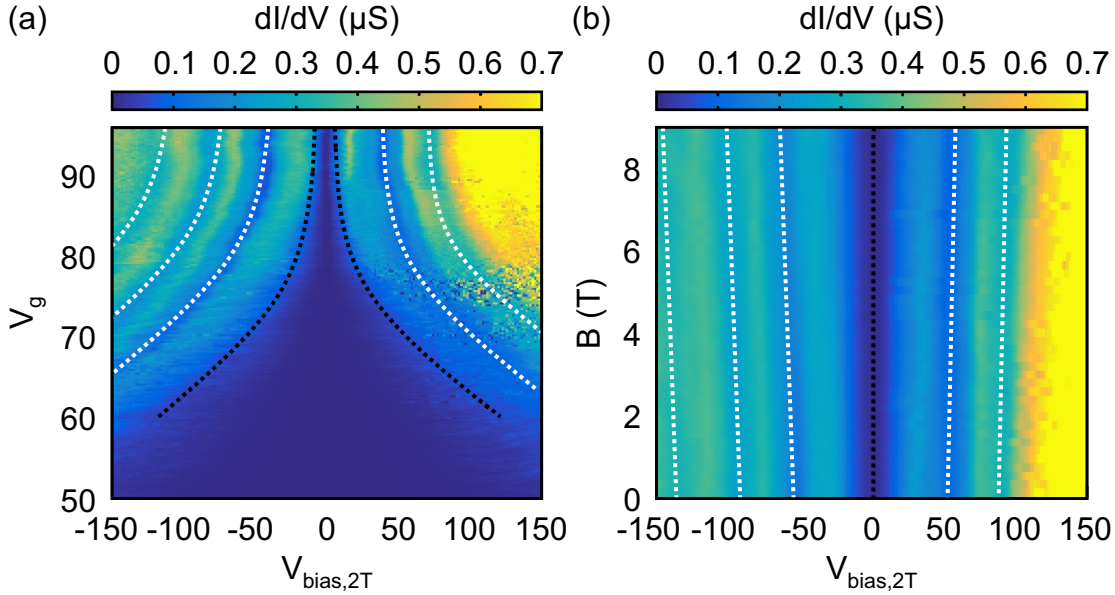

Figure 8.6: (a) Differential conductance dI/dV as a function of the applied bias voltage $V_{\mathrm{bias,2T}}$ and the applied gate voltage $\mathrm{V_g}$ at T=2 K after photodoping the device at T = 50 K and $\mathrm{V_g^{PD}} = -96$ V. (b) Differential conductance dI/dV as a function of the magnetic field B and $\mathrm{V_{bias}}$ at a fixed $\mathrm{V_g} = 85$ V. The white dashed lines indicate the up-shift of the dips in the differential conductance seen in (a) which corresponds roughly to 1 mV/T.

large leads at finite bias voltages and finite temperature while including specifically the band structure of the MoS_2 nanoconstriction. Additionally, they investigate the influence of defect states like vacancies (randomly missing molybdenum and sulfur atoms) or lattice deformation due to twists or ripples in the material on the quantum transport. Already the perfect nanoconstriction shows negative differential conductance with respect to the bias voltage driven by a change of the available states near the Fermi level due to the changing bias window which results in a change of the transmission transparency of the channel (s. [244] and Figure 8.7). Consequentially, a change of the density of states (DoS) due to deformations or vacancies which introduce a number of available states near the conduction band minimum alters the shape of the current-bias voltage characteristic (s. Figure 8.8). Especially to note are vacancies as they change the transmission spectrum most significantly by heavily reducing the peak-to-valley ratio as they can smear out the density of states while also leading to more NDC features in a given bias voltage regime because of isolated impurity states. In total, the results from A. Sengupta and S. Mahapatra qualitatively correspond to our measurements. Our relatively small PVR values indicate that we are strongly influenced by vacancies and lattice deformations. In particular, this seems to be the case for the second device where the maximum PVR is barely above one. Vacancies are very likely to be present in

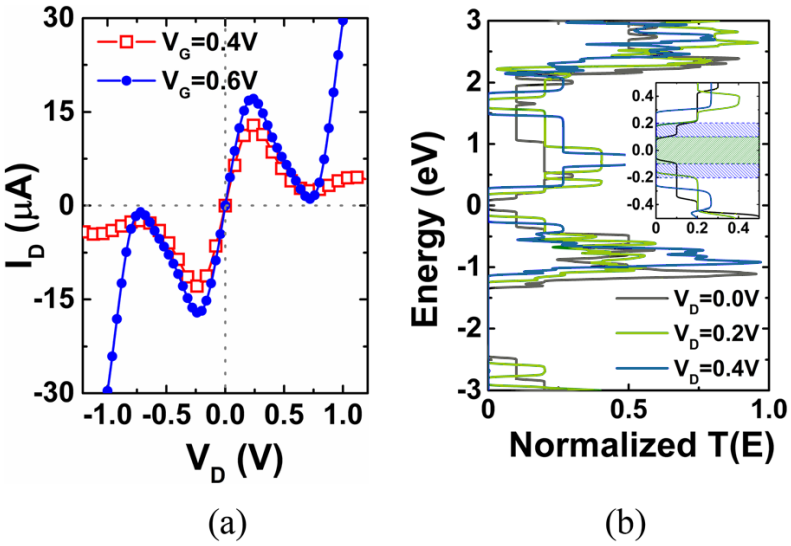

Figure 8.7: (a) Simulated current I as function of the bias voltage V_{bias} based on non-equilibrium Green's function theory for two different gate voltages V_g for a perfect MoS_2 armchair nanoconstriction with a width of 3.5 nm and length of 10 nm. (b) The corresponding transmission spectrum for V_{bias} = 0, 0.2 and 0.4 V at fixed V_g = 0.6 V. The inset shows a zoom of the region around zero energy. Both Figures have been reprinted from reference [244], with the permission of AIP Publishing.

our devices as MoS_2 is known to exhibit relatively large amount of sulfur vacancies [217, 219]. The deformations could be a result of the transfer process. As the defect states are not only present in the band gap but are also superimposed on the conduction band it is hard to extract quantitative numbers regarding defect energy or subband spacing. The tuning of the NDC features is potentially related to the shift of the Fermi energy with respect to the position of the DoS peaks. Following the interpretation of a ballistic current in a narrow short-channel, which is supported by the short-channel behavior of the gate chracteristic shown in section 8.2, we can note that in contrast to the lithographic dimension of our device, the photodoping might create much smaller nanoconstrictions on the order of a few tens of nanometer and the presence of a fairly high number of defect states. However, this does not explain the asymmetry observed in our devices. As the ballistic current is depending on the Fermi function in the source and drain contact a doping differences of the lead regions in the real devices might be the origin.

8.4 Conclusion

In summary, we present an approach to use the photodoping technique to fabricate nanoconstrictions based on MoS_2 encapsulated in hBN by further reducing the con-

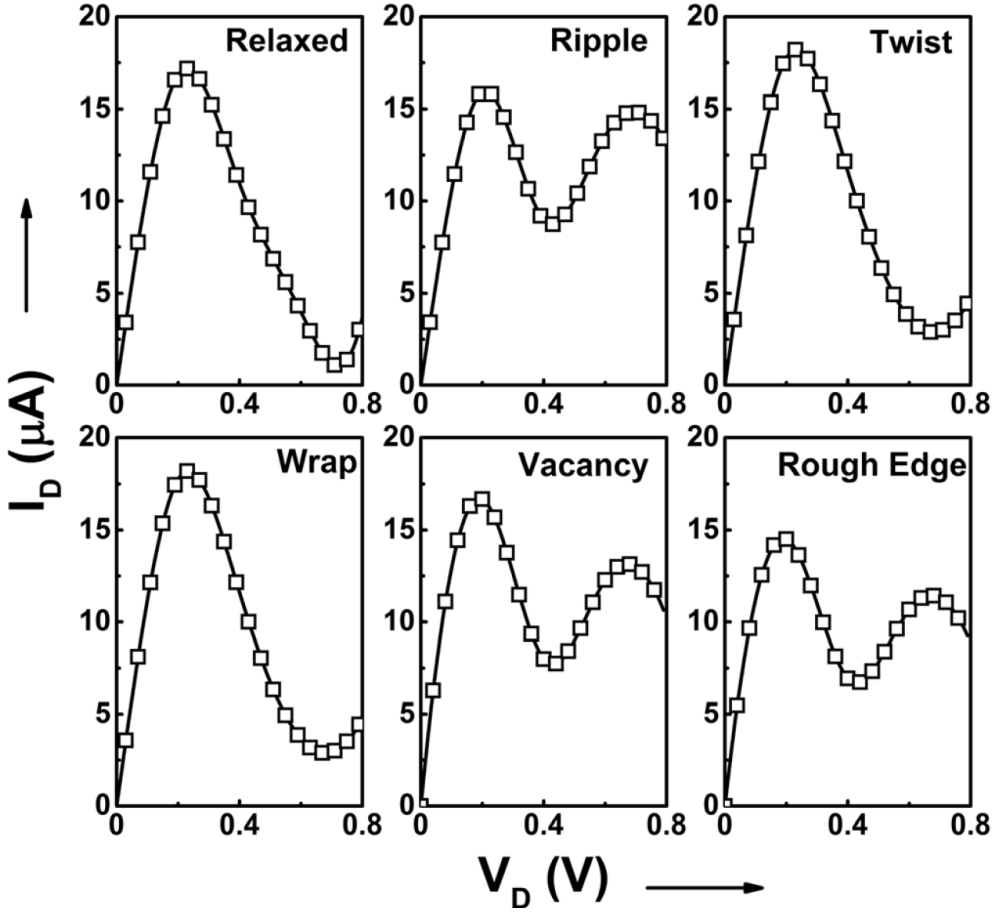

Figure 8.8: Simulated current I as function of the bias voltage V_{bias} at fixed $V_g = 0.6$ V for different disorder conditions. All Figures have been reprinted from reference [244], with the permission of AIP Publishing.

striction size compared to what has been shown in chapter 7. In low temperature transport measurements, we observe a gate and bias voltage tunable multilevel negative differential conductance (NDC). The NDC shows a maximum peak-to-valley ratio of 1.2 which decreases with decreasing gate voltage while simultaneous shifting upwards in bias voltage position. Comparing our results to simulations of a ballistic current through a nanoconstriction based on the non-equilibrium Green's function formalism performed by A. Sengupta and S. Mahapatra [244] shows a qualitative agreement but would indicate that our constrictions, in contrast to the lithographically defined dimensions, might only have a length on order of a few tens of nanometer and exhibit a fairly high number of defect states. In this case, the transport through our MoS_2 nanoconstriction can be regarded as being ballistic. Here, the observed multilevel NDC would result from a change on the number of

transmission modes near the Fermi level due to the changing bias window. As the transmission is crucially depending on the density of states the introduction of vacancies or lattice deformations significantly change the transmission probability and thus the shape of the current-bias voltage characteristic including the number of NDC feature compared to a pristine MoS_2 nanoconstriction. By further increasing the material quality and potentially by gaining control over the density of states near the conduction band minimum, these devices as a multi-level system can be an interesting alternative to their vertical counterparts. In contrast to the vertical geometry, our planar devices promise an easy integration in other electrical circuits. These multilevel devices are of great interest as a potential host for non-Boolean logic [230–232], logic-in-memory [233] or neuromorphic computing [234].

Chapter 9

Summary and outlook

In the framework of new concepts for data processing, scientists envision two-dimensional (2d) materials [24, 25, 61] as potential hosts for QDs. Graphene offers potentially long spin relaxation times due to its weak spin-orbit interaction [26, 27] and the weak hyperfine coupling [28]. For graphene, a great challenge is still the non-gaped bandstructure as it requires to etch graphene into nanostructures and using a disorder-induced transport gap [30–33], which results in limited control over the resulting tunnel barriers. A step towards reducing the disorder and to potentially increase the reproducibility and controllability is to fully encapsulate graphene in hBN [40], which prevents process induced contaminations on the graphene flake, although the edges are still exposed. Alternatively, the advances in making increasingly complex van-der-Waals heterostructures consisting of stacks of different 2d materials opens the door for investigating mesoscopic transport in MoS_2 where the finite band gap in combination with the spin-valley coupling could potentially be used for gate-defined spin-valley (Kramers) qubits [61]. This work focuses on exploring mesoscopic transport and quantum confinement of charge carriers in graphene and MoS_2 heterostructures. We employ state-of-the-art fabrication technology in order to improve the quality of etched graphene nanostructures and to explore an alternative approach to theses edge disorder dominated devices.

9.1 Main results

All investigated heterostructures have been fabricated via a well-established dry transfer method [40] described in chapter 4 and are based on mechanical exfoliation of all 2d materials. Crucial for the samples based on MoS_2 is to employ few-layer graphene (FLG) contacts, which have been shown to exhibit low Schottky barriers to the MoS_2, especially at high charge carrier densities of the graphene [62, 163, 164], but which so far involved multiple transfers of FLG flakes. In contrast to these studies, we only transfer one large FLG flake that is subsequently patterned. Using a single flake to contact multi-terminal MoS_2 devices saves several transfer steps or crystal phase engineering of the MoS_2 [165]. The dry transfer technique enables us to

fabricate graphene nanoribbons with a width around 40 nm and a length around 100 nm fully encapsulated in hBN which prevents process induced contaminations on the graphene flake. In chapter 5 we present the low temperature transport measurements on these nanostructured graphene constrictions. The measurements at zero magnetic field show a qualitatively similar transport characteristic as nanoconstrictions and on SiO_2 and hBN, but reveal a considerably smaller transport gap on the order of $\Delta V_{bg} = 5$ V and effective energy gap on the order of $E_g = 10$ meV. In section 5.3 the magnetotransport measurements are presented. We observe a crossover from the Coulomb blockade dominated transport at zero magnetic field to a regime at finite magnetic field where all transport is blocked due to an interaction induced energy gap around zero energy resulting from electronic correlation and edge effects, which is similar to what has been observed in suspended graphene sheets [110, 180, 181] and nanoconstrictions [183] or larger dual-gated graphene flakes supported on hBN [182]. The size of this energy gap increases roughly by 3 meV/T up to 20 meV at 9 T. The linear increase of this $\nu = 0$ energy gap points toward a valley symmetry breaking induced by the magnetic field. Compared to extended graphene sheets on hBN [182] our observed slope is a factor of three larger potentially due to an enhancement of the electron-electron interaction by the spacial confinement. Still, the fabrication involves etching where the edges get exposed to process induced contaminations which likely limit the device performance. Hence, we explore an alternative approach for charge carrier confinement by investigating quantum transport in semiconducting MoS_2 micro- and nanostructures. To characterize the material we first investigate the charge transport in few-layer MoS_2 Hall bar structures in chapter 6. As the as-fabricated devices are insulating at low temperatures (see section 6.4), we use a remote photodoping technique first observed in hBN/graphene heterostructures [67, 68, 199] to create free charge carriers in the MoS_2 layer of up to 10^{13} cm^{-2}, when using an additional gate voltage during light illumination (see section 6.5). After the photodoping the Hall bar remains well conductive at 2 K, while preserving the charge carrier mobility of up to $\mu = 600$ cm^2/(Vs) at low temperatures (2 K) indicating homogeneous and efficient doping process throughout the entire device. After we studied the influence of the photodoping on the transport properties of MoS_2, we demonstrate a way to use this technique to produce complex doping profiles on a scale close to the diffraction limit of the light used to photodope. This allows us to define MoS_2 constrictions by using metal shadow masks presented in chapter 7. Numerical simulations indicate an expected full-width-at-half-maximum of the photodoping intensity profile at slightly below the lithographically defined separation of the two shadow masks which we consider as an upper limit of the constriction width (see section 7.2). In section 7.3 and 7.4 we present low temperature transport measurements at zero and finite perpendicular magnetic field, where we reproducibly observe signatures of quantum confinement effects in these constrictions. Even though we are not sure about the exact confinement potential, the simulations and measurements show that the shadow masking technique can prove useful to confine charge carriers within arbitrary geometries in MoS_2 and po-

tentially other 2d materials. Still, a limiting factor for the device quality can be the relatively large amount of crystallographic defects like missing single sulfur atoms [216] or molybdenum replacing sulphur [219] in the MoS_2. In order to further investigate the influence of these defects on the quantum transport we fabricate even smaller constriction with a size likely far below 100 nm by harnessing the band gap of MoS_2, our photodoping technique and further reducing the size of the metallic shadow mask which is presented in chapter 8. These nanoconstrictions reveal negative differential conductance (NDC) shown in section 8.2. The NDR shows three pronounced peaks with a maximum peak-to-valley ratio of 1.2 which decreases with decreasing gate voltage. The observed multilevel NDC potentially results from a change on the number of transmission modes near the Fermi level due to a changing bias window (see section 8.3). As the transmission is crucially depending on the density of states vacancies and lattice deformations significantly change the transmission probability and thus heavily influence the shape of the current-bias voltage characteristic including the number of NDC feature. In summary in the course of this thesis we have investigated two different approaches to confine charge carriers in 2d materials. We show that in etched graphene nanoribbons encapsulated in hBN an insulating state arises at finite magnetic due to a interaction induced energy gap around zero energy. As an alternative, we explore quantum transport in semiconducting MoS_2. Here, we use a photo-induced remote doping technique to adjust the doping level in MoS_2, while preserving the charge carrier mobility. By using metal shadow masks combined with photodoping, we demonstrate a way to produce complex doping profiles on a scale close to the diffraction limit of the light, allowing to observe quantum confinement effects. By further reducing the size of the shadow mask we fabricate nanoconstrictions which show a gate and bias voltage tunable multilevel negative differential conductance (NDC).

9.2 Outlook

In order to further advance the field of quantum transport and especially quantum confinement of charge carriers in 2d materials there are two potential routes which could be pursuit. Although the high electronic quality of the graphene nanoconstriction is promising we still have to cope with process induced contaminations of the exposed edges. In order to fully exploit the extraordinary properties of graphene we could make the transition from tailoring graphene into nanostructures by etching to either grow graphene with perfect edges into the desired shape [141, 247, 248] or to electrostatically confine electrons in bilayer graphene by opening up a band gap with a perpendicular electric field [45–48] allowing for gate-defined soft-confinement similar to what has been pioneered in two-dimensional electron gases (2DEGs). This technique suffered until recently [49–52] from relatively limited maximum resistance. By increasing the homogeneity of the perpendicular electric field especially at the edges of the bilayer graphene flake the maximum resistance can be significantly in-

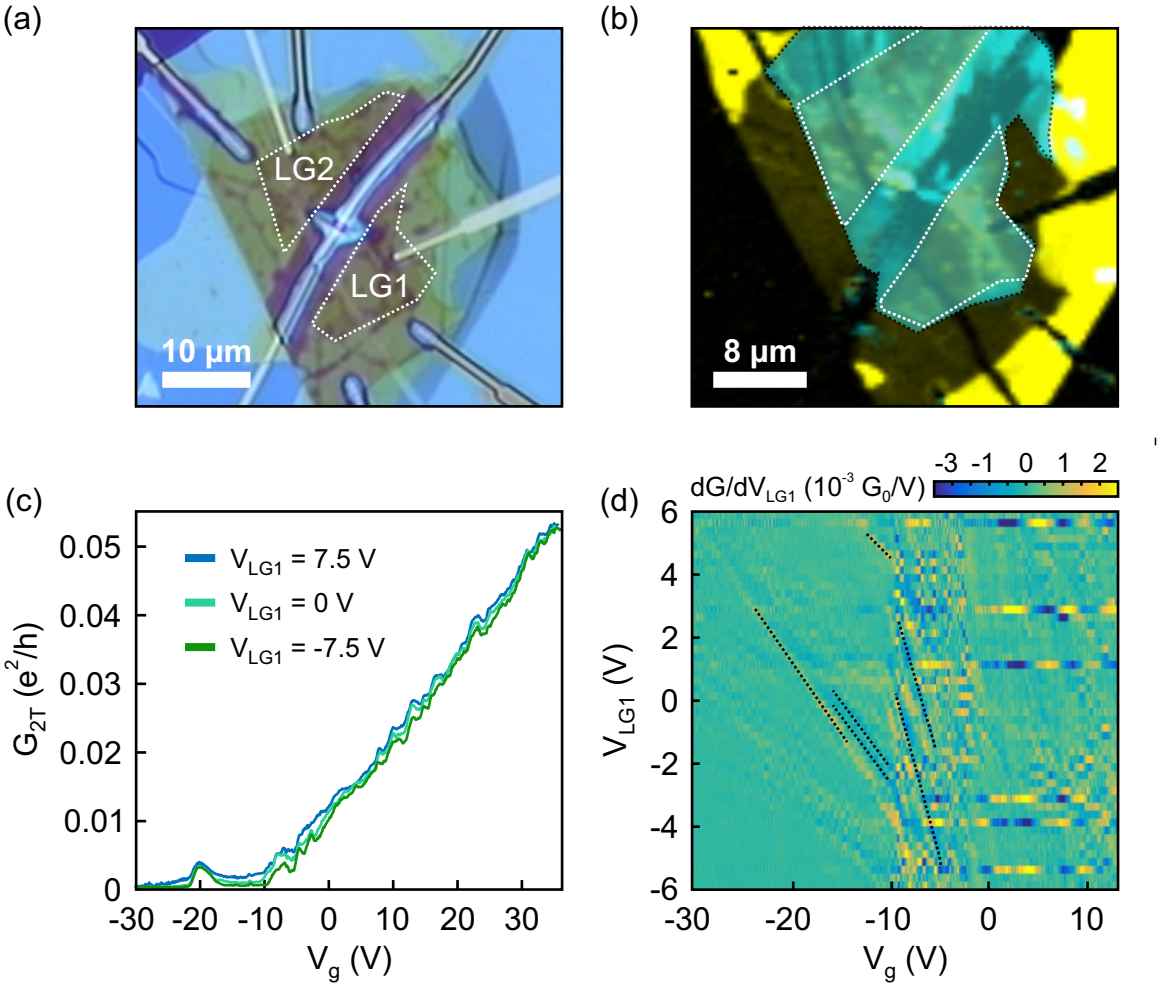

Figure 9.1: (a) Optical micrograph of a MoS_2 based van-der-Waals heterostructure with local few-layer graphene gates on top the lead region indicated by the white dashed lines. (b) Intensity map of the characteristic Raman peaks of the FLG and the MoS_2. Yellow depicts the G-peak intensity of the FLG flakes and blue shows the intensity of the A_{1g} mode of the MoS_2. The area marked by the white dashed lines again corresponds the areas of the local gates. (c) Two-terminal conductance G_{2T} as a function of back gate voltage V_g for three different local gate voltages. (d) Derivative of the conductance with respect to the applied local gate voltage.

creased to several GΩ and is thus very promising for future experiments on confining charge carriers in graphene. Considering MoS_2 we are still at the very beginning of the mesoscopic transport research. During this work we encountered several challenges especially in the fabrication process which we already partly tackled but where we identify two points to further improve the device performance. One point already known from conventional semiconductor 2DEGs is the challenge to fabricate low-ohmic contacts. As has been pointed out the few-layer graphene we use to con-

tact our devices is assumed to be an ideal material for MoS_2. As the contacts profit from a high charge carrier densities of the graphene [62, 163, 164] one potential method to improve the contact quality is to locally gate the injection region [64]. In Figure 9.1 we present a van-der-Waals heterostructures based on few-layers MoS_2 encapsulated in hexagonal boron nitride but involving two additional transfer and metalization steps compared to the process described in chapter 4. Here, after the deposition of the metal shadow mask and Ti/Au contacts we transfer one additional hBN and one FLG flake on top of the whole device. Subsequently, the top-most FLG is patterned to only cover the injection region and Ti/Au contacts are evaporated. An optical micrograph of the finished device is shown in Figure 9.1 (a). The dashed lines indicate the areas of the local gates on top the device leads (LG1 and LG2). In Figure 9.1 (b) we show the corresponding Raman map of the intensities of the characteristic Raman peaks of the FLG and the MoS_2. Yellow depicts the G-peak intensity of the FLG flakes and blue shows the intensity of the A_{1g} mode of the MoS_2. The area marked by the white dashed lines again corresponds the areas of the local gates. In contrast to the local metallic gates used in reference 64 our few-layer graphene gates offer the possibility to gate the injection region while still allowing to photodope the whole device. In Figure 9.1 (c) we show the current through the 275 nm wide constriction at constant bias of V_b = -10 mV as function of the back gate voltage for a lead gate voltage of $V_g = -6$ V (green), 0 V (turquoise) and 6 V (blue) after photodoping the device at 150 K and $V_g^{PD} = -90$ V). Although the current, especially at the current onset (see Figure 9.1 (d)), can be slightly increased with increasing lead gate voltage the overall impact of the local lead gate is relatively small indicating that the contact resistance can not be significantly reduced as the charge carrier density in the FLG is already large due to the photodoping. A second point which has to be considered is to fabricated the devices in a controlled argon atmosphere or even under vacuum as in ambient conditions airborne contaminations like hydrocarbons deposit on the surface of the 2d materials within minutes [249, 250] which e.g. heavily influences the quality of the contact/MoS_2 interface and thus the contact quality. Additionally, TMDs are highly susceptible to aging due to oxygen and moisture [251]. Despite these challenges, MoS_2 or other transition-metal dichalcogenides are a very promising material system for the development of new data processing concepts as they offer coupled spin-valley physics [61, 89, 104], the possibility to spatially confine charge carriers by electrostatic gating [63, 64, 66] or by our photodoping technique and the optical access especially when considering the huge speed the field of 2d materials has evolved within the last few years.

Appendix

A Weak localization in MoS_2 contacted by few-layer graphene

A.1 Introduction

As shown in chapters 6 and 7, atomically thin two-dimensional (2d) semiconductors such as MoS_2 hold great promises for investigating mesoscopic transport as they offer coupled spin-valley physics [61, 89, 104] and the opportunity to study the effect of soft confinement by electrostatic gating [63, 64, 66]. However, the material quality is still quite limited due to the relatively large amount of crystallographic defects like missing sulfur atoms in MoS_2 [217, 219]. Insight on the limitations imposed by these defects on quantum properties like the phase coherence, can be gained from low-temperature magneto-transport experiments which we perform on a MoS_2 Hall bar device with with few-layer graphene (FLG) contacts and a mobility on the order of $\mu = 600$ cm^2/(Vs). From weak localization (WL) measurements we extract a phase-coherence length on the order of 200 nm with no visible effect of the PD to the dephasing. However, during this work we encountered several challenges. One point already known from conventional semiconductor 2DEGs is the challenge to fabricate low-ohmic contacts. As has been pointed out, the few-layer graphene we use to contact our devices is assumed to be an ideal material for MoS_2. This fact imposes a another, more technical, challenge. As we will see in following chapter we can not exclude that the phase-coherent transport is governed by the FLG region or the MoS_2/FLG interface instead of the MoS_2 region as we only observe the effect in the two-terminal contact configuration and have no sperate contacts to the FLG region. This stresses again the importance of a high contact quality or at least the necessity of individual contacts to the FLG which should be included in future devices.

A.2 Transport characterization

We start by discussing the charge transport through the Hall bar shown in Figure A.1 (a) without applying a magnetic field. The Hall bar is fabricated using the well-established dry van-der-Waals stacking technique [40, 115] described in chapter 4.5.

A five-layer MoS_2 crystal gets partially encapsulated between two hBN flakes and contacted by a FLG flake, which is patterned into the required contact configuration (see Figure A.1 (a)). The sample has been cooled down three times in two different cryostats. Figure A.1 (b) shows the two-terminal conductance G_{2T} at a temperature of 2 K as function of the applied gate voltage V_g at a constant bias voltage of $V_b = 25$ mV measured for the three different cool-downs. In the first two cool-downs the bias voltage was applied between the source (S) to drain (D) contact (blue traces) and in the third cool-down between contact 3 to the drain (yellow trace). Initially, prior to the first photodoping (PD) the device is already well conducting at a temperature of 2 K but the initial doping changed significantly during the second cool-down. After the second cool-down the sample has been photodoped at $V_g^{PD} = -96$ V and T $=$ 150 K for 15 minutes in order to increase the charge carrier density. The gate characteristic shows the expected overall increase in conductance, which corresponds well to a shift of $\Delta V_g = 96$ V in gate voltage. For measurements below 2 K the sample is cooled down a third time in a dilution refrigerator. The overall G_{2T} is comparable to the previous measurements with an onset of conductance at a similar gate voltage after the PD at $V_g^{PD} = -96$ V indicating a similar doping level. At high gate voltages G_{2T} starts to saturate potentially due to an increased contact resistance. The four-terminal conductance G_{4T} as a function of the charge carrier density n prior and after the PD (not shown) behaves similar to what has been shown in chapter 6. At $n = 1.1\times10^{13}$ cm^{-2} a charge carrier mobility on the order of $\mu = 600$ cm^2/(Vs) is measured (see also chapter 6). Additionally, the subsequent cool-down does not change the four-terminal transport properties.

A.3 Weak localization measurements at 2 K

In the following paragraph, we focus on the phase-coherent transport by analyzing the phase coherence length extracted from weak localization (WL) measurements. In Figure A.3 (a) we show the magneto-conductance at finite magnetic field with respect to the conductance at $B = 0$ T, $\Delta\sigma = \sigma(B) - \sigma(0)$ for five different charge carrier densities n at $T = 2$ K measured before the photodoping. We only observe the WL feature in the current signal and estimate the conductance by subtracting the contact resistance extracted from the previous measurements. Additionally, the data is symmetrized by taking the average of the positive and negative B-field data. The resulting magneto-conductivity traces exhibit an increase for small B-fields, the WL dip, followed by a decrease due to the classical magneto-resistance which is linearly approximated and subtracted from the data for the further analysis.

This WL effect results from the quantum mechanical self-interference of an electron with its time-reversal path and allows to investigate phase-coherent transport properties in MoS_2. To obtain the phase coherence length l_φ we fit the Hikami-Larkin-Nagaoka (HLN) [253] model to the conductivity correction at small magnetic fields ($B < 100$ mT) using the following equation

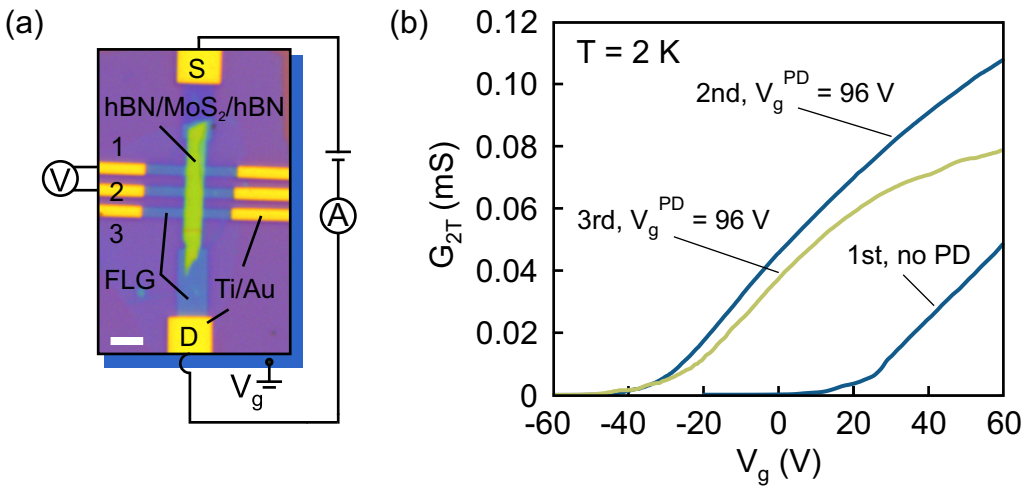

Figure A.1: (a) Optical microscope image of the MoS_2 Hall bar with an illustration of the measurement geometry. In the first two cool-downs the source (S) to drain (D) contacts and in the third cool-down contact 3 and the drain contact have been used. (b) Two-terminal conductance G_{2T} as function of the applied gate voltage V_g for the three different cool-downs.

$$\Delta\sigma(B) = \alpha \frac{e^2}{4\pi\hbar} F\left(\frac{B}{B_\varphi}\right). \tag{10.1}$$

Here, $F(z)$ is defined by $F(z) = \Psi(1/2+1/z)+\ln(z)$ with Ψ being the digamma function. B_φ relates to l_φ by $B_\varphi = \hbar/\left(4el_\varphi^2\right)$. α is an empirical fitting parameter [253, 254] and in case of no intervalley or spin orbit scattering for our five-layer MoS_2 Hall bar α should be 6 due to the two-fold spin degeneracy and three-fold valley degeneracy [63, 64, 255]. Intervalley or spin-orbit scattering leads to a reduction of α as these different conduction channels do not individually contribute to the WL effect anymore [254, 255]. Figure A.3 (c) shows l_φ as function of the charge carrier density n at $T = 2$ K prior (blue circle) and after (green circle) the PD. In contrast to previous studies on few-layer MoS_2 [255] we observe a clear increase of l_φ with increasing n up to 175 nm at $n = 1 \times 10^{13}$ cm^{-2}. The value of α (see Figure A.3 (b)) determined from fitting the experimental data is around 3, which would indicate that the weak localization is dominated by intervalley scattering [255] probably mediated by the relatively large amount of defects in natural MoS_2 [217, 219] assuming the phase coherent transport properties are governed by the MoS_2. Except of the physical interpretation of α the analysis presented so far is valid for either the MoS_2 and the FLG but we do not extend the analysis to any spin-orbit dependent analysis. Nevertheless, the gate-tunable phase-coherence length is in qualitative agreement with the Altshuler-Aronov-Khmelnitsky (AAK) theory [252] of an electron-electron interaction induced scattering mechanism of a

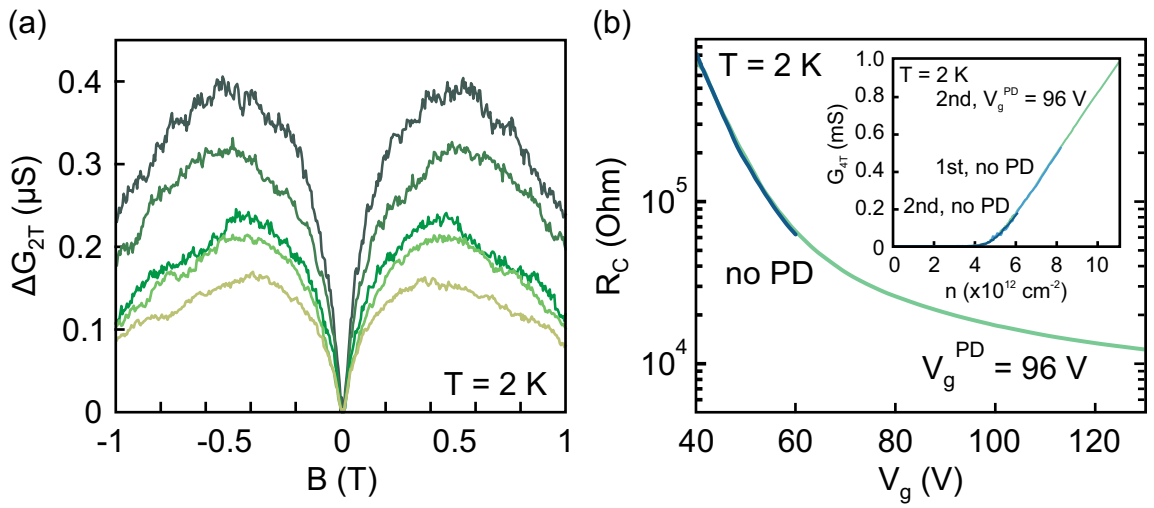

Figure A.2: (a) Magneto-conductance $\Delta\sigma$ as function of magnetic field B with respect to the conductance at $B = 0$ for five different charge carrier densities n at $T = 2K$ before the photodoping. (b) Contact resistance R_C as a function of gate voltage V_g prior (blue trace) and after (green trace) the PD estimated by comparing the two- and four-terminal conductance. To account for the photodoping the green trace has been shifted by 80 V. Inset: Four-terminal conductance as a function of gate voltage V_g before and after the photdoping.

two-dimensional system,

$$l_\varphi = \hbar g_\square (4m^* k_B T \log g_\square)^{-1/2}. \tag{10.2}$$

Here, $g_\square = \sigma/e^2$ is the dimensionless conductivity, m^* the effective electron mass and k_B the Boltzmann constant. We roughly approximate $g_\square = \sigma/e^2$ by subtracting the contact resistance R_C, which we obtained from additional Hall measurements (see also chapter 6), from the two-terminal conductance G_{2T}. Figure A.3 (d) shows the experimentally extracted l_φ as a function of $G_{2T} - R_C$. Using $m^* = 0.85\, m_e$ and $m^* = 0.55\, m_e$ determined by DFT calculations as the effective carrier mass in the Q-valley of few-layer MoS_2 [95, 256] in longitudinal and transversal direction we obtain the solid gray and black line in Figure A.3 (d). These results agree reasonably well with the extracted l_φ and would confirm the electron-electron interaction based scattering mechanism within the previously mentioned constraints. Additionally, we observe no significant effect of the PD on the phase coherence length. In the worst case the photodoping introduces elastic Coulomb scatterer into the system as it charges local defects in the hBN [67, 68, 199] which should have no effect on phase coherent transport [116, 257].

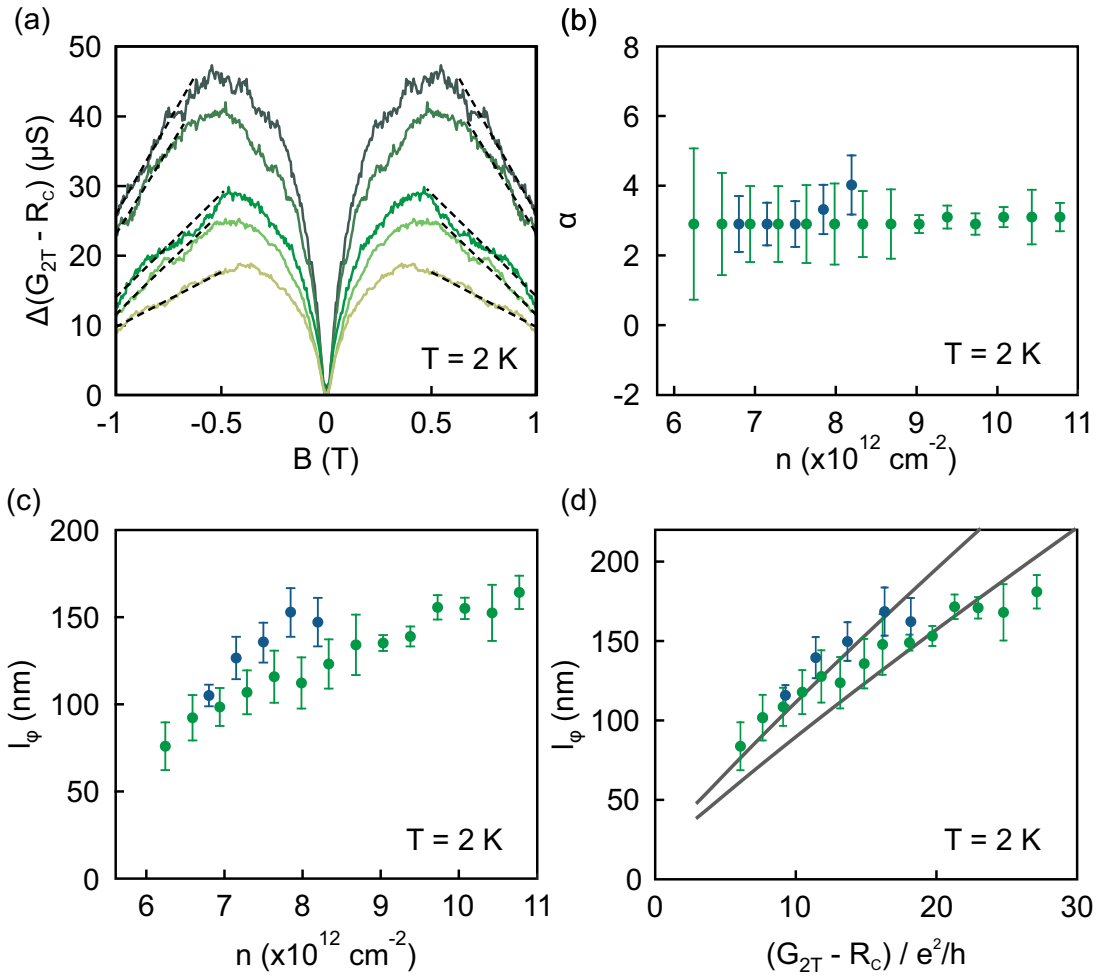

Figure A.3: (a) Symmetrized Magneto-conductance $\Delta\sigma$ as function of magnetic field B with respect to the conductance at $B = 0$ for five different charge carrier densities n at $T = 2$ K before the photodoping (form top to bottom: $n = 8.2 \times 10^{12}$, 7.8×10^{12}, 7.5×10^{12}, 71×10^{12} and 6.8×10^{12} cm^{-2}). (b) Empirical parameter α as function of the charge carrier density n. (c) Phase-coherence length l_φ as function of the charge carrier density n extracted from the weak localization measurements at $T = 2$ K before (blue circle) and after (green circle) the photodoping. (d) Phase coherence length l_φ as function of the two-terminal conductance G_{2T} with the contact resistance R_C being subtracted. The gray solid line displays the prediction of the Altshuler-Aronov-Khmelnitsky theory for $m^* = 0.85\, m_e$ (upper line) and $m^* = 0.55\, m_e$ (lower line) [252].

A.4 Weak localization measurements between 30 mK and 40 K

Next, we investigate the WL effect in a wide temperature range of 30 mK up to 40 K. It has to be pointed out that the device area investigated here is different compared to the previous presented measurements and that we only have access to a two-terminal configuration. For estimating the charge carrier density we assume a similar doping compared to the measurements in previous measurements as indicated by the gate characteristics shown in Figure A.1.

Figure A.4 (a) shows $\Delta\sigma_{2T}(B)$ for temperatures between 30 mK up to 40 K at $V_g = 50$ V corresponding to $n = 1 \times 10^{13}$ cm^{-2} if we assume the same doping as after the second cool-down. Up to $T = 4$ K the shape of the WL feature does not change significantly but then rapidly starts to widen and decrease in amplitude. This effect is much better visible when we look at the extracted l_φ as a function of $1/\sqrt{T}$ at different gate voltages (see Figure A.4 (b) to (d)). Consistent with the AAK theory at temperatures higher than $T = 10$ K, l_φ follows an inverse square root dependency while below this temperatures τ_φ saturates indicating an additional source for dephasing. To compare the results not only qualitatively with the AAK theory the dimensionless conductivity has to be estimated. A linear fit of eq. 10.2 using $m^* = 0.55\, m_e$ [95, 256] to the high temperature (> 10 K) data for the different V_g (solid line in Figure A.4 (b) to (d)) is used to extract $g_\square$ for the following quantitative analysis. It has to be noted that this assumes the phase coherent transport properties to be governed by the MoS_2 and, in any case, can only be regarded as a rough estimate as it does not account for the temperature dependent change of the device mobility. The extracted $g_\square$ is roughly a factor of two larger than the conductance estimated from the previous four-terminal measurements in the previous measurements which could be explained by the different regions probed in the different measurement setups. If we assume the phase coherent transport is governed by the FLG region and use an effective electron mass of $m^* = 0.06_e$ [17] the estimated $g_\square$ is a factor of two smaller compared to the previous four-terminal measurements.

The saturation of the phase-coherence time $\tau_\varphi = l_\varphi^2/D$ is attributed to an additional inelastic electron spin-flip scattering time τ_{SF}. In order to approximate τ_{SF} the AAK theory is modified similar to reference [258] and [259] which results in an overall scattering rate of ${\tau_\varphi}^{-1} = \tau_{SF}^{-1} + k_B T \log(g)/(\hbar g_\square)$. We use this expression to estimate τ_{SF}. In case of MoS_2 and assuming a linear carrier density dependence ($\tau_{SF} = \beta\, n$ with $\beta = 2 \times 10^{-24}$ cm^2 s) this modification yields a good agreement with all our experimental data of the third cool down (see dashed lines in Figure A.4 (b) to (d) and Figure A.5 (b)). The extracted τ_{SF} values are on the order of 20 ps. Performing the same analysis considering the FLG to be the dominant region in the WL measurements proofs to be difficult as we have no direct access to the n in the FLG. Assuming a charge carrier density of $n = 1 \times 10^{13}$ cm^{-2}, which is in the range reported in literature [17], and use $\beta = 0.75 \times 10^{-24}$ extracted for the

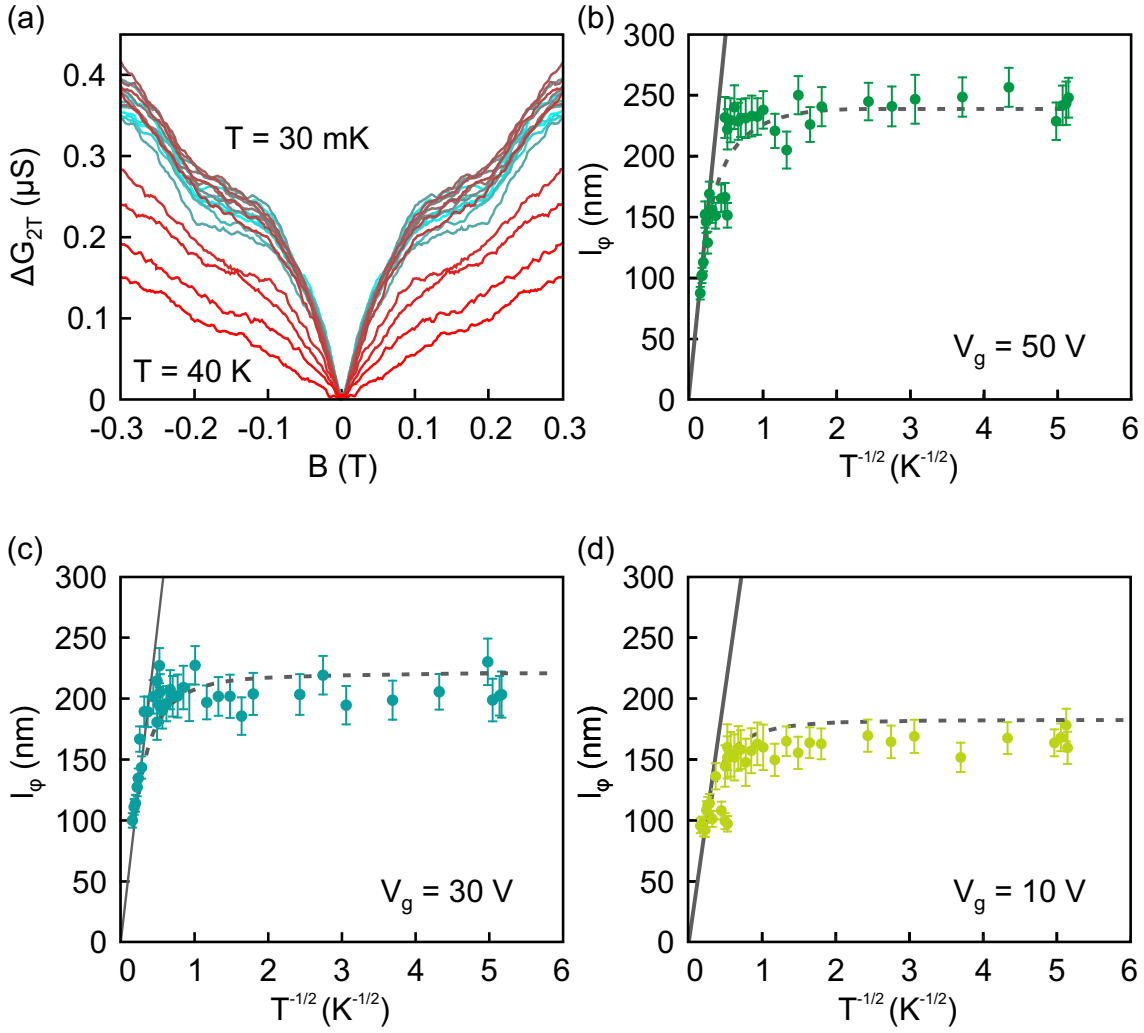

Figure A.4: (a) Two-terminal conductance $\Delta\sigma_{2T}(B)$ at $V_g = 50$ V for temperatures between 30 mK up to 40 K. (b)-(d) Phase-coherence length l_φ as function of $1/\sqrt{T}$ at different gate voltages. The solid line presents the prediction from the AAK theory whereas the dashed line results from including a finite electron spin-flip scattering time τ_{SF} (see text for details). From a fit of the AAK theory to the high temperature data we extract the dimensionless conductivity $g_\square$.

FLG yields τ_{SF} on the order of 5 to 10 ps, which would be one order of magnitude faster compared to what has been reported for example for graphene [260] or bilayer graphene [258]. A higher charge carrier density on the order of 1×10^{14} cm^{-2} or larger is usually only achieved by liquid gating [261, 262]. A similar density dependence of τ_{SF} was found by some of us in weak localization studies on bilayer graphene [258] and weak anti-localization studies on Bi_2S_3 [259]. For graphene this density dependence was found for resonant scattering at magnetic impurities [263] and spin-pseudospin dynamics [264]. In the material class of TMDs the intrinsic

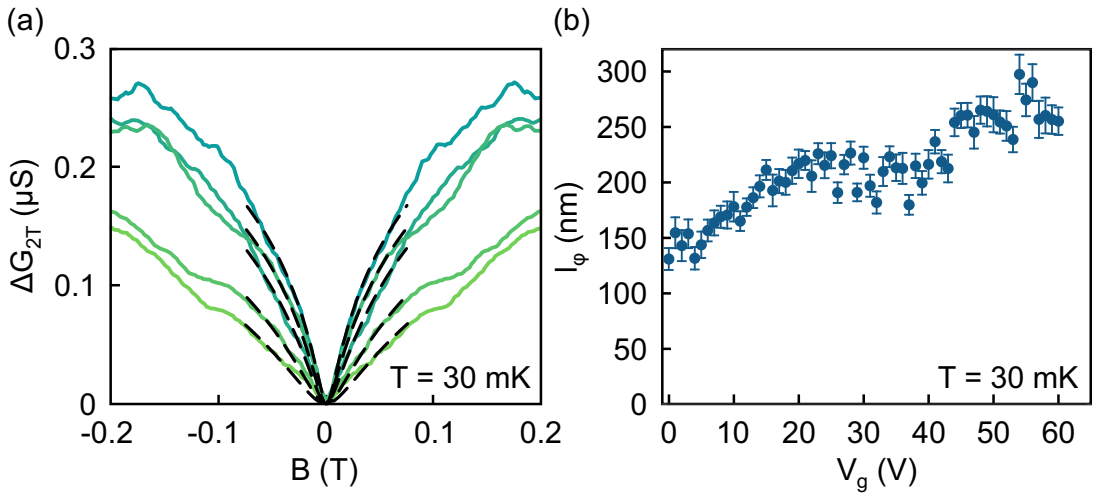

Figure A.5: (a) Two-terminal conductance $\Delta\sigma_{2T}(B)$ at $T = 30$ mK at (from top to bottom) $V_g = 45$, 30, 20, 10, 0 V. The black dashed lines represent the fitting of the weak localization model. (b) Phase-coherence length l_φ as function of the applied gate voltage V_g.

spin-orbit interaction [104] is likely the dominant spin-relaxation mechanism. Next, we take a look into the charge carrier dependency of the WL effect at 30 mK. Figure A.5 (a) shows $\Delta\sigma_{2T}(B)$ at $T = 30$ mK for five different back gate values $V_g = 45$, 30, 20, 10, 0 V. The WL feature is only fitted up to ± 75 mT (black dashed lines) as universal conductance fluctuations strongly influence the magnetoconductivity for higher B-fields. Figure A.5 (b) shows the extracted phase coherence length l_φ as a function of n. With increasing conductance l_φ increases roughly linear up to 250 nm which is again consistent with an electron-electron interaction induced scattering mechanism. But if we compare the results to the prediction of the AAK theory (solid gray line) the values deviate by a factor of 10 to 12 which can be well accounted for by including the previously introduced τ_{SF} without any further corrections (dashed gray line) validating the electron-electron interaction induced scattering limited by additional spin-flip mediated dephasing.

A.5 Conclusion

In conclusion, we performed low-temperature magneto-transport measurements on five-layer MoS_2 encapsulated in hBN with few-layer graphene contacts before and after photodoping. The device has a mobility on the order of $\mu = 600$ cm^2/(Vs) at high charge carrier densities and shows a pronounced dip in conductivity for small magnetic fields. From weak localization measurements we extract a phase-coherence lengths between 100 nm and 250 nm with no visible effect of the PD to the phase-coherent transport. The phase-coherence length follows a linear dependency on the

conductivity and the electron density consistent with electron-electron interaction predicted by Altshuler, Aronov and Khmelnitsky. We have to stress here that we can not entirely be sure in which area of the device the phase coherent transport occurs. If we consider the weak localization effect to result from the MoS_2 area intervalley scattering probably mediated by the relatively large amount of crystallographic defects like missing sulfur atoms in MoS_2 is dominating the WL effect which would be consistent with the literature [255]. At the lowest temperatures the phase coherence is then limit by spin-flip scattering on time scales of 20 ps. Regarding the FLG as the source of the phase-coherent transport and assuming a reasonable charge carrier density of $n = 1 \times 10^{13}$ cm^{-2} [17] would yield an even faster spin-flip time on the order of 5 to 10 ps which would be a few orders of magnitude faster compared to what has been reported e.g. for graphene [260] and bilayer graphene [258] where the relaxation is potentially governed by resonant scattering at localized magnetic moments [263, 265]. These measurements show again how important the contacts in our hybrid structures are and that their properties have to be taken into account when interpreting the results of these structures.

B Fabrication of nanostructures with integrated membrane based on hBN/graphene heterostructures on local gate structures

In the main part of this work we presented two potential concepts for novel mesoscopic transport devices in order to explore quantum confinement effects. Because of the extraordinary elasticity and material strength [22, 23, 266], graphene is also an ideal candidate for quantum electromechanical devices, where its electrical properties could be mechanically tuned [267–269]. This might allow for entirely new device schemes for confining electrons by straining the graphene. Graphene quantum devices with an additional mechanical degree of freedom are thus an interesting platform to investigate the interplay between structural, mechanical, and electronic properties. Recently a study on the transport across nanometer-scaled isolated, linearly-shaped strained regions reveling quantum transport has been performed [270] but lacks the control over mechanical degree of freedom. The fabrication of nanometer-scale devices with integrated membranes which can be tuned is very demanding as it requires a multitude of process steps which all need to be precisely aligned while keeping the membrane intact. In the following, the fabrication process of graphene nanostructure devices with integrated membranes will be outlined. A detailed list of all process parameters can be found in section D.

The fabrication of nanostructures with integrated membrane based on hexagonal boron nitride (hBN)/graphene heterostructures uses the same standard process steps as described in chapter 4. Also here, the core elements are the exfoliation of the layered material (see chapter 4.2) and subsequent transfer steps (see chapter 4.4).

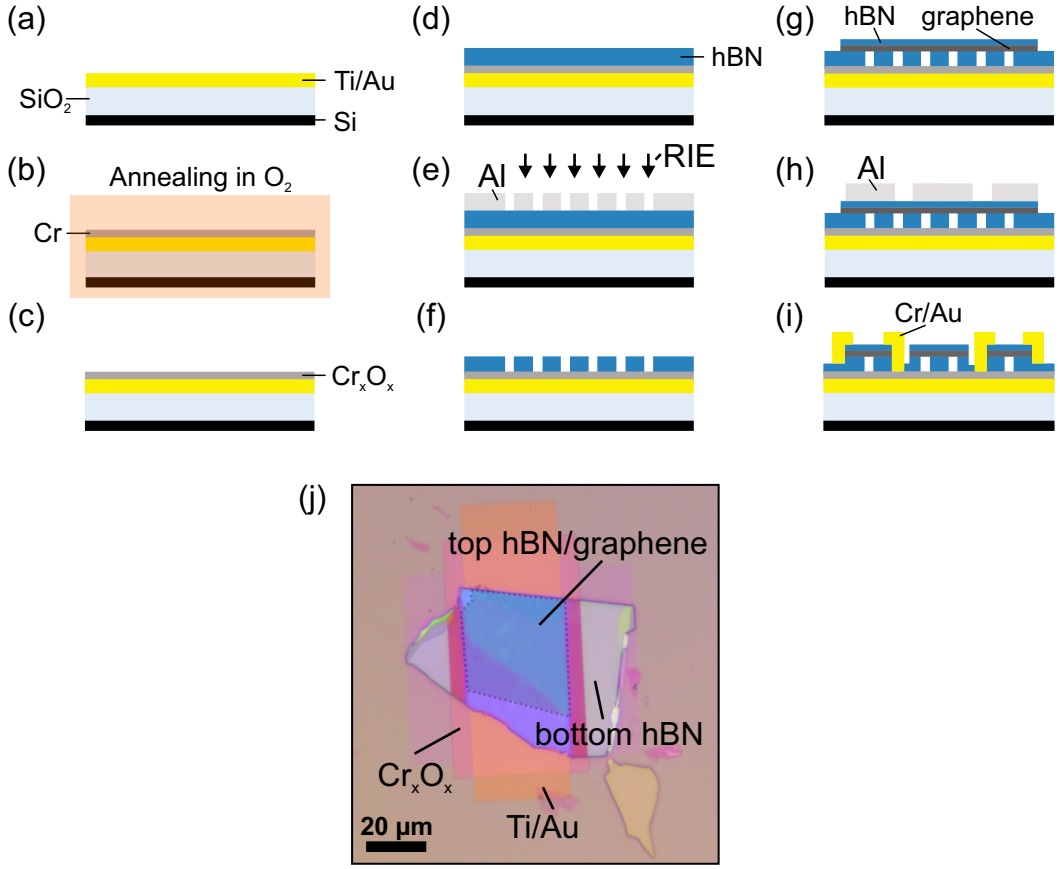

Figure B.6: Schematical illustration of the fabrication process. (a) A local gate structure is patterned onto an undoped Si/SiO_2 by electron beam lithography (EBL) and a subsequent metal evaporation of 5 nm Ti/ 50 nm Au. (b)-(c) The gate structure is covered by a local chromium oxide (Cr_xO_x) by patterned by EBL, evaporation of 5 nm Cr and a subsequent annealing step under pure oxygen (O_2) atmosphere at 350° C. (d) The standard transfer technique described in chapter 4.4 is used to place a hexagonal boron nitride flake onto the local oxide. (e)-(f) The hole geometry is patterned into the bottom hBN by EBL, deposition of an aluminum hardmask and reactive ion etching. (g) Using the transfer technique a graphene flake or hBN/graphene half-sandwich is placed onto the pre-patterend bottom hBN flake. (h) Subsequently the desired device geometry is patterned into the heterostructure by EBL, deposition of an aluminum hardmask and reactive ion etching. (i) The resulting device is contacted in a second EBL step and a subsequent metal evaporation of 5 nm Cr/ 50 nm Au contacts. (g) Optical micrograph of a complete hBN/graphene/hBN heterostructure on the local gate / local oxide structure.

For the fabrication of our heterosturctures we again use two different substrates. Key difference is the use of undoped silicon chips in order to reduce stray capacitances in high frequency measurements, covered by 285 nm thick thermal oxide (Si/SiO_2,

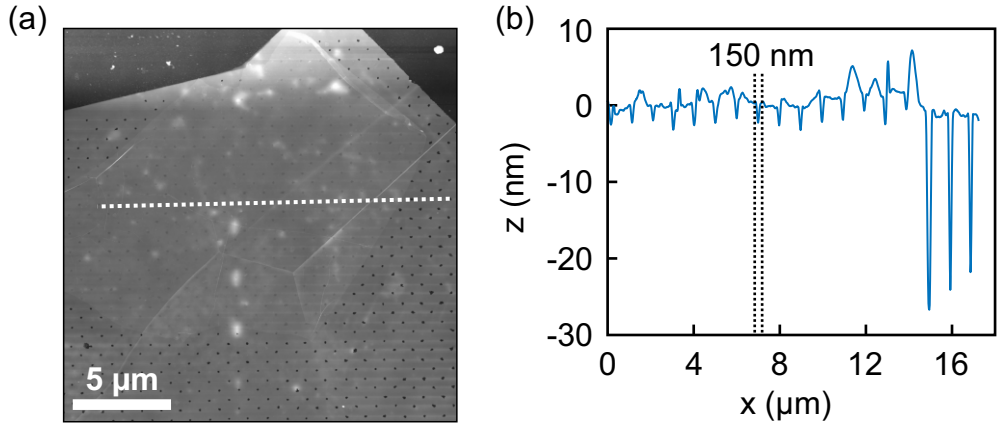

Figure B.7: (a) Atomic force micrograph of a bilayer graphene flake transfered onto the pre-patterned hBN flake. The white dashed line corresponds to the linecut shown in (b).

Nova Electronic Materials) and pre-structured by a local gate structure. Central and crucial aspect of the fabrication is the exact alignment of all process steps and hence we fabricate in a first step metal markers on the Si/SiO_2 substrates by standard electron beam lithography (EBL) and metal evaporation, which are used on all following EBL steps and yield a alignment precision below 5 nm.

In the next step (see schematic in Figure B.6 (a) and the optical micrograph in Figure B.6 (j)) we define the local gate structure by EBL and metal evaporation (5 nm Ti/ 50 nm Au). To guarantee a smooth lift-off we use a double resist stack of 70 nm polymethyl methacrylate (PMMA) 50k (AR-P 639.04) and 220 nm polymethyl methacrylate 950k (AR-P 679.04). The resulting gate structures have a width between 50 nm and 300 nm and a separation between 500 nm and 1 μ m, respectively. In order to prevent electrical shorts due to collapsing of individual structures in the following process steps or during the measurements we fabricate on parts of the gate structure a local chromium oxide (Cr_xO_x) by EBL, evaporation of 5 nm Cr and a subsequent annealing step under pure oxygen (O_2) atmosphere at 350° C (see Figure B.6 (b), (c) and (j)). Afterwards, we now employ our transfer technique to place a hexagonal boron nitride (hBN) flake with a thickness around 50 nm on the chromium oxide (Figure B.6 (d)). Subsequently, we patterned an array of holes with a diameter between 50 nm and 300 nm, depending on the width of the underlying gate structure, into the hBN flake using EBL, evaporation of a 20 nm aluminum hard mask and reactive ion etching (RIE) using a $SF_6/Ar/O_2$ plasma (flow: 20 sccm / 5 sccm / 5 sccm; power: 60 W) (Figure B.6 (e) and (f)). Again we use a double resist stack of 70 nm PMMA-50k and 220 nm PMMA-950k. The holes are precisely aligned with the local gate structure. A second transfer step is used to place a graphene flake or hBN/graphene half-sandwich onto the pre-patterend bottom hBN flake (Figure B.6 (g)).

An atomic force micrograph of a bilayer graphene flake transfered onto a pre-

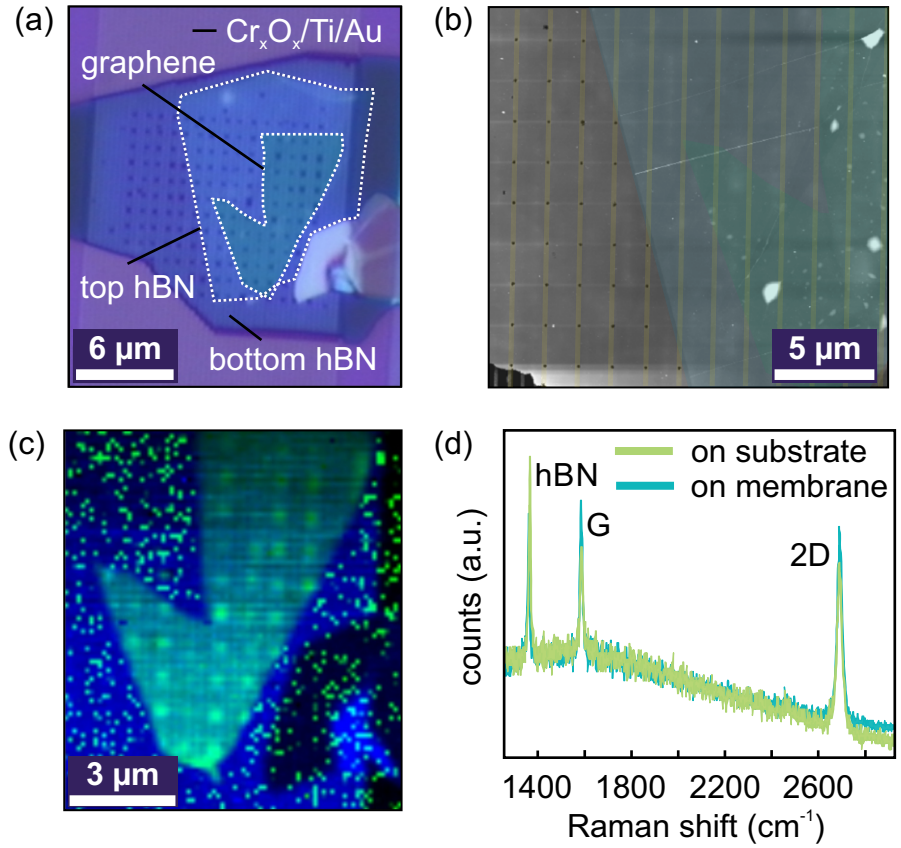

Figure B.8: (a) Optical micrograph of a complete hBN/graphene/hBN heterostructure on the local gate / local oxide structure. (b) Atomic force micrograph of a 3 nm thin hBN (blue shaded area) / single-layer graphene (green shaded area) half-sandwich transfered onto the pre-patterned hBN flake. The local gate structure is indicated by the yellow shaded area. (c) Corresponding Raman map showing the the integrated intensities of the hBN peak (blue) and of the graphene 2D peak (green). (d) Two Raman spectra recored on the substrate (yellow) and on the membrane (blue).

structured gate structure is shown in Figure B.7 (a). The hBN flake has a height of 27 nm with a hole diameter around 150 nm (see although the topography line cut in Figure B.7 (b)). Figure B.8 (a) shows an optical micrograph and Figure B.8 (b) the corresponding atomic force micrograph of a pre-structured hBN/single-layer graphene/hBN heterostructure. The holes have a diameter of 250 nm and a depth of around 85 nm which corresponds to the thickness of the bottom hBN flake. In order to not stiffen the membrane by the additional top hBN to strongly we choose the top hBN flake to be as thin as possible (here 3 nm). The atomic force micrograph clearly shows that the membranes are still suspended after the transfer process. This is underlined by the Raman spectroscopy measurement. Figure B.8

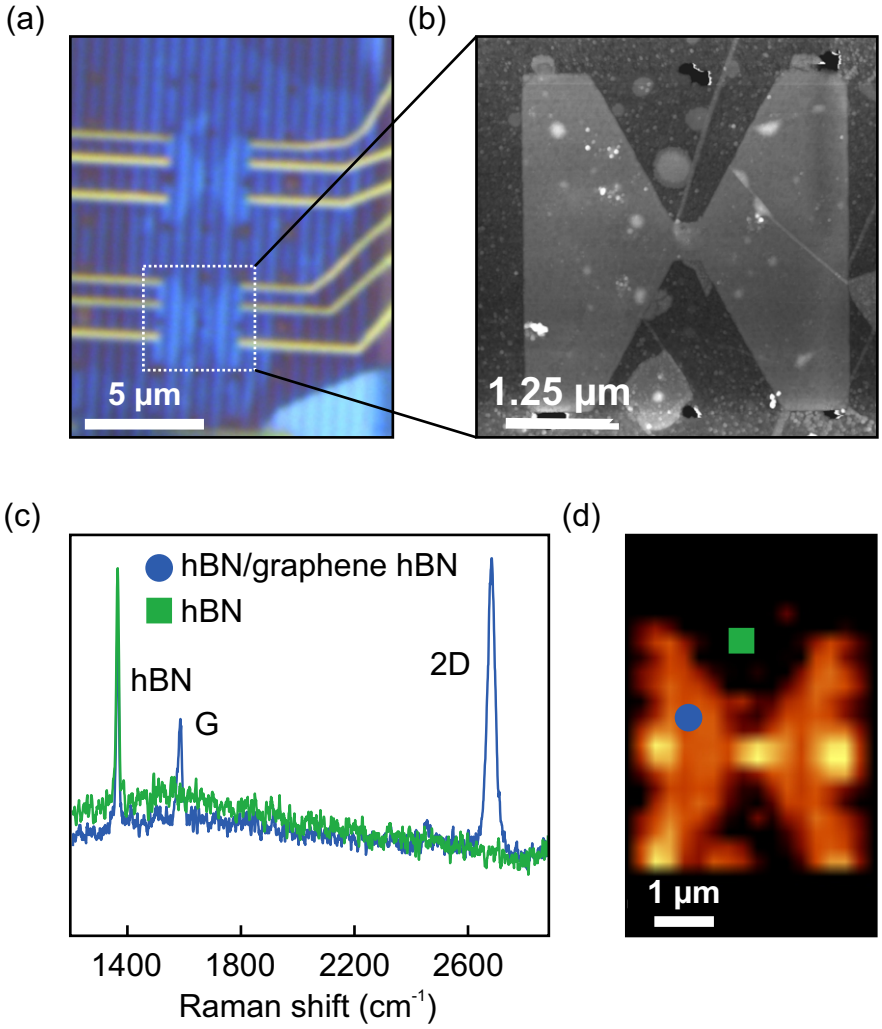

Figure B.9: (a) Optical micrograph of contacted single layer graphene constrictions with integrated membranes on a local gate structure. (b) Atomic force micrograph of the constriction device indicated by the white dashed lines in (a). The constriction has a width of 450 nm and the membrane has a diameter of 300 nm. (c) Two Raman spectra recored on the constriction device (blue) showing the hBN peak and the G and 2D peak of the single layer graphene and next to the device (green) where only the hBN peak is seen. (d) Raman map showing the the integrated intensity of the graphene 2D peak. The suspended areas are visible in form of increased intensity.

(a) shows a Raman map of the integrated intensities of the hBN peak (blue) and of the graphene 2D peak (green), where the holes are clearly visible due to an increased intensity (c.f. Figure B.8 (b)).

Depending on the depth of the hole, the intensity can either be increased or decreased due to cavity resonances. The large background results from the underlying metal. Subsequently the desired device geometry is patterned into the heterostruc-

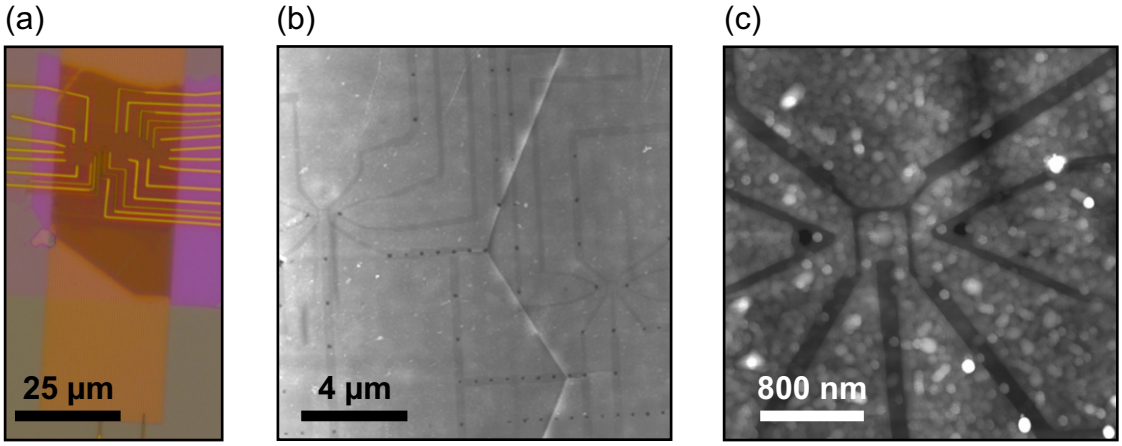

Figure B.10: (a) Optical micrograph of the local gate structure after contacting several single-layer graphene quantum dots (QDs) with integrated membranes. (b) Atomic force micrograph of two graphene QDs with two charge detectors each. (c) Atomic force micrograph of a graphene QDs with a island diameter of 350 nm. The membrane in the center of the island has a diameter of 300 nm.

ture by EBL (resist stack: 50k/950k PMMA), deposition of an aluminum hardmask (20 nm) and reactive ion etching with a CH_3/O_2 plasma (flow: 20 sccm/5 sccm; power: 60 W) (see the schematic in Figure B.6 (h)). The etching time is chosen in such a way that the bottom hBN layer is not completely etched through (etching rate roughly 0.5 nm/s). After the etching, the Al hardmask is removed by a solution of 2% tetramethylammonium hydroxide/98% DI water. The resulting constriction devices are then contacted in a last EBL step and a subsequent metal evaporation of Cr/Au (5 nm/50 nm) (Figure B.6 (i)). Figure B.9 (a) shows an optical micrograph and Figure B.9 (b) the corresponding atomic force micrograph of a single-layer graphene constriction with a constriction width of 450 nm and an integrated membrane in the center of the constriction with a diameter of 300 nm after the RIE and the removal of the hard mask. The atomic force micrograph again clearly shows that the membrane is still suspended after the etching. In Figure B.9 (a) the Raman spectrum on (blue) and next to (green) the final constriction device after the contact evaporation step is shown. The spectrum on the device shows the hBN peak located around 1356 cm^{-1} and the G peak around 1589 cm^{-1} and the 2D peak around 2681 cm^{-1} of the graphene. Beside the device only the hBN peak is visible. A map of the integrated intensity of the 2D peak is shown in Figure B.9 (b). Again we see the enhancement of the intensity showing the high alignment precision and indicating that the membrane is still suspended.

For the fabrication of quantum dots (QDs) the aluminum hard masks proved to be not feasible due to a bad reproducibility. We hence relied on a PMMA mask (PMMA-200k) to pattern the device geometry by EBL followed by reactive ion etching with a Ar/O_2 plasma (flow: 32 sccm/8 sccm; power: 60 W). A last EBL and

metal evaporation step (5 nm Cr/ 50 nm Au) is used to contact the device. Figure B.9 (a) shows an optical micrograph and Figure B.9 (b) and (c) the corresponding atomic force micrograph of a single-layer graphene QD with a island diameter of 300 nm and an integrated membrane in the center of the constriction with a diameter of 250 nm after the RIE and the removal of the hard mask. The atomic force micrograph again clearly shows the high alignment precision and that the membrane is still suspended after all process steps.

C Probing the nonlinear elasticity of 2d materials via nanoindentation experiments

C.1 Introduction

Since the discovery of a very simple fabrication method by Konstantin Novosolev and Andre Geim in 2004 [17] graphene's extraordinary mechanical properties have been subject of various studies employing different experimental techniques like force indentation measurements [22, 271–275], so called blister tests [276–278], Raman spectroscopy [152, 159, 278–282] or interferometric profilometry [281, 283]. The mechanical properties result from the 2d crystal structure and provide graphene a high in-plane stiffness and intrinsic strength [284–286]. In simple terms, graphene is predicted to be "stronger" than any other material making it highly interesting for a lot of applications [286]. In the following years, many other 2d materials, such as transition metal-dichalcogenides (TMDs) and hexagonal boron-nitride (hBN), have been discovered and investigated in a similar fashion [54, 266, 287–291].

Here, we determine the 2d Young's modulus (E_{2d}), which characterizes the material response to mechanical deformations, of different 2d materials by indentation experiments with an atomic force microscope. Here, a tip (diameter roughly 20 nm) at the end of a cantilever is used to deflect the center of a suspended 2d membrane. As a measurement signal the cantilever deflection and the indentation depth are recorded. So far these experiments have been analysed with a model that has been derived from membrane theory and assumes a constant Young's modulus. However, as 2d materials are extremely thin, the sensitivity to deformations (E_{2d}) depends on the deformation itself, which results in a strain dependent E_{2d}, and has so far not been considered within the analysis of an AFM indentation curve. We investigate the mechanical response of the membrane to an external load by solving the non-linear Föppl-von Kármán equations to simulate the experiment and extract the strain dependence of the elastic properties from the measurements.

C.2 Fabrication

The samples are fabricated by mechanical exfoliation of the 2d material as described in chapter 4 on silicon chips covered by 285 nm thick thermal oxide (Si/SiO_2)

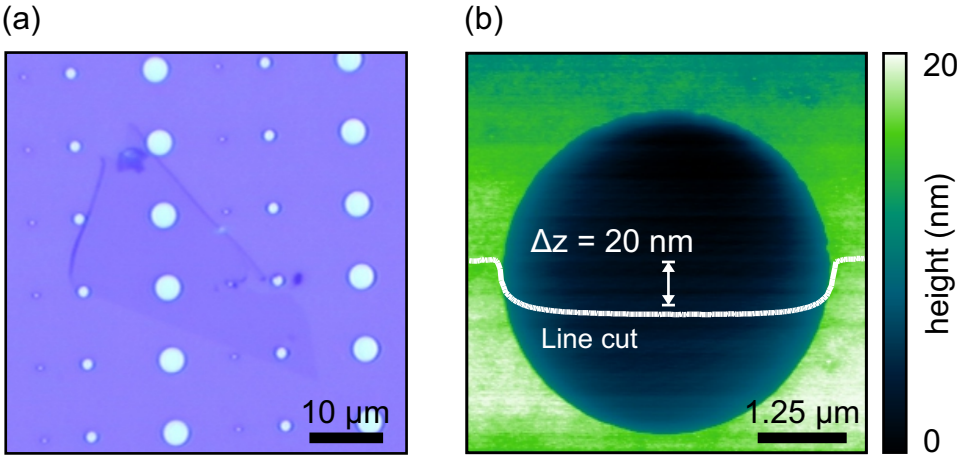

Figure C.11: (a) Optical micrograph of a single-layer gaphene flake exfoliated on a pre-structured Si/SiO_2 substrate. (b) Atomic force micrograph of a graphene membrane with a diameter of 4 μm.

pre-structured with holes between 1 μm and 6 μm (see Figure C.11(a)). The pre-structuring is performed by a combination of metal deposition, electron beam lithography (EBL), chemical wet etching and dry reactive ion etching (RIE). Initially, the bare Si/SiO_2 is covered completely by a 200 nm thick chromium (Cr) film. The hole structure is transfered into the Cr film by EBL using a single resist layer of 950k PMMA and a subsequent wet etching step with Chromium etch (Micro Chemicals, a mixtures of perchloric acid and ceric ammonium nitrate, 60 nm/minute). Afterwards, the holes are etched into the Si/SiO_2 substrate by RIE with a CHF_3/O_2 (20sccm/5sccm) plasma to remove the SiO_2 and a subsequent CF_4/O_2 (20sccm/5sccm) plasma to etch 500 nm into the Si for a total hole depth around 800 nm.

The Cr hard mask is then removed by a second wet etching step. Its important to note that the RIE process alters the surface of the Cr which reduces the etching rate of the Chromium etch. Consequently, the second wet etching step needs to be significantly prolonged to 15 min. The successful fabrication of the 2d membranes by the following exfoliation step is confirmed by topography measurements with an AFM (see Figure C.11(b)) which reveal a slight pull-in of the membrane, which is usually around 20 nm, due to van-der-Waals interactions with the sidewall of the hole. Additionally, we perform Raman spectroscopy measurements of each membrane in order to determine the layer number and, for graphene only, to map the FWHM of the 2D peak and the spatially resolved strain (see 4.3 and Figure C.12). The combination of the topography and the results from the Raman measurements indicate a homogeneous membrane suitable for the following force indentation measurements.

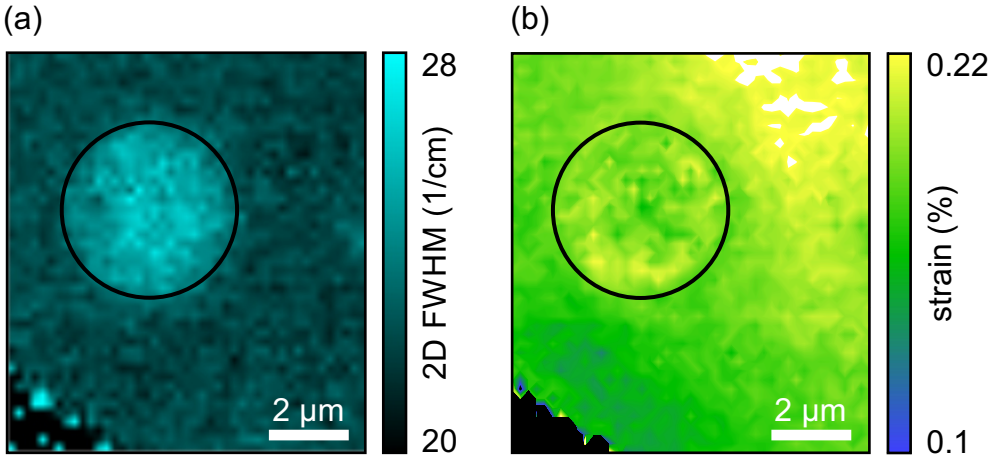

Figure C.12: (a) Spatially resolved Raman map of the FWHM of the 2D mode for the single-layer graphene membrane shown in Figure C.11(b). (b) The corresponding spatially resolved strain.

C.3 Force indentation measurements

Now, we turn to the force indentation measurements on single and bilayer graphene membranes as well as a trilayer molybdenum disulfide (MoS_2) and a four-layer tungsten diselenide (WSe_2) membrane which have been performed with an Asylum Research Cypher S atomic force microscope using diamond-like carbon coated silicon tips. Before each measurements series, we utilize the thermal self-excitation of the cantilever in order to determine the spring constant k of each cantilever [292] which is typically on the order of 1 N/m. The voltage-drop on the photodiode of the AFM is then calibrated with respect to the deflection of the cantilever by performing an indentation measurement on the Si/SiO_2 substrate which can be regarded as infinitely hard compared to the cantilever. Consequently, the known piezo movement z corresponds to the deflection. The actual nano-indentation experiment is then performed in the center of the membrane. An exemplary raw data trace and retrace of a single-layer graphene membrane with a diameter of 1 μm is shown in Figure C.13(a). By a linear fit, the range, where the tip is not in contact with the membrane (see (1) in Figure C.13(a)) is used to determine the zero separation s (see (3) in Figure C.13(a)), where no force is acting on the membrane, and the deflection off-set. The point (2) in Figure C.13(a) corresponds to the so-called snap-in where upon approaching the attractive forces are large enough to pull the tip onto the sample surface. Similar, upon retracting the tip snaps from the sample surface when the restoring force is larger than the adhesion forces ((5) in Figure C.13(a)).

In oder to perform the analysis of the Young's modulus of the 2d membranes we need to separate the deformation of the membrane from the deformation of the cantilever. This is achieved by subtracting the linear deformation of the cantilever using its known spring constant k ($s = z - F/k$). The membrane deformation

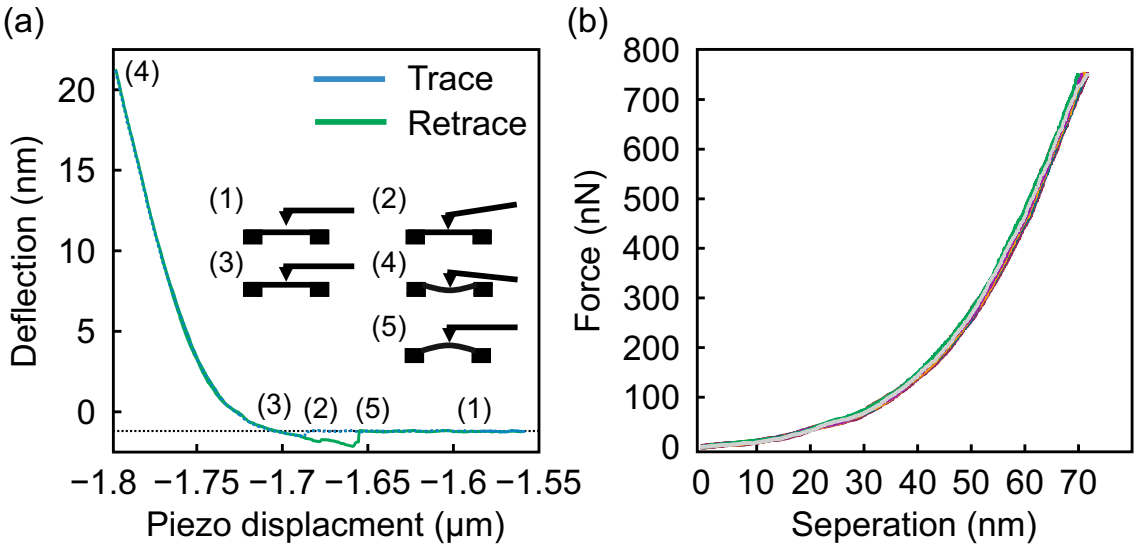

Figure C.13: (a) Raw data trace and retrace (deflection of the cantilever as function of the piezo displacement) from a nano-indentation measurement via an atomic force micropscop of a single-layer graphene membrane with a diameter of 1 μm. While approaching (trace) the tip of the cantilever is not yet in contact with the membrane and no deflection is measured (1). At (2) the attractive forces are large enough to pull the tip onto the sample surface of the membrane (so-called snap-in). At (3) again no force is acting on the membrane, marking the zero separation and the deflection off-set for the following analysis. (4) corresponds to the maximum deflection and marks the start of the retrace. Upon retracting, the tip snaps from the sample surface when the restoring force is larger than the adhesion forces (5). (b) The force-separation data from ten consecutive measurements after subtraction of the cantilever deformation, correction of deflection off-set and using the spring constant of the cantilever to calculate the force.

(separation) is then analyzed with respect to the applied force using an average of ten force-separation curves. Figure C.13(b) shows an exemplary data-set of 10 curves for the same membrane shown in Figure C.13(a) which exhibit a reasonable reproducibility. First, we analyze the data in the frame of linear membrane theory where an isotropic elastic circular clamped membrane is assumed. The deformation can then be approximated as

$$F = \sigma_{2d}\,\frac{\pi d}{2}\left(\frac{\delta}{d/2}\right) + E_{2d}\,\frac{q^3 d}{2}\left(\frac{\delta^3}{d/2}\right). \tag{10.3}$$

Here, F is the applied force, δ the deflection, $\sigma_{2\mathrm{d}}$ the pre-stress of the membrane, $q = 1/(1.05 - 0.15\nu - 0.16\nu^2) = 1.02$ a dimensionless constant related to the Poisson's ratio ν and E_{2d} the two-dimensional Young's modulus. Using this theory for

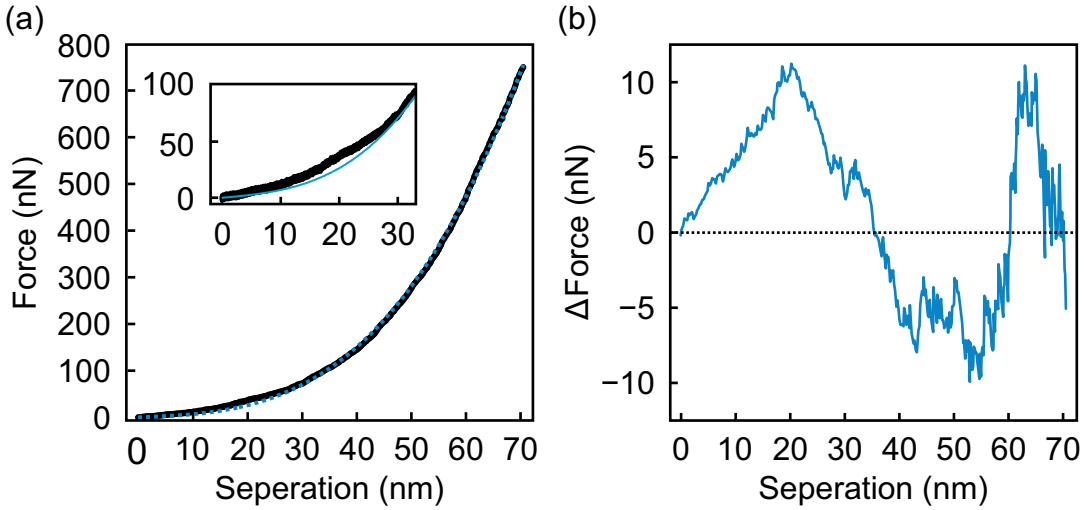

Figure C.14: (a) Force-separation data from a single-layer graphene membrane with a diameter of 1 μm with a fit to the data according to linear membrane theory. The inset shows the regime of small applied force. (b) The corresponding residuum of the fit.

the graphene membranes, we obtain similar results for E_{2d} of around 335 N/m as reported in previous studies [22, 273–275] and compatible with theoretical predictions [284–286] (see Figure C.14(a)). However, taking a closer look at the regime of small applied force reveals a significant deviation of up to 40% from the linear theory (see inset in Figure C.14(a) and the residuum of the fit shown in Figure C.14(b)), which potentially is related to a strain dependent E_{2d} [293] or the stretching of a crumpled membrane [281, 283].

To account for the strain dependence we numerically solve the full non-linear Föppl-von Kármán equations [294, 295] that describe the deformation of 2d membranes with a point-load in the center of the membrane

$$b\nabla^4 h - \frac{1}{r}\frac{\partial}{\partial r}\left(\frac{\partial X}{\partial r}\frac{\partial h}{\partial r}\right) = P \tag{10.4}$$

$$\nabla^4 X - E_{2d}\left(\frac{1}{r}\frac{\partial h}{\partial r}\frac{\partial h^2}{\partial r^2}\right) = 0. \tag{10.5}$$

Here, b is the bending rigidity, h is the out-of-plane displacement, X is the Airy stress function, P is the force per unit area and r is the the radial distance from the center of the membrane. The pre-stress is extracted from fitting the linear regime of the experimental data and is used in the boundary condition of X at r = 1. The numerical solution of these nonlinear partial differential equations yields the indentation and the strain on each position of the membrane. An example of the results for a membrane with a diameter of 1 μm under an applied force of 200 nN and assuming a E_{2d} of 335 N/m is shown in Figure C.15(a). We obtain a maximum

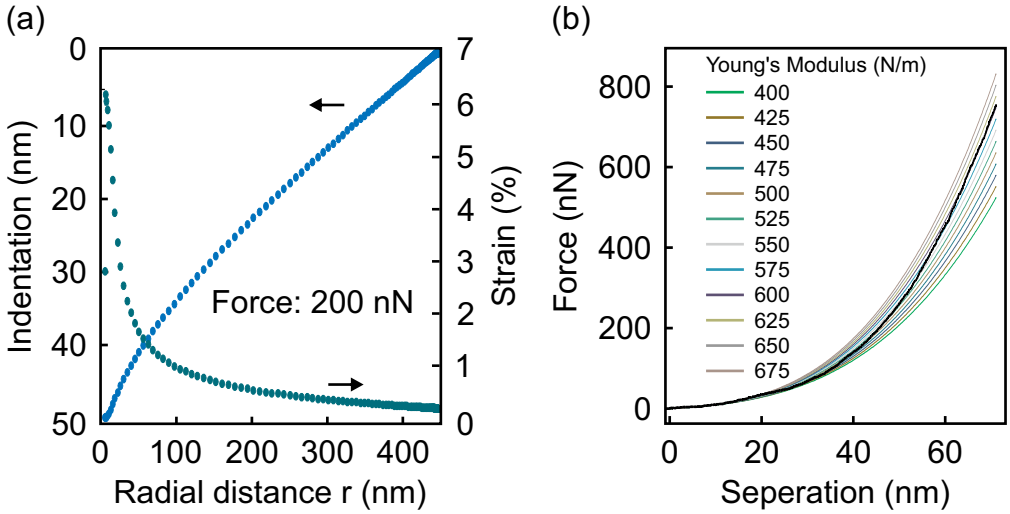

Figure C.15: (a) Indentation and strain as function of the radial distance from the center of the membrane derived from the numerical solution of the nonlinear Föppl-von Kármán equations for a two-dimensional membrane with a diameter of 1 μm assuming a Young's modulus of 335 N/m. (b) Measured force as function of separation of a single-layer graphene membrane with a diameter of 1 μm (black) and the corresponding simulated force-separation traces for a range of Young's moduli.

deflection of the membrane in its center of 50 nm which corresponds to an induced local strain of around 6.2 %. This analysis is performed for the whole range of applied force used in the experiment in order to fully simulate the force-separation trace for a large range of E_{2d} as shown in Figure C.15(b). By comparing the measurement at each data point with the numerical solution we extract an effective E_{2d} as function of separation (see blue trace in Figure C.16(a)).

As we also have access to the average strain of the membrane as function of separation deduced from the numerical solution (see yellow trace in Figure C.16(a)) the extracted effective E_{2d} can now be investigated as a function of the average strain (see Figure C.16(b)). The nonlinear analysis is performed for various single- and bilayer graphene membranes with different diameter d as shown in Figure C.17 (a) and (b). As has been recently observed by other groups [275, 281, 283], for single-layer graphene we extracted an increasing effective E_{2d} with increasing average strain which indicates that intrinsic ripples initially soften the membrane. Overall, we extracted a very high effective E_{2d} of up to 600 N/m at a the maximal average strain of 0.6 % which is in line with a recent study by López-Polín et al. which they related to the high impact of out of plane fluctuations making the elastic constants scale dependent. For bilayer graphene, we also extract a very high E_{2d} of up to 650 N/m per layer.

In contrast to the single-layer membranes, the maximum is reached at relatively small average strain values around 0.15 % indicating that rippling is less present

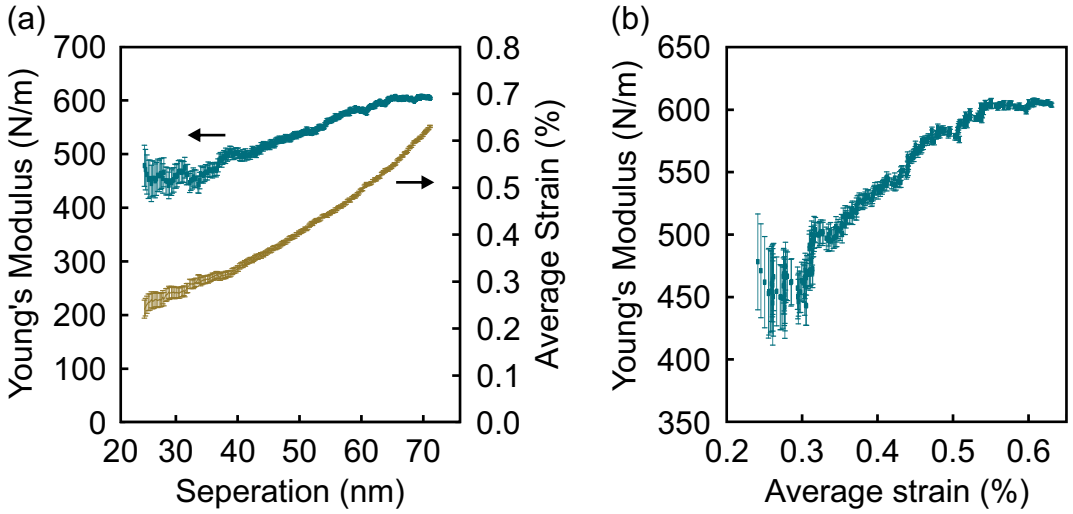

Figure C.16: (a) Average strain of a single-layer graphene membrane with a diameter of 1 μm deduced from the numerical solution (yellow) and extracted effective Young's modulus E_{2d} (blue) as function of separation (b) The corresponding effective Young's modulus as function of average strain.

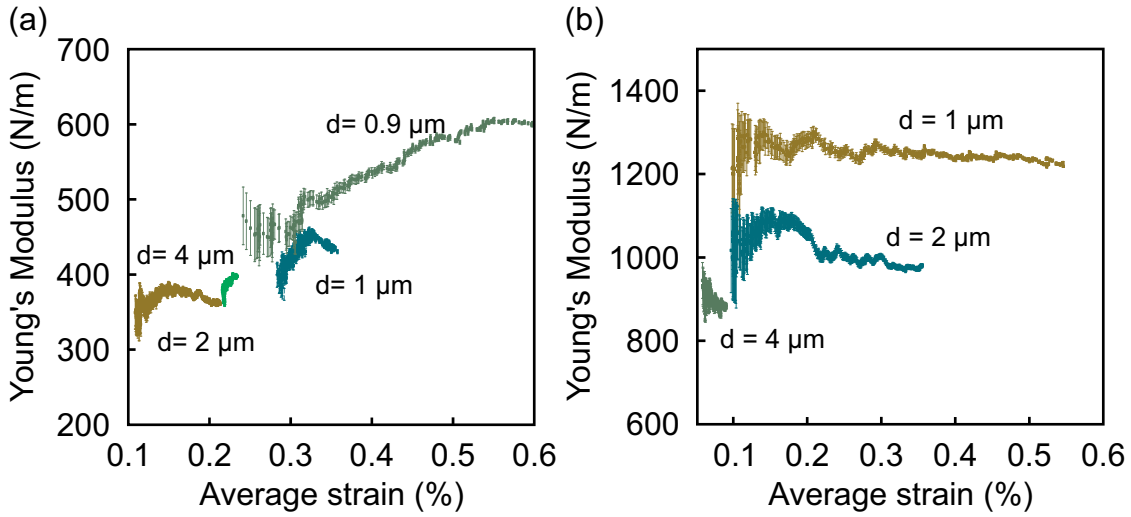

Figure C.17: (a) Effective Young's modulus as function of average strain for single-layer graphene membranes with diameters of d $= 0.9, 1, 2$ and 4 μm.(b) Effective Young's modulus as function of average strain for bilayer graphene membranes with diameters of d $= 1, 2$ and 4 μm.

due to the higher stiffness of the bilayer membrane. For increasing average strain the effective E_{2d} slightly decreases which would be expected due to softening of the carbon-carbon bonds with increasing strain. The same non-linear analysis has been performed for a trilayer MoS_2 membrane with a diameter of 6 μm (see Figure C.18)

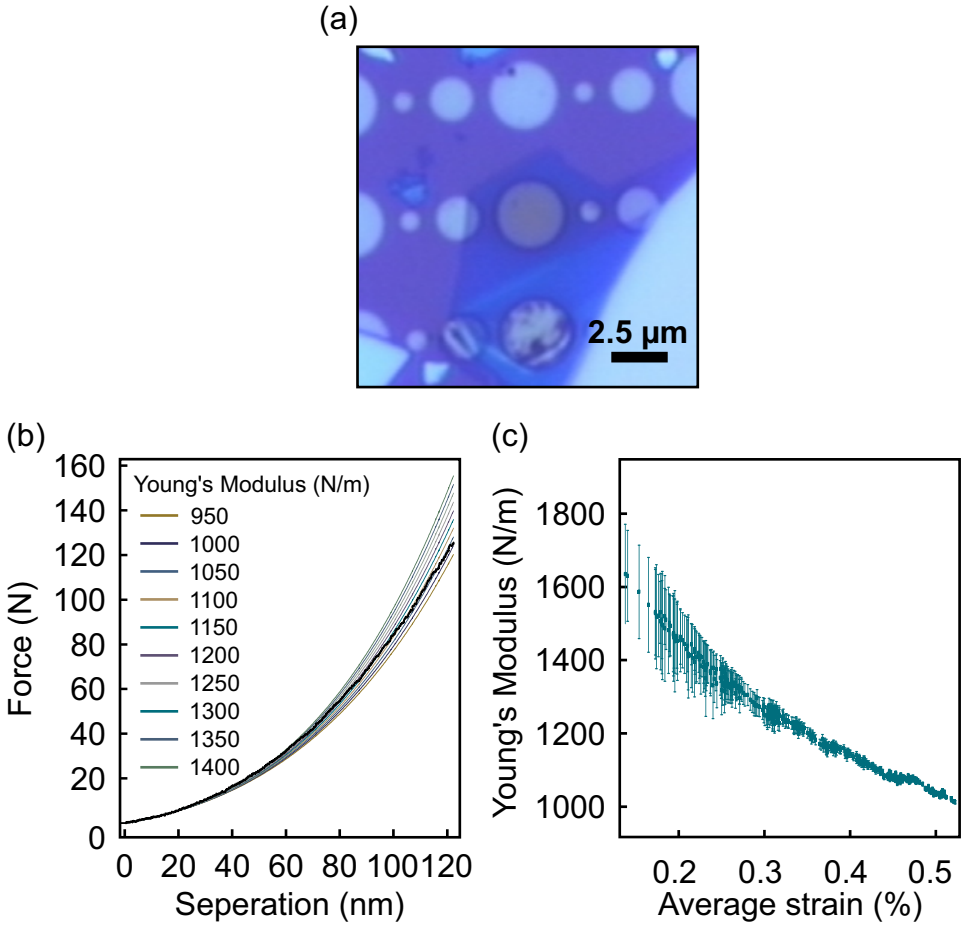

Figure C.18: (a) Optical micrograph of a trilayer molybdenum disulfide (MoS_2) flake exfoliated on a pre-structured Si^{++}/SiO_2 substrate. (b) Measured force as function of separation of a MoS_2 membrane with a diameter of 6 μm (black) and the corresponding simulated force-separation traces for a range of Young's moduli. (c) The extracted effective Young's modulus as function of average strain.

and a four-layer WSe_2 membrane with a diameter of 4 μm (see Figure C.19). The MoS_2 membrane shows a softening with a decrease of the effective E_{2d} of up to 40 % at an average strain around 0.5 % whereas the WSe_2 membrane initially slightly hardens. For larger average strain ($> 0.25\%$) the effective E_{2d} of the WSe_2 membrane is constant. Similar to the graphene membranes, overall the extracted effective Young's modulus of around 1500 N/m (MoS_2) and 1050 N/m (WSe_2) is significantly larger compared to the theoretical predictions of around 180 N/m per layer (MoS_2) [296] and around 170 N/m per layer (WSe_2) [297], which might be related similar to graphene to the out of plane fluctuations of two-dimensional membranes.

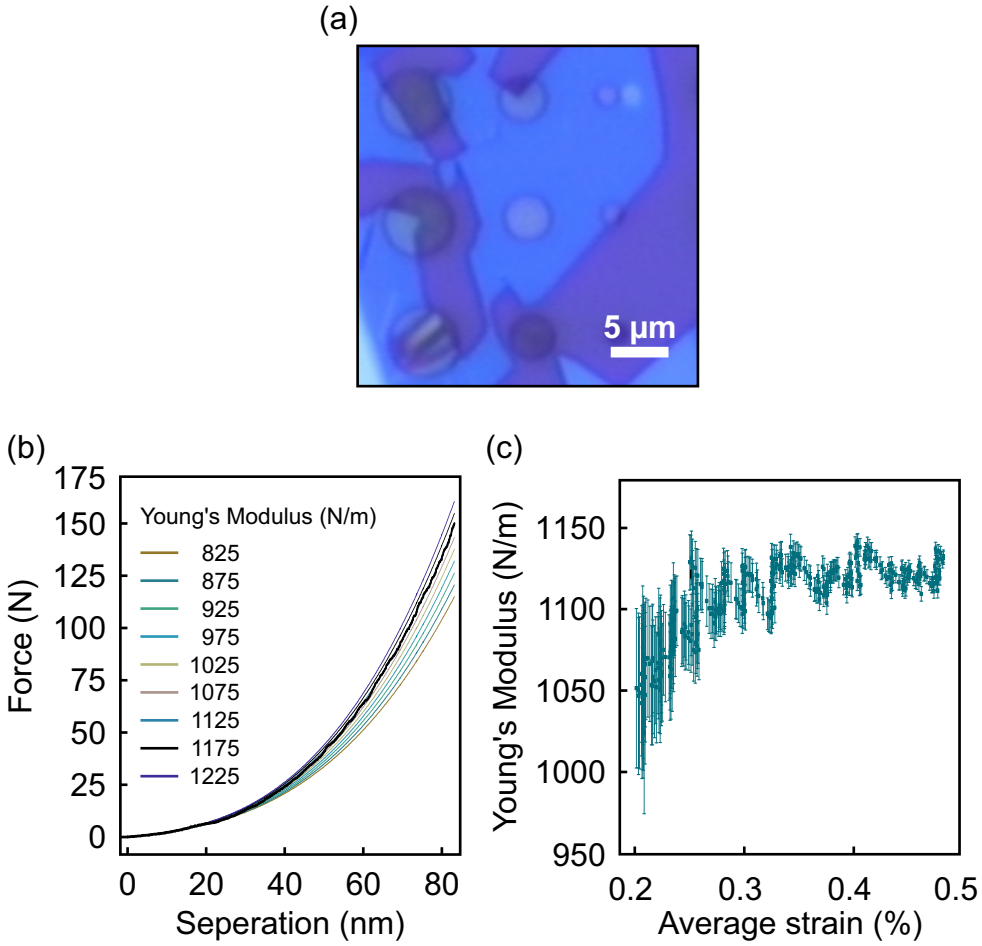

Figure C.19: (a) Optical micrograph of a four-layer tungsten diselenide (WSe_2) flake exfoliated on a pre-structured Si^{++}/SiO_2 substrate. (b) Measured force as function of separation of a WSe_2 membrane with a diameter of 4 μm (black) and the corresponding simulated force-separation traces for a range of Young's moduli. (c) The extracted effective Young's modulus as function of average strain.

C.4 Conclusion

In summary, we present the fabrication and basic device characterization of two dimensional membranes yielding a high homogeneity and perform nano-indentation experiments. Investigating the measurements with the generally accepted standard analysis derived from linear membrane theory yields elastic parameters as Young's modulus and pre-stress in good agreement with other studies [22, 273–275]. A closer investigation of the low and medium indentation regime shows a significant deviation of up to 40 % compared the standard analysis. A non-linear simulation of the indentation experiment using the non-linear Föppl-von Kármán equations offers the possibility to investigate the dependency of the effective Young's modulus to the applied strain. As has been recently shown by other groups [275, 281, 283]

for single-layer graphene we see an increase of the effective Young's modulus with increasing average strain indicating that intrinsic rippling softens the membrane. For low average strain values bilayer graphene shows a similar behavior as single-layer graphene. In contrast, for higher average strain values we see the decrease of the effective Young's modulus with increasing indentation as one would expect due to the softening of the carbon-carbon bonds with increasing strain. For MoS_2 and WSe_2 we observe similar effects. A trilayer MoS_2 membrane softens during the indentation whereas a four-layer WSe_2 membrane seems to be more prone for intrinsic rippling and hardens with applied strain.

D Process parameters

	Process details	
EBL markers (all wafer types)	1. Cleaning the wafer	a) 2 min. acetone, 1 min. ispropanol. b) blow dry with N_2.
	2. Coat with resist	a) prebake wafer at 170 °C for 5 min. b) spin first layer: AR-P 649.04 PMMA 200K, at 6000 rpm for 30 s, bake at 170 °C for 5 min. c) spin second layer: AR-P 669.04 PMMA 600K, at 6000 rpm for 30 s, bake at 170 °C for 10 min.
	3. Ebeam exposure	write marker scheme: dose of 460 μC/cm^2, beam current of 5 nA, beam step size of 12.5 nm, accelerating voltage of 50 kV.
	4. Development	60 s AR-600-55 developer, 30 s isopropanol, blow dry with N_2.
Marker evaporation (all wafer types)	1. Metal evaporation	5 nm Cr in 0.1 nm/s, 50 nm Au in 0.2 nm/s
	2. Lift off	15 min. in acetone until metal starts to lift, blow acetone with pipette and use ultra sound (US) (up to maximum power) until gold is removed
	3. Cleaning the wafer	a) 2 min. in acetone in US at maximum. b) 2 min. in isopropanol in US at maximum. c) blow dry with N_2.
Dicing wafer (all wafer types)	1. Protection resist	AZ-5214, at 4000 rpm for 30 s, bake for 3 min at 80°.
	2. Dicing	dice into 7x7 mm^2 dies (also called "chips")
Preparing the PVA/PMMA stack	1. Cleaning the Si wafer	a) 2 min. in acetone in US at maximum. b) 2 min. in isopropanol in US at maximum. c) blow dry with N_2.
	2. Coat with resist	a) prebake wafer at 110 °C for 5 min. b) spin first layer: 4 % PVA (polyvinylalcohol), at 3000 rpm for 30 s, bake at 110 °C for 2 min. c) spin second layer: AR-P 679.04 PMMA 950K, at 3000 rpm for 30 s, bake at 110 °C for 10 min.
	3. "Dicing"	Cut the wafer into appropriate pieces using a diamond scriber (c.f. figure 4.1).

	Process details	
Exfoliation of graphene, hBN or MoS_2	1. Cleaning the chips (only for Si^{++}/SiO_2)	a) 5 min. in acetone in US at max. power. b) 2 min in isopropanol in US at max. power. c) 5 min plasma ashing (O_2) at 600 W.
	2. Exfoliation	perform exfoliation according to section 4.2 right after plasma ashing (Si^{++}/SiO_2) or spin coating (PVA/PMMA stack)
Etching of graphene on hBN (PMMA mask)	2. Coat with resist	a) prebake the chip at 170 °C for 5 min. b) spin coat AR-P 649.04 PMMA 200K, at 6000 rpm for 30 s, bake at 170 °C for 15 min.
	3. Ebeam exposure	write etch mask: dose of 220 $\mu C/cm^2$, a beam current of 100 pA, beam step size of 1 nm, accelerating voltage of 50 kV.
	4. Development	60 s AR-600-55, 30 s isopropanol, blow dry with N_2.
	5. Reactive ion etching (RIE, Aachen)	a) without sample in chamber: O_2 flow 20 sscm, Ar flow rate 20 sscm, electrode power 300 W, pressure 0.025 mbar, time 15 min. b) with sample in chamber: O_2 flow 8 sscm, Ar flow rate 32 sscm, electrode power 60 W, pressure 0.025 mbar, time 8 s.
	6. Cleaning the samples	15 min. acetone, 30 min. DMSO (at 60 °C), 15 min. acetone, 5 min. isopropanol, blow dry with N_2.

	Process details	
Etching of hBN/graphene /hBN constrictions (metal hardmask)	1. Coat with resist	a) prebake chip at 170 °C for 5 min. b) spin coat AR-P 639.04 PMMA 50K, at 6000 rpm for 30 s, bake at 170 °C for 15 min. b) spin coat AR-P 679.04 PMMA 950K, at 6000 rpm for 30 s, bake at 170 °C for 15 min.
	3. Ebeam exposure	write etch mask: dose of 220 μC/cm^2, a beam current of 100 pA, beam step size of 1 nm, accelerating voltage of 50 kV.
	4. Development	60 s AR-600-55, 30 s isopropanol, blow dry with N_2.
	5. Metal evaportion	20 nm Al or Cr in 0.1 nm/sec.
	6. Lift off	15 min. in acetone until metal starts to lift, blow acetone with pipette until gold is removed.
	7. Cleaning the samples	5 min. acetone, 2 min. isopropanol, blow dry with N_2.
	8. Reactive ion etching (RIE Aachen)	a) without sample in chamber: O_2 flow 20 sscm, Ar flow rate 20 sscm, electrode power 300 W, pressure 3 Pa, time 15 min. b) with sample in chamber: O_2 flow 4 sccm, CHF_3 flow 40 sccm, electrode power 20 W, pressure of 3 Pa, time 30 s (etching rate 0.5 nm/s).
	9. Remove metal hardmask	a) Cr: rinse 30 s in chrome etch (MicroChemicals), Al: rinse 3 min in a solution of 2% tetramethylammonium hydroxide/98% DI water (e. g. AZ 326 MIF). b) rinse 10 min. in DI water (pre-clean basin) and 15 min. in (pure basin). c) rinse 5 min. isopropanol, blow dry with N_2.

	Process details	
Etching of MoS_2 heterostructures (metal hardmask)	1. Coat with resist	a) prebake chip at 170 °C for 5 min. b) spin coat AR-P 639.04 PMMA 50K, at 6000 rpm for 30 s, bake at 170 °C for 15 min. b) spin coat AR-P 679.04 PMMA 950K, at 6000 rpm for 30 s, bake at 170 °C for 15 min.
	3. Ebeam exposure	write etch mask: dose of 160 $\mu C/cm^2$, a beam current of 10 nA, beam step size of 5 nm, accelerating voltage of 20 kV.
	4. Development	60 s AR-600-55, 30 s isopropanol, blow dry with N_2
	5. Metal evaportion	20 nm Al or Cr in 0.1 nm/s.
	6. Lift off	15 min. in acetone until metal starts to lift, blow acetone with pipette until gold is removed.
	7. Cleaning the samples	5 min. acetone, 2 min. isopropanol, blow dry with N_2.
	8. Reactive ion etching (RIE Aachen)	a) without sample in chamber: O_2 flow 20 sscm, Ar flow rate 20 sscm, electrode power 300 W, pressure 3 Pa, time 15 min. b) with sample in chamber: O_2 flow 8 sscm, Ar flow rate 32 sscm, electrode power 60 W, pressure 3 Pa, time 45 s.
	9. Remove metal hardmask	a) Cr: rinse 30 s in chrome etch (MicroChemicals), Al: rinse 3 min in a solution of 2% tetramethylammonium hydroxide/98% DI water (e. g. AZ 326 MIF) b) rinse 10 min. in DI water (pre-clean basin) and 15 min. in (pure basin) c) rinse 5 min. isopropanol, blow dry with N_2.

	Process details	
Etching of holes into hBN (metal hardmask)	1. Coat with resist	a) prebake chip at 170 °C for 5 min. b) spin coat AR-P 639.04 PMMA 50K, at 4000 rpm for 30 s, bake at 170 °C for 15 min. b) spin coat AR-P 679.04 PMMA 950K, at 6000 rpm for 30 s, bake at 170 °C for 15 min.
	3. Ebeam exposure	write etch mask: dose of 260 μC/cm^2, a beam current of 100 nA, beam step size of 1.5 nm, accelerating voltage of 50 kV.
	4. Development	60 s AR-600-55, 30 s isopropanol, blow dry with N_2
	5. Metal evaportion	20 nm Al or Cr in 0.1 nm/s.
	6. Lift off	15 min. in acetone until metal starts to lift, blow acetone with pipette until gold is removed.
	7. Cleaning the samples	5 min. acetone, 2 min. isopropanol, blow dry with N_2.
	8. Reactive ion etching (RIE Aachen)	a) without sample in chamber: O_2 flow 20 sscm, Ar flow rate 20 sscm, electrode power 300 W, pressure 3 Pa, time 15 min. b) with sample in chamber: O_2 flow 5 sscm, Ar flow rate 5 sscm, SF_6 flow 20 sccm, electrode power 60 W, pressure 3 Pa, time 30 s.
	9. Remove metal hardmask	a) Cr: rinse 30 s in chrome etch (MicroChemicals), Al: rinse 3 min in a solution of 2% tetramethylammonium hydroxide/98% DI water (e. g. AZ 326 MIF) b) rinse 10 min. in DI water (pre-clean basin) and 15 min. in (pure basin) c) rinse 5 min. isopropanol, blow dry with N_2.

	Process details	
EBL contacts (Jülich)	1. Clean sample	a) 2 min. acetone, 1 min. ispropanol. b) blow dry with N_2.
	2. Coat with resist	a) prebake sample at 170 °C for 5 min. b) spin first layer: ARP 649.04 PMMA 200K, at 6000 rpm for 30 s, bake at 170 °C for 15 min. c) spin second layer: ARP 669.04 PMMA 600K, at 6000 rpm for 30 s, bake at 170 °C for 15 min.
	3. Ebeam exposure	a) small contacts: dose 450 μC/cm^2, beam current 100 pA and beam step size 1 nm (50 μm around the sample) at an accelerating voltage of 50 kV. b) medium contacts: dose of 400 μC/cm^2, beam current of 5 nA, beam step size of 12.5 nm (250 μm around the sample), accelerating voltage of 50 kV. c) large contacts and bond pads: dose of 300 μC/cm^2, beam current of 150 nA, beam step size of 50 nm, accelerating voltage of 50 kV.
	4. Development	60 s AR-600-55 developer, 30 s isopropanol, blow dry with N_2
EBL contacts (Aachen)	1. Clean sample	a) 2 min. acetone, 1 min. isopropanol. b) blow dry with N_2.
	2. Coat with resist	a) prebake sample at 170 °C for 5 min. b) spin first layer: ARP 639.04 PMMA 50K, at 6000 rpm for 30 s, bake at 170 °C for 5 min. c) spin second layer: ARP 679.04 PMMA 950K, at 6000 rpm for 30 s, bake at 170 °C for 5 min.
	3. Ebeam exposure	a) small contacts: dose 120 μC/cm^2, beam step size 5 nm, beam current 10 pA, accelerating voltage of 20 kV, aperture 7.5 μm, writing field size 350 μm (50 μm around the sample) b) large contacts and bond pads: dose 120 μC/cm^2, beam step size 60 nm, beam current 3.7 nA, accelerating voltage of 20 kV, aperture 120 μm, writing field size 2000 μm
	4. Development	60 s. AR-600-55 developer, 30 s isopropanol, blow dry with N_2
Contact evaporation	1. Metal evaporation	5 nm Cr in 0.1 nm/s, 50-100 nm Au in 0.2 nm/s.
	2. Lift off	15 min. in acetone until metal starts to lift, blow acetone with pipette until gold is removed.
	3. Cleaning the sample	2 min. in acetone, 1 min. in isopropanol, blow dry with N_2.

	Process details	
Local gates on Si/SiO_2	1. Clean sample	a) 2 min. acetone, 1 min. ispropanol. b) blow dry with N_2.
	2. Coat with resist	a) prebake sample at 170 °C for 5 min. b) spin first layer: ARP 639.04 PMMA 50K, at 6000 rpm for 30 s, bake at 170 °C for 15 min. c) spin second layer: ARP 679.04 PMMA 950K, at 6000 rpm for 30 s, bake at 170 °C for 15 min.
	3. Ebeam exposure	small contacts: dose 450 $\mu C/cm^2$, beam current 100 pA and beam step size 1 nm (50 μm around the sample) at an accelerating voltage of 50 kV.
	4. Development	60 s AR-600-55 developer, 30 s isopropanol, blow dry with N_2
	5. Metal evaporation	5 nm Ti in 0.1 nm/s, 50 nm Au in 0.2 nm/s.
	6. Lift off	15 min. in acetone until metal starts to lift, blow acetone with pipette until gold is removed.
	7. Cleaning the sample	2 min. in acetone, 1 min. in isopropanol, blow dry with N_2.
Chrome oxide on local gates	1. Clean sample	a) 2 min. acetone, 1 min. isopropanol. b) blow dry with N_2.
	2. Coat with resist	a) prebake sample at 170 °C for 5 min. b) spin first layer: ARP 639.04 PMMA 50K, at 6000 rpm for 30 s, bake at 170 °C for 5 min. c) spin second layer: ARP 679.04 PMMA 950K, at 6000 rpm for 30 s, bake at 170 °C for 5 min.
	3. Ebeam exposure	large contacts and bond pads: dose 120 $\mu C/cm^2$, beam step size 60 nm, beam current 3.7 nA, accelerating voltage of 50 kV, aperture 120 μm, writing field size 2000 μm
	4. Development	60 s. AR-600-55 developer, 30 s isopropanol, blow dry with N_2
	5. Metal evaporation	5 nm Cr in 0.1 nm/s.
	6. Lift off	15 min. in acetone until metal starts to lift, blow acetone with pipette until gold is removed.
	7. Cleaning the sample	2 min. in acetone, 1 min. in isopropanol, blow dry with N_2.
	8. Annealing	O_2 flow 200 sccm, 350 °C for 5 h.

E List of samples

The following tables show images and state the most important information of the devices investigated by transport measurements conducted within this thesis.

Name	Image	Device info	Measurement
Alex 122	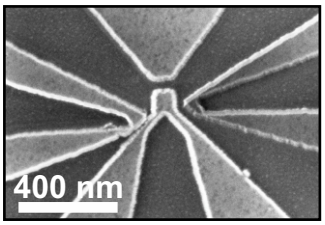	- hBN/SLG/hBN quantum dot - dot diameter: 100 nm - etching: Ar/SF_6 using an Al hard mask - contacts: Cr/Au	- Quantum dot measurements (chapter 5)
Alex 108	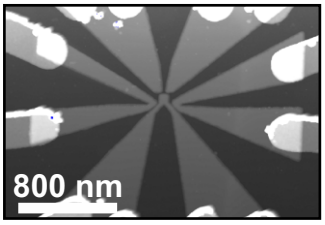	- hBN/SLG/hBN quantum dot - dot diameter: 100 nm - etching: Ar/SF_6 using an Al hard mask - contacts: Cr/Au	- Quantum dot measurements (chapter 5)
Alex6 73	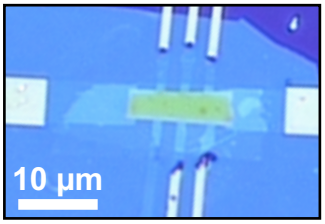	- hBN/five layer MoS_2/hBN Hall bar - etching: Ar/O_2 using a PMMA mask - contacts: Ti/Au/FLG	- Transport characterization before and after photodoping (chapter 6)
Alex6 86	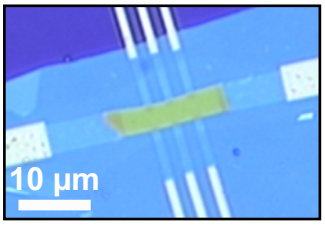	- hBN/trilayer MoS_2/hBN Hall bar - etching: Ar/O_2 using a PMMA mask - contacts: Ti/Au/FLG	- Transport characterization before and after photodoping (chapter 6) - Weak localization measurements (chapter A)

Name	Image	Device info	Measurement
BB 130	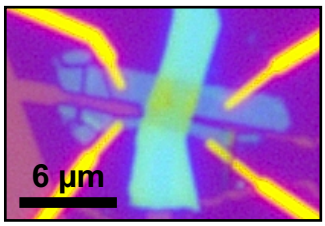	- SiO_2/five layer MoS_2/hBN flake - etching: Ar/O_2 using an Al mask - contacts: Ti/Au/FLG	- Measurements of "photodoping" on SiO_2 (chapter 7)
BT 72	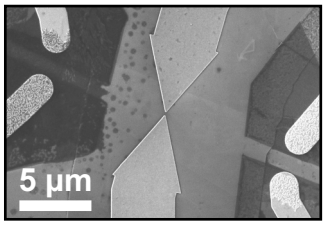	- hBN/ >five layer MoS_2/hBN constriction - constriction width: 150 nm - etching: Ar/O_2 using a PMMA mask - contacts: Ti/Au/FLG	- Quantum transport measurements (chapter 7)
BT 77	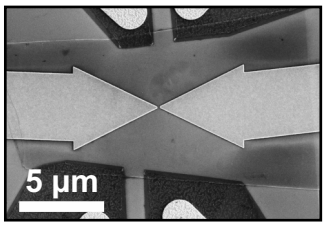	- hBN/trilayer MoS_2/hBN constriction - constriction width: 250 nm - etching: Ar/O_2 using a PMMA mask - contacts: Ti/Au/FLG	- Quantum transport measurements (chapter 7)
Alex6 109	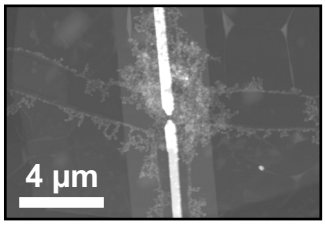	- hBN/bilayer MoS_2/hBN constriction - constriction width: 275 nm - etching: Ar/O_2 using a PMMA mask - contacts: Ti/Au/FLG	- Quantum transport measurements (chapter 7)

Name	Image	Device info	Measurement
Alex5 70	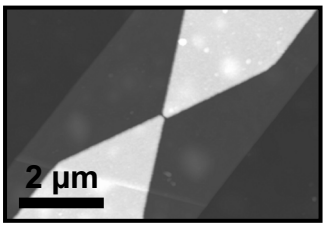	- hBN/bilayer MoS_2/hBN constriction - constriction width: 75 nm - etching: Ar/O_2 using a PMMA mask - contacts: Ti/Au	- Quantum transport measurements (chapter 7)
BD 29	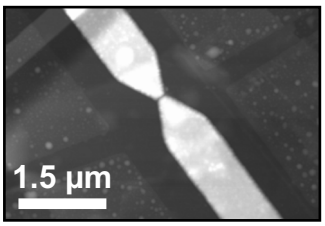	- hBN/seven layer MoS_2/hBN constriction - constriction width: 100 nm - etching: Ar/O_2 using an Al mask - contacts: Ti/Au/FLG	- Negative differential conductance measurements (chapter 8)
BB 129	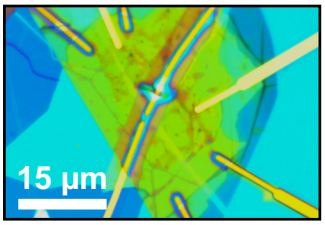	- hBN/four layer MoS_2/hBN constriction - constriction width: 250 nm - etching: Ar/O_2 using an Al mask - contacts: Ti/Au/FLG	- Fabrication of local FLG gate structures (chapter 9)
RFB 36	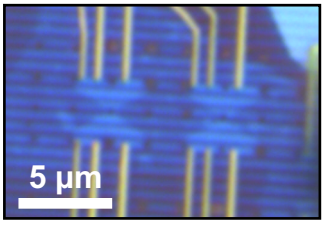	- hBN/SLG/hBN constriction with integrated membrane - constriction width: 450 nm - membrane diameter: 300 nm - etching: Ar/CHF_3 using an Al mask - contacts: Cr/Au	- Fabrication of graphene constrictions with integrated membranes (chapter 9)

Publications

Insulating state in low-disorder graphene nanoribbons
A. Epping*, C. Volk, F. Buckstegge, K. Watanabe, T. Taniguchi, and C. Stampfer*
Phys. Status Solidi B **256**, 1900269 (2019)

Gate-defined electron-hole double dots in bilayer graphene
L. Banszerus, B. Frohn, ***A. Epping****, D. Neumaier, K. Watanabe, T. Taniguchi, and C. Stampfer*
Nano Lett. **18**, 4785-4790 (2018)

Quantum transport through MoS_2 constrictions defined by photodoping
A. Epping*, L. Banszerus, J. Güttinger, L. Krückeberg, K. Watanabe, T. Taniguchi, F. Hassler, B. Beschoten, and C. Stampfer*
J. Phys.: Condens. Matter, **30**, 205001 (2018)

Aharonov-Bohm oscillations and magnetic focusing in ballistic graphene rings
J. Dauber, M. Oellers, F. Venn, ***A. Epping****, K. Watanabe, T. Taniguchi, F. Hassler, and C. Stampfer*
Phys. Rev. B **96**, 205407 (2017)

Identifying suitable substrates for high-quality graphene-based heterostructures
L. Banszerus, H. Janssen, M. Otto, ***A. Epping****, T. Taniguchi, K. Watanabe, B. Beschoten, D. Neumaier, and C. Stampfer*
2D Mater. **4**, 025030 (2017)

Chapter: Graphene Quantum dots,
C. Volk, C. Neumann, S. Engels, ***A. Epping****, and C. Stampfer*
Carbon Nanomaterials Sourcebook: Graphene, Fullerenes, Nanotubes, and Nanodiamonds, ed. K. D. Sattler, CRC Press (2016)

Limitations to carrier mobility and phase-coherent transport in bilayer graphene
S. Engels, B. Terrés, ***A. Epping****, T. Khodkov, K. Watanabe, T. Taniguchi, B. Beschoten, and C. Stampfer*
Phys. Rev. Lett. **113**, 126801 (2014)

Etched graphene single electron transistors on hexagonal boron nitride in high magnetic fields
A. Epping*, S. Engels, C. Volk, K. Watanabe, T. Taniguchi, S. Trellenkamp, and C. Stampfer*
Physica Status Solidi B **250**, 2692 (2013)

Etched graphene quantum dots on hexagonal boron nitride
S. Engels, ***A. Epping****, C. Volk, S. Korte, B. Voigtländer, K. Watanabe, T. Taniguchi, S. Trellenkamp, and C. Stampfer*
Appl. Phys. Lett **103**, 073113 (2013)

Dielectric screening of the Kohn anomaly of graphene on hexagonal boron nitride
F. Forster, A. Molina-Sanchez, S. Engels, ***A. Epping****, K. Watanabe, T. Taniguchi, L. Wirtz, and C. Stampfer*
Phys. Rev. B **88**, 085419 (2013)

Bibliography

[1] G. Moore, *Cramming more components onto integrated circuits*, Electronics **1**, 114 (1965).

[2] J. Cartwright, *Intel enters the third dimension*, Nature News **274** (2011).

[3] S. A. Wolf, D. D. Awschalom, R. A. Buhrman, J. M. Daughton, S. von Molnár, M. L. Roukes, A. Y. Chtchelkanova, and D. M. Treger, *Spintronics: a spin-based electronics vision for the future*, Science **294**, 1488 (2001).

[4] D. P. DiVincenzo, *Quantum computation*, Science **270**, 255 (1995).

[5] D. Loss and D. P. DiVincenzo, *Quantum computation with quantum dots*, Phys. Rev. A **57**, 1 (1998).

[6] R. Hanson, L. P. Kouwenhoven, J. R. Petta, S. Tarucha, and L. M. K. Vandersypen, *Spins in few-electron quantum dots*, Rev. Mod. Phys. **79**, 1217 (2007).

[7] F. A. Zwanenburg, A. S. Dzurak, A. Morello, M. Y. Simmons, L. C. L. Hollenberg, G. Klimeck, S. Rogge, S. N. Coppersmith, and M. A. Eriksson, *Silicon quantum electronics*, Rev. Mod. Phys. **85**, 961 (2013).

[8] M. J. Manfra, *Molecular beam epitaxy of ultra-high-quality AlGaAs/GaAs heterostructures: enabling physics in low-dimensional electronic systems*, Annu. Rev. Condens. Matter Phys. **5**, 347 (2014).

[9] R. Petta, A. C. Johnson, J. M. Taylor, E. A. Laird, A. Yacoby, M. D. Lukin, C. M. Marcus, M. P. Hanson, and A. C. Gossard, *Coherent manipulation of coupled electron spins in semiconductor quantum dots*, Science **309**, 2180 (2005).

[10] H. Bluhm, S. Foletti, I. Neder, M. Rudner, D. Mahalu, V. Umansky, and A. Yacoby, *Dephasing time of GaAs electron-spin qubits coupled to a nuclear bath exceeding 200μs*, Nat. Phys. **7**, 109 (2011).

[11] J. P. Kestner, Xin Wang, Lev S. Bishop, Edwin Barnes, and S. Das Sarma, *Noise-resistant control for a spin qubit array*, Phys. Rev. Lett. **110**, 140502 (2013).

[12] F. Setiawan, H.-Y. Hui, J. P. Kestner, X. Wang, and S. Das Sarma, *Robust two-qubit gates for exchange-coupled qubits*, Phys. Rev. B **89**, 085314 (2014).

[13] T. Botzem, R. P. G. McNeil, J.-M. Mol, D. Schuh, D. Bougeard, and H. Bluhm, *Quadrupolar and anisotropy effects on dephasing in two-electron spin qubits in GaAs*, Nat. Commun. **7**, 11170 (2016).

[14] D. M. Zajac, A. J. Sigillito, M. Russ, F. Borjans, J. M. Taylor, G. Burkard, J. R. Petta, *Resonantly driven CNOT gate for electron spins*, Science **359**, 439 (2018).

[15] T. F. Watson, S. G. J. Philips, E. Kawakami, D. R. Ward, P. Scarlino, M. Veldhorst, D. E. Savage, M. G. Lagally, M. Friesen, S. N. Coppersmith, M. A. Eriksson, and L. M. K. Vandersypen, *A programmable two-qubit quantum processor in silicon*, Nature **555**, 633 (2018).

[16] D. Castelvecchi, *Silicon gains ground in quantum-computing race*, Nature **553**, 136 (2018).

[17] K. S. Novoselov, A. K. Geim, S. V. Morozov, D. Jiang, Y. Zhang, S. V. Dubonos, I. V. Grigorieva, and A. A. Firsov, *Electric field effect in atomically thin carbon films*, Science **306**, 666 (2004).

[18] A. H. Castro Neto, F. Guinea, N. M. R. Peres, K. S. Novoselov, and A. K. Geim, *The electronic properties of graphene*, Rev. Mod. Phys. **81**, 109 (2009).

[19] L. Banszerus, T. Sohier, A. Epping, F. Winkler, F. Libisch, F. Haupt, K. Watanabe, T. Taniguchi, K. Müller-Caspary, N. Marzari, F. Mauri, B. Beschoten, and C. Stampfer, *Extraordinary high room-temperature carrier mobility in graphene-wse$_2$ heterostructures*, arXiv:1909.09523 (2019).

[20] G. Fiori, F. Bonaccorso, G. Iannaccone, T. Palacios, D. Neumaier, A. Seabaugh, S. K. Banerjee, and L. Colombo, *Electronics based on two-dimensional materials*, Nat. Nanotechnol. **9**, 768 (2014).

[21] M. Wang and E.-H. Yang, *THz applications of 2D materials: graphene and beyond*, Nano-Structures and Nano-Objects (2017).

[22] C. Lee, X. Wei, J. W. Kysar, and J. Hone, *Measurement of the elastic properties and intrinsic strength of monolayer graphene*, Science **321**, 385 (2008).

[23] H. Jang, Y. J. Park, X. Chen, T. Das, M.-S. Kim, and J.-H. Ahn, *Graphene-based flexible and stretchable electronics*, Adv. Mater. **28**, 4184 (2016).

[24] F. Sols, F. Guinea, and A. H. C. Neto, *Coulomb blockade in graphene nanoribbons*, Phys. Rev. Lett. **99**, 166803 (2007).

[25] L. A. Ponomarenko, F. Schedin, M. I. Katsnelson, R. Yang, E. W. Hill, K. S. Novoselov, and A. K. Geim, *Chaotic Dirac billiard in graphene quantum dots*, Science **320**, 356 (2008).

[26] D. Huertas-Hernando, F. Guinea, and A. Brataas, *Spin-orbit coupling in curved graphene, fullerenes, nanotubes, and nanotube caps*, Phys. Rev. B **74**, 155426 (2006).

[27] H. Min, E. J. Hill, N. A. Sinitsyn, B. R. Sahu, L. Kleinman, and A. H. MacDonald, *Intrinsic and Rashba spin-orbit interactions in graphene sheets*, Phys. Rev. B **74**, 165310 (2006).

[28] B. Trauzettel, D. V. Bulaev, D. Loss, and G. Burkard, *Spin qubits in graphene quantum dots*, Nat. Phys. **3**, 192 (2007).

[29] M. I. Katsnelson, K. S. Novoselov, and A. K. Geim, *Chiral tunnelling and the Klein paradox in graphene*, Nat. Phys. **2**, 620 (2006).

[30] M. Y. Han, B. Özyilmaz, Y. Zhang, and P. Kim, *Energy band-gap engineering of graphene nanoribbons*, Phys. Rev. Lett. **98**, 206805 (2007).

[31] C. Stampfer, E. Schurtenberger, F. Molitor, J. Güttinger, T. Ihn, and K. Ensslin, *Tunable graphene single electron transistor*, Nano Lett. **8**, 2378 (2008).

[32] X. Liu, J. B. Oostinga, A. F. Morpurgo, and L. M. K. Vandersypen, *Electrostatic confinement of electrons in graphene nanoribbons*, Phys. Rev. B **80**, 121407 (2009).

[33] K. Todd, H.-T. Chou, S. Amasha, and D. Goldhaber-Gordon, *Quantum dot behavior in graphene nanoconstrictions*, Nano Lett. **9**, 416 (2009).

[34] J. Güttinger, C. Stampfer, F. Libisch, T. Frey, J. Burgdörfer, T. Ihn, and K. Ensslin, *Electron-hole crossover in graphene quantum dots*, Phys. Rev. Lett. **103**, 046810 (2009).

[35] J. Güttinger, T. Frey, C. Stampfer, T. Ihn, and K. Ensslin, *Spin states in graphene quantum dots*, Phys. Rev. Lett. **105**, 116801 (2010).

[36] C. Volk, C. Neumann, S. Kazarski, S. Fringes, S. Engels, F. Haupt, A. Müller and C. Stampfer, *Probing relaxation times in graphene quantum dots*, Nat. Commun. **4**, 1753 (2013).

[37] D. Bischoff, M. Eich, O. Zilberberg, C. Rössler, T. Ihn, and K. Ensslin, *Measurement back-action in stacked graphene quantum dots*, Nano Lett. **15**, 6003 (2015).

[38] C. R. Dean, A. F. Young, I. Meric, C. Lee, L. Wang, S. Sorgenfrei,K. Watanabe, T. Taniguchi, P. Kim, K. L. Shepard, and J. Hone, *Boron nitride substrates for high-quality graphene electronics*, Nat. Nanotechnol. **5**, 722 (2010).

[39] J. Xue, J. Sanchez-Yamagishi, D. Bulmash, P. Jacquod, A. Deshpande, K. Watanabe, T. Taniguchi, P. Jarillo-Herrero, and B. J. LeRoy, *Scanning tunnelling microscopy and spectroscopy of ultra-flat graphene on hexagonal boron nitride*, Nat Mater. **10**, 282 (2011).

[40] L. Wang, I. Meric, P. Y. Huang, Q. Gao, Y. Gao, H. Tran, T. Taniguchi, K. Watanabe, L. M. Campos, D. A. Muller, J. Guo, P. Kim, J. Hone, K. L. Shepard, and C. R. Dean, *One-dimensional electrical contact to a two-dimensional material*, Science **342**, 614 (2013).

[41] G.-H. Lee, G.-H. Park and H.-J. Lee, *Observation of negative refraction of Dirac fermions in graphene*, Nat. Phys. **11**, 925 (2015).

[42] I.V. Borzenets, F. Amet, C.T. Ke, A.W. Draelos, M.T. Wei, A. Seredinski, K. Watanabe, T. Taniguchi, Y. Bomze, M. Yamamoto, S. Tarucha, and G. Finkelstein, *Ballistic graphene Josephson junctions from the short to the long junction regimes*, Phys. Rev. Lett. **117**, 237002 (2016).

[43] S. Engels, A. Epping, C. Volk, S. Korte, B. Voigtländer, K. Watanabe, T. Taniguchi, S. Trellenkamp, and C. Stampfer, *Etched graphene quantum dots on hexagonal boron nitride*, Appl. Phys. Lett. **103**, 073113 (2013).

[44] O. Herrmann, C. Gould, and L. W. Molenkamp, *Coulomb-blockade peak spacing statistics of graphene quantum dots on SiO_2*, J. Appl. Phys. **120**, 164304 (2016).

[45] J. M. Pereira, P. Vasilopoulos, and F. M. Peeters, *Tunable quantum dots in bilayer graphene*, Nano Lett. **7**, 946 (2007).

[46] T. Taychatanapat and P. Jarillo-Herrero, *Electronic transport in dual-gated bilayer graphene at large displacement fields*, Phys. Rev. Lett. **105**, 166601 (2010).

[47] M. T. Allen, J. Martin, and A. Yacoby, *Gate-defined quantum confinement in suspended bilayer graphene*, Nat. Commun. **3**, 934 (2012).

[48] A. (Stijn) M. Goossens, S. C. M. Driessen, T. A. Baart, K. Watanabe, T. Taniguchi, and L. M. K. Vandersypen, *Gate-defined confinement in bilayer graphene-hexagonal boron nitride hybrid devices*, Nano Lett. **12**, 4656 (2012).

[49] H. Overweg, H. Eggimann, X. Chen, S. Slizovskiy, M. Eich, R. Pisoni , Y. Lee, P. Rickhaus, K. Watanabe , T. Taniguchi, V. Falko, T. Ihn, and K.

Ensslin, *Electrostatically induced quantum point contacts in bilayer graphene*, Nano Lett. **18**, 553 (2018).

[50] H. Overweg, P. Rickhaus, M. Eich, Y. Lee, R. Pisoni, K. Watanabe, T. Taniguchi, T. Ihn, and K. Ensslin, *Edge channel confinement in a bilayer graphene n-p-n quantum dot*, New J. Phys. **20**, 013013 (2018).

[51] M. Eich, F. Herman, R. Pisoni, H. Overweg, Y. Lee, P. Rickhaus, K. Watanabe, T. Taniguchi, M. Sigrist, T. Ihn, and K. Ensslin, *Spin and valley states in gate-defined bilayer graphene quantum dots*, Phys. Rev. X **8**, 031023 (2018).

[52] L. Banszerus, B. Frohn, A. Epping, D. Neumaier, K. Watanabe, T. Taniguchi, and C. Stampfer, *Gate-defined electron-hole double dots in bilayer graphene*, Nano Lett. **18**, 4785 (2018).

[53] K. F. Mak, C. Lee, J. Hone, J. Shan, and T. F. Heinz., *Atomically thin MoS_2: a new direct-gap semiconductor*, Phys. Rev. Lett. **105**, 136805 (2010).

[54] D. Lloyd, X. Liu, J. W. Christopher, L. Cantley, A. Wadehra, B. L. Kim, B. B. Goldberg, A. K. Swan, and J. S. Bunch, *Band gap engineering with ultralarge biaxial strains in suspended monolayer MoS_2*, Nano Lett. **16**, 5836 (2016).

[55] F. Schwierz, *Graphene transistors*, Nat. Nanotechnol. **5**, 487 (2010).

[56] S. Fathipour, and H.-M. Li, and M. Remškar, and L. Yeh, and W. Tsai, and Y. Lin, and S. Fullerton-Shirey, and A. Seabaugh, *Record high current density and low contact resistance in mos_2 fets by ion doping*, Proceedings of the 2016 International Symposium on VLSI Technology, Systems and Application (VLSI-TSA) pp. 1–2 (2016).

[57] B. Radisavljevic, A.Radenovic, J.Brivio, V. Giacometti and A. Kis, *Single-layer MoS_2 transistors*, Nat. Nanotechnol. **6**, 147 (2011).

[58] D. Kufer, and I. Nikitskiy, and T. Lasanta, and G. Navickaite, and F. H. L. Koppens, and G. Konstantatos, *Hybrid 2d-0d mos_2-pbs quantum dot photodetectors*, Adv. Mater. **27**, 176 (2015).

[59] N. Huo, and G. Konstantatos, *Ultrasensitive all-2d mos_2 phototransistors enabled by an out-of-plane mos_2 pn homojunction*, Nat. Commun. **8**, 572 (2017).

[60] Y. J. Zhang, T. Oka, R. Suzuki, J. T. Ye, and Y. Iwasa, *Electrically switchable chiral light-emitting transistor*, Science **344**, 725 (2014).

[61] A. Kormányos,V. Zólyomi, N. D. Drummond, and G. Burkard, *Spin-orbit coupling, quantum dots, and qubits in monolayer transition metal dichalcogenides*, Phys. Rev. X **4**, 011034 (2014).

[62] X. Cui, G.-H. Lee, Y. D. Kim, G. Arefe, P. Y. Huang, C.-H. Lee, D. A. Chenet, X. Zhang, L. Wang, F. Ye, F. Pizzocchero, B. S. Jessen, K. Watanabe, T. Taniguchi, D. A. Muller, T. Low, P. Kim, and J. Hone, *Multi-terminal transport measurements of Mo using a van der Waals heterostructure device platform*, Nat. Nanotechnol. **10**, 534 (2015).

[63] Z. Wu, S. Xu, H. Lu, A. Khamoshi, G.-B. Liu, T. Han, Y. Wu, J. Lin, G. Long, Y. He, Y. Cai, Y. Yao, F. Zhang, and N. Wang, *Even-odd layer-dependent magnetotransport of high-mobility Q-valley electrons in transition metal disulfides*, Nat. Commun. **7**, 12955 (2016).

[64] R. Pisoni, Y. Lee, H. Overweg, M. Eich, P. Simonet, K. Watanabe, T. Taniguchi, R. Gorbachev, T. Ihn, and K. Ensslin, *Gate-defined one-dimensional channel and broken symmetry states in MoS_2 van der Waals heterostructures*, Nano Lett. **17**, 5008 (2017).

[65] X.-X. Song, D. Liu, V. Mosallanejad, J. You, T.-Y. Han, D.-T. Chen, H.-O. Li, G. Cao, M. Xiao,ab G.-C. Guo, and G.-P. Guo, *A gate defined quantum dot on the two-dimensional transition metal dichalcogenide semiconductor WSe_2*, Nanoscale **7**, 16867 (2015).

[66] K. Wang, K. De Greve, L. A. Jauregui, A. Sushko, A. High, Y. Zhou, G. Scuri, T. Taniguchi, K. Watanabe, M. D. Lukin, H. Park, and P. Kim, *Electrical control of charged carriers and excitons in atomically thin materials*, Nat. Nanotechnol. **13**, 128 (2018).

[67] L. Ju, J. Velasco Jr., E. Huang, S. Kahn, C. Nosiglia, H.-Z. Tsai, W. Yang, T. Taniguchi, K. Watanabe, Y. Zhang, G. Zhang, M. Crommie, A. Zettl and F. Wang, *Photoinduced doping in heterostructures of graphene and boron nitride*, Nat. Nanotechnol. **9**, 348 (2014).

[68] C. Neumann, L. Rizzi, S. Reichardt, B. Terrés, T. Khodkov, K. Watanabe, T. Taniguchi, B. Beschoten, and C. Stampfer, *Spatial control of laser-induced doping profiles in graphene on hexagonal boron nitride*, ACS Appl. Mater. **8**, 9377 (2016).

[69] N. M. R. Peres, *Colloquium: the transport properties of graphene: an introduction*, Rev. Mod. Phys. **82**, 2673 (2010).

[70] S. Das Sarma, S. Adam, E. H. Hwang, and E. Rossi, *Electronic transport in two-dimensional graphene*, Rev. Mod. Phys. **83**, 407 (2011).

[71] Q. H. Wang, K. Kalantar-Zadeh, A. Kis, J. N. Coleman, and M. S. Strano, *Electronics and optoelectronics of two-dimensional transition metal dichalcogenides*, Nat. Nanotechnol. **7**, 699 (2012).

[72] R. Ganatra and Q. Zhang, *Few-layer MoS_2: a promising layered semiconductor*, ACS Nano **8**, 4074 (2014).

[73] S. Manzeli, D. Ovchinnikov, D. Pasquier, O. V. Yazyev, and A. Kis, *2D transition metal dichalcogenides*, Nat. Rev. Mater. **2**, 17033 (2017).

[74] P. Wallace, *The band theory of graphite*, Phys. Rev. **71**, 622 (1947).

[75] A. K. Geim and K. Novoselov, *The rise of graphene*, Nature Materials **6**, 183 (2007).

[76] K. S. Novoselov, A. K. Geim, S. V. Morozov, D. Jiang, M. I. Katsnelson, I. V. Grigorieva, S. V. Dubonos, and A. A. Firsov, *Two-dimensional gas of massless Dirac fermions in graphene*, Nature **438**, 197 (2005).

[77] M. I. Katsnelson and K. S. Novoselov, *Graphene: new bridge between condensed matter physics and quantum electrodynamics*, Sol. Stat. Comm. **143**, 1 (2007).

[78] L. Banszerus, M. Schmitz, S. Engels, M. Goldsche, K. Watanabe, T. Taniguchi, B. Beschoten, and C. Stampfer, *Ballistic transport exceeding 28 ìm in CVD grown graphene*, Nano Lett. **16**, 1387 (2016).

[79] B. J. van Wees, H. van Houten, C. W. J. Beenakker, J. G. Williamson, L. P. Kouwenhoven, D. van der Marel and C. T. Foxon, *Quantized conductance of point contacts in a two dimensional electron gas*, Phys. Rev. Lett. **60**, 848 (1988).

[80] D. Goldhaber-Gordon, H. Shtrikman, D. Mahalu, D. Abusch-Magder, U. Meirav, and M. A. Kastner, *Kondo effect in a single-electron transistor*, Nature **391**, 156 (1998).

[81] R. A. Bromley, R. B. Murray, and A. D. Yoffe, *The band structures of some transition metal dichalcogenides. III. group VIA: trigonal prism materials*, J. Phys. C: Solid State Phys. **5**, 759 (1972).

[82] E. Cappelluti, R. Roldán, J. A. Silva-Guillén, P. Ordejón, and F. Guinea, *Tight-binding model and direct-gap/indirect-gap transition in single-layer and multilayer MoS_2*, Phys. Rev. B **88**, 075409 (2013).

[83] S. Fang, R. K. Defo, S. N. Shirodkar, S. Lieu, G. A. Tritsaris, and E. Kaxiras, *Ab initio tight-binding Hamiltonian for transition metal dichalcogenides*, Phys. Rev. B **92**, 205108 (2015).

[84] D. Xiao, G.-B. Liu, W. Feng, X. Xu, and W. Yao, *Coupled spin and valley physics in monolayers of MoS_2 and other group-VI sichalcogenides*, Phys. Rev. Lett. **108**, 196802 (2012).

[85] F. Zahid, L. Liu, Y. Zhu, J. Wang, and H. Guo, *A generic tight-binding model for monolayer, bilayer and bulk MoS_2*, AIP Adv. **3**, 052111 (2013).

[86] X. Li, J. T. Mullen, Z. Jin, K. M. Borysenko, M. B. Nardelli, and K. W. Kim, *Intrinsic electrical transport properties of monolayer silicene and MoS_2 from first principles*, Phys. Rev. B **87**, 115418 (2013).

[87] G.-B. Liu, W.-Y. Shan, Y. Yao, W. Yao, and D. Xiao, *Three-band tight-binding model for monolayers of group-VIB transition metal dichalcogenides*, Phys. Rev. B **88**, 085433 (2013).

[88] E. Ridolfi, D. Le, T. S. Rahman, E. R. Mucciolo, and C. H. Lewenkopf, *A tight-binding model for MoS_2 monolayers*, J. Phys.: Condens. Matter **27**, 365501 (2015).

[89] Z. Y. Zhu, Y. C. Cheng, and U. Schwingenschlögl, *Giant spin-orbit-induced spin splitting in two-dimensional transition-metal dichalcogenide semiconductors*, Phys. Rev. B **84**, 153402 (2011).

[90] A. Kuc, N. Zibouche, and T. Heine, *Influence of quantum confinement on the electronic structure of the transition metal sulfide TS_2*, Phys. Rev. B **83**, 245213 (2011).

[91] A. Kumara and P.K. Ahluwalia, *Electronic structure of transition metal dichalcogenides monolayers 1H-MX_2 (M = Mo, W; X = S, Se, Te) from ab-initio theory: new direct band gap semiconductors*, Eur. Phys. J. B **85**, 186 (2012).

[92] S. Ahmad and S. Mukherjee, *A comparative study of electronic properties of bulk MoS_2 and its monolayer using DFT technique: application of mechanical strain on MoS_2 monolayer*, Graphene **3**, 52 (2014).

[93] I. A. Rahman and A. Purqon, *First principles study of molybdenum disulfide electronic structure*, J. Phys.: Conf. Ser. **877**, 012026 (2017).

[94] W. S. Yun, S. W. Han, S. C. Hong, I. G. Kim, and J. D. Lee, *Thickness and strain effects on electronic structures of transition metal dichalcogenides: 2h-MX_2 semiconductors (M = Mo, W; X = S, Se, Te)*, Phys. Rev. B **85**, 033305 (2012).

[95] T. Cheiwchanchamnangij and W. R. L. Lambrecht, *Quasiparticle band structure calculation of monolayer, bilayer, and bulk MoS_2*, Phys. Rev. B **85**, 205302 (2012).

[96] D. Y. Qiu, F. H. da Jornada, nad S. G. Louie, *Optical spectrum of MoS_2: many-body effects and diversity of exciton states*, Phys. Rev. Lett. **111**, 216805 (2013).

[97] H. Shi, H. Pan, Y.-W. Zhang, and B. I. Yakobson, *Quasiparticle band structures and optical properties of strained monolayer MoS_2 and WS_2*, Phys. Rev. B **87**, 155304 (2013).

[98] L. F. Mattheiss, *Energy bands for 2H-$NbSe_2$ and 2H-MoS_2*, Phys. Rev. Lett. **30**, 784 (1973).

[99] Y. L. Huang, Y. Chen, W. Zhang, S. Y. Quek, C.-H. Chen, L.-J. Li, W.-T. Hsu, W.-H. Chang, Y. J. Zheng, W. Chen, and A. T.S. Wee, *Bandgap tunability at single-layer molybdenum disulphide grain boundaries*, Nat. Commun. **6**, 6298 (2014).

[100] C. Zhang, A. Johnson, C.-L. Hsu, L.-J. Li, and C.-K. Shih, *Direct imaging of band profile in single layer MoS_2 on graphite: quasiparticle energy gap, metallic edge states, and edge band bending*, Nano Lett. **14**, 2443 (2014).

[101] A. F. Rigosi, H. M. Hill, K. T. Rim, G. W. Flynn, and T. F. Heinz, *Electronic band gaps and exciton binding energies in monolayer Mo_x $W_{1-x}S_2$ transition metal dichalcogenide alloys probed by scanning tunneling and optical spectroscopy*, Phys. Rev. B **94**, 075440 (2016).

[102] A. Molina-Sanchez, D. Sangalli, K. Hummer, A. Marini, and L. Wirtz, *Effect of spin-orbit interaction on the optical spectra of singlelayer, double-layer, and bulk MoS_2*, Phys. Rev. B **88**, 045412 (2013).

[103] J. E. Padilha, H. Peelaers, A. Janotti, and C. G. Van de Walle, *Nature and evolution of the band-edge states in MoS_2: from monolayer to bulk*, Phys. Rev. B **90**, 205420 (2014).

[104] X. Fan, D. J. Singh, and W. Zheng, *Valence band splitting on multilayer MoS_2: mixing of spin-orbit coupling and interlayer coupling*, J. Phys. Chem. Lett **7**, 2175 (2016).

[105] B. Arnaud, S. Lebègue, P. Rabiller, and M. Alouani, *Huge excitonic effects in layered hexagonal boron nitride*, Phys. Rev. Lett. **96**, 026402 (2006).

[106] N. Lindvall, A. Kalabukhov, and A. Yurgens, *Cleaning graphene using atomic force microscope*, J. Appl. Phys. **111**, 064904 (2012).

[107] J. Yamaguchia, K. Hayashi, S. Satob, and N. Yokoyama, *Passivating chemical vapor deposited graphene with metal oxides for transfer and transistor fabrication processes*, Appl. Phys. Lett. **102**, 143505 (2013).

[108] N. J. Couto, D. Costanzo, S. Engels, D.-K. Ki, K. Watanabe, T. Taniguchi, C. Stampfer, F. Guinea, and A. F. Morpurgo, *Random strain fluctuations as dominant disorder source for high-quality on-substrate graphene devices*, Phys. Rev. X **4**, 041019 (2014).

[109] L. Museur, G. Brasse, A. Pierret, S. Maine, B. Attal-Tretout, F. Ducastelle, A. Loiseau, J. Barjon, K. Watanabe, T. Taniguchi, and A. Kanaev, *Exciton optical transitions in a hexagonal boron nitride single crystal*, Phys. Stat. Sol. RRL **5**, 214 (2011).

[110] A. F. Young, C. R. Dean, I. Meric, S. Sorgenfrei, H. Ren, K. Watanabe, T. Taniguchi, J. Hone, K. L. Shepard, and P. Kim, *Electronic compressibility of layer-polarized bilayer graphene*, Phys. Rev. B **85**, 235458 (2012).

[111] P. Kumar, Y. S. Chauhan, A. Agarwal, and S. Bhowmick, *Thickness and stacking dependent polarizability and dielectric constant of graphene-hexagonal boron nitride composite stacks*, J. Phys. Chem. C **120**, 17620 (2016).

[112] A. Laturia, M. L. Van de Put, and W. G. Vandenberghe, *Dielectric properties of hexagonal boron nitride and transition metal dichalcogenides: from monolayer to bulk*, NPJ 2D Mater Appl **2**, 6 (2018).

[113] X. Blase, A. Rubio, S. G. Louie, and M. L. Cohen, *Quasiparticle band structure of bulk hexagonal boron nitride and related systems*, Phys. Rev. B **51**, 6868 (1995).

[114] G. Cappellini, G. Satta, M. Palummo, and G. Onida, *Optical properties of BN in cubic and layered hexagonal phases*, Phys. Rev. B **64**, 035104 (2001).

[115] L. Banszerus, M. Schmitz, S. Engels, J. Dauber, M. Oellers, F. Haupt, K. Watanabe, T. Taniguchi, B. Beschoten, and C. Stampfer, *Ultrahigh-mobility graphene devices from chemical vapor deposition on reusable copper*, Sci. Adv. **1**, e1500222 (2015).

[116] C. W. J. Beenakker and H. Van Houten, *Quantum transport in semiconductor nanostructures*, Solid State Phys. **44**, 229 (1991).

[117] C. W. J. Beenakker, *Theory of coulomb-blockade oscillations in the conductance of a quantum dot*, Phys. Rev. B **44**, 1646 (1991).

[118] T. Ihn, *Semiconductor nanostructures - quantum states and electronic transport* (Oxford University Press, 2010).

[119] N. Tombros, A. Veligura, J. Junesch, M. H. D. Guimaraes, I. J. Vera Marun, H. T. Jonkman, and B. J. van Wees, *Quantized conductance of a suspended graphene nanoconstriction*, Nat. Phys. **7**, 697 (2011).

[120] B. Terrés, L. A. Chizhova, F. Libisch, J. Peiro, D. Jörger, S. Engels, A. Girschik, K. Watanabe, T. Taniguchi, S. V. Rotkin, J. Burgdörfer, and C. Stampfer, *Size quantization of Dirac fermions in graphene constrictions*, Nat. Commun. **7**, 11528 (2016).

[121] C. Stampfer, J. Güttinger, S. Hellmüller, F. Molitor, K. Ensslin, and T. Ihn, *Energy gaps in etched graphene nanoribbons*, Phys. Rev. Lett. **102**, 056403 (2009).

[122] P. Gallagher, K. Todd, and D. Goldhaber-Gordon, *Disorder-induced gap behavior in graphene nanoribbons*, Phys. Rev. B **81**, 115409 (2010).

[123] F. Molitor, S. Dröscher, J. Güttinger, A. Jacobsen, C. Stampfer, T. Ihn, and K. Ensslin, *Transport through graphene double dots*, Appl. Phys. Lett. **94**, 222107 (2009).

[124] S. Moriyama, D. Tsuya, E. Watanabe, S. Uji, M. Shimizu, T. Mori, T. Yamaguchi, and K. Ishibashi, *Coupled quantum dots in a graphene-based two-dimensional semimetal*, Nano Lett. **9**, 2891 (2009).

[125] X. L. Liu, D. Hug, and L. M. K. Vandersypen, *Gate-defined graphene double quantum dot and excited state spectroscopy*, Nano Lett. **10**, 1623 (2010).

[126] K. L. Chiu, M. R. Connolly, A. Cresti, J. P. Griffiths, G. A. C. Jones, and C. G. Smith, *Magnetic-field-induced charge redistribution in disordered graphene double quantum dots*, Phys. Rev. B. **92**, 155408 (2015).

[127] H. Grabert, *Single charge tunneling: a brief introduction*, Z. Phys. B Condensed Matter **85**, 319 (1991).

[128] M. H. Devoret, D. Esteve, and C. Urbina, *Single-electron transfer in metallic nanostructures*, Nature **360**, 547 (1992).

[129] S. Engels, Master's thesis, RWTH Aachen (2011).

[130] X. Li, W. Cai, J. An, S. Kim, J. Nah, D. Yang, R. Piner, A. Velamakanni, I. Jung, E. Tutuc, S. K. Banerjee, L. Colombo, R. S. Ruoff, *Large-area synthesis of high-quality and uniform graphene films on copper foils*, Science **324**, 1312 (2009).

[131] S. Bae, H. Kim, Y. Lee, X. Xu, J.-S. Park, Y. Zheng, J. Balakrishnan, T. Lei, H. R. Kim, Y. I. Song, Y.-J. Kim, K. S. Kim, B. Özyilmaz, J.-H. Ahn, B. H. Hong, and S. Iijima, *Roll-to-roll production of 30-inch graphene films for transparent electrodes*, Nat. Nanotechnol. **5**, 574 (2010).

[132] Y. Hao, M. S. Bharathi, L. Wang, Y. Liu, H. Chen, S. Nie, X. Wang, H. Chou, C. Tan, B. Fallahazad, H. Ramanarayan, C. W. Magnuson, E. Tutuc, B. I. Yakobson, K. F. McCarty, Y.-W. Zhang, P. Kim, J. Hone, L. Colombo, and R. S. Ruoff, *The role of surface oxygen in the growth of large single-crystal graphene on copper*, Science **342**, 720 (2013).

[133] Y. Zhan, Z. Liu, S. Najmaei, P. M. Ajayan, and J. Lou, *Large-area vapor-phase growth and characterization of MoS_2 atomic layers on a SiO_2 substrate*, Small **8**, 966 (2012).

[134] A. M. van der Zande, P. Y. Huang, D. A. Chenet, T. C. Berkelbach, Y. You, G.-H. Lee, T. F. Heinz, D. R. Reichman, D. A. Muller, and J. C. Hone, *Grains and grain boundaries in highly crystalline monolayer molybdenum disulphide*, Nat. Mater. **12**, 554 (2013).

[135] S. Najmaei, Z. Liu, W. Zhou, X. Zou, G. Shi, S. Lei, B. I. Yakobson, J.-C. Idrobo, P. M. Ajayan, and J. Lou, *Vapour phase growth and grain boundary structure of molybdenum disulphide atomic layers*, Nat Mater. **12**, 754 (2013).

[136] K. Kang, S. Xie, L. Huang, Y. Han, P. Y. Huang, K. F. Mak, C.-J. Kim, D. Muller, and J. Park, *High-mobility three-atom-thick semiconducting films with wafer-scale homogeneity*, Nature **520**, 656 (2015).

[137] G. H. Ahn, M. Amani, H. Rasool, D.-H. Lien, J. P. Mastandrea, J. W. Ager III, M. Dubey, D. C. Chrzan, A. M. Minor, and A. Javey, *Strain-engineered growth of two-dimensional materials*, Nat. Commun. **8**, 608 (2017).

[138] C. Berger, Z. Song, X. Li, X. Wu, N. Brown, C. Naud, D. Mayou, T. Li, J. Hass, A. N. Marchenkov, E. H. Conrad, P. N. First, and W. A. de Heer, *Electronic confinement and coherence in patterned epitaxial graphene*, Science **312**, 1191 (2006).

[139] J.-H. Lee, E. K. Lee, W.-J. Joo, Y. Jang, B.-S. Kim, J. Y. Lim, S.-H. Choi, S. J. Ahn, J. R. Ahn, M.-H. Park, C.-W. Yang, B. L. Choi, S.-W. Hwang, and D. Whang, *Wafer-scale growth of single-crystal monolayer graphene on reusable hydrogen-terminated germanium*, Science **344**, 286 (2014).

[140] H. Li, Y. Li, A. Aljarb, Y. Shi, and L.-J. Li, *Epitaxial growth of two-dimensional layered transition-metal dichalcogenides: growth mechanism, controllability, and scalability*, Chem. Rev. (2017).

[141] J. Cai, P. Ruffieux, R. Jaafar, M. Bieri, T. Braun, S. Blankenburg, M. Muoth, A. P. Seitsonen, M. Saleh, X. Feng, K. Müllen, and R. Fasel, *Atomically precise bottom-up fabrication of graphene nanoribbons*, Nature **466**, 470 (2010).

[142] P. Ruffieux, and S. Wang, and B. Yang, and C. Sánchez-Sánchez, and J. Liu, and T. Dienel, and L. Talirz, and P. Shinde, and C. A. Pignedoli, and D. Passerone, and T. Dumslaff, and X. Feng, and K. Müllen, and R. Fasel, *On-surface synthesis of graphene nanoribbons with zigzag edge topology*, Nature **531**, 489 (2016).

[143] S. Engels, Ph.D. thesis, RWTH Aachen University (2015).

[144] S. Reichardt and L. Wirtz, *Optical properties of graphene, chapter 3: Raman spectroscopy of graphene* (World Scientific Publishing Company, 2017).

[145] P. Tonndorf, R. Schmidt, P. Böttger, X. Zhang, J. Börner, A. Liebig, M. Albrecht, C. Kloc, O. Gordan, D. R. T. Zahn, S. Michaelis de Vasconcellos, and R. Bratschitsch, *Photoluminescence emission and Raman response of monolayer MoS_2, $MoSe_2$, and WSe_2*, Opt. Express **21**, 4908 (2013).

[146] X. Zhang, X.-F. Qiao, W. Shi, J.-B. Wu, D.-S. Jianga, and P.-H. Tan, *Phonon and Raman scattering of two-dimensional transition metal dichalcogenides from monolayer, multilayer to bulk material*, Chem. Soc. Rev. **44**, 2757 (2015).

[147] A. Molina-Sánchez and L. Wirtz, *Phonons in single-layer and few-layer MoS_2 and WS_2*, Phys. Rev. **84**, 155413 (2011).

[148] A. C. Ferrari, J. C. Meyer, V. Scardaci, C. Casiraghi, M. Lazzeri, F. Mauri, S. Piscanec, D. Jiang, K. S. Novoselov, S. Roth, and A. K. Geim, *Raman spectrum of graphene and graphene layers*, Phys. Rev. Lett. **97**, 187401 (2006).

[149] D. Graf, F. Molitor, K. Ensslin, C. Stampfer, C. H. A. Jungen, and L. Wirtz, *Spatially resolved Raman spectroscopy of single- and few-layer graphene*, Nano Lett. **7**, 238 (2007).

[150] T. M. G. Mohiuddin, A. Lombardo, R. R. Nair, A. Bonetti, G. Savini, R. Jalil, N. Bonini, D. M. Basko, C. Galiotis, N. Marzari, K. S. Novoselov, A. K. Geim, and A. C. Ferrari, *Uniaxial strain in graphene by Raman spectroscopy: G peak splitting, Grüneisen parameters, and sample orientation*, Phys. Rev. B **79**, 205433 (2009).

[151] D. Yoon, Y.-W. Son, and H. Cheong, *Strain-dependent splitting of the doubleresonance raman scattering band in graphene*, Phys. Rev. Lett. **106**, 155502 (2011).

[152] J. E. Lee, G. Ahn, J. Shim, Y. S. Lee, and S. Ryu, *Optical separation of mechanical strain from charge doping in graphene*, Nat. Commun. **3**, 1024 (2012).

[153] N. S. Mueller, S. Heeg, M. P. Alvarez, P. Kusch, S. Wasserroth, N. Clark, F. Schedin, J. Parthenios, K. Papagelis, C. Galiotis, M. Kalbáč, A. Vijayaraghavan, U. Huebner, R. Gorbachev, O. Frank, and S. Reich, *Evaluating arbitrary strain configurations and doping in graphene with Raman spectroscopy*, 2D Mater. **5**, 015016 (2018).

[154] S. Pisana, M. Lazzeri, C. Casiraghi, K. S. Novoselov, A. K. Geim, A. C. Ferrari, and F. Mauri, *Breakdown of the adiabatic born-oppenheimer approximation in graphene*, Nat. Mater. **6**, 198 (2007).

[155] C. Casiraghi, S. Pisana, K. S. Novoselov, A. K. Geim, and A. C. Ferrari, *Raman fingerprint of charged impurities in graphene*, Appl. Phys. Lett. **91**, 233108 (2007).

[156] C. Casiraghi, *Doping dependence of the Raman peaks intensity of graphene close to the Dirac point*, Phys. Rev. B **80**, 233407 (2009).

[157] L. G. Cancado, A. Jorio, E. H. Martins Ferreira, F. Stavale, C. A. Achete, R. B. Capaz, M. V. O. Moutinho, A. Lombardo, T. S. Kulmala, and A. C. Ferrari, *Quantifying defects in graphene via Raman spectroscopy at different excitation energies*, Nano Lett. **11**, 3190 (2011).

[158] A. J. Pollarda, B. Brennan, H. Stec, B. J. Tyler, M. P. Seah, I. S. Gilmore, and D. Roy, *Quantitative characterization of defect size in graphene using Raman spectroscopy*, Appl. Phys. Lett. **105**, 253107 (2014).

[159] C. Neumann, S. Reichardt, P. Venezuela, M. Drögeler, L. Banszerus, M. Schmitz, K. Watanabe, T. Taniguchi, F. Mauri, B. Beschoten, S. V. Rotkin, and C. Stampfer, *Raman spectroscopy as probe of nanometer-scale strain variations in graphene*, Nat. Commun. **6**, 8429 (2015).

[160] C. Volk, Ph.D. thesis, RWTH Aachen University (2016).

[161] A. Allain, J. Kang, K. Banerjee, and A. Kis, *Electrical contacts to two-dimensional semiconductors*, Nat. Mater. **14**, 1195 (2015).

[162] B. H. Moon, G. H. Han, H. Kim, H. Choi, J. J. Bae, J. Kim, Y. Jin, H. Y. Jeong, M.-K. Joo, Y. H. Lee, and S. C. Lim, *Junction-structure-dependent Schottky barrier inhomogeneity and device ideality of monolayer MoS_2 field-effect transistors*, ACS Appl. Mater. Interfaces **9**, 11240 (2017).

[163] T. Roy, M. Tosun, J. S. Kang, A. B. Sachid, S. B. Desai, M. Hettick, C. C. Hu, and A. Javey, *Field-effect transistors built from all two-dimensional material components*, ACS Nano **8**, 6256 (2014).

[164] L. Yu, Y.-H. Lee, X. Ling, E. J. G. Santos, Y. C. Shin, Y. Lin, M. Dubey, E. Kaxiras, J. Kong, H. Wang, and T. Palacios, *Graphene/MoS_2 hybrid technology for large-scale two-dimensional electronics*, Nano Lett. **14**, 3055 (2014).

[165] R. Kappera, D. Voiry, S. E. Yalcin, B. Branch, G. Gupta, A. D. Mohite, and M. Chhowalla, *Phase-engineered low-resistance contacts for ultrathin MoS_2 transistors*, Nat. Mater. **13**, 1128 (2014).

[166] L.M. Malard, M.A. Pimenta, G. Dresselhaus, and M.S. Dresselhaus, *Raman spectroscopy in graphene*, Phys. Rep. **473**, 51 (2009).

[167] R. Gorbachev, I. Riaz, R. R. Nair, R. J. L. Britnell, B. D. Belle, E. W. Hill, K. S. Novoselov, A. K. Geim, and P. Blake, *Hunting for monolayer boron nitride: optical and Raman signatures*, Small **7**, 465 (2011).

[168] K. Nakada, M. Fujita, G. Dresselhaus, and M. S. Dresselhaus, *Edge state in graphene ribbons: nanometer size effect and edge shape dependence*, Phys. Rev. B **54**, 17954 (1996).

[169] L. Brey and H. A. Fertig, *Electronic states of graphene nanoribbons studied with the Dirac equation*, Phys. Rev. B **73**, 235411 (2006).

[170] Y.-W. Son, M. L. Cohen, and S. G. Louie, *Energy gaps in graphene nanoribbons*, Phys. Rev. Lett. **97**, 216803 (2006).

[171] S. Dutta, S. Lakshmi, and S. K. Pati, *Electron-electron interactions on the edge states of graphene: a many-body configuration interaction study*, Phys. Rev. B **77**, 073412 (2008).

[172] A. A. Shylau, I. V. Zozoulenko, H. Xu, and T. Heinzel, *Generic suppression of conductance quantization of interacting electrons in graphene nanoribbons in a perpendicular magnetic field*, Phys. Rev. B **82**, 121410(R) (2010).

[173] A. A. Shylau and I. V. Zozoulenko, *Interacting electrons in graphene nanoribbons in the lowest Landau level*, Phys. Rev. B **84**, 075407 (2011).

[174] V. N. Kotov, B. Uchoa, V. M. Pereira, F. Guinea, and A. H. Castro Neto, *Electron-electron interactions in graphene: current status and perspectives*, Rev. Mod. Phys. **84**, 1067 (2012).

[175] S. Ihnatsenka and G. Kirczenow, *Effect of edge reconstruction and electron-electron interactions on quantum transport in graphene nanoribbons*, Phys. Rev. B **88**, 125430 (2013).

[176] A. D. Güçlü, M. Grabowski, and P. Hawrylak, *Electron-electron interactions and topology in the electronic properties of gated graphene nanoribbon rings in Möbius and cylindrical configurations*, Phys. Rev. B **87**, 035435 (2013).

[177] S. S. Kahnoj, S. B. Touski, and M. Pourfath, *The effect of electron-electron interaction induced dephasing on electronic transport in graphene nanoribbons*, Appl. Phys. Lett. **105**, 103502 (2014).

[178] C. R. Dean, L. Wang, P. Maher, C. Forsythe, F. Ghahari, Y. Gao, J. Katoch, M. Ishigami, P. Moon, M. Koshino, T. Taniguchi, K. Watanabe, K. L. Shepard, J. Hone, and P. Kim, *Hofstadter's butterfly and the fractal quantum Hall effect in moiré superlattices*, Nature **497**, 598 (2013).

[179] L. A. Ponomarenko, R. V. Gorbachev, G. L. Yu, D. C. Elias, R. Jalil, A. A. Patel, A. Mishchenko, A. S. Mayorov, C. R. Woods, J. R. Wallbank, et al., *Cloning of Dirac fermions in graphene superlattices*, Nature **497**, 594 (2013).

[180] X. Du, I. Skachko, F. Duerr, A. Luican, and E. Y. Andrei, *Fractional quantum Hall effect and insulating phase of Dirac electrons in graphene*, Nature **462**, 192 (2009).

[181] K. I. Bolotin, F. Ghahari, M. D. Shulman, H. L. Stormer, and P. Kim, *Observation of the fractional quantum Hall effect in graphene*, Nature **462**, 196 (2009).

[182] F. Amet, J. R. Williams, K. Watanabe, T. Taniguchi, and D. Goldhaber-Gordon, *Insulating behavior at the neutrality point in single-layer graphene*, Phys. Rev. Lett. **110**, 216601 (2013).

[183] D.-K. Ki and A. F. Morpurgo, *Crossover from Coulomb blockade to quantum Hall effect in suspended graphene nanoribbons*, Phys. Rev. Lett. **108**, 266601 (2012).

[184] J. Moser and A. Bachtold, *Fabrication of large addition energy quantum dots in graphene*, Appl. Phys. Lett. **95**, 173506 (2009).

[185] J. B. Oostinga, B. Sacé pé, M. F. Craciun, and A. F. Morpurgo, *Magneto-transport through graphene nanoribbons*, Phys. Rev. B **81**, 193408 (2010).

[186] M. Y. Han, J. C. Brant, and P. Kim, *Electron transport in disordered graphene nanoribbons*, Phys. Rev. Lett. **104**, 056801 (2010).

[187] D. Bischoff, A. Varlet, P. Simonet, M. Eich, H. C. Overweg, T. Ihn, and K. Ensslin, *Localized charge carriers in graphene nanodevices*, Appl. Phys. Rev **2**, 031301 (2015).

[188] D. Bischoff, T. Krähenmann, S. Dröscher, M. A. Gruner, C. Barraud, T. Ihn, and K. Ensslin, *Reactive-ion-etched graphene nanoribbons on a hexagonal boron nitride substrate*, Appl. Phys. Lett. **101**, 203103 (2012).

[189] S. Somanchi, B. Terrés, J. Peiro, M. Staggenborg, K. Watanabe, T. Taniguchi, B. Beschoten, and C. Stampfer, *From diffusive to ballistic transport in etched graphene constrictions and nanoribbons*, Ann. Phys. **529**, 1700082 (2017).

[190] J. Dauber, B. Terres, C. Volk, S. Trellenkamp, and C. Stampfer, *Reducing disorder in graphene nanoribbons by chemical edge modification*, Appl. Phys. Lett. **104**, 083105 (2014).

[191] F. Molitor, C. Stampfer, J. Güttinger, A. Jacobsen, T. Ihn, and K. Ensslin, *Energy and transport gaps in etched graphene nanoribbons*, Semicond. Sci. Technol. **25**, 034002 (2010).

[192] J. Alicea and M. P. A. Fisher, *Graphene integer quantum hall effect in the ferromagnetic and paramagnetic regimes*, Phys. Rev. B **74**, 075422 (2006).

[193] S. Russo, J. B. Oostinga, D. Wehenkel, H. B. Heersche, S.S. Sobhani, L. M. Vandersypen, and A. F. Morpurgo, *Observation of Aharonov-Bohm conductance oscillations in a graphene ring*, Phys. Rev. B **77**, 085413 (2008).

[194] D. Bischoff, F. Libisch, J. Burgdörfer, T. Ihn, and K. Ensslin, *Characterizing wave functions in graphene nanodevices: electronic transport through ultrashort graphene constrictions on a boron nitride substrate*, Phys. Rev. B **90**, 115405 (2014).

[195] K. Lee, G. Kulkarni, and Z. Zhong, *Coulomb blockade in monolayer MoS_2 single electron transistor*, Nanoscale **8**, 7755 (2016).

[196] Z.-Z. Zhang, X.-X. Song, G. Luo, G.-W. Deng, V. Mosallanejad, T. Taniguchi, K. Watanabe, H.-O. Li, G. Cao, G.-C. Guo, F. Nori, and G.-P. Guo, *Electrotunable artificial molecules based on van der Waals heterostructures*, Sci. Adv. **3**, e1701699 (2017).

[197] C. H. Sharma and M. Thalakulam, *Split-gated point-contact for electrostatic confinement of transport in MoS_2/h-BN hybrid structures*, Sci. Rep. **7**, 735 (2017).

[198] S. Bhandari, K. Wang, K. Watanabe, T. Taniguchi, P. Kim, and R. M. Westervelt, *Imaging electron motion in a few layer MoS_2 device*, Phys.: Conf. Ser. **864**, 012031 (2017).

[199] D. Wong, J. Velasco Jr, L. Ju, J. Lee, S. Kahn, H.-Z. Tsai, C. Germany, T. Taniguchi, K. Watanabe, A. Zettl, F. Wang and M. F. Crommie, *Characterization and manipulation of individual defects in insulating hexagonal boron nitride using scanning tunnelling microscopy*, Nat. Nano **10**, 949 (2015).

[200] T.Taniguchi and K.Watanabe, *Synthesis of high-purity boron nitride single crystals under high pressure by using Ba-BN solvent*, J. Cryst. Growth **303**, 525 (2007).

[201] C. Attaccalite, M. Bockstedte, A. Marini, A. Rubio, and L. Wirtz, *Coupling of excitons and defect states in boron-nitride nanostructures*, Phys. Rev. B **83**, 144115 (2011).

[202] S. Das Sarma, E. H. Hwang, S. Kodiyalam, L. N. Pfeiffer, and K. W. West, *Transport in two-dimensional modulation-doped semiconductor structures*, Phys. Rev. B **91**, 205304 (2015).

[203] Y. D. Kim, M.-H. Bae, J.-T. Seo, Y. S. Kim, H. Kim, J. H. Lee, J. R. Ahn, S. W. Lee, S.-H. Chun, and Y. D. Park, *Focused-laser-enabled p-n junctions in grapehne field-effect transistors*, ACS Nano **7**, 5850 (2013).

[204] A.Yurgens, N. Lindvall, J. Sun, Y. Nam, and Y. W. Park, *Control of the Dirac point in graphene by UV*, JETP Lett. **98**, 796 (2013).

[205] Z. Luo, N. J. Pinto, Y. Davila, and A. T. C. Johnson, *Controlled doping of graphene using ultraviolet irradiation*, **100**, 253108 (2012).

[206] B. Radisavljevic and A. Kis, *Mobility engineering and a metal-insulator transition in monolayer MoS_2.*, Nat. Mater. **12**, 815 (2013).

[207] B. W. H. Baugher, H. O. H. Churchill, Y. Yang, and P. Jarillo-Herrero, *Intrinsic electronic transport properties of high-quality monolayer and bilayer MoS_2*, Nano Lett. **13**, 4212 (2013).

[208] H. Schmitt, S. Wang, L. Chu, M. Toh, R. Kumar, W. Zhao, A. H. Castro Neto, J.Martin, S. Adam, B. Özyilmaz, and G. Eda, *Transport properties of monolayer MoS_2 grown by chemical vapor deposition*, Nano Lett. **14**, 1909 (2014).

[209] H. Shi, R. Yan, S. Bertolazzi, J. Brivio, B. Gao, A. Kis, D. Jena, H. G. Xing, and L. Huang, *Exciton dynamics in suspended monolayer and few-layer MoS_2 2D crystals*, ACS Nano **7**, 1072 (2013).

[210] M. Palummo, M. Bernardi, and J. C. Grossman, *Exciton radiative lifetimes in two-dimensional transition metal dichalcogenides*, Nano Lett. **15**, 2794 (2015).

[211] R. Dingle, H. L. Störmer, A. C. Gossard, and W. Wiegmann, *Electron mobilities in modulation-doped semiconductor heterojunction superlattices*, Appl. Phys. Lett. **33**, 665 (1978).

[212] J. M. Elzerman, R. Hanson, L.W. Van Beveren, B. Witkamp, L.M.K. Vandersypen, and L.P. Kouwenhoven, *Single-shot read-out of an individual electron spin in a quantum dot*, Nature **430**, 431 (2004).

[213] I. van Weperen, S. R. Plissard, E. P. A. M. Bakkers, S. M. Frolov, and L. P. Kouwenhoven, *Quantized conductance in an InSb nanowire*, Nano Lett. **13**, 387 (2013).

[214] A. T. Johnson, L. P. Kouwenhoven, W. De Jong, N. C. Van der Vaart, C. J. P. M. Harmans, and C. T. Foxon, *Zero-dimensional states and single electron charging in quantum dots*, Phys. Rev. Lett. **69**, 1592 (1992).

[215] S. Ghatak, A. N. Pal, and A. Ghosh, *Nature of electronic states in atomically thin MoS_2 field-effect transistors*, ACS Nano **5**, 7707 (2011).

[216] D. Liu, Y. Guo, L. Fang, and J. Robertson, *Sulfur vacancies in monolayer MoS_2 and its electrical contacts*, Appl. Phys. Lett. **103**, 183113 (2013).

[217] H. Qiu, T. Xu, Z. Wang, W. Ren, H. Nan, Z. Ni, Q. Chen, S. Yuan, F. Miao, F. Song, G. Long, Y. Shi, L. Sun, J. Wang, and X. Wang, *Hopping transport through defect-induced localized states in molybdenum disulphide*, Nat. Commun. **4**, 2642 (2013).

[218] S. McDonnell, R. Addou, C. Buie, R. M. Wallace, and C. L. Hinkle, *Defect-dominated doping and contact resistance in MoS_2*, ACS Nano **8**, 2880 (2014).

[219] J. Hong, Z. Hu, M. Probert, K. Li, D. Lv, X. Yang, L. Gu, N. Mao, Q. Feng, L. Xie, J. Zhang, D. Wu, Z. Zhang, C. Jin, W. Ji, X. Zhang, J. Yuan, and Z. Zhang, *Exploring atomic defects in molybdenum disulphide monolayers*, Nat. Commun. **6**, 6293 (2015).

[220] L. Britnell, R.V. Gorbachev, A.K. Geim, L.A. Ponomarenko, A. Mishchenko, M.T. Greenaway, T. M. Fromhold, K.S. Novoselov, and L. Eaves, *Resonant tunnelling and negative differential conductance in graphene transistors*, Nat. Commun. **4**, 1794 (2013).

[221] A. Mishchenko, J. S. Tu, Y. Cao, R. V. Gorbachev, J. R. Wallbank, M. T. Greenaway, V. E. Morozov, S. V. Morozov, M. J. Zhu, S. L. Wong, et al., *Twist-controlled resonant tunnelling in graphene/boron nitride/graphene heterostructures*, Nat. Nanotechnol. **9**, 808 (2014).

[222] B. Fallahazad, K. Lee, S. Kang, J. Xue, S. Larentis, C. Corbet, K. Kim, H. C. P. Mowa, T. Taniguchi, K. Watanabe, L. F. Register, S. K. Banerjee, and E. Tutuc, *Gate-tunable resonant tunneling in double bilayer graphene heterostructures*, Nano Lett. **15**, 428 (2015).

[223] S. Kang, B. Fallahazad, K. Lee, H. Movva, K. Kim, C. M. Corbet, T. Taniguchi, K. Watanabe, L. Colombo, L. F. Register, E. Tutuc, and S. K. Banerjee, *Bilayer graphene-hexagonal boron nitride heterostructure negative differential resistance interlayer tunnel FET*, IEEE Electron Device Lett. **36**, 405 (2015).

[224] G. W. Burg, N. Prasad, B. Fallahazad, A. Valsaraj, K. Kim, T. Taniguchi, K. Watanabe, Q. Wang, M. J. Kim, L. F. Register, and E. Tutuc, *Coherent interlayer tunneling and negative differential resistance with high current density in double bilayer graphene-WSe_2 heterostructures*, Nano Lett. **17**, 3919 (2017).

[225] Y.-C. Lin, R. K. Ghosh, R. Addou, N. Lu, S. M. Eichfeld, H. Zhu, M.-Y. Li, X. Peng, M. J. Kim, L.-J. Li, R. M. Wallace, S. Datta, and J. A. Robinson, *Atomically thin resonant tunnel diodes built from synthetic van der Waals heterostructures*, Nat. Commun. **6**, 7311 (2015).

[226] T. Roy, M. Tosun, X. Cao, H. Fang, D.-H. Lien, P. Zhao, Y.-Z. Chen, Y.-L. Chueh, J. Guo, and A. Javey, *Dual-gated MoS_2/WSe_2 van der Waals tunnel diodes and transistors*, ACS Nano **9**, 2071 (2015).

[227] R. Yan, S. Fathipour, Y. Han, B. Song, S. Xiao, M. Li, N. Ma, V. Protasenko, D. A. Muller,De. Jena, and H. G. Xing, *Esaki diodes in van der Waals heterojunctions with broken-gap energy band alignment*, Nano Lett. **15**, 5791 (2015).

[228] A. Nourbakhsh, A. Zubair, M. S. Dresselhaus, and T. Palacios, *Transport properties of a MoS_2/WSe_2 heterojunction transistor and its potential for application*, Nano Lett. **16**, 1359 (2016).

[229] S. Kang, X. Mou, B. Fallahazad, N. Prasad, X. Wu, A. Valsaraj, H. C. P. Movva , K. Kim, E. Tutuc, L. F. Register and S. K. Banerjee, *Interlayer tunnel field-effect transistor (ITFET): physics, fabrication and applications*, J. Phys. D: Appl. Phys. **50**, 383002 (2017).

[230] F. Capasso, S. Sen, F. Beltram, L. M. Lunardi, A. S. Vengurlekar, P. R. Smith, N. J. Shah, R. J. Malik, and A. Y. Cho, *Quantum functional devices: resonant-tunneling transistors, circuits with reduced complexity, and multiple valued logic*, IEEE Transactions on Electron Devices **36**, 2065 (1989).

[231] P. Mazumder, S. Kulkarni, M. Bhattacharya, J. P. Sun, and G. I. Haddad, *Digital circuit applications of resonant tunneling devices*, Proceedings of the IEEE **86**, 664 (1998).

[232] G. Liu, S. Ahsan, A. G. Khitun, R. K. Lake, and A. A. Balandin, *Graphene-based non-Boolean logic circuits*, J. Appl. Phys. **114**, 154310 (2013).

[233] J. Borghetti, G. S. Snider, P. J. Kuekes, J. J. Yang, D. R. Stewart, and R. S. Williams, *'Memristive' switches enable 'stateful' logic operations via material implication*, Nature **464**, 873 (2010).

[234] M. D. Pickett, G. Medeiros-Ribeiro, and R. S. Williams, *A scalable neuristor built with Mott memristors*, Nat. Mater. **12**, 114 (2013).

[235] W. Mönch, *Valence-band offsets and Schottky barrier heights of layered semiconductors explained by interface-induced gap states*, Appl. Phys. Lett. **72**, 1899 (1998).

[236] I. Popov, G. Seifert, and D. Tomànek, *Designing electrical contacts to MoS_2 monolayers: a computational study*, Phys. Rev. Lett. **108**, 156802 (2012).

[237] S. Das, H.-Y. Chen, A. V. Penumatcha, and J. Appenzeller, *High performance multilayer MoS_2 transistors with scandium contacts*, Nano Lett. **13**, 100 (2013).

[238] C. Gong, L. Colombo, R. M. Wallace, and K. Cho, *The unusual mechanism of partial Fermi level pinning at metal-MoS_2 interfaces*, Nano Lett. **14**, 1714 (2014).

[239] H. Liu, M. Si, Y. Deng, A. T. Neal, Y. Du, S. Najmaei, P. M. Ajayan, J. Lou, and P. D. Ye, *Switching mechanism in single-layer molybdenum disulfide transistors: an insight into current flow across Schottky barriers*, ACS Nano **8**, 1031 (2014).

[240] K. Fu, *Mobility degradation due to the gate field in the inversion layer of MOSFET's*, IEEE Electron Device Lett. **3**, 292 (1982).

[241] R. van Langevelde and F. M. Klaassen, *Effect of gate-field dependent mobility degradation on distortion analysis in MOSFET's*, IEEE Trans. Electron Devices **44**, 2044 (1997).

[242] S. Das and J. Appenzeller, *Where does the current flow in two-dimensional layered systems?*, Nano Lett. **13**, 3396 (2013).

[243] L. Esaki, *New phenomenon in narrow germanium p-n junctions*, Phys. Rev. **109**, 603 (1958).

[244] A. Senguptaa and S. Mahapatra, *Negative differential resistance and effect of defects and deformations in MoS_2 armchair nanoribbon metal-oxide-semiconductor field effect transistor*, J. Appl. Phys. **114**, 194513 (2013).

[245] H. Haug and A.-P. Jauho, *Quantum kinetics in transport and optics of semiconductors, Springer series in solid-state sciences* (Springer, 1996).

[246] S. Datta, *Quantum transport: atom to transistor* (Cambridge University Press, 2005).

[247] Y.-C. Chen, T. Cao, C. Chen, Z. Pedramrazi, D. Haberer, D. G. de Oteyza, F. R. Fischer, S. G. Louie, and M. F. Crommie, *Molecular bandgap engineering of bottom-up synthesized graphene nanoribbon heterojunctions*, Nat. Nanotechnol. **10**, 156 (2015).

[248] M. Corso, E. Carbonell-Sanromà, and D. G. de Oteyza, *On-surface synthesis II, fabrication of atomically precise graphene nanoribbons* (Springer, Cham, 2018).

[249] Z. Li, Y. Wang, A. Kozbial, G. Shenoy, F. Zhou, R. McGinley, P. Ireland, B. Morganstein, A. Kunkel, S. P. Surwade, L. Li, and H. Liu, *Effect of airborne contaminants on the wettability of supported graphene and graphite*, Nat. Mater. **12**, 925 (2013).

[250] A. Kozbial, X. Gong, H. Liu, and L. Li, *Understanding the intrinsic water wettability of molybdenum disulfide (MoS_2)*, Langmuir **31**, 8429 (2015).

[251] J. Gao, B. Li, J. Tan, P. Chow, T.-M. Lu, and N. Koratkar, *Aging of transition metal dichalcogenide monolayers*, ACS Nano **10**, 2628 (2016).

[252] B. L. Altshuler, A. G. Aronov, and D. E. Khmelnitsky, *Effects of electron-electron collisions with small energy transfers on quantum localisation*, J. Phys. C **15**, 7367 (1982).

[253] S. Hikami, A. I. Larkin, and Y. Nagaoka, *Spin-orbit interaction and magnetoresistance in the two dimensional random system*, Prog. Theor. Phys. **63**, 707 (1980).

[254] H. Fukuyama, *Effects of intervalley impurity scattering on the non-metallic behavior in two-dimensional systems*, J. Phys. Soc. Jpn. **49**, 649 (1980).

[255] A. T. Neal, H. Liu, J. Gu, and P. D. Ye, *Magneto-transport in MoS_2: phase coherence, spin-orbit scattering, and the Hall factor*, ACS Nano **7**, 7077 (2013).

[256] H. Peelaers and C. G. Van de Walle, *Effects of strain on band structure and effective masses in MoS_2*, Phys. Rev. B **86**, 241401(R) (2012).

[257] F. Pierre, A. B. Gougam, A. Anthore, H. Pothier, D. Esteve, and N. O. Birge, *Dephasing of electrons in mesoscopic metal wires*, Phys. Rev. B **68**, 085413 (2003).

[258] S. Engels, B. Terrès, A. Epping, T. Khodkov, K. Watanabe, T. Taniguchi, B. Beschoten, and C. Stampfer, *Limitations to carrier mobility and phase-coherent transport in bilayer graphene*, Phys. Rev. Lett. **113**, 126801 (2014).

[259] R. Ockelmann, A. Müller, J. H. Hwang, S. Jafarpisheh, Drögeler, B. Beschoten, and C. Stampfer, *Phase-coherent transport in catalyst-free vapor phase deposited Bi_2Se_3 crystals*, Phys. Rev. B **92**, 075417 (2015).

[260] M. B. Lundeberg, R. Yang, J. Renard, and J. A. Folk, *Defect-mediated spin relaxation and dephasing in graphene*, Phys. Rev. Lett. **110**, 156601 (2013).

[261] R. S. Gonnelli, F. Paolucci, E. Piatti, Kanudha Sharda, A. Sola, M. Tortello, Jijeesh R. Nair, C. Gerbaldi, M. Bruna, and S. Borini, *Temperature dependence of electric transport in few-layer graphene under large charge doping induced by electrochemical gating*, Sci. Rep. **5**, 9554 (2015).

[262] R. S. Gonnelli, E. Piatti, A. Sola, M. Tortello, F. Dolcini, S. Galasso, J. R. Nair, C. Gerbaldi, E. Cappelluti, M. Bruna, and A. C. Ferrari, *Weak localization in electric-double-layer gated few-layer graphene*, 2D Mater. **4**, 035006 (2017).

[263] D. Kochan, M. Gmitra, and J. Fabian, *Spin relaxation mechanism in graphene: resonant scattering by magnetic impurities*, Phys. Rev. Lett. **112**, 116602 (2014).

[264] D. V. Tuan, F. Ortmann, D. Soriano, S. O. Valenzuela, and S. Roche, *Pseudospin-driven spin relaxation mechanism in graphene*, Nat. Phys. **10**, 857 (2014).

[265] D. Kochan, S. Irmer, M. Gmitra, and J. Fabian, *Resonant scattering by magnetic impurities as a model for spin relaxation in bilayer graphene*, Phys. Rev. Lett. **115**, 196601 (2015).

[266] D. Akinwande, C. J. Brennana. S. Bunch, P. Egberts, J. R. Felts, H. Gao, R. Huang, J.-S. Kim, T. Li, Y. Li, K. M. Liechti, N. Lu, H. S. Park, E. J.Reed, P. Wang, B. I.Yakobson, T. Zhang, Y.-W. Zhang, Y. Zhou, and Y. Zhu, *A review on mechanics and mechanical properties of 2D materials-graphene and beyond*, Extreme Mech. Lett. **13**, 42 (2017).

[267] V. M. Pereira and A. H. Castro Neto, *Strain engineering of graphenes electronic structure*, Phys. Rev. Lett. **103**, 046801 (2009).

[268] F. Guinea, M. Katsnelson, and A. Geim, *Energy gaps and a zero-field quantum Hall effect in graphene by strain engineering.*, Nat. Phys. **6**, 30 (2010).

[269] F. Guinea, *Strain engineering in graphene*, Solid State Commun. **152**, 1437 (2012).

[270] Y. Wu, D. Zhai, C. Pan, B. Cheng, T. Taniguchi, K. Watanabe, N. Sandler, and M. Bockrath, *Quantum wires and waveguides formed in graphene by strain*, Nano Lett. **18**, 64 (2018).

[271] I. W. Frank, D. M. Tanenbauma, A. M. van der Zande, and P. L. McEuen, *Mechanical properties of suspended graphene sheets*, J. Vacuum Sci. Technol. B **25**, 2558 (2007).

[272] M. Poot and H. S. J. van der Zant, *Nanomechanical properties of few-layer graphene membranes*, Appl. Phys. Lett. **92**, 063111 (2008).

[273] C.-L. Wong, M. Annamalai, Z.-Q. Wang, and M. Palaniapan, *Characterization of nanomechanical graphene drum structures*, J. Micromech. Microeng. **20**, 115029 (2010).

[274] C. S. Ruiz-Vargas, H. L. Zhuang, P. Y. Huang, A. M. van der Zande, S. Garg, P. L. McEuen, D. A. Muller, R. G. Hennig, and J. Park, *Softened elastic response and unzipping in chemical vapor deposition graphene membranes*, Nano Lett. **11**, 2259 (2011).

[275] G. López-Polín, M. Jaafar, F. Guinea, R. Roldán, C. Gómez-Navarro, and J. Gómez-Herrero, *The influence of strain on the elastic constants of graphene*, Carbon **124**, 42 (2017).

[276] J. S. Bunch, S. S. Verbridge, J. S. Alden, A. M. van der Zande, J. M. Parpia, H. G. Craighead, and P. L. McEuen, *Impermeable atomic membranes from graphene sheets*, Nano Lett. **8**, 2458 (2008).

[277] S. P. Koenig, N. G. Boddeti, M. L. Dunn, and J. S. Bunch, *Ultra-strong adhesion of graphene membranes*, Nat. Nanotechnol. **6**, 543 (2011).

[278] D. Metten, F. Federspiel, M. Romeo, and S. Berciaud, *All-optical blister test of suspended graphene using micro-Raman spectroscopy*, Phys. Rev. Appl. **2**, 054008 (2014).

[279] F. Ding, H. Ji, Y. Chen, A. Herklotz, K. Dörr, Y. Mei, A. Rastelli, and O. G. Schmidt, *Stretchable graphene: a close look at fundamental parameters through biaxial straining*, Nano Lett. **10**, 3453 (2010).

[280] J. Zabel, R. R. Nair, A. Ott, T. Georgiou, A. K. Geim, K. S. Novoselov, and C. Casiraghi, *Raman spectroscopy of graphene and bilayer under biaxial strain: bubbles and balloons*, Nano Lett. **12**, 617 (2012).

[281] R. J. T. Nicholl, N. V. Lavrik, I. Vlassiouk, B. R. Srijanto, and K. I. Bolotin, *Hidden area and mechanical nonlinearities in freestanding graphene*, Phys. Rev. Lett. **118**, 266101 (2017).

[282] M. Goldsche, J. Sonntag, T. Khodkov, G. Verbiest, S. Reichardt, C. Neumann, T. Ouaj, N. von den Driesch, D. Buca, and C. Stampfer, *Tailoring mechanically-tunable strain fields in graphene*, Nano Lett. **18**, 1707 (2018).

[283] R. J. Nicholl, H. J. Conley, N. V. Lavrik, I. Vlassiouk, Y. S. Puzyrev, V. P. Sreenivas, S. T. Pantelides, and K. I. Bolotin, *Mechanics of free-standing graphene: stretching a crumpled membrane*, Nat. Commun. **6**, 8789 (2015).

[284] J.-W. Jiang, J.-S. Wang, and B. Li, *Young's modulus of graphene: a molecular dynamics study*, Phys. Rev. B **80**, 113405 (2009).

[285] M. M.Shokrieh and R. Rafiee, *Prediction of Young's modulus of graphene sheets and carbon nanotubes using nanoscale continuum mechanics approach*, Mater. Design **31**, 790 (2010).

[286] D. G. Papageorgiou, I. A. Kinloch, and R. J. Young, *Mechanical properties of graphene and graphene-based nanocomposites*, Prog. Mater. Sci. **90**, 75 (2017).

[287] S. Bertolazzi, J. Brivio, and A. Kis, *Stretching and breaking of ultrathin MoS_2*, ACS Nano **5**, 9703 (2011).

[288] A. Gupta, T. Sakthivel, and S. Seal, *Recent development in 2D materials beyond graphene*, Prog. Mater. Sci. **73**, 44 (2015).

[289] R. Zhang, V. Koutsos, and R. Cheung, *Elastic properties of suspended multilayer WSe_2*, Appl. Phys. Lett. **108**, 042104 (2016).

[290] A. Falin, Q. Cai, E. J. Santos, D. Scullion, D. Qian, R. Zhang, Z. Yang, S. Huang, K. Watanabe, T. Taniguchi, et al., *Mechanical properties of atomically thin boron nitride and the role of interlayer interactions*, Nat. Commun. **8**, 15815 (2017).

[291] D. Lloyd, N. B. X. Liu, L. Cantley, R. Long, M. L. Dunn, and J. S. Bunch, *Adhesion, stiffness, and instability in atomically thin MoS_2 bubbles*, Nano Lett. **17**, 5329 (2017).

[292] R. Levy and M. Maaloum, *Measuring the spring constant of atomic force microscope cantilevers: thermal fluctuations and other methods*, Nanotechnology **12**, 33 (2002).

[293] G. Kalosakas, N. N. Lathiotakis, C. Galiotis, and K. Papagelis, *In-plane force fields and elastic properties of graphene*, J. Appl. Phys. **113**, 134307 (2013).

[294] A. Föppl, *Vorlesungen über technische Mechanik, Bd. 5: die wichtigsten Lehren der höheren Elastizitätstheorie* (Teubner, Leipzig, 1907).

[295] T. Kármán, *Encyklopädie der Mathematischen Wissenschaften, Vol. IV:4* (Teubner, Leipzig, 1910).

[296] B. Mortazavi, A. Ostadhossein, T. Rabczuk, and A. C. T. van Duin, *Mechanical response of all-MoS_2 single-layer heterostructures: a ReaxFF investigation*, Phys. Chem. Chem. Phys. **18**, 23695 (2016).

[297] L.-P. Feng, N. Li, M.-H. Yang, and Z.-T. Liu, *Effect of pressure on elastic, mechanical and electronic properties of WSe_2: a first-principles study*, Mater Res Bull. **50**, 503 (2014).

Acknowledgements

At last, I would like to thank all the people who made this thesis possible:
First of all, I would like to thank Prof. Dr. Stampfer for giving me the opportunity to become a member of his great research team. This enabled me to work on such a recent and novel topic as graphene and other two-dimensional materials with all the excitement and challenges attached to it. The state-of-the art equipment and laboratories, which he provided in his institute, enabled me to perform cutting-edge experiments. Prof. Dr. Stampfer's continued encouragement to try completely new things and his endless enthusiasm and joy regarding them was always infectious. All this and his constructive support helped me to overcome any set backs and obstacles and was imperative for the outcome of my research.
I would like to thank Prof. Dr. Knoch for being my co-examiner and for his input on the negative differential conductance chapter. I would like to thank Prof. Hassler for the all the hours spent on discussing the theoretical background of my experiments; in particular regarding the quantum transport measurements in the MoS_2 constrictions. Dr. Bernd Beschoten for always having an open ear, the valuable input on my experiments and the administrative support.
Special thanks and all my gratitude goes to Luca Banszerus for all the days and nights in the clean room and lab fabricating, measuring and discussing the experiments, but also for all the time spent outside the institute. Without you, especially the MoS_2 part of the thesis would not have been possible.
I would like to thank Marc Drögeler, Michael Schmitz, Jens Sonntag and Markus Müller for the wonderful time doing physics, sports, and cooking. I definitely miss our weekly running sessions. I would also like to thank Sven Reichardt, Jan Dauber, Stephan Engels, Bernat Terrés, Christian Volk, Christoph Neumann, Regine Ockelmann, Martin Öllers, Shaham Jafarpisheh, Julian Peiro, Frank Volmer, Sowmya Somanchi and everyone who I might have missed from the group for the joyful but also very invigorating atmosphere!
I like to thank Stefan Trellenkamp for his most valuable input regarding the electron beam lithography and, of course, for the many ebeam jobs written. I am also very grateful for all the hours spent by Jörg Schirra and Sascha Mohr fixing the helium and nitrogen liquefier even over the weekends and seasonal holidays. I would like to thank Uwe Wichmann, Lars van Hove and Guido Geulen for all their technical support regarding electronics and vacuum techniques and the mechanical workshop for their quick solutions to all those small problems I encountered with the various se-

tups. Last but not least I would like to thank Beatrix Dangela for her administrative support and the little chats once in a while.
At the very end I would like to thank my family for always believing in me and supporting me in every possible way. Sarah, I would like to thank you for your patience, for your comfort after the inevitable small setbacks, for motivating me time and again, for bearing my little paranoia, for your helping hand, and just for being there together with our wonderful daughter Johanna, who made the last three months such a great joy despite the challenges of finishing this thesis.